City, University of London Institutional Repository

Full-vectorial study of light and sound interactions in low and high index contrast silica waveguides

Mohammed Moseeur Rahman

School of Mathematics, Computer Science and Engineering
City University London

This dissertation is submitted for the degree of
Doctor of Philosophy

Department of EEE

February 2016

I would like to dedicate this thesis to my loving parents.

Declaration

I hereby declare that except where specific reference is made to the work of others, the contents of this dissertation are original and have not been submitted in whole or in part for consideration for any other degree or qualification in this, or any other university. This dissertation is my own work and contains nothing which is the outcome of work done in collaboration with others.

<div align="right">

Mohammed Moseeur Rahman
February 2016

</div>

Acknowledgements

Abstract

A full-vectorial finite element based approach has been developed to find accurate modal solutions of acoustic modes in Ge-doped and un-doped planar silica waveguides. The structural symmetry is exploited and Aitken's extrapolation is also used to improve the accuracy of the solutions. The spatial dependences of the dominant and non-dominant displacement vectors are shown for the fundamental and higher order shear and longitudinal modes for Ge-doped core. The modal hybridness and modal birefringence between the two fundamental shear modes are also presented for this low index contrast waveguide. Further, rigorous analyses of the interactions between the guided acoustic and optical modes are performed for higher Ge-doped planar, for this case 10% doping is used. The Stimulated Brillouin Scattering (SBS) frequency and the overlaps between the fundamental and the higher order shear and longitudinal acoustic modes and the fundamental quasi-TE optical mode are presented. Brillouin gain spectrum for this moderate index contrast waveguide is determined. Furthermore, for a high index contrast air-clad rectangular silica strip waveguide, this program is used to accurately study the evolution of the acoustic modes. The existing structural symmetry is also exploited to reduce modal degeneration and to enhance the accuracy of the solutions. The interactions between the guided acoustic and optical modes are calculated after considering the full-vectorial nature of the modal fields. The SBS frequency and the overlaps between the fundamental and higher order acoustic modes with the fundamental quasi-TE optical mode are presented. The peak Brillouin gain, Brillouin gain spectrum (BGS), strength of Bragg gratings and threshold SBS power for this air-clad silica guide are also evaluated. Further comments are added on figure of merit (FOM) and acoustic attenuation coefficient for this air-clad silica waveguide.

Table of contents

List of figures

List of tables

List of Acronyms

AAOF   Acoustically Anti-guiding Optical Fibre

BDG   Brillouin Dynamic Grating

BGS   Brillouin Gain Spectrum

CHHM   Complex Highly Hybrid Acoustic Mode

DCF   Dispersion Compensated Fibre

DDF   Dispersion Decreasing Fibres

DSF   Dispersion Shifted Fibre

FDFD   Finite difference frequency Domain

FDTD   Finite Difference Time Domain Method

FEA   Finite Element Analysis

FEM   Finite Element Method

FFT   Fast Fourier Transform

FHD   Flame Hydrolysis Deposition

FVTD   Finite Volume Time Domain Method

FWM	Four-wave Mixing
FWHM	Full Width Half Maxima
GAWBS	Guided Acoustic Wave Brillouin Scattering
GVD	Group Veloctiy Dispersion
HBPCF	Highly Birefringent Photonic Crystal Fibre
HSW	Horizontal Sonic Wall
LEAF	Large Effective Area Fibre
OTDR	Optical Time Domain Reflectometry
PCF	Photonic Crystal Fibre
PECVD	Plasma Enhanced Chemical Vapour Deposition
PHDC	Perfect Horizontal Displacement Carrier
PIC	Photonic Integrated Circuit
PSTD	Pseudospectral Time Domain
PVDC	Perfect Vertical Displacement Carrier
PZT	Piezoelectric Transducer
RS	Rayleigh Scattering
SAW	Surface Acoustic Wave
SBS	Stimulated Brillouin Scattering

SBST   Stimulated Brillouin Scattering Threshold

SMF   Single Mode Fibre

SPM   Self-phase Modulation

SRS   Stimulated Raman Scattering

VSW   Vertical Sonic Wall

WDM   Wavelength Division Multiplexing

XPM   Cross-phase Modulation

List of Symbols

A Area

A_{eff} Effective Core Area

a Acceleration

C Elastic constant

c Light Speed in Vacuum

$[D]$ Symbol to represent symmetric gradient matrix

E Young's modulus

$\mathbf{E}(x,y,t)$ Total Electric Field

$\mathbf{E_t}$ Transverse electric field vector

E_1 Electric field of the First Signal

E_2 Electric field of the Second Signal

G_p Gain Contributed by Pump

Hb_X Hybridness (U_X/U_Z) for longitudinal mode

Hb_Y Hybridness (U_Y/U_Z) for longitudinal mode

I_o	Optical Intensity
j	Unit imaginary number $\left(\sqrt{-1}\right)$
k	Acoustic Propagation Constant or Wave Vector
k_o	Optical wavenumber in free space
K	Bulk modulus
$\Bbbk$	Prescribed constant value
L	Length of the fibre or guide
L_B	Polarization Beat Length
L_C	Phase Coherence Length
L_D	Dispersion Length
L_{eff}	Effective Length
L_{NL}	Non-linear Length
m	Mass
n	Refractive Index
$\mathbf{n}$	Unit vector normal to the surface
n_{eff}	Effective index
n_g	Group Refractive Index
n_x	Refractive Index Along x-direction

n_y	Refractive Index Along y-direction
n_o	Linear Refractive Index
n_2	Non-linear Refractive Index
$[N]$	Matrix for interpolation shape function
p_{12}	Elasto-optic coefficient
P_m	Peak Optical Power
P_p	Pump Power
S	Strain
∇_S	Symmetric gradient matrix
T	Stress
u	Displacement
$\mathbf{u}$	Displacement vector
u_x	Particle displacement vector along the x-axis
u_y	Particle displacement vector along the y-axis
u_z	Particle displacement vector along the z-axis
$\mathbf{U}$	Nodal displacement vector
U	Amplitude of Acoustic Displacement
U_i	Molecular displacement for acoustic wave

v	Velocity
$\bigvee$	Volume
V	Acoustic velocity
V_L	Longitudinal acoustic velocity
V_S	shear acoustic velocity
V_{L1}	Longitudinal acoustic velocity at material 1
V_{L2}	Longitudinal acoustic velocity at material 2
α	Optical attenuation coefficient
β_2	Group velocity dispersion
$\wp$	Polarization
$\chi^{(n)}$	n^{th}-order optical susceptibility
τ_o	Pulse Width
κ	Phase Mismatch
π	Pi $\simeq 3.14\ldots$
ε_o	Permittivity in free space
μ_o	Permeability in free space
Ω_w	Cross section area of waveguide
Ω_e	Domain of an element

$\hat{\varepsilon}$	Permittivity
$\hat{\mu}$	Permeability
θ_1	Incident angle of light
θ_2	Refracted angle of light
ϕ_{LI}	Potential of incident longitudinal wave
ϕ_{LR}	Potential of reflected longitudinal wave
Ψ_{SR}	Potential of reflected shear wave
λ	Lame constant
λ_a	Acoustic wavelength
λ_o	Optical Wavelength
ω	Acoustic angular frequency
ν	Poisson's ratio
μ	Sear modulus Lame constant
ρ	Material Density
$\Phi_{(NL)}$	Non-linear Phase Shift
$\Phi_{(NL)}^{\omega_{o1}}$	Non-linear Phase Shift Caused by the First Signal
$\Phi_{(NL)}^{\omega_{o2}}$	Non-linear Phase Shift Caused by the Second Signal
Ω	Acoustic Angular Frequency

ω_o Optical Angular Frequency

ω_{o1} Optical Angular Frequency of the First Signal

ω_{o2} Optical Angular Frequency of the Second Signal

ω_{o3} Optical Angular Frequency of the Third Signal

ω_{o4} Optical Angular Frequency of the Forth Signal

α_R Rayleigh Attenuation Coefficient

γ Measure of Non-linear Effect

g_R Gain of Raman Scattering

Chapter 1

Introduction

Stimulated Brillouin scattering (SBS) is a non-linear process of light-sound interaction in an inelastic manner in materials. The first prediction of this inelastic scattering of light by acoustic phonon was made by Brillouin in 1922 [Brillouin, 1922]. However, in 1918 Mandelstam suggested that the light could be scattered by thermally generated phonons, and this was published in 1926. That is why this process was referred before as Brillouin-Mandelstam light scattering process [Eggleton, 2013]. In 1964, the first ever observation of SBS process and coherent generation of intense hypersonic wave was reported in [Chiao, 1964]. This experiment was performed using a pulse ruby laser of 694 *nm* wavelength on quartz and sapphire crystals, where the SBS frequency shift were measured as 0.9 *cm*$^{-1}$ ($\sim$ 29.7 *GHz*) and 2.07 *cm*$^{-1}$ ($\sim$ 62 *GHz*), respectively for these two materials.

In early 1970s, acoustic waves in electromagnetic waveguides were studied and documented [Auld, 1973]. Even higher order finite element based analysis on surface elastic wave in guides was reported in [Lagasse, 1973] and for inhomogeneous structures was reported in [Stone, 1973]. Following that SBS process has been characterized and exploited by many researcher, categorically some specific contributions are presented below.

Study and characterization of the guidance of acoustic waves in optical waveguides and its interaction with optical waves have been researched extensively. Based on a perturbation analysis, the characterization of radial, flexural and torsional acoustics modes were reported in [Saffaai-Jazi, 1988]. For the first time the theory of forward stimulated Brillouin scattering in duel-mode single-core fibres was presented by [Russell, 1991]. The SBS process in single mode fibre (SMF) was studied by [Yeniay, 2002] and the accurate numerical solution of Brillouin gain spectrum (BGS) in SMF was reported in [Koyamada, 2004]. SBS process in dispersion engineered fibre has also been reported. [McIntosh, 1997] investigated SBS process in dispersion compensated fibre (DCF) using two laser sources of different linewidth at 1556 nm. Utilizing the feature of multiple-peak BGS due to the existence of multiple

acoustic modes in single-mode dispersion shifted fibre (DSF), [Zou, 2013] demonstrated an all-optical generation of Brillouin dynamic grating (BDG).

The effect of dopant concentration variation in fibre on parameters of SBS has also been investigated. For the first time, the pump and probe technique for Brillouin gain measurements in SMF was reported by [Nikles, 1997], where the researchers investigated how the BGS can be affected by strain, temperature and by variation in Ge doping in the core. A simplified model to study the effect of Ge doping in silica fibre on acoustic longitudinal modulus and damping coefficient was presented by [Dragic, 2009]. The influence of Fluorine doping in SMF on Brillouin scattering properties was reported in [Zou, 2008] and [Cannat, 2008] demonstrated shorter Brillouin shift with 1.6 times broader spectrum in Erbium-Ytterbium doped fibre compared with the undoped one. The experimental measurements of BGS in highly P-doped silica fibre was reported by [Law, 2011], along with they modelled the effects of dopant concentration variation on acoustic damping and temperature sensitivity coefficients. The detailed analysis of Brillouin properties of Al-doped silica fibre was reported by [Dragic, 2012], where the measurements showed that the thermal- and strain-acoustic coefficients of this fibre were not influenced strongly by the molar density of alumina.

Based on the measurements of stimulated Brillouin scattering threshold (SBST) carried over SMF with different refractive indices, [Ruffin, 2005] demonstrated the importance of considering refractive-index-dependent interaction between the acoustic and optical fields in addition to the optical effective area to account the difference in the SBST between fibre types. The importance of considering radial material displacements in acousto-optical interaction in fibres with complex radial index profile was demonstrated by [McCurdy, 2005]. Residual stresses inside optical fibres can influence BGS significantly, the effect of residual stress was analysed by [Mamdem, 2012].

SBS process imposes dominant nonlinear penalty among the problems arises in the communication systems. That is why, SBS suppression or SBST enhancement attracted lots of researchers attention and they used several techniques to achieve that. [Shiraki, 1996] reported a non-uniform dopant concentration along fibre's length can achieve 7 dB larger SBST than that of the conventional fibre in a 138 km transmission line with an input power of 16 dBm. A 8 dB enhancements of SBST was achieved by applying 40-step stair-ramp tensile-strain distributions in 580 m DSF by [Boggio, 2005], where the Brillouin frequency is observed to shift at a rate of 0.464 GHz/% as a function of the strain. Whereas, [Mishra, 2005] achieved 3 dB increase in SBST for SMF by incorporating a variation of refractive index along radius. A large effective area fibre (LEAF) for laser with Yb-doped double clad and Al/Ge co-doped core yielded [Li, 2007] a 6 dB higher SBST than that of LEAF without a co-doping scheme. A 4.3 dB higher SBST achieved was reported in [Mermelstein, 2009]

in Al-doped SMF compared to the Ge-doped SMF. Whereas, incorporating a non-uniform acoustic velocity profile with 5% velocity variation in the core, a 11 dB SBS suppression was achieved by [Ward, 2009]. A well known method for SBS suppression in optical fibres is broadening linewidth by phase and/or intensity modulation. Modulating phase by a filtered noise source a significant enhancement of linewidth was achieved by [Supradeepa, 2013] in a short fibre length. In [Park, 2014] a quasi-mode interpretation method was presented to analysis radiating acoustic modes in terms of discrete quasi-modes for an acoustically anti-guiding optical fibre (AAOF).

So far, many researchers also concentrated in characterizing acoustic modes and acousto-optical interactions with SBS suppression in photonic crystal fibre (PCF). Few selective highlights are presented here. The characterization of acoustic modes in PCF was presented by [Laude, 2005], where highly localized acoustic waves were generated by introducing defects in the transverse plane and aspect of this property in enhancing collinear acousto-optical interactions was considered. Nano-scale micro-structuring can affect significantly the Brillouin scattering. It was reported by [Dainese, 2006] that a PCF of solid silica core with a diameter around 70% of the light wavelength allowed much more tighter confinement of light compared with that of solid core glass SMF and generated a multi-peaked spectrum with Stokes frequency shift in 10 GHz range. [Haakested, 2006] reported an axial variations in acousto-optic phase-mismatch coefficient can increase coupling bandwidth significantly as compared to an axially uniform two-mode birefringent PCF. The acousto-optical coupling between torsional acoustic mode and fundamental two optical polarization modes were reported in [Lee, 2008] for an highly birefringent photonic crystal fibre (HBPCF). Taking in account both acoustic and optical birefringence a model for acousto-optical coupling for PCF was formulated and presented by [Lim, 2008]. [Pyatakova, 2009] demonstrated the influence of the frequency dependence of Bragg angle in formation of partial forbidden bands of optical and acoustic waves in 2D photonic crystals. The influence of the size of fibre core on the acoustic modes and Brillouing spectrum for PCF were illustrated in [Yuan, 2010]. Experimental and FEM based numerical results of simultaneous frequency-selective excitation of guided acoustic waves in a PCF with multi-scale structured design were presented in [Stiller, 2011], where strong impact of structural irregularities of the fibre on the frequency and modal shape of the acoustic wave were also discussed. Considering electrostriction, a model for acousto-optical interaction was presented by [Beugnot, 2012] to generate BGS in PCF, which showed strong proximity with experimental results. For SBS suppression, [Beugnot, 2007, Jan.] demonstrated a three-fold increase in SBST in a 160 m long solid-core PCF by introducing strain only. Later the same author reported [Beugnot, 2007, Nov.] forward Brillouin scattering in PCF can be enhanced substantially only for

fundamental acoustic waves because of the efficient transverse acousto-optic field overlap, which showed a completely different SBS dynamics comparing that of the standard silica fibres.

Comparatively very high Brillouin gain was achieved using chalcogenide as guide material. Some contributions in this field are illustrated here. Acoustic properties of evaporated chalcogenide glass films are reported in [Kushibiki, 1981], where it was shown that with appropriate composition ratio of As/S/Se the acoustic impedance of the chalcogenide film can be controlled with in a range of $5.53 - 9.3 \times 10^6$ $kgm^{-2}s^{-1}$. The Brillouin gain coefficient of As_2S_3 and As_2Se_3 chalcogenide glasses were estimated to be 20 times greater than that of fused silica by [Ogusu, 2004]. [Pant, 2011] demonstrated on-chip SBS at low-average power in a 7 cm long waveguide with a cross section of 4 $\mu m \times 850$ nm made by As_2S_3 rib on silica over Si wafer using pump-probe technique and backscattered signal. The measured Brillouin gain coefficient, linewidth and Brillouin frequency shift were 0.715×10^{-9} m/W, ~ 6 MHz and ~ 7.7 GHz respectively. Using SBS based broadband on-chip isolator in dispersion engineered As_2Se_3 chalcogenide rib waveguide with a length less than 10 cm, [Poulton, 2012] demonstrated a significant isolation greater than 20 dB. SBS process has emerged as a promising technology for microwave signal processing and generation with greater efficiency through the demonstration of low noise laser, continuously tunable delay, optical phase shifting, dynamically controlled grating and realization at on-chip scale. To incorporate the SBS process in photonic integrated devices with single pass and resonator geometry, chalcogenide as a choice of material, the device properties were presented by [Pant, 2014]. A 134 times larger Brillouin gain coefficient than fused silica fibre was demonstrated by [Abedin, 2005] in a 5 m long As_2Se_3 chalcogenide based SMF, where Brillouin frequency shift, gain linewidth and gain coefficient measured were 7.95 GHz, 13.2 MHz and 6×10^{-9} m/W respectively. Acouto-optical transmission resonance with a depth up to -9 dB and tunable over 235 nm around 1450 nm by creating a long period grating with variable period in a As_2Se_3 chalcogenide based SMF, was demonstrated by [Littler, 2006]. Also, [Florea, 2006] investigated Brillouin scattering in As_2S_3 and As_2Se_3 chalcogenide based SMF. An experimental demonstration of multi-wavelength Bragg grating, internally written by two-phonon absorption by 1550 nm pump and its backscattered first and second Stokes generated by cascaded SBS, in a As_2Se_3 chalcogenide fibre was made by [Buttner, 2012]. Whereas, [Beugnot, 2014, Feb] reported even further enhancement in SBS gain compared with both chalcogenide and silica optical fibres using a hybrid polymer-chalcogenide optical microwires.

As the SBS process provides a promising implication in nano-scale devices for the coming future, nano-structured and small-core optical waveguides have attracted attention to harness

and harvest stimulated Brillouin scattering (SBS), recently, by co-confining acoustic and optical waves and ensuring potentially strong interactions between them. It was also recently reported [Aryanfar 2014] that nearly 10% of the acousto-optical interactions value in nano-scale photonic devices could be due to radiation pressure and motion of boundaries. Some recent contributions based on small-core silica and nano-scale silicon waveguides are present here. A full-vectorial formulation of SBS coupling taking in account both electrostriction and radiation pressure for a nano-scale silicon waveguide was presented by [Qiu, 2013], where it had been shown that both played a significant role in SBS coupling when modal confinement approached sub-wavelength scale. Whereas, [Shin, 2013] reported SBS coupling over a range of 1 to 18 *GHz* by forward SBS process through tailorable travelling wave in a nano-scale silicon waveguide. A simulation based on SBS generated mode conversion in a high-contrast suspended silicon nano-scale waveguide with a dimension of $350 \times 300 \ nm^2$ was presented by [Aryanfar, 2014]. By considering the electrostriction [Laude, 2013] presented elastic energy spectrum for both forward and backward SBS scattering for small-core air-clad strip waveguide composed of silica and silicon, separately, with a dimension of $1.5 \times 1 \ \mu m^2$. The first experimental observation of SBS using surface acoustic wave was reported by [Beugnot, 2014, Oct.], where backscattering of light took place by a Rayleigh type hypersound wave travelling with velocity of 3400 *m/s* over a 8 *cm* long tapered silica microwire surface of diameter 1 *μm*. The Doppler shift was measured as 6 *GHz*. The author claimed that surface acoustic wave (SAW) Brillouin scattering possesses great potential in microwave photonics, non-linear plasmonics and sensing operation, as this acoustic resonance was found to be highly sensitive to surface defects and features. The author also observed a hybrid acoustic wave with a velocity of 5900 *m/s* at 9 *GHz* acoustic frequency in a silica microwire of diameter 0.5 *μm*.

This chapter, further, discusses the basic introduction to the non-linear effects in optical waveguides, giving emphasis, especially to the light scattering non-linearities. In addition it highlighted, some numerical methods in a brief, aims, objectives and area of expectation of this dissertation. It concludes with the illustration of the structure of this thesis.

1.1   Non-linear effects in optical waveguides

Relatively lower threshold towards optical non-linearities is one of the unique characteristics of optical fibres. The core size and the length can strongly enhance optical non-linearities. Mainly following three parameters are important in optical non-linearities,

- Effective core area A_{eff}: It is assumed that along A_{eff} the optical beam is uniformly distributed and is zero outside. The effective area for conventional single mode fibre

(SMF) is $\sim 80 \ \mu m^2$, for dispersion shifted fibre (DSF) is $\sim 50 \ \mu m^2$ and for dispersion compensated fibre (DCF) is $\sim 20 \ \mu m^2$ [Toulouse, 2005].

- Effective length L_{eff}: It is the length of the fibre or guide along which the signal amplitude is constant and zero beyond. For SMF with loss $\alpha = 0.2 \ dB/km$ the effective length is 21 km. Mathematically,

$$L_{eff} = \frac{1}{\alpha}\left(1 - e^{-\alpha L}\right) \tag{1.1}$$

here, α is the optical attenuation coefficient and L is fibre length.

- Group velocity dispersion (GVD) β_2: It is defined as, $\beta_2 \equiv -(\lambda_o^2/2\pi c^2)(dn_g/d\lambda_o)$, where n_g is group refractive index and $n_g \equiv n - \lambda_o(dn/d\lambda_o)$, λ_o is the optical wavelength, n if the refractive index. Positive β_2 indicates normal dispersion, here longer wavelength travels faster and negative β_2 indicates anomalous dispersion, here shorter wavelength travels faster.

The optical non-linearities outlined here are results from the interactions of optical fields and acoustic wave simultaneously present in the fibre or waveguide. These non-linearities are involved with switching, the controlling of the spectral and temporal shape of pulses, the generation of new frequency or wavelength, the wavelength conversions and giving rise to gain. Generally optical non-linearities can be divided in two groups [Agrawal, 2013]:

1. The non-linearities resulted from the change of refractive index by optical signals. This may cause either phase modulation or generation and mixing of channel frequencies. It includes,

    - Self-phase modulation (SPM)
    - Cross-phase modulation (XPM)
    - Four-wave mixing (FWM)

2. The non-linearities resulted by scattering. It includes,

    - Stimulated Raman scattering (SRS)
    - Stimulated Brillouin scattering (SBS)

If any real physical system is over driven it may exhibit non-linear response. In an optical system if the intensity of the pump is sufficient, it will also exhibit non-linearity. This

non-linearity is demonstrated in the polarization of the guide material. All these type of non-linearities, addressed above, may be raised due to the intensity of optical field, which may modify the material response and can be found from the power series expansion of the polarization in terms of total applied optical field E [Boyd, 2008] as below,

$$\wp = \varepsilon_o \left(\chi^{(1)} E + \chi^{(2)} EE + \chi^{(3)} EEE + \dots \right) \quad (1.2)$$

here, $\wp$ is the polarization, ε_o is free space permittivity and $\chi^{(n)}$ is the nth-order susceptibility at optical frequencies.

The FWM can be expressed in terms of the real part of the susceptibility that is related with the refractive index. Whereas, both SRS and SBS can be related to the imaginary part of the susceptibility, which is associated with the material response time or phase delay [Toulouse, 2005]. At this stage it is important to define some other important lengths those can be associated with the development of these non-linearities. These length become important only if they are shorter or at least comparable to L_{eff} of the fibre. In addition some other essential terms are defined below, as well.

- Dispersion length (L_D): The dispersion length is $L_D \equiv \tau_o^2/|\beta_2|$, where τ_o is the width of a pulse and β_2 is the GVD.

- Non-linear length (L_{NL}): A co-propagating pump with a signal in a medium can contribute to the non-linearities, as long as it is strong enough. $L_{NL} = (G_p P_p)$, is the length over which the pump can effectively contribute towards the gain. Here G_p is the gain and P_p is the pump power.

- Phase coherence length (L_C): It is defined as, $L_C = 2\pi/|\kappa|$, where κ is phase mismatch. This length is important while considering phase mismatch non-linearities, along which co-propagating optical waves may lose their mutual phase coherence.

- Polarization beat length (L_B): It is defined as, $L_B = 2\pi/|n_x - n_y|$, here n_x, n_y are the refractive indices along x and y-direction, respectively. A 2π phase difference can be developed between x and y polarized fields of optical wave along this length. This length is important while considering polarization effects.

- Non-linear refractive index (n_2): The refractive index of a medium can be expressed as, $n = n_o + n_2 I_p$, where n_o is the linear refractive index, n_2 is the non-linear coefficient of refractive index and I_p is the pump intensity. The third-order susceptibility can be related to n_2 by, $n_2 = \frac{3}{8n_o} Re\left(\chi^{(3)}\right)$. For silica $n_2 \approx 2.6 \times 10^{-20} m^2/W$ [Toulouse, 2005].

- Measure of non-linear effect (γ): The magnitude of the non-linear effect can be expressed by, $\gamma = \frac{2\pi n_2}{\lambda_o A_{eff}}$, where λ_o is optical wavelength and A_{eff} effective area of the core. For silica based SMF, $\gamma \approx 20 km^{-1}W^{-1}$ [Toulouse, 2005].

- Non-linear Phase Shift $\Phi_{(NL)}$: Fibre non-linearities can introduces phase shift in the optical wave and this non-linear phase shift can be expressed as,$\Phi_{(NL)}(z) = \gamma P_m z = z/L_{eff}$, where P_m is the maximum peak power of optical signal and L_{eff} is the effective length of fibre given in Eq. 1.1.

1.1.1 Self-phase modulation (SPM)

All non-scattering type non-linearities mentioned earlier, are referred as $\chi^{(3)}$ non-linearities and resulted from the refractive index modulation due to the propagating optical wave intensity.

When a pulse propagates through a optical waveguide, it introduces variation in refractive index due to optical Kerr effect. This variation in refractive index will induce a phase shift in the propagating pulse, which broaden the frequency spectrum of the pulse. This spectral broadening can be calculated by taking time dependent derivative of non-linear phase shift as,

$$\triangle \omega_o(z,t) = -\frac{\partial \Phi_{(NL)}(z)}{\partial t} = -n_2 \frac{dI_p(t)}{dt} k_o z \qquad (1.3)$$

here, $\triangle \omega_o$ is the change in optical angular frequency, k_o is the optical wavenumber and I_p is the optical signal intensity. The time dependent derivative in the above equation ensures that due to SPM the leading edge of the propagating pulse with be red-shifted, whereas the tailing edge will be blue-shifted. The chromatic dispersion of fibre can either compensate or amplify this non-linear spectral broadening effect. Including the chromatic dispersion of the fibre, the pulse characteristics, such as, its temporal shape, spectrum and initial chirp influence the total effect of SPM. In the anomalous dispersion regime SPM can raise two other non-linear effects, soliton generation and modulation instability.

1.1.2 Cross-phase modulation (XPM)

If two optical signal co-propagate through a material, the intensity modulation of one signal will modulate the phase of the other signal. This is due to XPM. If the total electric field can be written as, $E(x,y,t) = 1/2[E_1 e^{-j\omega_{o1}t} + E_2 e^{-j\omega_{o2}t}] + c.c$, here E_1 and ω_{o1} are the electric

field and angular frequency, respectively, for the first optical signal, E_2 and ω_{o2} are the electric field and angular frequency, respectively, for the second optical signal. Then the non-linear phase change can be written as,

$$\Phi_{(NL)}^{\omega_{o1}}(z) = \gamma[|E_1|^2 + 2|E_2|^2] \tag{1.4}$$

The first term is due to SPM and the second term is due to XPM. So, XPM caused spectral broadening is twice as large as that of in SPM. A similar non-linear phase change, $\Phi_{(NL)}^{\omega_{o2}}(z)$, can be written for the second signal as well. The condition for these phase change to occur is that the group velocities need to be same, so that, two signals can overlap in time and in space. In case of pulses two signals should have equal GVDs to avoid the walk-off from each other. Energy exchange between signals does not happen in XPM, rather it has significant effect on pulse time and shape changing. For this reason XPM can have advantageous role in control application.

The XPM attracted attention in wavelength conversion for being a very fast process. It can results in simultaneous multiple wavelengths conversion and can scale to a high bit rates with negligible signal degeneration or none at all. On the other hand, XPM can cause problem in WDM communication network by inducing cross-talk between nearby channels. If a limited amount of residual dispersion can be introduced to the system, this problem can be addressed.

1.1.3 Four-wave mixing (FWM)

When two or more optical signal wavelengths interact in a guide, this give rise to a non-linear parametric process known as four-wave mixing. In addition to the requirement of a high level of optical power, this coherent process also needs that the optical signals should have same phase velocity, i.e., be phase matched. In general, interacting three optical wavelengths can generate a new forth wavelength (idler) and this process requires the energy conservation and wave vector conservation should be maintained.

One of the most common application of FWM is wavelength conversion. Another application is parametric amplification. It is the basis of parametric optical amplifiers and lasers, which results from the degenerate FWM process. Where a strong pump at ω_{o1}, if launched with a weak signal of frequency ω_{o3}, amplifies the weak signal and generates the idler of frequency ω_{o4}. It can also be applied for optical regeneration of reshaping of pulses. It can also be used for simultaneous measurement of the chromatic dispersion and non-linear coefficient of fibre by evaluating FWM generating efficiency [O. Aso, 2000]. The

detrimental effect of FWM in WDM is that it can generate a similar wavelength signal from the interactions of the existing wavelengths, and can be minimized by ensuring unequal channel spacing in WDM network.

1.1.4   Stimulated Raman Scattering (SRS)

Raman scattering is an inelastic process and to address it, vibrational modes that exists in molecular structure is to be considered. Raman scattering results from the interaction between these molecular vibrational modes and incident light and its energy can be expressed in terms of phonon [Cho, 2002]. In this process the incident phonon either gains or losses energy. Thus Stokes signal generates in case of energy is lost and anti-Stokes in case energy is gained. Raman scattering occurs over a wide range of frequencies in silica glass for the reason that the molecules in silica are amorphous or non-crystalline in nature, which leads to different vibrational energies for different groups of molecules with in its structure. The Stokes and anti-Stokes exhibits broadband spectra for this reason. In fact, the wavelength range for this scattering process can extend up to 230 nm from the incident wavelength with peak at 100 nm [Seo, 2001].

Raman scattering can be applicable in distributed temperature sensing [Alahbabi, 2005]. Since the SRS gain can be found at a large shifted wavelength from pump (13 THz of 100 nm at 1550 nm in silica), this process can be used in wavelength conversion [Toulouse, 2005]. From late 90s it has attracted attention in fibre amplifiers and lasers, and has been exploited in optical modulation and switching.

1.1.5   Stimulated Brillouin scattering (SBS)

Light scattering can happen with fluctuations of optical properties in guide material. If this fluctuation is induced thermally, the light scattering is process is called spontaneous and if this fluctuation is caused by the electric field of the guided optical wave, it is said to be stimulated. Stimulated light scattering is much more efficient than spontaneous scattering [Boyd, 2008]. SBS is the most important example among stimulated light scattering processes.

The SBS is an inelastic nonlinear process that results from two-way interaction between mechanical and electromagnetic waves, where the optical wave generates acoustic wave in the waveguide through which it is guided and also can be scattered by it [Eggleton, 2013]. This phenomenon generally takes place when an intense optical pump wave, while being guided through the medium, produces a mechanical vibration in the material due to its large electric field, through electrostriction process. This vibration produces density fluctuations and modulates the refractive index of the medium [Agrawal, 2007]. This modulated refractive

index acts as an index grating and scatters the optical wave as Stokes waves. Beating of the Stokes and the pump waves further stimulates this scattering process [Boyd, 2008].

Through two different mechanisms the interference of pump and Stokes waves can drive the acoustic vibrations. The first mechanism is electrostriction, it is the tendency of the material to become more dense in the presence of high optical intensity. The other mechanism is optical absorption. In the high optical intensity regions due to optical absorption heat is generated and the material tends to expand causing acoustic disturbance. Absorptive SBS occurs only in lossy optical media, so this process is seldom used.

SBS process can either be a generation process or an amplification process. In SBS generation only pump is applied externally. In the interaction region from thermally generated noise the Stokes and acoustic waves start to grow. Whereas, in SBS amplification both pump and Stokes wave are applied externally as counter propagating. Because the spatial overlap of the pump and Stokes waves is greater if they are counter propagating, backscattered SBS process is usually observed [Boyd, 2008].
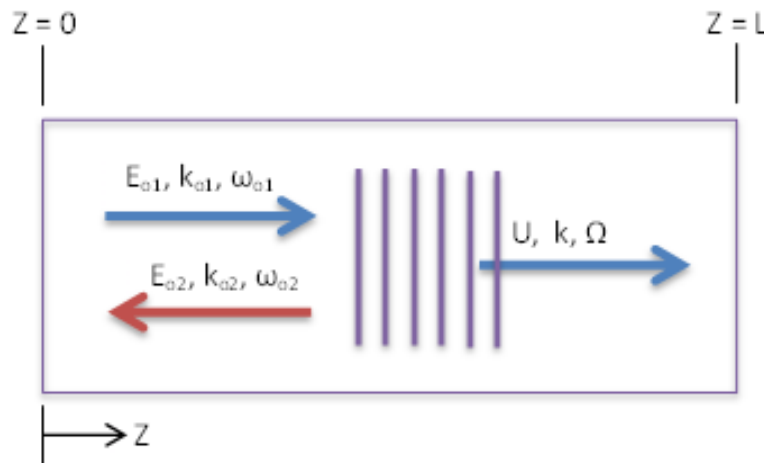
Fig. 1.1 Schematic representation of SBS process.

Even the scattered light can become quite intense when the incident pump field has sufficiently high intensity in spontaneous scattering. Through the beating of these two light fields density variations in the material can arise by means of electrostriction, as stated earlier. The incident pump can then further scattered off by refractive index modulation induced by these density variations. This generated Stokes will constructively add up with the previously created scattered light that started the acoustic vibration. By this way, until the acoustic wave and Stokes attain sufficiently large amplitude, they continue to reinforce each other's development. This whole process is illustrated in Fig. 1.1, where the blue arrows represent the forward propagation directions and the red arrow represents the backward

motion direction. The incident pump of amplitude E_1, wave vector k_{o1} and angular frequency ω_{o1} is scattered off as Stokes of amplitude E_2, wave vector k_{o2} and angular frequency ω_{o2} due to acoustic vibration of amplitude U, wave vector k and angular frequency Ω.

Since, the incident light is being scattered by the co-propagating acoustic wave as Stokes, the angular frequency of the Stokes, ω_{o2}, will be down shifted and can be expressed as,

$$\omega_{o2} = \omega_{o1} - \Omega. \tag{1.5}$$

The acoustic angular frequency can be related to the acoustic wave vector by phonon dispersion relation as,

$$\Omega = |k|v \tag{1.6}$$

here v is the velocity of acoustic wave. It was assumed that the acoustic wave is driven by the beating of Stokes and incident wave, so, the acoustic wave vector can be expressed as,

$$k = k_{o1} - k_{o2}. \tag{1.7}$$

Replacing Eq. (1.7) in Eq. (1.6), the acoustic angular frequency,

$$\Omega = \frac{vn}{c}(\omega_{o1} + \omega_{o2}) \tag{1.8}$$

here n is the refractive index and c is the speed of light at vacuum, which are related to the optical wave vector as, $|k_i| = n\omega_i/c$. Now, placing Eq. (1.5) in the above equation and approximating $v \ll c/n$, the Eq. (1.8) can be rewritten as,

$$\Omega = \frac{2vn}{c}\omega_{o1} \tag{1.9}$$

At this stage, the acoustic wave vector can be expressed as,

$$k = 2k_{o1} \tag{1.10}$$

which indicates that phase matching and energy conservation is the condition for ensuring interaction of incident light wave and acoustic wave.

Materials of choice

SBS process may appear in all states of materials, such as, in gases, liquids, solids and plasma. So far, SBS has been explored in quite a good number of materials through various experiments in last few decades. The optimization of the choice of material for a particular system to explore SBS, the factors [Damzen, 2003] play the role are, lasing wavelength, pulse duration, gain coefficient, absorption in the medium, phonon life time etc, but mainly the Brillouin gain coefficient, acoustic frequency and decay time. Other secondary considerations are, threshold power for other non-linear effects, specially for breakdown and material transparency for the chosen wavelength. For the system that works in low power and have short pulse duration, high Brillouin gain and short decay time will be suitable choices.

Applications of SBS

Recently, integrated on-chip and nano-structured optical waveguides have attracted attention to harness and harvest stimulated Brillouin scattering (SBS) by co-confining acoustic and optical waves and ensuring potentially strong interactions between them [Laude, 2011 and Eggleton, 2013]. Although SBS impairs the possibility of high power delivery, as it occurs at lower power level than other known non-linear scattering effects [Agrawal, 2007 and Boyd, 2008], however, SBS can also be enormously useful and being exploited in a number of fields, such as, tailoring the acousto-optical interaction [Shin, 2013], distributed strain and temperature sensing [Thevenaz, 1998], Brillouin cooling [Bahl, 2012], slow and fast light [Song, 2006], both microwave signal processing [Chin, 2010] and generation [Li, 2013], chip based microwave filter [Marpaung, 2015], and on-chip based nano-photonic devices [Shin, 2013]. It was also recently reported [Aryanfar, 2014] that nearly 10% of the acousto-optical interactions value in nano-scale photonic devices could be due to radiation pressure and motion of boundaries. SBS process can also be effective in imprinting dynamic gratings in guiding material [Sancho, 2012] to produce intense phase-conjugate beams through Brillouin-enhanced four-wave mixing [Buttner, 2014] non-linear process. It can also be useful in opto-mechanics [Bahl, 2013] and development of ultra narrow bandwidth lasers [Al-Mansoori, 2009].

1.1.6   Comparison of Brillouin and Raman scattering in silica fibre

Mainly SRS differs from SBS in three different ways. Firstly, although its gain ($g_R = 1 \times 10^{-13} m/W$) is lower than SBS gain, SRS occurs at much higher power, typically greater than $\sim 1W$ [Toulouse, 2005]. Secondly, the Raman frequency shift, which is 13 THz in silica, is much greater than SBS frequency shift, which is in 11 GHz level. Thirdly, in SRS both Stokes and anti-Stokes are generated [Vilhelmsson, 1986]. Some Comparisons between SRS and SBS in different medium are presented below, these are according to [Damzen, 2003].

- The frequency shift in SBS is considerably smaller with a order of 0.1 cm^{-1}, whereas in SRS appears with a order of 1000 cm^{-1}. As the gain bandwidth in most of the materials is quite larger than the Brillouin shift, it offers the potential of re-amplification for backscatter pulse in many laser system.

- The phonon damping time in SBS is in nano-second range that may produce some transient phenomena in the scattering process. But for SRS it is in pico-second range.

- For the requirement of phase matching condition in SBS, it is not possible to have any forward scattering in isotropic medium, only backward scattering occurs. Whereas, in SRS both types of scattering may occur. Usually gain is maximum in forward direction.

- Relatively large frequency shift of the Stokes put forward limitations for phase-conjugation possibility in Raman Scattering. Whereas, in Brilloin scattering as Stokes is spontaneously generated from acoustic vibration, it frequently induces phase-conjugated backscattered signal.

Table 1.1 Few properties of spontaneous Brillouin and Raman scattering for silica fibre at 1550 nm wavelength

Parameters	Brillouin	Raman
Gain bandwidth	$\sim 20 - 100 \; MHz$	$\sim 5 \; THz$
Gain peak	$\sim 5 \times 10^{-11} \; m/W$	$\sim 0.7 \times 10^{-13} \; m/W$
Frequency shift	$\sim 11 \; GHz$	$\sim 13 \; THz$
Power scattered	$\sim 15 \; dB$	$\sim 25 \; dB^{[Opalinska, 1993]}$

To have more insight, key differences between spontaneous Brillouin and Raman scattering are listed in Table 1.1 [Al-Ahbabi, Ph.D. thesis, 2005], based on the results in silica fibre at 1550 nm wavelength.

1.1.7   Rayleigh Scattering (RS)

Beside SRS and SBS another type of scattering process can be observed in optical fibres. This scattering process is known as Rayleigh scattering. In this scattering process no frequency shift takes place, so it is some times termed as elastic scattering process and the scattering occurs from non-propagating density fluctuations in the material. Rayleigh scattering may be resulted from random inhomogeneities in material density and variations in composition frozen in optical fibres during fabrication process. These disparities may cause variation in refractive index, which results in scattering process and the scattered light is guided backward than the incident light. Rayleigh scattering is an elastic process as in this process the frequency in the incident and backscattered light remain same. It is an intrinsic loss mechanism and it causes the leading loss in low-loss regime of optical fibres. Rayleigh attenuation coefficient is proportional to λ_o^{-4} and at 1550 nm for SMF it is $\alpha_R \approx 4.56 \times 10^{-5} \ m^{-1}$, which is equivalent to $\sim 0.2 \ dB/km$ fibre loss [Al-Ahbabi, Ph.D. Thesis, 2005].

In measuring fibre attenuation and detecting fibre damage, optical time domain reflectometry (OTDR) systems based on Rayleigh scattering has been successfully exploited. Distributed temperature sensing by using liquid core fibre based on Rayleigh backscattered measurements was reported in [Hartog, 1983], although, the performance of Rayleigh scattering based sensing process is very poor in measuring strain and temperature change.

1.2   Numerical methods

Numerical simulation and modelling has become important tool for analysing and comprehending any scientific task with the enormous growth of computing power. This growth brings forth many numerical methods. Any good researcher should have the knowledge and understanding about the proper uses of these methods in wherever these are applicable. Few such methods related to the electromagnetic problem solution, such as, Finite Difference Time Domain method, Finite Volume methods, Finite Element methods and Spectral methods are briefly illustrated below.

1.2.1   Finite difference time domain (FDTD) method

Although, FDTD method has its advantage of being a very simple numerical method, as the derivation of difference equation is straight forward, but before 1990s, its progress was hindered due to lack of computing memory [Inan, 2011]. As, here, the simulation space needs to be discretized in sub-wavelength scale with very small time steps. With the growth of computing power FDTD method has overcome this hurdle. For a transient or broadband

analysis the FDTD method is very useful. But it faces hardship in implementing dispersive materials, as in this case, it either requires auxiliary equations or convolution terms. The FDTD method has following advantages,

- *Short development time*: Its discretization process is very simple, needs short time of development.

- *Ease of comprehension*: Simple discretization procedure leads to simplicity in understanding.

- *Explicit in nature*: No linear algebra of matrix inversion is required.

However, it faces the following disadvantages,

- *Stair-stepping edges*: The orthogonal grid structure of the FDTD method creates problem in simulating curve boundaries if greater accuracy is sought, as creates staircase effect at the boundaries. So, it is restricted to regular structured grids.

- *Computational time*: In the FDTD method, the solution advancement time-step is limited by the spatial size, which cannot be larger than a certain maximum size.

1.2.2 Finite volume Time Domain (FVTD) method

The FVTD method has extreme flexibility in simulating irregular structures. It defines any working fields with small volume of spaces rather than nodes. These unit volumes can be arbitrarily defined, but usually considered as triangle in 2D and tetrahedra in 3D structures. The governing equation become very simple due to these structures and can be implemented with ease around complex and curved structure. To conserve the field quantities, this method uses integral forms of equations. For instance, the change in flux inside a unit volume with a given surface area in adjacent time steps must be balanced by the moving flux across the boundary area that moves into or out of the adjacent cells. The disadvantage of this method is that it needs to define or create an irregular grid of tetrahedral cells.

1.2.3 Finite difference frequency Domain (FDFD) method

The FDFD method is very useful and efficient in determining steady state solution in a single frequency, as it does not need the time stepping and the process is completed through a simple matrix inversion. It becomes very easy to implement dispersive material by the FDFD method, using scalar quantities (or vector quantities, for anisotropic dispersive material) for

permittivity and permeability at particular frequency. The problems associated with single frequency solution is suitable for this method. However, to deal with spectral response with FDFD, multiple simulations need to be run, one for each frequency of interest, where the resolution is limited by the number of computed simulations only. Thus it can be useful for problems associated with dispersive media.

1.2.4   Finite element (FEM) method

The FEM method was originated based on the work of A. Hrennikoff and R. Courant around 1940s and was known as Finite Element Analysis (FEA) as it was used for airframe structural analysis in the 1950s [Inan, 2011].

  The FEM method is very suitable for complex structure. In this method the simulation space can be divided with arbitrarily oriented, arbitrary shaped elements, commonly used triangle for 2D and tetrahedra for 3D. Here the governing equation is approximated over each element by some basis functions, which is a low-order polynomial. The solutions are made continuous at the boundaries of each element, and must be fit with in the enforced global boundary conditions. Its only disadvantage is the inherent complexity, as it requires some level of global knowledge of the simulation space. Although the used basis functions are local, as they are defined in each element, to enforce continuity at element boundaries a large sparse matrix needs to be solved, which enhances the computational time a lot. FEM is discussed in details later in Chapter 3.

  For last couple of year discontinuous Galerkin methods leap forefront in the field of electromagnetic simulations. By relaxing the continuity between elements this method enforces strict locality rule. This idea of connecting the elements along their boundaries was borrowed from the finite volume method. Thus it provides explicitly localized and highly accurate algorithms.

1.2.5   Spectral methods

To ensure result accuracy each of the methods above needs to discretise space with the resolution of 1/10 of a smallest wavelength in the simulation. This condition accumulate complexity and increase simulation time for multiscale problem solution. Whereas, the spectral methods only use two points per wavelength to perfectly reconstruct a wave, this concept was borrowed from the Nyquist theorem. The spectral methods are global. Here the simulation space are broken down to grid cells and a function, which covers the entire simulation space and usually a Fourier decomposition, approximates the solutions in a given time step.

The Pseudospectral Time Domain (PSTD) method has attracted attention in Maxwell's equation time domain simulation. Here, the approximation of spatial derivatives are completed by first taking the Fast Fourier Transform (FFT) of the spatial distribution of a field along a given axis, multiplying by jk_o, then taking the inverse FFT. This is used in the update equations and thus time marching proceeds. For this method, coarse grid is sufficient. The disadvantage are, slightly strict stability criteria by a factor $\pi/2$ and minimal increased numerical dispersion.

1.3   Aim and objectives

The main objective of this research is to develop further a full-vectorial FEM based computer simulation code to perform rigorous characterization of acoustic waves in low and hight index contrast optical waveguides and simultaneously study the interaction between optical and acoustic waves, specially due to SBS process. To ensure maximum SBS gain, prudent and effective contemplations are to be taken while considering design aspects of the optical waveguides with low and high index contrast. To achieve these targets the aim and objectives are stepwise illustrated below.

1. To study the essential parameters associated with acoustic wave propagation in material, mainly the physical quantities, for instance, stress, strain, elasticity, particle displacement and velocity etc.

2. To give emphasis in developing acoustic wave propagation model in optical waveguides relating material stress and strain, induced by propagating acoustic waves, through Hook's law by considering what ever particle displacement is caused in the material is small enough to hold the implication of this law.

3. To develop a full-vectorial FEM based computer simulation code for this model, so that real eigenvalue solver can be used to get the modal solutions and perform rigorous characterization and study the evolution of fundamental and higher-order acoustic modes profiles that may exists in low and high index contrast optical waveguides, giving prominence to the shear and longitudinal acoustics waves mainly. And compare these results with the other published literature.

4. To exploit symmetry boundary conditions to ensure modal solution accuracy that may be applicable for a given waveguide and thus to eliminate modal degenerations.

5. To incorporate denser mash topology in the developed computer simulation code to bring further accuracy in the acoustic modal solution that may be applicable for low and high index contrast silica waveguides.

6. To identify the fundamental and higher-order longitudinal and shear acoustic modes in embedded low Ge-doped silica core in pure silica cladding to form low index contrast optical waveguide and study their spatial variations to identify the mode patterns.

7. To study the variations of dispersion curves, variation of the modal hybridness with the acoustic frequency for the the fundamental and higher-order acoustics modes and thus find the influence of higher Ge doping in the core of silica planar waveguide. Also investigate the variation of overlap with guide width between the fundamental and higher-order acoustic modes and fundamental quasi-TE optical mode and calculate SBS frequency shift for this waveguide.

8. To incorporate air as one of the cladding medium in the simulation code for the acoustic wave.

9. To perform study on the evolution of the displacement vector profiles of the longitudinal and shear fundamental and higher-order acoustics modes with frequency in high index contrast silica waveguide with air cladding.

10. To investigate the light-sound interactions in an air-clad silica waveguide to study the effect of SBS and associated frequency shift. The overlap between the highly hybrid acoustic modes and fundamental H_{11}^Y optical mode also need to be calculated, thus to determine the Brillouin gain spectrum for a given bandwidth.

1.4   A brief comparison of COMSOL and in-house developed code

COMSOL Multiphysics is a finite element analysis based solver and Simulation software package for varieties of engineering and physics based applications, particularly for coupled phenomena. COMSOL is not an acronym, it is thought that the founder might be inspired by the words "**COMPUTER**" and "**SOL**UTION". COMSOL Multiphysics also permits for entering coupled systems of partial differential equation, besides conventional physics-based user interfaces. The PDEs can either be incorporated directly or using the weak form. Several add-on products are also available for COMSOL Multiphysics.

COMSOL Multiphysics software package works with electrical field while handling optical modal analysis in waveguides using finite element method for solving electromagnetic field problems by use of edge element, which has become very popular [Mur, 1994]. Edge elements can be used for computing electromagnetic fields in both homogeneous and inhomogeneous domains. They are vital tool for the modelling of electromagnetic fields along interfaces between regions with different medium properties. It can also facilitate the modelling of the field near a singularity.

To put forward a brief comparison of available commercial Software COMSOL Multiphysics and the in-house developed simulation code, I have no hesitation to accept the fact that COMSOL has the upper hand, but it would be interesting if the advantages of using nodal elements (which is used for in-house code) over edge elements in FEM can be presented that might instigate some things to ponder upon. The discussion is strictly kept limited on the facts revealed in the literature [Mur, 1994].

- *Numerical accuracy and efficiency*: For a triangular element in incorporating FEM, the edge element has only three unknowns, one on each edge. Whereas, a nodal triangular element has 9 unknowns, three at each of its three vertices. So, edge element yields higher local approximation error. Nodal elements are more efficient and accurate than edge elements, by a factor of 2 or even more.

- *Advantages in practical case implementation*: Nodal elements are more advantageous than edge elements for many practical cases, due to mainly two reasons. Firstly, many non-zero entries in the matrix turn out to be zero due to the orthogonality of the Cartesian directions used in nodal elements that can be used for optimization of a nodal element based code. Secondly, for imposing the continuity conditions at the interfaces between edge elements, the connectivity of the matrices increase significantly.

- *Storage requirements*: For using edge elements, the storage requirements become more than twice as expensive as linear nodal elements.

- *In terms of ill-condition*: Nodal elements, for the use of Cartesian coordinate system with mutually perpendicular coordinate directions, are therefore optimum when representing a vector field even in an extremely elongated element. Whereas, edge elements use base vectors that follow the orientation of the faces of the relevant element. When element deviates strongly from the optimum, being extremely elongated, these orientation of the vectors no longer remain mutually perpendicular. This will generate large error due to the resulting ill-condition of the system matrices.

- *Weakness in eliminating spurious solution*: Edge element allows the normal components of the field being represented to jump across the interfaces between adjacent elements. So, the edge elements cannot be used to ensure the elimination of unwanted solutions. Whereas, the in-house optical code uses a penalty function to minimise the spurious solution.

1.5 Structure of the thesis

The structure of this thesis is organized in such a way to cover the development of the model for the molecular displacements to depict the propagation of the acoustic waves, generation of a full-vectorial finite element method based computer code to simulate this model and implications of this simulation code to characterize acoustic waves, rigorously, in low and high index contrast silica waveguides. Further to evaluate interactions of light and sound in these optical waveguides, specially the stimulated Brillouin scattering, in terms of overlap between the fundamental and higher order shear and longitudinal acoustics modes and fundamental quasi-TE, H_{11}^{Y}, optical mode, SBS frequency shift and Brilloin gain spectrum.

Chapter: 1 commences with a categorical literature review and incorporates the brief introduction of this research work, also highlights the aim and objectives and presents the structure of the thesis. It also briefly illustrates the non-linearities presents in optical waveguides, emphasizing the stimulated Brillouin scattering process. Further it provides the introduction to the numerical methods.

Chapter: 2 will begin with the introduction to the basic concepts of acoustic waves in isometric medium, showing that the acoustic wave propagates through a optical guide by displacement of particles, where the guide material density and elasticity has major roles, thus modulates the optical refractive index through variation of material density along transverse plane and longitudinal direction, respectively. It will also discuss in greater details the physical quantities, those are related to the acoustic wave propagation and may arises the possibility of maximum interactions with optical waves in planar silica optical waveguides. Also it will aid to categorize acoustic modes depending on the placements of dominating acoustic displacement components related to the direction of propagation.

Chapter: 3 will describe the Variational approach based finite element method. Moreover, it will show the path way how to incorporate FEM formulation using real eigenvalue solver in acoustic wave propagation, and thus generation of 2D molecular displacement profiles of acoustic modes at end results. It will also show the introduction of symmetry boundary conditions, used for the first time in acoustic mode profile generation, to bring modal solution accuracy and elimination of modal degeneration. Furthermore, it will demon-

strate the strength of this simulation code proving its solution convergence with the help of Aitken's formula, also will provide some comparison with the previous work done in complex domain and with the published results of [H. -Hennion, 1996] for a 1 cm^2 steel waveguide in vacuum.

Chapter: 4 will report rigorous analysis of acoustic waves in the low index contrast silica planar waveguide consisting of a 3% Ge-doped core and pure silica cladding. Based on the pattern of spatial variations of displacement vector profiles of fundamental and higher order shear and longitudinal acoustic modes, this chapter will introduce the general concept of mode recognition in low index contrast silica planar waveguide. Furthermore, it will provide the detail study of the variations of dispersion, birefringence and hybridness with acoustic frequency for these acoustic modes, first considering decoupled modes, then considering co-existence of both shear and longitudinal modes. Also, the demonstrations of the influence of increasing doping concentration in the core will be presented here. Thus, this chapter will mainly concentrate on characterization of acoustic waves in this waveguide.

Chapter: 5 will mainly focus on the interactions between the fundamental and higher order shear and longitudinal acoustic modes and fundamental quasi-TE optical H_{11}^Y mode in terms of their coupling in phased matched condition through determining overlap between their mode profiles by considering displacement vector for acoustic wave and full-vectorial **H**-field for optical wave. This study will be performed in a moderately higher index contrast silica planar waveguide with a 10% Ge-doped core embedded in a pure silica cladding. It will highlight also, the displacement vector profiles, variation of modal dispersions, hybridness and birefringence with acoustic frequency and SBS frequency shift with the guide width variation.

Chapter: 6 will demonstrate the study of the unique feature of mode evolution in a high index contrast optical waveguide formed by an air-clad strip silica. For the first time it will show in details, how the highly hybrid acoustic modes in silica planar waveguide evolves with frequency - just for the choice of index combinations with relatively higher contrast. And the displacement vector profiles will be compared with the published results in [Laude, 2013]. Moreover, this chapter will also provide the analysis of variations of the modal dispersions, hybridness and birefringence with acoustic frequency for these highly hybrid acoustic modes and will show the interactions with quasi-TE optical mode through overlap and SBS frequency shift and thus will deliver the Brilloin gain spectrum for a specific bandwidth for this optical waveguide.

Chapter: 7 being a conclusive chapter, will demonstrate the strength of this newly developed full-vectorial finite element based computer simulation code in determining and analysing acoustic wave propagation in optical waveguide and also evaluating interactions

with the phase matched optical wave in optical waveguide of micro-meter dimension. Further, it will present the weakness of this code in determining acousto-optical interactions in nano-scale on-chip integrated optics, as it does not considered optical radiation pressure and motion of boundaries while formulation. Based on the recently published paper [Aryanfar, 2014] nearly 10% of the acousto-optical interactions value in nano-scale photonic devices could be due to radiation pressure and motion of boundaries. This chapter will conclude providing hints, how to incorporate these two important force parameters in the existing program to make it a strong simulation tool for on-chip nano-scale photonic devices as future expansion of this research work.

1.6   Summary

This chapter consists of the basic introduction to the research field of light-sound interactions in low and hight index contrast silica planar waveguide, particularly to emphasize the detrimental effect of non-linear SBS process in high power delivery and study the acoustic mode evolution. Also some discussions have been presented to highlight other optical non-linearities and existing numerical methods to study their effects. A brief illustration has also been given regarding the aims and objectives of this research. A comparison between the commercial software package COMSOL and in-house developed code was also incorporated. At the end the structure of the thesis also presented outlining the content of each chapter.

Chapter 2

Theory: Acoustic Wave Propagation

2.1 Introduction

Sound is a mechanical wave and generally created by object vibration. Periodic motion, in the particles close to the vibrating object, is set and thus energy is transferred through the medium by this mechanical vibration. Beside that acoustic wave can also be generated by time varying deformation or displacement of particles, consisting many atoms, in the material, where the atoms move in an accord to create the mechanical wave. Any particle displacement from equilibrium position gives rises a restoring force with it. The particles inertia in addition with in between elastic restoring forces lead to the oscillatory motion of the medium.

Acoustic waves can be associated with the material properties such as density, elasticity, Young's modulus, and Poisson's ratio [Auld, 1973]. The propagation of acoustic waves is associated with the displacement of the particles of the waveguide materials along the longitudinal direction and in the transverse plane. Modes in acoustic waveguides are complex in nature and have been traditionally categorized as torsional, bending, flexural, rotational or longitudinal [Thurston, 1978 and Saffaai-Jazi, 1988] type. However, the modes in acoustic waveguides with two-dimensional confinement are also hybrid in nature [Rahman, 2014].

Acoustic wave propagations need to be expressed in terms of the tensors and interrelation between those tensor quantities. The fact that, all solids are not isotropic, made the acoustic wave propagation in solids more complicated to express. For the sake of simplicity in presentation one assumption can be made, which is, the existing acoustic waves are either pure longitudinal or shear type and the corresponding physical quantities, such as, stress and strain, elasticity, particle velocity and displacement can be presented in one dimensional forms. This chapter commence with the one dimensional representation of the acoustic wave propagation, but actually, since the research works covered in this thesis, are associated

with the acoustic wave propagation in two dimensional straight waveguides, with uniform cross-section, 2D formulations will also be incorporated. The guided wave solutions are considered to have e^{-jkz} dependence, where z is the direction of wave propagation and k is the acoustic propagation constant.

2.2 Acoustic waves in non-piezoelectric materials: one dimensional concept

Among the propagating acoustic wave in material, two types are considered to be important, these are shear or transverse and longitudinal waves. In case of longitudinal wave the motion of the propagating particles are in the direction of the wave propagation. That is why, when longitudinal wave propagates medium is expanded and contracted periodically in the z-direction, which is depicted in Fig. 2.1(a). Whereas, for the shear wave, the particles motion occur in the transverse direction of the wave propagation, as shown in Fig. 2.1(b). Since the particles along the whole cross-section do not displace with equal magnitude, shear waves cannot be associated as merely as flexing or bending action of material, there occurs density variation in the transverse plane. But for simplicity sake, in one dimensional theory, it can be considered that there arises no volume or density variation with shear wave propagation, as illustrated in Fig. 2.1(b).

| (a) | (b) |
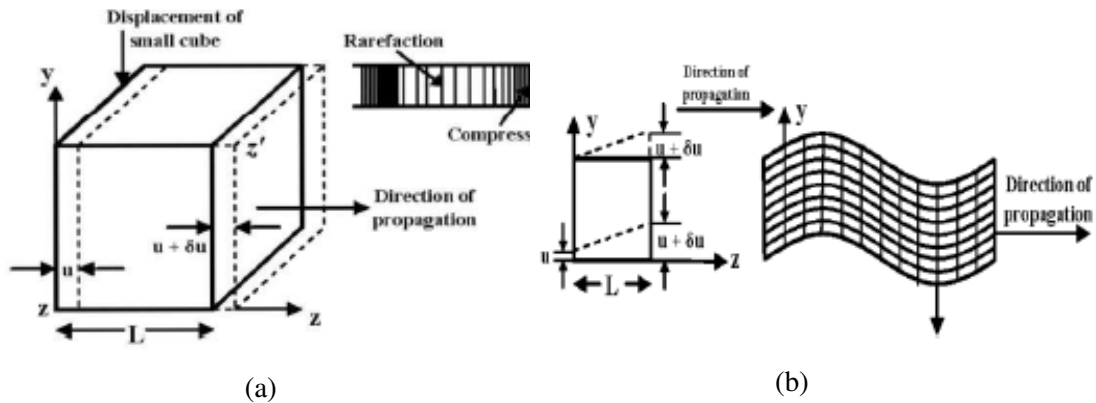
Fig. 2.1 (a) Longitudinal and (b) shear waves propagation [Sriratanavaree, Thesis, 2014].

Generally, when acoustic wave propagates through a material, it consists of both the shear and longitudinal waves. For crystalline medium with anisotropic elastic properties, as the direction of wave propagation, if one of the principle axes of the crystal lattice is considered, then the basic waves can be of purely transverse or longitudinal. The equation of motion for

acoustic wave propagation can be formulated considering longitudinal wave. However, if the shear wave propagation is considered the results would be similar.

2.2.1 Single dimensional stress

In general stress is defined as the applied force per unit area of material. The material is deformed whenever a force is applied to it. For one dimensional perspective, this deformation is either in the form of compression or rarefaction, depending on the direction of applied force. If we consider a material of infinitesimal length, L, the stress, $T(z)$ would the force per unit area on particles to the left side of the z plane, as shown in Fig. 2.2. The longitudinal stress, as depicted in Fig. 2.2(a), is considered to be positive if the applied external stress is on the right side of the slab, that is in the z-direction. And it is considered to be negative, if the external stress in applied on the left, in the opposite to the z-direction. Same definitions are applicable to the shear stress, if stress are taken to be positive in the transverse $+x$ or $+y$-directions.

(a)

(b)
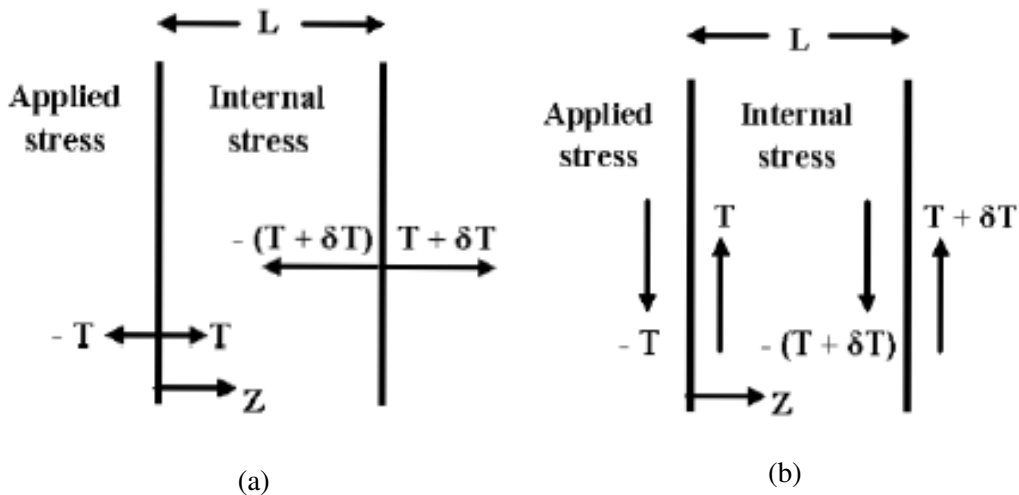
Fig. 2.2 For a slab of infinitesimal length L (a) stress in the longitudinal direction and (b) stress in the transverse direction [Sriratanavaree, Thesis, 2014].

The net difference in between the externally applied stresses on each side of the infinitesimal slab, if considered as $L(\frac{\partial T}{\partial z})$, then to move a unit volume of the mass relative to the mass centre the necessary force need to applied is $\frac{\partial T}{\partial z}$.

2.2.2   One dimensional displacement and strain

As a consequence of applied force, if due to the longitudinal stress the z-plane, in Fig. 2.1(a), is considered to be moved in the z-direction by an amount u, and in the some other plane z' after a distance L, if the displacement is varied to $u + \delta u$, then, the first order change in u in a unit length of L can be found using Taylor's expansion, as,

$$\delta u = L \frac{\partial u}{\partial z} = LS \tag{2.1}$$

The fractional extension of the material is called strain and can be defined as,

$$S = \frac{\partial u}{\partial z} \tag{2.2}$$

Here it is to be noted that u is merely a displacement and is a function of z. If the displacement remained constant for all over the length it would be nothing but bulk translation, which is out of the interest of this chapter. For transverse displacement in case of shear wave, same concept can be applicable and shear strain can be defined as, $S = \frac{\partial u}{\partial z}$, the only difference would be, u is transverse displacement in the x or y-directions, which is perpendicular to the direction of propagation.

As Fig. 2.1(b) indicates, no change in area occurs as the shear motion distorts the rectangle, but in case of longitudinal motion the change in volume can be calculated as $A\partial u$, here A is the area of x, y face. So, the relative change in volume is $\frac{\partial V}{V} = \frac{A\partial u}{LA} = \frac{\partial u}{L} = S$.

Hook's law state that for small distortion the stress is proportional to the strain, and for one dimensional model it can be represented as,

$$T = CS \tag{2.3}$$

here C is the elastic constant of material, usually for a general system the terms, T and C are tensors but for one dimensional model for longitudinal or shear wave propagation, these can be expressed as single components. This is because of the fact that for a solid bending is easier than stretching it and the longitudinal elastic constant is larger than the shear elastic constant.

2.2.3   Equation of motion

Considering the force applied to the per unit area of the material is $L(\frac{\partial T}{\partial z})$, and since this is a small time-variable stress, following the Newton's 2nd law the equation of motion can be describe as a point in the material as,

$$
\begin{aligned}
F = ma = \rho \bigvee a &= \rho \bigvee \dot{v} \\
\Rightarrow \frac{F}{\bigvee} &= \rho \dot{v} \\
\Rightarrow \frac{F}{\partial x \partial y \partial z} &= \rho \dot{v} \\
\Rightarrow \frac{T}{\partial z} = \rho \dot{v} \quad [as\ T &= \frac{F}{\partial x \partial y}] \\
\therefore \frac{\partial T}{\partial z} &= \rho \dot{v} = \rho \ddot{u}
\end{aligned}
\tag{2.4}
$$

here u is the displacement, v is velocity, $\bigvee$ is the volume, m is mass, ρ is density, a is acceleration and ($\dot{}$) indicates time derivative.

2.3   Constitutive relations and tensor notations

Here wave interactions are presented in a one dimensional form, while referring to shear or longitudinal waves, provided that direction of wave propagation is along a symmetry axis of a crystal. Therefore, to represent the ongoing phenomenon in a quantitative way, at first Hooke's law, equation of motion and crystal's elastic parameters are to be stated and then to be reduced to one dimensional terms. Onward tensor notations and reduced subscript notations are introduced for simplicity of the equations, some are illustrated in Appendix A.

2.3.1   Relating displacement and strain

The displacement $\mathbf{u}$ consists of three components u_x, u_y and u_z, each of which may be a function of three Cartesian components x, y and z at a given position. So, $\mathbf{S}$ is a tensor consisting nine components with variation of u_i, where i is a Cartesian coordinate. For instance,

$$
S_{xx} = \frac{\partial u_x}{\partial x}
\tag{2.5}
$$

and

$$S_{xy} = \frac{1}{2} \left[\frac{\partial u_x}{\partial y} + \frac{\partial u_y}{\partial x} \right] \tag{2.6}$$

Considering symmetry notation of the crystal form, $S_{xy} = S_{yx}$. Similarly, S_{xz}, S_{yx}, S_{yy}, S_{yz}, S_{zx}, S_{zy} and S_{zz} can be defined. Whereas, for one dimensional model, one component is sufficient to represent the longitudinal strain, S_{xx} or S_{zz} and the shear strain, S_{xy}.

2.3.2 Stress in a rectangular cube

Consider a cube with volume $\delta x \, \delta y \, \delta z$, the developed stresses in this cube after applying traction force, F, are presented in Fig. 2.3.
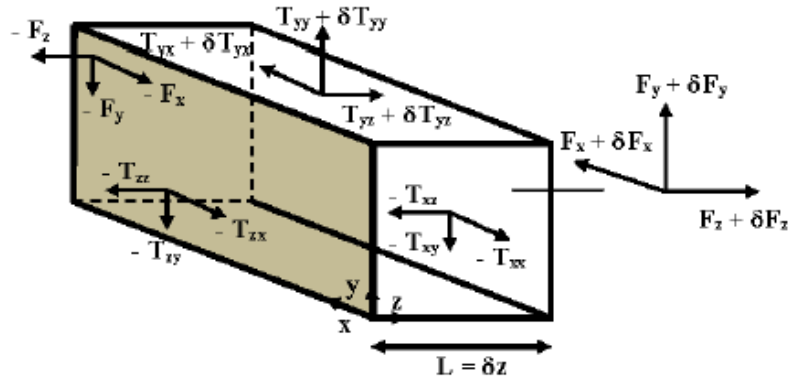
Fig. 2.3 General stress components in a cube [Auld, 1973].

The left-hand side surface of area $\delta x \, \delta y$ is indicated by a shade, where the traction force is applied. This applied force has three components, $-F_x$ and $-F_y$ are parallel to the shaded plane and $-F_z$ is perpendicular to it. The opposite side traction force has components, $F_x + \delta F_x$, $F_y + \delta F_y$ and $F_z + \delta F_z$. The parameter L represented in Section 2.2 is equivalent to δz. By considering Taylor expansion to first order in δz, in z-direction these force components can be expressed as $F_x + (\partial F_x/\partial z)$, $F_y + (\partial F_y/\partial z)$ and $F_z + (\partial F_z/\partial z)$. The stresses developed on the shaded plane perpendicular to the z-axis can be defined as,

$$\textbf{Shear stress}: \quad T_{zx} = \frac{F_x}{\delta x \delta y} \tag{2.7}$$

$$\textbf{Shear stress}: \quad T_{zy} = \frac{F_y}{\delta x \delta y} \tag{2.8}$$

$$\textbf{Longitudinal stress}: \quad T_{zz} = \frac{F_z}{\delta x \delta y} \tag{2.9}$$

here the first subscript of the tensor **T** indicates the coordinate axis, which is normal to the given plain and the second subscript indicates the axis parallel to the traction. There will be nine stress components, among which T_{xx}, T_{yy} and T_{zz} are longitudinal stress components and $T_{xy} = T_{yx}$, $T_{xz} = T_{zx}$ and $T_{yz} = T_{zy}$ are shear stress components. Shear stress components are shown in equal in pairs as internal stresses cannot raise any net rotation to the body of the cube. Based on this equality, nine components reduces to six independent stress components as,

$$\mathbf{T} = \begin{bmatrix} T_{xx} & T_{xy} & T_{xz} \\ T_{yx} & T_{yy} & T_{yz} \\ T_{zx} & T_{zy} & T_{zz} \end{bmatrix} = \begin{bmatrix} T_1 & T_6 & T_5 \\ T_6 & T_2 & T_4 \\ T_5 & T_4 & T_3 \end{bmatrix} = \begin{bmatrix} T_1 \\ T_2 \\ T_3 \\ T_4 \\ T_5 \\ T_6 \end{bmatrix} \tag{2.10}$$

The net resultant force per unit volume in z-direction applied on the infinitesimal cube is,

$$f_z = \frac{\partial T_{zx}}{\partial x} + \frac{\partial T_{zy}}{\partial y} + \frac{\partial T_{zz}}{\partial z} \tag{2.11}$$

Using concept of Eq. (2.4) in Eq. (2.11), the equation for the motion in z-direction is,

$$\rho \ddot{u}_z = \rho \dot{v}_z = \frac{\partial T_{zx}}{\partial x} + \frac{\partial T_{zy}}{\partial y} + \frac{\partial T_{zz}}{\partial z} \tag{2.12}$$

Similarly, corresponding equations for the other components of u and v can be found, those are discussed in depth in Appendix A.

The full tensor form of the equation of motion in the z-direction, by adding all the forces terms, can be expressed as,

$$\rho \frac{\partial^2 u_z}{\partial t^2} = \frac{\partial T_{zx}}{\partial x} + \frac{\partial T_{zy}}{\partial y} + \frac{\partial T_{zz}}{\partial z} \qquad (2.13)$$

Using reduced notation Eq. (2.13) can be rewritten as,

$$\rho \frac{\partial^2 u_z}{\partial t^2} = \frac{\partial T_5}{\partial x} + \frac{\partial T_4}{\partial y} + \frac{\partial T_3}{\partial z} \qquad (2.14)$$

Similarly, relations for the equations of motion in the x and y-directions can also be generated. For convenience the following symbolic notation for stress is often used [Auld, 1973], which is discussed in details in Appendix A,

$$\nabla . \mathbf{T} = \hat{x}\left(\frac{\partial T_{xx}}{\partial x} + \frac{\partial T_{xy}}{\partial y} + \frac{\partial T_{xz}}{\partial z}\right) + \hat{y}\left(\frac{\partial T_{yx}}{\partial x} + \frac{\partial T_{yy}}{\partial y} + \frac{\partial T_{yz}}{\partial z}\right) + \hat{z}\left(\frac{\partial T_{zx}}{\partial x} + \frac{\partial T_{zy}}{\partial y} + \frac{\partial T_{zz}}{\partial z}\right)$$
$$(2.15)$$

In compact form Eq. (2.15) can be rewritten as,

$$(\nabla . \mathbf{T})_i = \sum_i \frac{\partial T_{ij}}{\partial u_j} \quad i, j = x, y, z. \qquad (2.16)$$

Using Cartesian coordinates the translational equation of motion is,

$$\frac{\partial T_{ij}}{\partial u_j} = \rho \frac{\partial^2 u_i}{\partial t^2} - F_i \qquad (2.17)$$

here F_i is the external force, which for this case is considered as zero.

2.3.3 Hooke's law and elasticity coefficients

For an elastic system the Hooke's law, in simple form, states that the stress is proportional to the strain when distortion or displacement is small. The generalized form of Hooke's law, in term of components with respect to an orthonormal basis, can be written as,

$$T_{ij} = C_{ijkl} S_{kl} \qquad (2.18)$$

here, C_{ijkl} (**C**) is the stiffness or elastic coefficient tensor, which is consists of 81 (9×9) components, T_{ij} (**T**) is the stress tensor and S_{kl} (**S**) is the strain tensor, both consists of 9 components each.

For those materials that become electrically polarized when strained, Hooke's law relation does not fully describe their response under acoustic strain. It is a linear phenomenon and when the sign of strain changes the polarization changes sign. It accompanied with another linear phenomenon, known as converse piezoelectric effect. In piezoelectric material these terms generates internal stress in presence of an electric field [Auld, 1973]. So, piezoelectric materials need additional terms with Eq. (2.18) to represent these effects, which is not the interest of present discussion.

If symmetry conditions are applied the 81 independent components of stiffness tensor can be reduced to 36 and the 9 independent components of stress or strain can be reduced to 6 components, then Eq. (2.18) can be expressed in compact form using engineering or Voigt notations [MIT Module 3] as,

$$[\mathbf{T}] = [\mathbf{C}][\mathbf{S}] \tag{2.19}$$

The structure of these matrices are clearly discussed at Section 2.3.5. It is to be noted that the relation between applied strains S_{xx} and S_{yy}, and stress T_{xx} can be given as,

$$T_{xx} = C_{xxxx}S_{xx} + C_{xxyy}S_{yy} \tag{2.20}$$

Due to symmetry as $S_{xz} = S_{zx}$ and $C_{xzxz} = C_{xzzx}$, the relation between T_{xz} and S_{xz} can be given as,

$$T_{xz} = 2C_{xzxz}S_{xz} \tag{2.21}$$

First two subscripts among the four subscripts of stiffness tensor represents the subscripts of stress tensor and last two corresponds to the subscripts of strain tensor.

2.3.4   Notation for tensors

Some simple notations are adopted to denote the components of the vectors and tensors discussed in this thesis, which are elaborated in Appendix A. The subscripts i and j are used to denote any one of the three axes of interest in tensor components, whereas k and l are

floating subscripts. In Eq. (2.18), since both stress, T_{ij}, and strain, S_{kl}, are symmetric, this reflects in stiffness tensor, C_{ijkl}, which is symmetric as well. The stiffness tensor may have the following two symmetry conditions,

$$\textbf{Lack of rotation}: \quad C_{ijkl} = C_{jikl} = C_{ijlk} = C_{jilk} \tag{2.22}$$

$$\textbf{Reciprocity}: \quad C_{ijkl} = C_{klij} \tag{2.23}$$

These symmetry conditions reduces the number of independent elements in fourth-order stiffness tensor from 81 to 21. As strain is dimensionless, based on the Eq. (2.18), the unit for the elastic coefficient is same as unit of stress, i.e., unit of pressure. Based on the symmetry applicable to the crystals, the independent number of elements in stiffness tensor are listed in Table 2.1 [Mouhat, 2014].

Table 2.1 Number of independent elastic constants in different symmetric crystals.

Applicable symmetry	Number of independent elements
Anisotropic	21
Orthorhombic	9
Hexagonal (transversely isotropic)	5
Cubic	3
Isotropic	2 (Two Lame constants)

It is to be noted that for isotropic solids the number of independent elements required are only 2. These two elements are Lame constants λ and μ, which will be introduces later in Section 2.4.

2.3.5   Subscript notation in reduced form

As symmetry is applicable for all the components in Eq. (2.18), reduced notation can be used to represent the subscripts in elements of stress, strain and stiffness tensors. For instance, T_R will replace the longer notation of stress tensor, T_{ij}, whereas, S_R will replace the longer notation of strain tensor, S_{kl}. Table 2.2 [Sriratanavaree, Thesis, 2014] summarises the reduced notation for the stress and strain tensors and Table 2.3 [Sriratanavaree, Thesis, 2014] presents in brief the reduced notation of stiffness tensor including their meaning.

Based on the illustrations used in Tables 2.2 and 2.3, for any non-piezoelectric material, Eq. (2.18) can be rewritten as,

Table 2.2 Reduced subscript notation used for stress and strain tensors elements.

Tensor element	All elements	Connotations
Stress: T_R	T_1 (where R = 1) = T_{xx}	Longitudinal stress in the *x*-direction
	T_2 (where R = 2) = T_{yy}	Longitudinal stress in the *y*-direction
	T_3 (where R = 3) = T_{zz}	Longitudinal stress in the *z*-direction
	T_4 (where R = 4) = T_{yz}	shear stress about the *x*-axis
	T_5 (where R = 5) = T_{zx}	shear stress about the *y*-axis
	T_6 (where R = 6) = T_{xy}	shear stress about the *z*-axis
Strain: S_R	S_1 (where R = 1) = S_{xx}	Longitudinal strain in the *x*-direction
	S_2 (where R = 2) = S_{yy}	Longitudinal strain in the *y*-direction
	S_3 (where R = 3) = S_{zz}	Longitudinal strain in the *z*-direction
	S_4 (where R = 4) = $2S_{yz}$	shear strain: motion about *x*-axis, shear in the *y* and *z*-directions
	S_5 (where R = 5) = $2S_{zx}$	shear strain: motion about *y*-axis, shear in the *x* and *z*-directions
	S_6 (where R = 6) = $2S_{xy}$	shear strain: motion about *z*-axis, shear in the *x* and *y*-directions

Table 2.3 Reduced subscript notation used for stiffness tensor elements.

Reduced notation	Standard notation	Connotations
C_{IJ}	C_{ijkl}	The ratio of the *I*th stress component to the *J*th strain component
C_{11}	C_{1111}	The longitudinal elastic constant relating longitudinal stress and strain elements in the *x*-direction
C_{44}	C_{2323}	The shear elastic constant relating shear stress and strain elements in the *4*-direction (motion about *x*-axis)
$C_{12} = C_{21}$	$C_{1122} = C_{2211}$	$C_{IJ} = C_{JI}$

$$T_R = C_{IJ}S_R \qquad (2.24)$$

For simplicity neglecting initial stress and the effect due to change in temperature, also referring the components of strain and stress to some appropriate basis function, the Eq. (2.24) in matrix form,

$$\begin{bmatrix} T_1 \\ T_2 \\ T_3 \\ T_4 \\ T_5 \\ T_6 \end{bmatrix} = \begin{bmatrix} C_{11} & C_{12} & C_{13} & C_{14} & C_{15} & C_{16} \\ C_{21} & C_{22} & C_{23} & C_{24} & C_{25} & C_{26} \\ C_{31} & C_{32} & C_{33} & C_{34} & C_{35} & C_{36} \\ C_{41} & C_{42} & C_{43} & C_{44} & C_{45} & C_{46} \\ C_{51} & C_{52} & C_{53} & C_{54} & C_{55} & C_{56} \\ C_{61} & C_{62} & C_{63} & C_{64} & C_{65} & C_{66} \end{bmatrix} \begin{bmatrix} S_1 \\ S_2 \\ S_3 \\ S_4 \\ S_5 \\ S_6 \end{bmatrix} \tag{2.25}$$

If reduced notation is used the original stiffness matrix consisting 9×9 elements can be reduced to a matrix of 6×6 elements. As it can be seen in Eq. (2.25) that all the elements in elastic coefficient matrix are not independent as $C_{IJ} = C_{JI}$. Thus only 21 elements of the matrix [C] are independent. The number of independent terms can be reduced further based on the symmetry conditions lies within different crystals. As an example, for a crystal exhibiting cubic symmetry following relations among some of the elements in [C] can be shown,

$$C_{11} = C_{22} = C_{33}$$
$$C_{12} = C_{21} = C_{13} = C_{31} = C_{23} = C_{32}$$
$$C_{14} = C_{15} = C_{16} = 0 \tag{2.26}$$
$$C_{24} = C_{25} = C_{26} = 0$$
$$C_{34} = C_{35} = C_{36} = 0$$

Based on the equations set shown in Eq. (2.26), it becomes clear that there remains only three independent components and these are, C_{11}, C_{12} and C_{44}. If the material is considered to be isotropic, then the existing relation among these three components will be,

$$C_{11} - C_{12} = 2C_{44} \tag{2.27}$$

This case is further illustrated in Section 2.4.

2.4   Lame constants and their relations with wave velocity in isotropic material

For the reason of crystal symmetry in isotropic material, the number of the independent elements in elastic coefficient matrix reduce to two, based on the relation shown in Eq. (2.27).

These two independent constants are λ and μ, which are known as Lame constants. The parameter μ is the shear modulus or modulus of rigidity. These constants are helpful in determining total stored energy of the system. These can also be related [Royer, 2000] to the elastic constants as,

$$C_{11} = C_{22} = C_{33} = \lambda + 2\mu \tag{2.28}$$

$$C_{12} = C_{21} = C_{13} = C_{31} = C_{23} = C_{32} = \lambda \tag{2.29}$$

$$C_{44} = C_{55} = C_{66} = \mu = \frac{C_{11} - C_{12}}{2} \tag{2.30}$$

Rest of the terms are zero. Thus the elastic coefficient matrix for isotropic material becomes,

$$C_{IJ} = \begin{bmatrix} \lambda + 2\mu & \lambda & \lambda & 0 & 0 & 0 \\ \lambda & \lambda + 2\mu & \lambda & 0 & 0 & 0 \\ \lambda & \lambda & \lambda + 2\mu & 0 & 0 & 0 \\ 0 & 0 & 0 & \mu & 0 & 0 \\ 0 & 0 & 0 & 0 & \mu & 0 \\ 0 & 0 & 0 & 0 & 0 & \mu \end{bmatrix} \tag{2.31}$$

In general the acoustic wave velocity is related to the elastic coefficient and material density by the following relation,

$$V = \sqrt{\frac{C_{ij}}{\rho}} \tag{2.32}$$

here V is the velocity of sound in the material, C_{ij} is the elastic constant and ρ is the material density. Depending upon which elastic constant is used or what type of wave velocity is to be determined, the Eq. (2.32) may take different forms. It is worthy of mentioning that the subscripts of the elastic constant in Eq. (2.32) are used to indicate the directionality of the elastic constant itself with respect to the type and travelling direction of the acoustic wave. For all directions within the isotropic material the elastic constants are same. But, for each direction within the anisotropic material the elastic constants are different.

The relations of the shear and longitudinal wave velocities with elastic coefficients and the Lame constants can be given as,

$$V_L = \sqrt{\frac{C_{11}}{\rho}} \tag{2.33}$$

$$\frac{V_L}{V_S} = \sqrt{\frac{C_{11}}{C_{44}}} = \sqrt{2 + \frac{\lambda}{\mu}} \tag{2.34}$$

then

$$V_S = \sqrt{\frac{C_{44}}{\rho}} \tag{2.35}$$

To calculate the shear wave velocity shear modulus is commonly used and while determining longitudinal wave velocity Poisson's ratio and Young's modulus are used. However, it is convenient to use Lame constants to calculate these terms. These Lame constants can be derived from Poisson's ratio and Young's modulus.

On the other hand, instead of using Lame constants and elastic coefficients, an isotropic materials can also be characterized equally well using alternative pair of the following parameters,

- *Young's modulus (*$\mathbf{E}$*)*: It is a measure of stiffness of an isotropic material and can be expressed as a proportionality constant between uni-axial stress and strain. Unit is Pascal.

- *Bulk modulus (*$\mathbf{K}$*)*: It is a measure of incompressibility of a body under hydrostatic pressure. Its unit is also Pascal.

- *Poisson's ratio (*ν*)*: It is the ratio of transverse or radial strain to longitudinal or axial strain. It is dimensionless.

The interrelation between these parameters [Royer, 2000] are listed in the Table 2.4.

2.5   Refraction of acoustic wave and Snell's law

When acoustic wave passes through an interface of two materials having different refractive indices with an oblique angle, it may both reflected and/or refracted depending upon incident

Table 2.4 Interrelation between different moduli, elastic constant, Poisson's ratio in isotropic solid.

Parameters	In terms of			
	E, v	E, μ	λ, μ	C_{11}, C_{12}
λ	$\frac{Ev}{(1+v)(1-2v)}$	$\frac{\mu(E-2\mu)}{3\mu-E}$	λ	C_{12}
μ	$\frac{E}{2(1+v)}$	μ	μ	$\frac{C_{11}-C_{12}}{2}$
E	E	E	$\frac{\mu(3\lambda+2\mu)}{\lambda+\mu}$	$C_{11} - \frac{2C_{12}^2}{C_{11}+C_{12}}$
K	$\frac{E}{3(1-2v)}$	$\frac{\mu E}{3(3\mu-E)}$	$\lambda + \frac{2\mu}{3}$	$\frac{C_{11}+2C_{12}}{3}$
v	v	$\frac{E-2\mu}{2\mu}$	$\frac{\lambda}{2(\lambda+\mu)}$	$\frac{C_{12}}{C_{11}+C_{12}}$

angle. The effect is similar as in case of light passing through similar interfaces and that is why objects seen through an interface seemed to be shifted relative to their actual positions.

Incident acoustic wave refracted when two materials making an interface allow different sound velocities. The material properties, such as, material density and elastic modulus, determine the acoustic velocity in that material. When acoustic plane wave, shown in Fig. 2.4, travelling in one material enters in another material possessing higher acoustic velocity then a portion of the wave in the second material will move faster than the portion of the wave in the first material and will cause the wave to bend.
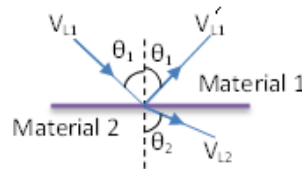
Fig. 2.4 Reflected and refracted longitudinal acoustic waves [NDT Course Material].

here V_{L1} is the longitudinal acoustic velocity at material 1, V_{L2} is the longitudinal acoustic velocity at material 2, θ_1 is the incident angle and θ_2 is the refracted angle.

It is to be noted in Fig. 2.4 that the reflected longitudinal wave is shown with velocity V'_{L1}. This wave is reflected at the same angle as the incident wave because the two waves are travelling in the same material, and hence can be considered to have the same velocities. This reflected wave is not important for this discussion.

2.5.1 Snell's law for acoustic wave

The Snell's Law depicts the relationship between the incident and refracted angles and the velocities of the waves in materials. Snell's law states the ratio of acoustic velocities V_{L1} and V_{L2} is equal to the ratio of the sine's of incident angle, θ_1 and refracted angle, θ_2, as,

$$\frac{sin(\theta_1)}{sin(\theta_2)} = \frac{V_{L1}}{V_{L2}} \tag{2.36}$$

When a longitudinal wave travelling through a medium with lower acoustic velocity (V_{L1} = 340 m/s for air) and passes an interface to another medium having higher acoustic velocity (V_{L2} = 1500 m/s for water) with an incident angle equal to the first critical angle, the wave may be refracted with a 90° angle, which can be calculated from Eq. (2.36). Much of the acoustic wave energy remains in the form of inhomogeneous compression wave at the critical angle of incidence, travelling along the interface and decays exponentially with depth from the interface. Some times this wave is referred as creep wave [NDT Course Material]. For their rapid decaying and inhomogeneous nature, creep waves are not used as extensively as Rayleigh surface waves in practical applications. However, due to their longer wavelength, creep waves suffers less from course material micro-structure and surface irregularities, so, it is sometimes considered to be more useful than Rayleigh waves.

2.5.2 Reflection and refraction of plane wave

Les us consider the reflection of an infinite plane wave from a free surface. When a longitudinal or shear wave incidents normally on a surface, the reflected wave will be of same type and with similar amplitude. The required boundary condition is that normal component of stress at the surface needs to be zero. Figure 2.5 illustrates, when a longitudinal wave is incident in the *x-y* plane on a free surface ($y = 0$) at an angle θ_{LI}, two reflected waves, longitudinal and shear, will be generated, with an angle to the normal θ_{LR} and θ_{SR}, respectively. The reflected shear wave's displacement will have a vertical component, named, shear vertical wave.

Let us represent the incident longitudinal wave in terms of potential ϕ_{LI} with a variation $e^{-jk_L r}$, where vector *r* represents the direction of propagation of the wave. In Fig. 2.5, the potential of incident longitudinal wave can be presented as,

$$\phi_{LI} = A_{LI} e^{-jk_L(xsin\theta_{LI} + ycos\phi_{LI})} \tag{2.37}$$

Similarly, the potential of reflected longitudinal wave can be given as,
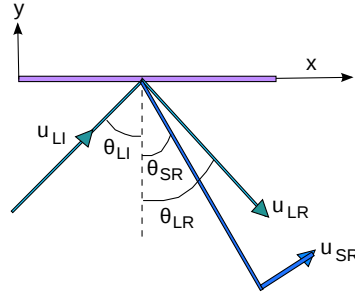
Fig. 2.5 Reflected longitudinal and shear waves from incident of a longitudinal wave on a free surface [Sriratanavaree, Thesis, 2014].

$$\phi_{LR} = A_{LR}e^{-jk_L(xsin\theta_{LR}+ycos\phi_{LR})} \tag{2.38}$$

And the potential of reflected shear wave, Ψ_{SR} in z-direction has a form,

$$\Psi_{SR} = A_{SR}e^{-jk_S(xsin\theta_{SR}+ycos\phi_{SR})} \tag{2.39}$$

Any other components in Ψ_{SR} would give rise of additional stress and displacement components and thus will not satisfy the boundary condition. At surface the boundary condition requires the total normal stress component must be zero. Hence, the stress components at surface are,

$$
\begin{aligned}
T_2 &= T_{yy} = 0 \\
T_6 &= T_{xy} = 0
\end{aligned}
\tag{2.40}
$$

These are the sum of the components of the longitudinal and shear waves. Therefore, at any point of surface, $y = 0$, all shear and longitudinal waves components must have same phase variation along the surface to satisfy the boundary conditions.

Using Eqs. (2.37), (2.38) and (2.39), we have,

$$k_L sin\theta_{LI} = k_L sin\theta_{LR} = k_S sin\theta_{SR} \tag{2.41}$$

Similar to the reflection of electromagnetic wave, it can be concluded that the incident angle is equal to the angle of reflection in this case,

$$\theta_{LI} = \theta_{LR} \tag{2.42}$$

It also can be concluded that,

$$\frac{sin\theta_{SR}}{sin\theta_{LI}} = \frac{k_L}{k_S} = \frac{V_S}{V_L} = \sqrt{\frac{\mu}{\lambda + 2\mu}} \tag{2.43}$$

This is nothing but the Snell's law and similar to the electromagnetic wave reflection and developed on the same considerations. As for all isotropic solids $V_S < V_L$, reflected shear wave propagates at a closer angle to the normal than that of the reflected longitudinal wave.
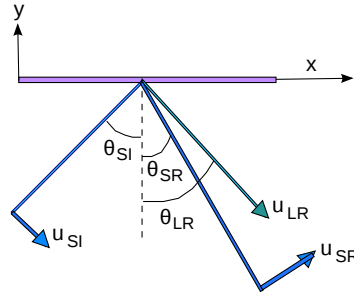
Fig. 2.6 Reflected longitudinal and shear waves from incident of a shear wave on a free surface [Sriratanavaree, Thesis, 2014].

If the excitation is considered to be by incident shear wave, as illustrated in Fig. 2.6, it can be concluded,

$$\frac{sin\theta_{LR}}{sin\theta_{SI}} = \frac{k_S}{k_L} = \frac{V_L}{V_S} = \sqrt{\frac{\lambda + 2\mu}{\mu}} \tag{2.44}$$

2.6   Modes of acoustic wave propagation

Acoustic wave travels through air by compression and rarefaction of air molecules in the direction of propagation. But in solids, particles can support motions in other directions as well. So, acoustic wave propagation in solids can be classified in different types. Waves are characterized in space by oscillatory patterns and can propagate in a stable manner maintaining their shapes. These specific patterns of waves are called wave modes.

Acoustic wave propagation in solids can be in four principle modes, which are based on the manner the particles oscillate. Acoustic wave can propagate as longitudinal waves, shear

waves, surface waves, and as plate waves in thin materials. Among these most widely used propagation modes are longitudinal and shear modes. The particles movements associated along the propagation of longitudinal and shear waves are depicted in Fig. 2.7.

As mentioned earlier, longitudinal and shear waves in solids are most often used in different inspections. Moreover, various types of elliptical or complex vibrations of the particles at interfaces and surfaces make other waves possible too. Some of these wave modes, for instance, Rayleigh and Lamb waves also attracted attention in different inspections.
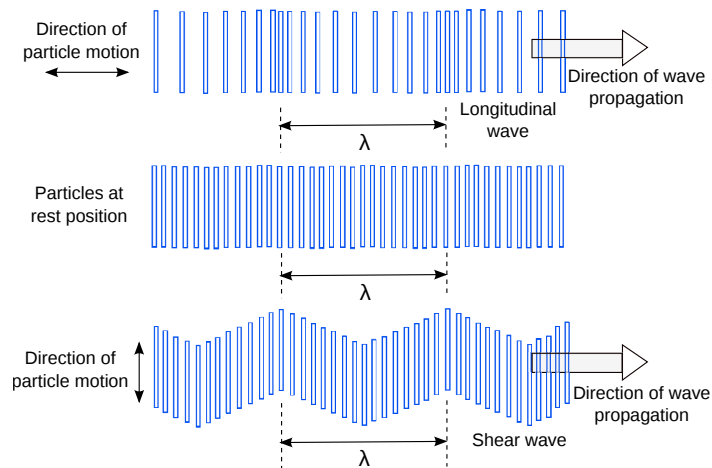
Fig. 2.7 Particles motion and direction of propagation for longitudinal and shear waves [NDT Course Material].

The Table 2.5 summarizes some possible wave modes in solids.

Table 2.5 Some possible wave modes in solid [NDT Course Material].

Type of waves	Particle vibrations
Longitudinal	Parallel to the wave propagation direction
Shear	Perpendicular to the wave propagation direction
Surface - Rayleigh	symmetrical mode with elliptical orbit
Plate wave - Lamb	Extensional wave - component perpendicular to surface
Plate wave - Love	Perpendicular to the propagation direction and parallel to plane layer
Leaky Rayleigh waves (Stoneley)	Wave guided along interface
Sezawa	Antisymmetric mode

In a thick solid material surface or Rayleigh waves travels along the surface with a penetration depth of one wavelength. The elliptic orbit motion in surface wave is created

by the combination of both longitudinal and transverse motions. The major elliptical axis is perpendicular to the solid surface. Because the width of its elliptical motion decreases with the increasing depth of an individual atom from the surface. When a longitudinal wave intersects a surface near the second critical angle and they travel at a velocity between 0.87 and 0.95 of a shear wave then surface waves are generated. Rayleigh waves attracted interest because of their sensitivity to surface defects and features, and they can follow the surface around curves. Because of these features, Rayleigh waves can be used in ultrasonography to inspect areas that other waves might have difficulty to reach. Plate waves are similar to surface waves. But they can be generated in materials with thickness of a few wavelengths. Among plate waves, Lamb waves are the most commonly used. Lamb waves propagate parallel to the surface throughout the thickness of the material in a form of complex vibrational waves. On the density and the elastic properties of material component the propagation of Lamb waves depends. These waves are also influenced by the frequency of interest and material thickness. Lamb waves are generated at particular incident angle when the parallel component of the source wave velocity is equal to the wave velocity that can be persisted in the material. These waves are useful to scan tubes, wire and plates as they can travel several meters in steel. A number of modes of particle vibration are possible with Lamb waves, however, the two most common are symmetrical and asymmetrical. The particles complex motion is similar to the elliptical orbits for surface waves. About the median plane of the plate the symmetrical Lamb waves move in a symmetrical fashion. Because the wave stretches and compresses the plate in the wave motion direction when propagates, so, sometimes it is called the extensional mode. The symmetrical mode of wave motion is most efficiently produced when the applied force is parallel to the plate. Whereas, in the asymmetrical Lamb wave mode a large portion of the movement occur in a normal direction to the plate, and a little motion occurs in the direction parallel to the plate, so it is often called flexural mode. In this mode as the two surfaces of the plate move in the same direction, the body of the plate bends.

2.7   Two dimensional acoustic waveguide

As the main interest of this thesis is to determine the acousto-optical interraction in waveguides, this section focuses on guidance of wave in two dimensional optical waveguides. It is already mentioned that acoustic waves propagate inside a waveguide due to the periodic displacement of the molecules and the wave guidance is pretty complex. These propagation properties can be characterized by the material density, elasticity, Young's modulus, and Poisson's ratio [Auld, 1973]. The particle displacement can either be in the longitudinal direction or in the transverse plane. An acoustic mode can be supported strongly in a waveg-

uide provided that at least one of the shear or longitudinal velocities in the cladding must exceeds that of the core. The propagation of such a mode can be classified as being of the torsional, bending, rotational, flexural or longitudinal type [Thurston, 1978 and Saffaai-Jazi, 1988].

Two dimensional waveguide consists of two materials, core and cladding. To guide the light through the core, the core materials must have lower wave velocity. It is equivalent to the core acoustic index to be higher than that of the clad. The higher acoustic index causes lower velocity in the core, so that, acoustic wave can be guided and sustained. To confine the guided light in the core, core and clad materials of an optical waveguide, such as embedded Ge-doped silica optical waveguide, is doped in a way that the core refractive index remains higher than that of the clad. Depending on the requirement of higher or lower acoustic velocity in the core, the doping materials are considered. Two different types of waveguides are shown in Fig. 2.8.
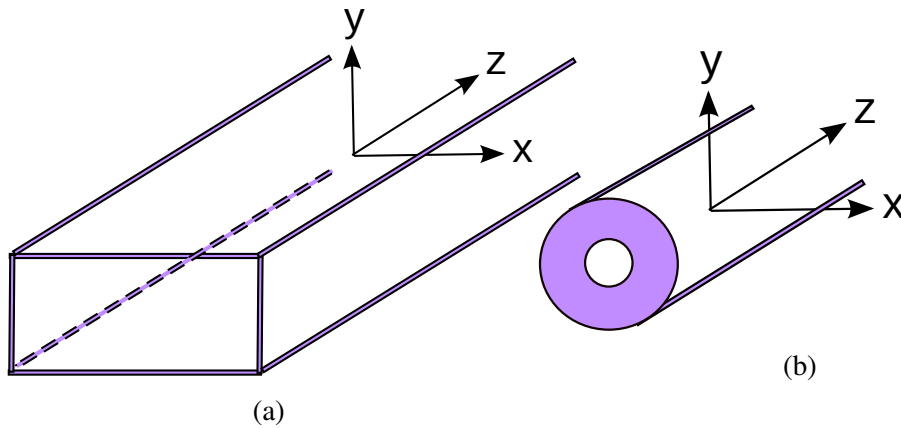
Fig. 2.8 (a) Rectangular and (b) circular two dimensional optical waveguides with indicated direction of propagation.

Here direction of propagation is considered to be *z*-direction, where the molecular displacement in longitudinal acoustic wave will be in direction of propagation and in shear wave it will be perpendicular to the direction of propagation.

The propagation of an acoustic wave along the axial direction, taken here as the *z*-axis, is associated with the molecular displacement, $\mathbf{U_i}$, and a time harmonic wave can be written in the following form [Lagasse, 1973],

$$\mathbf{U_i} = \mathbf{u}\,(u_x, u_y, ju_z)\,exp[j\,(\omega t - kz)] \qquad (2.45)$$

here the acoustic angular frequency, ω, identifies the time dependence; the propagation constant, k identifies the axial dependence of the acoustic wave and u_x, u_y and u_z are the particle displacement vectors along the x, y and z directions, respectively. For a loss-less system, the longitudinal component u_z is $90°$ out of phase with the two transverse components, u_x and u_y. In this case, by defining u_z as an imaginary component, as shown in Eq. (2.45), the system equation can be transformed to a much simpler real eigenvalue equation. A similar approach is adopted in [Rahman, 1985] for a loss-less optical waveguide. Where a complex eigenvalue problem has been transformed to a simpler real eigenvalue problem. The deformation in an acoustically vibrating body can be described by the strain field, **S**, given by,

$$\mathbf{S} = \nabla \mathbf{u} \tag{2.46}$$

The elastic restoring forces can be defined in terms of the stress field, **T** and the inertial and elastic restoring forces in a freely vibrating medium are related through the translational equation of motion as,

$$\nabla \cdot \mathbf{T} = \rho \frac{\partial^2 \mathbf{u}}{\partial t^2} \tag{2.47}$$

here ρ is the material density.

Hooke's Law states that for small displacement the strain and stress are linearly proportional to each other and can be given by,

$$T_{ij} = C_{ijkl} S_{kl} \qquad i, j, k, l \ = \ x, y, z \tag{2.48}$$

here, the microscopic spring constants, C_{ijkl}, are called the elastic stiffness constants. The compliance and stiffness tensors can be denoted in matrix form as,

$$[T] = [C][S] \tag{2.49}$$

where the forth order tensor term, C_{ijkl}, obeys symmetry conditions and thus can be expressed with two suffix notation, which has been explained in Section 2.3.5. Further it has been also

shown in Section 2.4 that these elastic stiffness constants are related to the longitudinal and shear velocities.

Classically, in the FEM [Zienkiewicz, 2013] for a solid structure, the displacement field, **u**, can be written with the help of the interpolation shape function $[N]$ and vector of nodal values of the displacement field **U**, and its spatial derivatives and integrations can be easily carried out over the elements. So, we have,

$$\mathbf{u} = [\mathbf{N}]\,\mathbf{U} \tag{2.50}$$

here $[N]$ is the matrix for interpolation shape function

$$\mathbf{u} = \begin{bmatrix} u_x \\ u_y \\ ju_z \end{bmatrix} = \begin{bmatrix} N_1 & 0 & 0 & N_2 & 0 & 0 & N_3 & 0 & 0 \\ 0 & N_1 & 0 & 0 & N_2 & 0 & 0 & N_3 & 0 \\ 0 & 0 & N_1 & 0 & 0 & N_2 & 0 & 0 & N_3 \end{bmatrix} \begin{bmatrix} u_{x1} \\ u_{y1} \\ ju_{z1} \\ u_{x2} \\ u_{y2} \\ ju_{z2} \\ u_{x3} \\ u_{y3} \\ ju_{z3} \end{bmatrix} \tag{2.51}$$

The wave equation associated with the acoustic wave propagation can be developed by employing powerful Variational approach and minimizing the energy functional, a corresponding eigenvalue equation can be formed, which is detailed in Chapter 3 and can be given as:

$$\left([A] - \omega^2\,[B]\right)\mathbf{U} = \mathbf{F} \tag{2.52}$$

where $[A]$ is the stiffness matrix, related to strain energy and $[B]$ is the mass matrix related to the kinetic energy. These matrices are generated for a given propagation constant, k. The column vectors, **F**, contain the nodal values of the applied forces, which in this case are taken to be equal to zero. Solving this generalized eigenvalue equation of the system yields the eigenvalue as ω^2, where ω is the acoustic angular frequency and the eigenvector **U**, the displacement vector. From a given input, k, and its corresponding output, ω, the phase velocity of the acoustic wave, v, can be calculated from,

$$v = \omega/k \tag{2.53}$$

However, if it is necessary to calculate the propagation constant for a given frequency, a simple iterative approach can be considered. Numerically efficient computer code has been developed by using the sparse matrix solver along with the versatile mesh generation for an arbitrary shaped waveguide and modal solutions of acoustic modes in practical optical waveguides can be obtained.

To implement finite element method for this two dimensional analysis, first the waveguide is meshed using first order triangular elements. All three node components of magnetic and acoustic field for each element are presented by piece-wise polynomials within the element. details discussion on finite element method is presented in Chapter 3.

2.8   Guided wave properties in waveguide

The fundamental concept of guided waves is generally based on acoustic plane waves or bulk waves in materials, propagating through a medium, which is bounded by regular boundaries of the structure. In general, acoustic planes waves are either longitudinal or shear in nature. Altogether, for corresponding structural geometries, they form specific types of frequency dependent wave motions consisting of individual propagation properties. They only exists beyond their cut-off frequencies and have increasingly complex mode shapes with increasing frequency. Their frequency dependency can be modelled with dispersion curves by showing phase and group velocities.

This thesis covers weakly, strongly and leaky guidance of acoustic waves using low and high index contrast silica optical waveguides. For each of these cases, the guided wave can be classified into families of wave modes according to their spatial distribution and propagation nature. Low and high index contrast was incorporated in embedded and strip silica optical waveguides, those supported families of similar modes. To have non-degenerated modes height and width of the waveguides were taken unequal and also waveguides symmetry were exploited to increase modal solution accuracy.

The wave modes are either symmetric or anti-symmetric in nature, along the mid plane throughout the thickness of the waveguides as shown in Fig. 2.9. These characteristics have been used to categorize them into wave families. In general wave modes are divided into three different families. The longitudinal modes have purely axially symmetric wave motion, the flexural modes are anti-symmetric and those involve bending motion along the direction

of propagation and a twisting motion along the centre axis is persists by the torsional modes. The three families of guided modes are shown in Fig. 2.10. A torsional mode can be of the radial type having motion either radially inward or outward from the central axis and the torsional-radial type having a squeezing motion starting from the side of the core that spreads towards the centre.
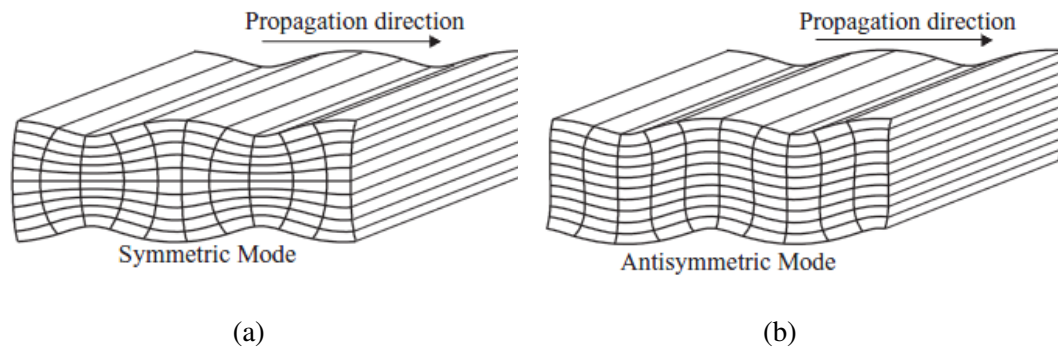
Fig. 2.9 (a) Symmetric and (b) Antisymmetric modes of guided wave motion in plates [Fong, Thesis, 2005].
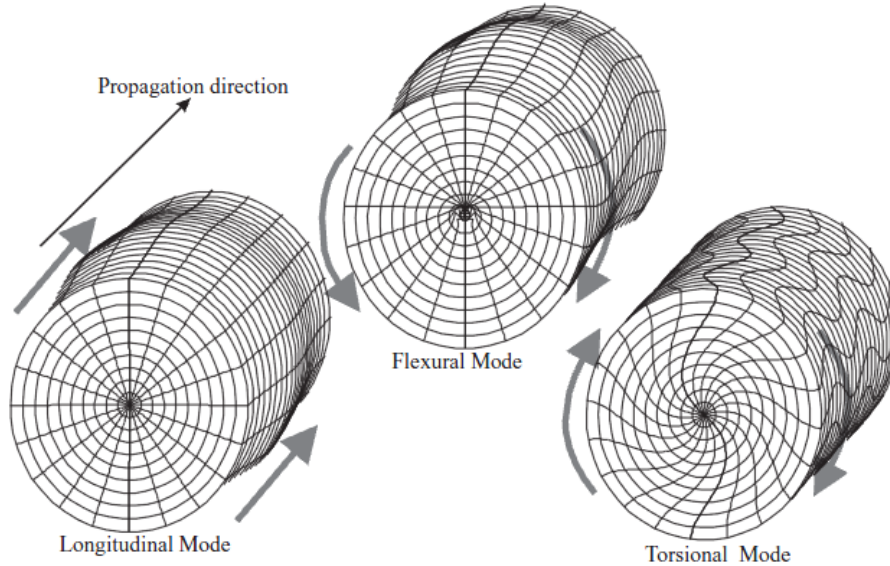
Fig. 2.10 Longitudinal, flexural and torsional modes of guided wave motion in bars / pites [Fong, Thesis, 2005].

2.9   Summary

Reduced form of stress and stain notations have been introduced in this chapter to generate the systems of governing equations of the acoustic wave propagation with help of strain field related to the acoustically vibrating body, equation of motion and Hooke's law. These basic concepts are used in finding the governing wave equation considering the particle displacements in the two dimensional guide are considerably small. Also, for an isotropic solid, longitudinal and shear wave velocities relation with the various elastic constants and material density are shown. At the end, families of acoustic wave propagation modes, for instance, longitudinal, shear, surface and plate wave have been introduced.

Chapter 3

Finite Element Method: Implementation

3.1 Introduction

The Finite Element Method (FEM) is now broadly acknowledged and adopted as one of the most potent and resourceful numerical solution techniques in solving complex problems in engineering and science. FEM originated following the study performed by Courant [Courant, 1943] in 1940s, on torsional problems in structural mechanic, where a numerical solution to a unknown function was approximated by using a collection of triangular elements. In the year 1960 the term 'Finite Elements' was first introduced by Clough [Clough, 1960] in defining a new technique for plane stress analysis. Ahmed [Ahmed, 1969] first introduced this method in the field of electromagnetic in year 1969. Afterwards, FEM has been incorporated in many other fields like, biomedical engineering, thermodynamics, fluid mechanics, semiconductor devices, optical waveguides, etc.

As a numerical technique finite element method provides an approximate solution of a problem base on a set of governing equations, generally, in the algebraic, integral or differential forms through a discretization process of the domain in interest. Its main characteristics is to discretise the domain of the problem into a set of smaller sub-domains or elements. Instead solving the problem as a whole in one go, in FEM solutions are formulated in a simplistic manner by each element, expressed in terms of values at element nodes and then is given a global form to obtain the solution of the original whole domain.

Finite element method is a systematic technique for generating the basic functions used in the variational method (Rayleigh-Ritz) and weighted residual method (Galerkin). The differential equation in the variational technique is first put into an equivalent variational form, then solution is approximated by combining a given approximation functions called trial functions. Whereas, in the weighted residual method the differential equation domain is first discretized and then the overall solution is obtained by minimising the error residual

of the differential equation. However, constructing approximation functions and imposing the boundary conditions, for the problems with irregular shaped boundaries and arbitrary domains, are very difficult by using such method.

Two well known features of finite element method may help in discriminating its dominance over other methods. Firstly, in this method any geometrically complex domain can be assumed as disintegration of simple sub-domains named finite-element, which can be of different shapes, for instance, triangular or rectangular. Secondly, a fundamental idea that any continuous function can be correspondent to by a linear combination of algebraic polynomials governs the derivation of the approximation functions over each finite-element.

The FEM always follows an orderly step-by-step process in providing solution of any problem. These steps are briefly enlisted below, but will be developed later in details.

- Discretization of the continuum: The first step is to discretize a continuous problem into elements. Two dimensional cross-section of optical waveguides are discretized, in this thesis, using triangular shaped elements.

- Selecting interpolation functions: Then it is important to assign nodes to each triangular elements and selecting the type of interpolation functions to present the field variable's variation over the element. Because of the easiness in determining the differentiation and integration, often polynomials are chosen as interpolation functions for field variables. Depending on the nodes number assigned to an element, the unknowns and nature of each node and even on the continuity requirements at nodes and along element boundaries, the degree of polynomial is selected.

- Find the properties of element: After selecting the shape of element and the order of the polynomial as interpolation functions, a system of equations in matrix form for each elements are generated. They represent each individual elements. Then a global purse matrix is formed and solved.

3.2 Boundary conditions across material interfaces

It has been illustrated before that an acoustic waveguide can support many type of acoustic modes and these can be hybrid in nature. This thesis mainly concentrated on the shear and longitudinal acoustic modes only. Each of these modes consists of three vectorial displacement components with dominating vector only in any one direction, considering they are not highly hybrid in nature. If the dominating displacement vectors are either in x or y-direction, they are identified as transverse or shear acoustic modes. When the displacement

vectors are dominant in *z*-direction, they are called longitudinal acoustic modes. These acoustic modes may be fundamental or higher order, considering dimension and material of choice. To ease the illustration of boundary conditions along the material interfaces, Fig. 3.1 represents displacement vector sets of shear and longitudinal acoustic modes along with a planar waveguide. Where, the vector sets U_{mn}^X and U_{mn}^Y represents the displacement vectors for shear acoustic modes with dominant vector (with double arrow heads) along in the *x* and *y*-directions, respectively. U_{mn}^Z represents the displacement vectors for longitudinal acoustic modes with dominant vector along in the *z*-direction.
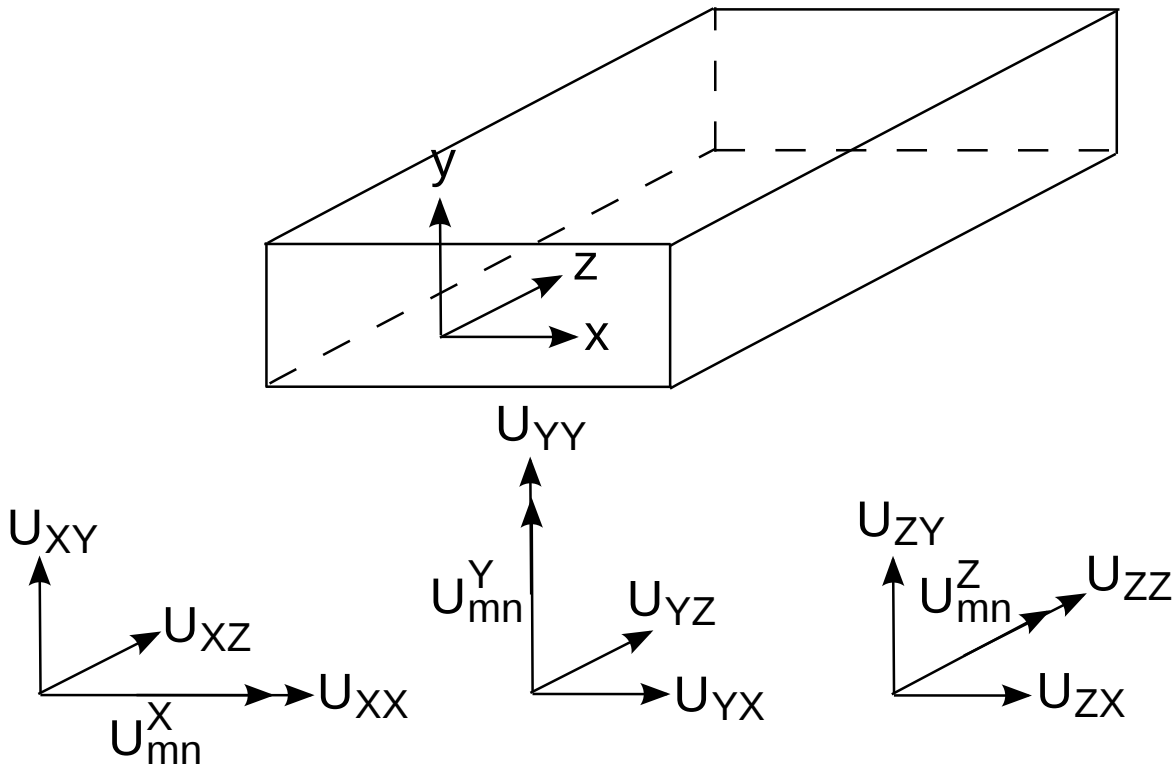
Fig. 3.1 Hybrid components of shear and longitudinal acoustic modes and planar waveguide.

In the absence of external forces (F = 0) applied on the surfaces, boundary conditions can be the following:

1. The tangential components of the displacement vectors at the boundary of materials interface must be continuous.

   - For U_{mn}^X acoustic shear modes:

$$U_{XZ1} = U_{XZ2} \tag{3.1}$$

   where subscripts 1 and 2 represents two different materials.

- For U_{mn}^{Y} acoustic shear modes:

$$U_{YZ1} = U_{YZ2} \tag{3.2}$$

- For U_{mn}^{Z} acoustic longitudinal modes:

$$U_{ZZ1} = U_{ZZ2} \tag{3.3}$$

2. The normal components of the displacement vectors at the boundary of material interfaces must also be continuous.

- For U_{mn}^{X} acoustic shear modes:

$$U_{XX1} = U_{XX2} \tag{3.4}$$

$$U_{XY1} = U_{XY2} \tag{3.5}$$

- For U_{mn}^{Y} acoustic shear modes:

$$U_{YX1} = U_{YX2} \tag{3.6}$$

$$U_{YY1} = U_{YY2} \tag{3.7}$$

- For U_{mn}^{Z} acoustic longitudinal modes:

$$U_{ZX1} = U_{ZX2} \tag{3.8}$$

$$U_{ZY1} = U_{ZY2} \tag{3.9}$$

In addition, two more boundary conditions are incorporated that are encountered in practical waveguide problems. By which waveguide symmetry can be exploited and the number of FEM elements and corresponding order of matrices can also be reduced. These boundary conditions are applicable for those waveguide, which posses structural symmetry.

Perfect horizontal displacement carrier (PHDC) or horizontal sonic wall (HSW), where the displacements along the *x*-axis are continuous across the symmetry boundary, which implies,

$$\mathbf{n} \times \mathbf{U} = 0 \quad or \quad \mathbf{n} \cdot \mathbf{U} = 0 \quad (where \ \mathbf{n} = \hat{y}) \tag{3.10}$$

In the absence of external force, this boundary condition requires that certain displacement vectors must vanish.

Perfect vertical displacement carrier (PVDC) or vertical sonic wall (VSW), where the displacements along the *y*-axis are continuous across the symmetry boundary, so,

$$\mathbf{n} \times \mathbf{U} = 0 \quad or \quad \mathbf{n} \cdot \mathbf{U} = 0 \quad (where \ \mathbf{n} = \hat{x}) \tag{3.11}$$

this boundary condition ensures the continuity of some displacement vectors at the boundary.

The classification of boundary conditions in the nomenclature of partial differential equations are presented in the Section 3.3. This general classification describes the nature of the displacement vector (and in some cases its derivative) values at the computational domain boundary. Classifications of the boundary conditions aids in the choice of appropriate solution technique for any given domain of interest.

3.3 Boundary conditions: natural and forced

Boundary conditions can be categorized based on the imposed conditions upon the formulation and mathematical representation. Those boundary conditions are called natural, if the boundaries are left free when the displacement field decays at the boundary. It is needed to have explicitly defined field values at the boundaries for the other cases. These are the forced boundary conditions and are classified as,

$$Homogeneous \ Dirichlet: \quad \Phi = 0 \tag{3.12}$$

$$Inhomogeneous \ Dirichlet: \quad \Phi = \Bbbk \tag{3.13}$$

where Φ is a specific component of the displacement vector field and $\Bbbk$ is a prescribed constant value.

$$\text{\textit{Homogeneous Neumann}}: \qquad \frac{\partial \Phi}{\partial \mathbf{n}} = 0 \qquad\qquad (3.14)$$

here $\mathbf{n}$ is the unit vector normal to the surface.

The Neumann boundary condition denotes the rate of the change of the displacement vector field when it is heading out of the surface. This way explicit boundary conditions have impact upon the way of formulation of FEM.

3.4   Implementation of FEM by the Variational approach

The formulation of the FEM depends on either variational method or the weighted residual method. The weighted residual method, for instance, Galerkin method is more straight forward to apply with the finite element method. But the variational method is more advantageous, specially, when only one global parameter, the propagation constant, is required to solve for the final solution. However, in this thesis, the variational method is considered for implementing optical waveguides by using FEM.

After the choice of formulation method, it can be converted into a standard eigenvalue problem by applying FEM in the form of,

$$[A][U] = \omega^2 [B][U] \qquad\qquad (3.15)$$

here $[A]$ and $[B]$ are real symmetric sparse matrices and $[B]$ is also positive definite matrix.

Equation (3.1) can be rewritten as,

$$[A][U] - \omega^2 [B][U] = 0 \qquad\qquad (3.16)$$

where ω^2 is the eigenvalue and ω is the acoustic angular frequency. The eigenvector $[U]$ represents the unknown value of nodal displacements vectors. Being of canonical form, Eq. (3.16) allows for a more efficient solution by applying one of the standard subroutines to obtain different eigenvectors and eigenvalues.

Once, for a given acoustic propagation constant (k), ω is obtained then, acoustic velocity, v can be determined from,

$$v = \omega/k \tag{3.17}$$

where v is the acoustic wave velocity in *m/s*.

3.4.1 Discretization of domain and generalization of an element
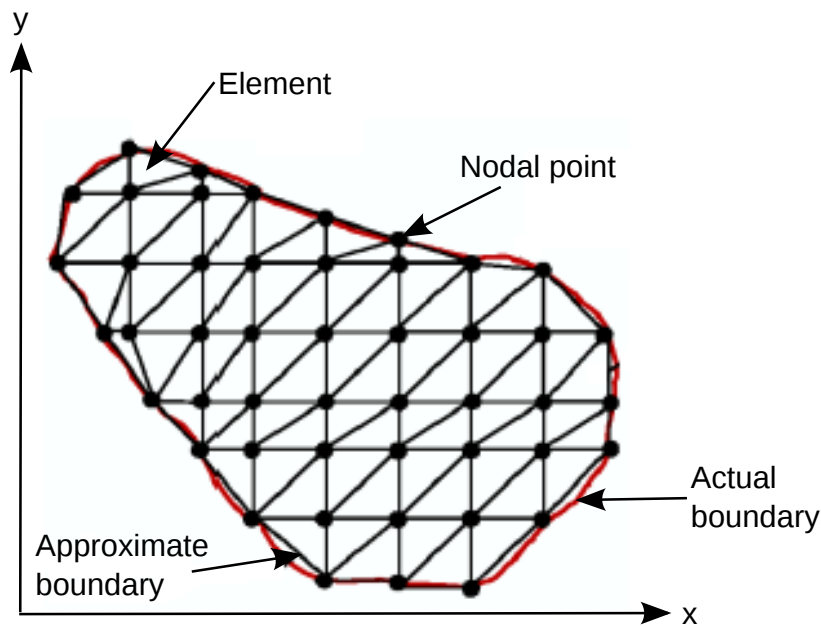
Fig. 3.2 Arbitrary two dimensional domain sub-divided into triangular elements [Leung, Thesis, 2013].

The fundamental concept in FEM is to divide the domain of interest into a finite number of sub-domains or elements. Some elements in the domain may share nodal points and element boundaries. Thus the domain looks like a collection of elements as shown in Fig. 3.2. Element boundaries of an finite element are, generally straight lines. When the domain of interest has curved or irregular boundaries, approximation at the edge is made by using series of straight or flat segments or even by the use of isoparametric elements.

In implementation of FEM, after the domain of interest has been discretized by proper choice of elements, the unknown field variable's behaviour over each element is approximated by continuous functions represented in terms of nodal values of the field variable and sometimes by its derivatives of certain order. The function defined over each element is named as shape function or interpolation function. The collection of the interpolation function for the domain of interest as a whole provide a piecewise approximation of the filed variable

for that domain. In this thesis triangular elements are used to discretize two dimensional waveguide.

3.4.2 Shape functions

After discretization of the domain the unknown filed variable values at the vertices of the triangular shaped element is approximated by a set of polynomial approximation named the shape function. Because polynomials can be easily manipulated both algebraically and computationally, furthermore, any continuous function may be arbitrarily approximated closely by a suitable polynomial, so these are used as shape function. These shape functions are considered to be continuous within the element and across the element boundaries as well. It would not be possible to add separate contribution from each element to get the final solution without inter-element continuity. The physical significance is that the shape functions should possess continuity characteristics similar to that of the physical fields they approximated.

Although it is preferred that interpolation elements to be isotropic or geometrically invariant, however, shape functions may not be invariant. To ensure the solution isotropy, in each element the polynomial expression must be complete, without any preference for either x or y-directions. It means, if the function has an order q, the polynomial that approximating it should contain all possible terms $x^{a1}y^{b1}$ such that,

$$0 \leq a1 + b1 \leq q \qquad (3.18)$$

This type of polynomial should contain $l = \frac{1}{2}(q+1)(q+2)$ terms. The polynomial to be unique the number of terms in it should be equal to the total number of degree of freedom, i.e., the number of nodes associated with the element. For instance, a triangular element requires a polynomial consists of three terms. Equation 3.18 represents the relationship between the nodes in an element and the order of the shape function. The number of terms necessary for all possible polynomials upto the 3rd order is shown in Fig. 3.3 by Pascal triangle.

The triangle is one the most commonly used elements in two dimensional structure, although, rectangles and even quadrilaterals are also used. In this thesis triangle is used as element and first degree polynomials are used as shape functions, which consists of three coefficients, as stated earlier. These can be corresponded to the three nodal values of the triangular element's vertices.
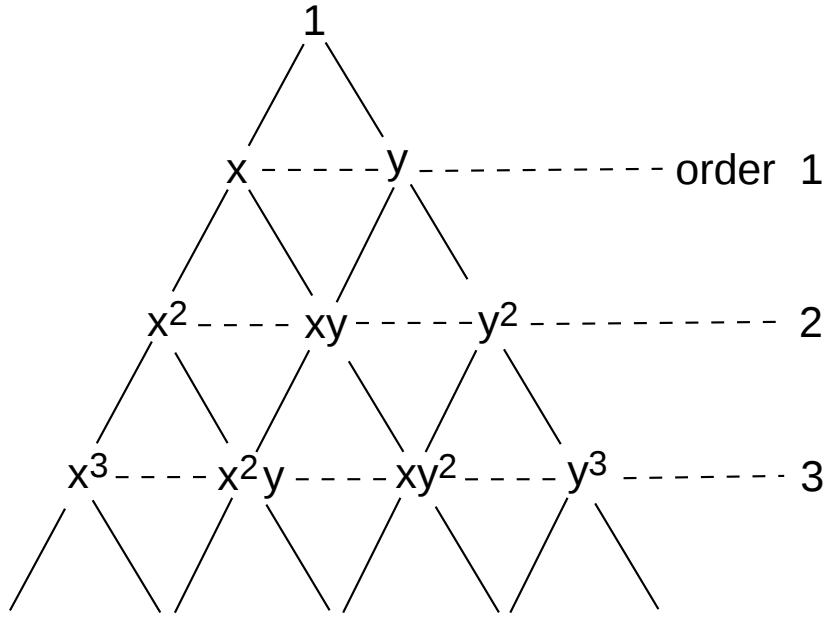
Fig. 3.3 The Pascal triangle [Rahman, Book, 2013].

Let us consider the continuous field function in the domain of interest is $\Phi(x,y)$, which can be replaced by set of discrete values (Φ_e, where $e = 1$, 2 and 3) as shown in Fig. 3.4. Such functions are considered as continuous across adjacent triangles. Field across the elements boundaries should be continuous for these functions to be permissible. A first degree polynomial of the type $a + bx + cy$ can be used to represent the field.

The field in first order element can therefore be expressed as,

$$\Phi_e(x,y) = a^e + b^e x + c^e y \tag{3.19}$$

here a^e, b^e and c^e are constants. At each of the three vertices of the triangle we, then, have,

$$\Phi_e(x_i, y_i) = \Phi_i \qquad i = 1, 2, 3 \tag{3.20}$$

Then Φ_i, the nodal values can be expressed as,

$$\Phi_1 = \Phi_e(x_1, y_1) = a^e + b^e x_1 + c^e y_1 \tag{3.21}$$
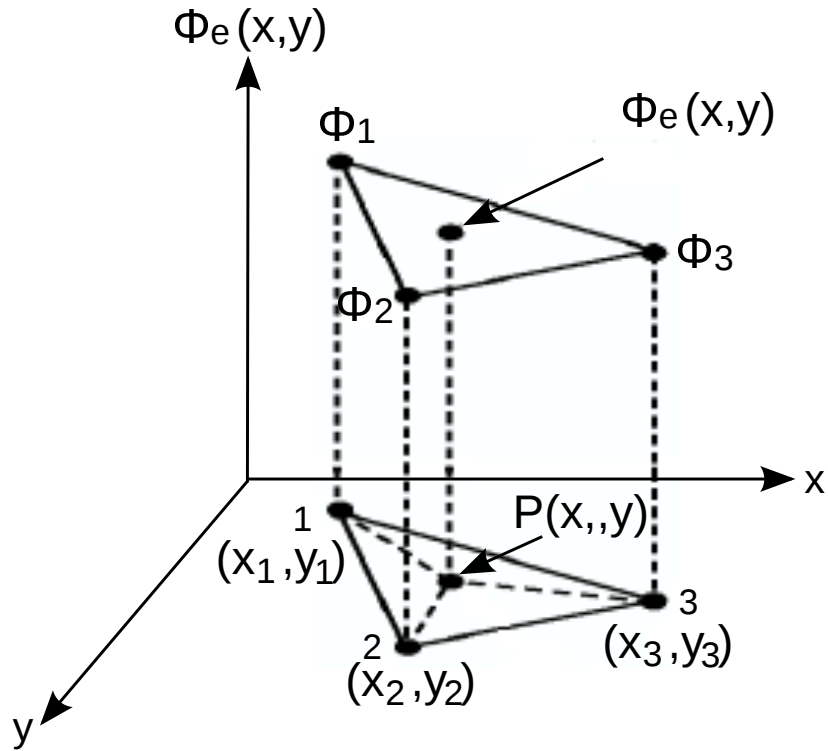
Fig. 3.4 A typical first order triangular element [Leung, Thesis, 2013].

$$\Phi_2 = \Phi_e(x_2, y_2) = a^e + b^e x_2 + c^e y_2 \qquad (3.22)$$

$$\Phi_3 = \Phi_e(x_3, y_3) = a^e + b^e x_3 + c^e y_3 \qquad (3.23)$$

In matrix form,

$$
\begin{bmatrix} \Phi_1 \\ \Phi_2 \\ \Phi_3 \end{bmatrix} =
\begin{bmatrix} 1 & x_1 & y_1 \\ 1 & x_2 & y_2 \\ 1 & x_3 & y_3 \end{bmatrix}
\begin{bmatrix} a^e \\ b^e \\ c^e \end{bmatrix} \qquad (3.24)
$$

In terms of Φ_i the constants a^e, b^e and c^e can be found as,

$$
\begin{bmatrix} a^e \\ b^e \\ c^e \end{bmatrix} =
\begin{bmatrix} 1 & x_1 & y_1 \\ 1 & x_2 & y_2 \\ 1 & x_3 & y_3 \end{bmatrix}^{-1}
\begin{bmatrix} \Phi_1 \\ \Phi_2 \\ \Phi_3 \end{bmatrix} \qquad (3.25)
$$

In expanded form we can write from Eq. (3.25),

$$a^e = \frac{1}{2A_e}[\Phi_1(x_2y_3 - x_3y_2) + \Phi_2(x_3y_1 - x_1y_3) + \Phi_3(x_1y_2 - x_2y_1)] \qquad (3.26)$$

$$b^e = \frac{1}{2A_e}[\Phi_1(y_2 - y_3) + \Phi_2(y_3 - y_1) + \Phi_3(y_1 - y_2)] \qquad (3.27)$$

$$c^e = \frac{1}{2A_e}[\Phi_1(x_3 - x_2) + \Phi_2(x_1 - x_3) + \Phi_3(x_2 - x_1)] \qquad (3.28)$$

here A_e is the area of the triangular element and can be presented as,

$$A_e = \frac{1}{2}\begin{vmatrix} 1 & x_1 & y_1 \\ 1 & x_2 & y_2 \\ 1 & x_3 & y_3 \end{vmatrix} = \frac{1}{2}[(x_2y_3 - x_3y_2) + (x_3y_1 - x_1y_3) + (x_1y_2 - x_2y_1)] \qquad (3.29)$$

Substituting for a^e, b^e, c^e from Eqs. (3.25)-(3.28) into Eq. (3.19) and rearranging will provide,

$$\Phi_e(x,y) = N_1(x,y) \cdot \Phi_1 + N_2(x,y) \cdot \Phi_2 + N_3(x,y) \cdot \Phi_3 \qquad (3.30)$$

or,

$$\Phi_e(x,y) = [N][\Phi_e] \qquad (3.31)$$

where $[N]$ is the shape function matrix and the column vector $[\Phi_e]$ is the vector corresponding to the element nodal field values.

Therefore, after discretizing the domain by using small triangular elements, the unknown field Φ_e in every element, can be written in terms of an interpolation of the field values at each node, as given by Eq. (3.31). It can be shown that the element shape function can be written in the matrix notation form [Davies, 1989] as,

$$[N]^T = \begin{bmatrix} N_1 \\ N_2 \\ N_3 \end{bmatrix} = \frac{1}{2A_e} \begin{bmatrix} x_2y_3 - x_3y_2 & y_2 - y_3 & x_3 - x_2 \\ x_3y_1 - x_1y_3 & y_3 - y_1 & x_1 - x_3 \\ x_1y_2 - x_2y_1 & y_1 - y_2 & x_2 - x_1 \end{bmatrix} \begin{bmatrix} 1 \\ x \\ y \end{bmatrix} \qquad (3.32)$$

here T represents the transpose. This shape function matrix can also be expressed as,

$$[N]^T = \begin{bmatrix} N_1 \\ N_2 \\ N_3 \end{bmatrix} = \frac{1}{2A_e} \begin{bmatrix} a_1^e + b_1^e x + c_1^e y \\ a_2^e + b_2^e x + c_2^e y \\ a_3^e + b_3^e x + c_3^e y \end{bmatrix} \qquad (3.33)$$

The coefficients a_i^e, b_i^e and c_i^e (for $i = 1, 2, 3$) can be calculated as,

$$a_1^e = x_2y_3 - x_3y_2 \qquad (3.34)$$

$$b_1^e = y_2 - y_3 \qquad (3.35)$$

$$c_1^e = x_3 - x_2 \qquad (3.36)$$

with cyclic exchange of $1 \to 2 \to 3$ in Eqs. (3.34)-(3.36), the other six coefficients can also be found.

The shape function N_i has useful property of taking the value 1 at the node i and 0 at all other nodes as,

$$N_i(x_j, y_j) = \delta_{ij} = \begin{cases} 1 & \text{for } i = j \\ 0 & \text{for } i \neq j \end{cases} \qquad (3.37)$$

Relationship of linear shape functions with area coordinates

Let us consider an arbitrary point $P(x, y)$ inside the bottom triangle shown in Fig. 3.4. The area coordinates functions L_i can be represented by utilizing the areas of the triangles as,

$$L_1 = \frac{\text{Area of the sub triangle P23}}{\text{Area of the full triangle 123}} \tag{3.38}$$

in similar way L_2 and L_3 can also be defined. The area coordinates functions L_i has the following property,

$$\sum_{i=1}^{3} L_i = 1 \tag{3.39}$$

The perpendicular distance from P to side 23 is proportional to L_1, which takes the value of 1 at node-1 and 0 in the other nodes. So, it is a unique first degree interpolating polynomial for node-1. Similarly, L_2 and L_3 can also be defined. The interpolating polynomials or local area coordinates, L_i, can be related to the global Cartesian coordinates by interpolation polynomial properties by,

$$x = x_1 L_1 + x_2 L_2 + x_3 L_3 \tag{3.40}$$

$$y = y_1 L_1 + y_2 L_2 + y_3 L_3 \tag{3.41}$$

The Eqs. (3.40) and (3.41) can be expressed in matrix form as,

$$\begin{bmatrix} 1 \\ x \\ y \end{bmatrix} = \begin{bmatrix} 1 & 1 & 1 \\ x_1 & x_2 & x_3 \\ y_1 & y_2 & y_3 \end{bmatrix} \begin{bmatrix} L_1 \\ L_2 \\ L_3 \end{bmatrix} \tag{3.42}$$

By using inverse transformation from Eq. (3.42), we have,

$$\begin{bmatrix} L_1 \\ L_2 \\ L_3 \end{bmatrix} = \frac{1}{2A_e} \begin{bmatrix} a_1^e & b_1^e & c_1^e \\ a_2^e & b_2^e & c_2^e \\ a_3^e & b_3^e & c_3^e \end{bmatrix} \begin{bmatrix} 1 \\ x \\ y \end{bmatrix} \tag{3.43}$$

In terms of the normalized local area coordinates the operation like integration in global coordinates can be attained, where it needs to perform only once. Most of those can be found

in [Zienkiewicz, Book, 2005]. For instance, to obtain integration, following equation can be used,

$$\int\int_e L_1^d L_2^g L_3^f \, dx\, dy = 2A_e \frac{d!\,g!\,f!}{(d+g+f+2)!} \tag{3.44}$$

For the first order polynomial interpolation function, both area coordinates and shape functions are identical, i.e., $N_i = L_i$. The area coordinates are useful in constructing higher order shape functions.

3.5 Implementation of FEM for acoustic wave analysis

The beauty of the FEM technique lies in taking the wave equation like complex differential equation and transforming it into a simpler eigenvalue equation matrix, which can be solved by available standard methods to attain the required solution. So far, the basic concept of FEM has been discussed in this chapter. In this section, the concentration is given on the matrices arises from the choice of interpolation function and the calculation regarding those.

As the problem of interest is the analysis of the acoustic wave propagation, we need to reduce the problem into a two dimensional problem. Let us first consider the direction of wave propagation along the waveguide is in the z-direction. Also the waveguide is uniform and infinite in the direction of propagation. The cross-section of the waveguide is set in xy plane. Further, consider an acoustic wave with a propagation constant k is guided through the optical waveguide. Then the displacement vector field $\mathbf{u}$, due to the propagation of acoustic wave can be expressed as,

$$\mathbf{u} = \begin{bmatrix} u_x(x,y) \\ u_y(x,y) \\ u_z(x,y) \end{bmatrix} e^{j(\omega t - kz)} \tag{3.45}$$

Using the first order triangular element in incorporating FEM the problem can be solved. We need to apply specific phase relation between the nodes of end surfaces. The waveguide particle displacement for the propagation of acoustic wave can be in transverse plane and in longitudinal, i.e., in z-direction. By using bi-dimensional mesh it is possible to solve the problem and reconstruct it. The system of equations associated with the problem concern is stated in Eq. (3.15), which is, $[A][U] = \omega^2 [B][U]$, where $[A]$ is the stiffness matrix corresponds to strain energy and $[B]$ is the mass matrix. Here, the nodal values of externally applied

forces are considered to be zero. The attained modal solution provides ω^2 as eigenvalues and the displacement eigenvectors $\mathbf{U}$.

3.5.1 Formulation of finite element

By subdividing cross-section of an waveguide into a number of triangular elements, the solution for unknown displacement field $\mathbf{u}$ for each element can be approximated by,

$$\mathbf{u}_e = \sum_{i=1}^{q} N_i U_i^e \tag{3.46}$$

here q is the number of nodes, U_i^e is the displacement field at each element node and N_i is a set of interpolation function.

In matrix form, by slightly changing Eq. (2.50), we have,

$$\mathbf{u}_e = [N][U]_e \tag{3.47}$$

As the main interest is to have all the x, y and z components of the field, Eq. (3.47) can be expanded as,

$$\mathbf{u}_e = \begin{bmatrix} N_1 & 0 & 0 & N_2 & 0 & 0 & jN_3 & 0 & 0 \\ 0 & N_1 & 0 & 0 & N_2 & 0 & 0 & jN_3 & 0 \\ 0 & 0 & N_1 & 0 & 0 & N_2 & 0 & 0 & jN_3 \end{bmatrix} \begin{bmatrix} U_{x1} \\ U_{y1} \\ U_{z1} \\ U_{x2} \\ U_{y2} \\ U_{z2} \\ U_{x3} \\ U_{y3} \\ U_{z3} \end{bmatrix} \tag{3.48}$$

here U_x, U_y and U_z are the nodal displacement values in the x, y and z directions, respectively, The second subscripts in the displacements indicated the node numbers. The term j in Eq. (3.48) arises in the matrix for lossless cases, where the U_z components are $90°$ out of phase with the corresponding transverse components.

Now, as stated earlier in Chapter 2, based on the Hooke's law we can relate the stress and strain for small displacements, which is presented in Eq. (2.48). Utilizing that, we can write,

$$\nabla \cdot \mathbf{T} = \nabla \cdot (C\mathbf{S}) \tag{3.49}$$

here **T** represents the stress, **S** is the strain and C is the elastic stiffness coefficient, which can be affected by the crystal symmetry. Details of the elastic stiffness coefficient, its reduced subscript notation and the affect of symmetric nature of crystal with isotropic symmetry on the matrix of C have been presented in Sections 2.3.4, 2.3.5 and 2.4 in Chapter 2.

Next, the stiffness matrix, which incorporates strain tensor, can be expressed as [Auld, 1973],

$$
\begin{bmatrix} S_1 \\ S_2 \\ S_3 \\ S_4 \\ S_5 \\ S_6 \end{bmatrix} = \begin{bmatrix} \frac{\partial U_x}{\partial x} \\ \frac{\partial U_y}{\partial y} \\ \frac{\partial U_z}{\partial z} \\ \frac{\partial U_y}{\partial z} + \frac{\partial U_z}{\partial y} \\ \frac{\partial U_x}{\partial z} + \frac{\partial U_z}{\partial x} \\ \frac{\partial U_x}{\partial y} + \frac{\partial U_y}{\partial x} \end{bmatrix} = \begin{bmatrix} \frac{\partial}{\partial x} & 0 & 0 \\ 0 & \frac{\partial}{\partial y} & 0 \\ 0 & 0 & \frac{\partial}{\partial z} \\ 0 & \frac{\partial}{\partial z} & \frac{\partial}{\partial y} \\ \frac{\partial}{\partial z} & 0 & \frac{\partial}{\partial x} \\ \frac{\partial}{\partial y} & \frac{\partial U_y}{\partial x} & 0 \end{bmatrix} \begin{bmatrix} u_x^e \\ u_y^e \\ u_z^e \end{bmatrix} \tag{3.50}
$$

here u_x^e, u_y^e and u_z^e are the element's nodal displacement vectors in the x, y and z directions, respectively.

Equation (3.50) can be written as,

$$
S_i = \nabla_{ij} u_j^e \tag{3.51}
$$

The strain-displacement relation can also be shown in symbolic notation [Auld, 1973] as, $\mathbf{S} = \nabla_S \mathbf{u}_e$, where the subscript s in the gradient symbol stands for symmetric. In Eq. (3.51) the symmetric gradient operator, $\nabla_{ij} = \nabla_S$, has a matrix form of,

$$
\nabla_S \Rightarrow \nabla_{ij} = \begin{bmatrix} \frac{\partial}{\partial x} & 0 & 0 \\ 0 & \frac{\partial}{\partial y} & 0 \\ 0 & 0 & \frac{\partial}{\partial z} \\ 0 & \frac{\partial}{\partial z} & \frac{\partial}{\partial y} \\ \frac{\partial}{\partial z} & 0 & \frac{\partial}{\partial x} \\ \frac{\partial}{\partial y} & \frac{\partial U_y}{\partial x} & 0 \end{bmatrix} = [D] \tag{3.52}
$$

here for simplicity, $[D]$ is used as symbol to represent symmetric gradient matrix. So, Eq. (3.51) can be rewritten as,

$$
\begin{aligned} \mathbf{S} &= [D]\mathbf{u}_e \\ \Rightarrow \mathbf{S} &= [D][N][U]_e \end{aligned} \tag{3.53}
$$

Now, the elastic restoring forces has been defined in terms of the stress field, $\mathbf{T}(u_j, t)$ and the inertial and elastic restoring forces, i.e. stresses, in a freely vibrating medium has also been related through the translational equation of motion and shown by Eq. (2.47) in Chapter 2. Again, in this thesis, the stress matrix is considered to be symmetric as shown by Eq. (2.10). So, the spatial variation of stress, $\mathbf{T}$, can be determined by the divergence of $\mathbf{T}$, as shown by the left hand side of Eq. (3.49) and can be represented as,

$$\nabla \cdot \mathbf{T} = \begin{bmatrix} \frac{\partial}{\partial x} T_{xx} + \frac{\partial}{\partial y} T_{xy} + \frac{\partial}{\partial z} T_{xz} \\ \frac{\partial}{\partial x} T_{yx} + \frac{\partial}{\partial y} T_{yy} + \frac{\partial}{\partial z} T_{yz} \\ \frac{\partial}{\partial x} T_{zx} + \frac{\partial}{\partial y} T_{zy} + \frac{\partial}{\partial z} T_{zz} \end{bmatrix} = \begin{bmatrix} \frac{\partial}{\partial x} & 0 & 0 & 0 & \frac{\partial}{\partial z} & \frac{\partial}{\partial y} \\ 0 & \frac{\partial}{\partial y} & 0 & \frac{\partial}{\partial z} & 0 & \frac{\partial}{\partial x} \\ 0 & 0 & \frac{\partial}{\partial z} & \frac{\partial}{\partial y} & \frac{\partial}{\partial x} & 0 \end{bmatrix} \begin{bmatrix} T_1 \\ T_2 \\ T_3 \\ T_4 \\ T_5 \\ T_6 \end{bmatrix} = [D]^T \begin{bmatrix} T_1 \\ T_2 \\ T_3 \\ T_4 \\ T_5 \\ T_6 \end{bmatrix} \tag{3.54}$$

here $[D]^T$ represents the transpose of symmetric gradient matrix.

Using Eqs. (3.49), (3.53), (3.54) and (2.47) it can be shown that,

$$\nabla \cdot \mathbf{T} = [D]^T [C][D][N][U]_e = \rho (j\omega)^2 [N][U]_e \tag{3.55}$$

Multiplying both sides of Eq. (3.55) with the conjugate transpose of the nodal displacement vector of element $[N][U]_e$ and integrating over whole domain of element, Ω_e, we have, Using Eqs. (3.49), (3.53), (3.54) and (2.47) we can conclude that,

$$-\int\int_e [N]^*[U]_e^*[D]^T[C][D][N][U]_e d\Omega_e - \omega^2 \int\int_e \rho [N^*][U]_e^*[N][U]_e d\Omega_e = 0 \tag{3.56}$$

here * represents the conjugate transpose.

Finally by incorporating FEM procedure with aid of acoustic translational equation of motion as given by Eq. (2.47), stress-displacement relation as given by Eq. (3.53) and Hooke's law, the stress-strain relation in each element by applying variational principle can generally be expressed as,

$$\int\int_e \left(-[N]^*[U]_e^*[D]^T[C][D][N][U]_e - \omega^2 \rho [N]^*[U]_e^*[N][U]_e \right) d\Omega_e = 0 \tag{3.57}$$

The integral can be evaluated by summing over the whole region, Ω_e. Furthermore, the Eq. (3.57) can be formulated as a standard eigenvalue problem by rearranging and rewriting it in matrix form, as,

$$[A][U] - \omega^2[B][U] = 0 \qquad (3.58)$$

here ω^2 is the eigenvalue, $[U]$ is the eigenvector, $[A]$ is reduce to a real symmetric form and is known as stiffness matrix, which is related to the strain energy. $[B]$ is real symmetric and also positive definite matrix. It is also known as mass matrix that relates to the kinetic energy.

The matrices $[A]$ and $[B]$ can be defined as,

$$[A] = -\int\int_e ([Q]^*[C][Q])d\Omega_e \qquad (3.59)$$

$$[B] = \rho \int\int_e [N]^*[N]d\Omega_e \qquad (3.60)$$

where $[Q]$ is replaced the matrix multiplication $[D][N]$ and ρ is the waveguide material density.

These matrices can be generated for a provided acoustic propagation constant k. Solving the generalize eigenvalue system equation, given by Eq. (3.58), yields eigenvalue ω^2, where ω is acoustic angular frequency and eigenvector $[U]$ as the displacement vector. For a provided input k and generated output ω, using Eq. (3.17) acoustic velocity, v, can be determined. Beside that if for a given acoustic frequency, the propagation constant is to be determined, then a simple iteration process needs to be considered.

3.6   Formulation for optical analysis

In this thesis, for optical mode analysis, a FEM approach based on the vector **H**-field formulation is used. This is one of the most numerically efficient and accurate approaches to obtain the modal field profiles and the propagation constants of the fundamental and higher order quasi-TE and quasi-TM modes. The full-vectorial formulation is based on the minimization of the full **H**-field energy functional [Rahman, 1985],

$$\omega_o^2 = \frac{\int \left[(\nabla \times \mathbf{H})^* . \hat{\varepsilon}^{-1}(\nabla \times \mathbf{H}) + p(\nabla . \mathbf{H})^*(\nabla . \mathbf{H}) \right] dxdy}{\int \mathbf{H}^* . \hat{\mu}\mathbf{H}dxdy} \qquad (3.61)$$

here $\omega_o{}^2$ is the eigenvalue for optical system of equations and ω_o is the angular frequency of the optical wave, **H** is the full-vectorial magnetic field and $*$ represents the complex conjugate transpose. To eliminate spurious solutions, p, the weighing factor for the penalty term is considered. $\hat{\varepsilon}$ and $\hat{\mu}$ are the permittivity and permeability, respectively.

3.7 Convergence test and benchmarking with steel wave-guide

A numerically efficient computer simulation code has been generated based on the methodology discussed in Section 3.5 and eigenvector $[U]$ and eigenvalue ω^2 are obtained by using real eigenvalue solver computer programme. The solution convergence test for this programme has been studied, using a Ge-doped silica planar waveguide of structural dimension $2 \ \mu m \ \times$ $1 \ \mu m$ embedded in un-doped silica, on the fundamental acoustic shear wave. Furthermore, numerical analysis has been performed on a steel rod of square cross-section with dimension $1 \ cm^2$ being exposed in air and the modal solutions are compared with the results found for the analysis performed with the similar waveguide exposed in Xenon gas [Sriratanavaree, Thesis, 2014] and also in vacuum [Hennion, 1996].

3.7.1 Convergence test

At the beginning, for convergence test a 3% Ge-doped silica core with dimension $2 \ \mu m \ \times \ 1$ μm embedded in un-doped silica has been considered. The longitudinal and shear acoustic wave velocities of the un-doped silica cladding are taken as, $V_{LC} = 5933 \ m/s$ and $V_{SC} = 3764$ m/s, respectively. Similarly, the longitudinal and shear wave velocities for 3% Ge-doped core are taken as $V_{LG} = 5806 \ m/s$ and $V_{SG} = 3677 \ m/s$, respectively [Jen, 1986]. In this study, to get pure shear wave both the longitudinal velocities of core and cladding are set to 5933 m/s. The densities of the both doped and un-doped silica are taken as 2202 kg/m^3. The values of the elastic coefficients are calculated using Eqs. (2.30), (2.33) and (2.35) given in Chapter 2. This waveguide supports both the longitudinal and shear modes. In this section, however, the convergence test of the modal solution for the fundamental acoustic shear mode has been focused only. These modes are more complex, details of which will be discussed in Chapter 4. The data presented above along with the values of the elastic coefficients for both the materials are listed in the Table 3.1.

Aitken's extrapolation [Rahman, 1985] technique can be used to improve the solution accuracy. To use this technique, the structure needs be refined in a fixed geometric ratio.

Table 3.1 Material properties of the Ge-doped planar silica waveguide used for convergence testing

Material	Velocity (m/s)		Density (kg/m^3)	Elastic Coefficient (GPa)		
	V_L	V_S	ρ	C_{11}	C_{12}	C_{44}
3% Ge-doped	5933	3677	2202	77.5115	17.9680	29.7718
Un-doped silica	5933	3764	2202	77.5115	15.1170	31.1972

From three successive mesh refinements, final solutions can be extrapolated for a possible infinite mesh refinement as given below,

$$\omega_\infty = \omega_3 - \frac{(\omega_3 - \omega_2)^2}{\omega_3 - 2\omega_2 + \omega_1} \tag{3.62}$$

where, ω_1, ω_2, and ω_3 are results obtained by successively using higher mesh divisions and ω_∞ is the extrapolated result equivalent to infinite mesh divisions. Here, this geometric ratio does not have to be 1:2:4 but other ratio can also be used, but it should be noted that mesh divisions can only be of integer value and in all the regions the same mesh refinement ratio must be maintained.

Variations of the acoustic frequency of the fundamental shear U_{11}^x mode for $k = 17 \ \mu m^{-1}$ with the mesh division are shown in Fig. 3.5. In this case, equal mesh divisions are used in both the transverse directions. It can be noted that as the number of the mesh division is increased, these solutions rapidly converge to their exact solutions. However, it can be easily observed that modal solutions convergence with increasing mesh division when the full structure is simulated as shown by a dashed blue line. Besides that, when Aitken's extrapolation is used, the solution accuracy is much improved. For the full structure, when the geometric ratio 1:2:4 and 1:1.5:2.25 (or 4:6:9) are used, as identified as ATF(1:2:4) and ATF(4:6:9), and shown by the red dashed and yellow solid lines, respectively, it can be observed that better solution accuracy can be obtained. However, it can be noted that 4:6:9 geometric ratio, shown by a yellow solid line, converges better than use of 1:2:4 (dashed red line). To show this region more clearly, an expanded version of this region is shown as an inset. Along with its displacement profiles the details of this shear mode will be discussed in Chapter 4.
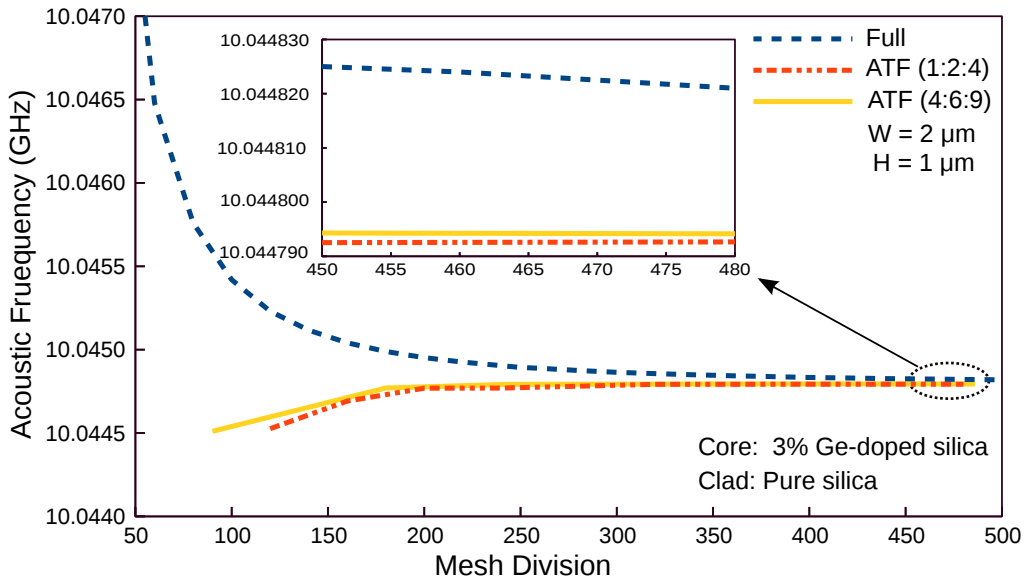
Fig. 3.5 Variation of eigen frequency with the mesh division for the U_{11}^x mode at $k = 17$ μm^{-1}.

3.7.2 Benchmarking with steel waveguide

Initially, a steel waveguide of square cross-section (1 cm^2) has been selected to benchmark the developed FEM based computer simulation code. The modal solutions are compared with two of the research works, where both the researcher used similar waveguide but different environments as cladding. In one steel waveguide was exposed in Xenon gas [Sriratanavaree, Thesis, 2014] and in the other steel waveguide was placed in vacuum [Hennion, 1996].

It is well known that the air surrounded steel waveguide can carry acoustic waves. In this section the acoustic longitudinal and shear wave velocities and density of mild steel are taken as $V_{LG} = 5797.4978$ m/s, $V_{SG} = 3098.8923$ m/s and $\rho_G = 7850$ kg/m^3, respectively [Sriratanavaree, Thesis, 2014]. Air does not support any shear wave. For the air cladding, these are considered to be $V_{LC} = 340$ m/s and $\rho_C = 1.29$ kg/m^3, respectively [Jiang, 2011]. The required acoustic properties of mild steel and air are listed in Table 3.2.

Table 3.2 Acoustic properties of steel and air

Material	Velocity (m/s)		Density (kg/m^3)	Elastic Coefficient (GPa)		
	V_L	V_S	ρ	C_{11}	C_{12}	C_{44}
Steel	5797.4978	3098.8923	7850	263.8462	113.0770	75.3846
Air	340	0.0	1.29	149.124×10^{-6}	149.124×10^{-6}	0.0

This steel waveguide supports many acoustic modes, among which we have considered one of the shear acoustic mode, U_{21}^X, to benchmark the work as it closely resembles with the eigenvalues reported in [Hennion, 1996] where the guide is in vacuum. Also the results are compared with the eigenvalues reported in [Sriratanavaree, Thesis, 2014] where the guide is exposed in Xenon gas. All results found are in close proximity.

Table 3.3 Compared results for the eigen frequencies of steel waveguide.

k (m^{-1})	Acoustic frequency (kHz)		
	Steel in air	Steel in Xenon	Steel in vacuum
200	94.8	98.9221	94.66
400	194.08	188.6422	189.43
600	293.45	279.3516	285.23

Table 3.3 listed the eigenfrequencies obtained by using 250×250 mesh division for different values of propagation constants, k. This table also includes its comparison with the previously reported works [Sriratanavaree, Thesis, 2014 and Hennion, 1996], where the same propagation constants are considered.

3.7.3 Few acoustic modes in steel waveguide

The displacement mode profiles along with the displacement vectors variations of the fundamental and second-order shear acoustic modes in the steel waveguide is presented in this section. It is found that both of these shear modes are highly hybrid modes.
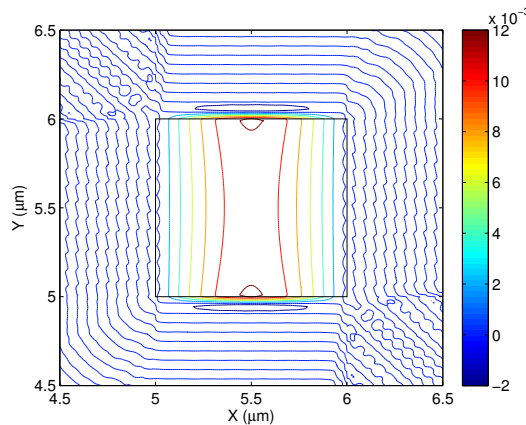
Fig. 3.6 Displacement vector profile of the dominant U_X component of fundamental U_{11}^x acoustic mode at $k = 400\ m^{-1}$.

The acoustic frequency of the U_{11}^X mode was found to be 197.29 kHz and with a group velocity of 3098.98 m/s. Figure 3.6 shows the displacement vector profile of U_X component of the fundamental U_{11}^X acoustic shear mode at a propagation constant of $k = 400\ m^{-1}$. The black square boundary at the centre represents the steel waveguide boundaries. It is to be noted that this component is confined in the core and maximum displacement occurs at the centre. The U_Y component of this mode is shown in Fig. 3.7.
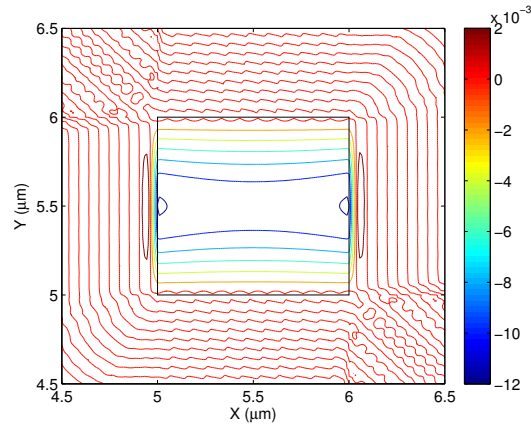
Fig. 3.7 Displacement vector profile of the non-dominant U_Y component of fundamental U_{11}^x acoustic mode at $k = 400\ m^{-1}$.

The displacement vectors of the resultant transverse U_T mode, found by vectorial addition of both the transverse components U_X and U_Y is presented in Fig. 3.8. It is obvious that at the propagation constant $k = 400\ m^{-1}$ the fundamental shear mode tends to bend the steel waveguide.
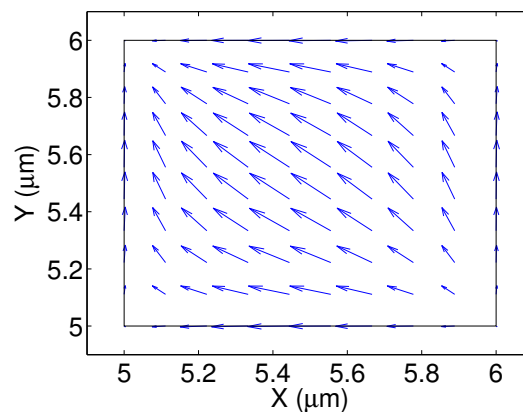
Fig. 3.8 Displacement vectors of U_T mode at $k = 400\ m^{-1}$.

Figure 3.8 shows the displacement vector profile of U_Z component of the fundamental U_{11}^X acoustic shear mode at a propagation constant of $k = 400 \ m^{-1}$.
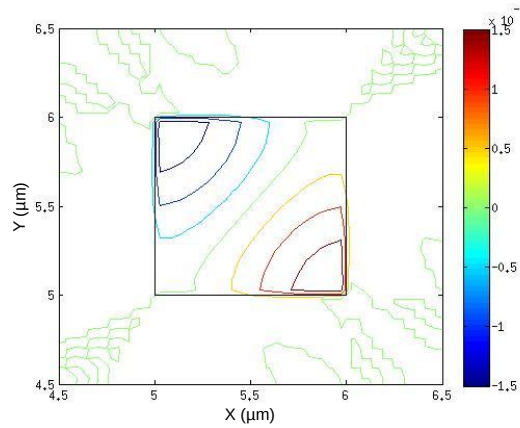
Fig. 3.9 Displacement vector profile of the non-dominant U_Z component of fundamental U_{11}^x acoustic mode at $k = 400 \ m^{-1}$.

The acoustic mode, which eigenvalue is compared at different propagation constant in Table 3.3, attains a group velocity of 2979.83 m/s at a propagation constant of $k = 200 \ m^{-1}$. Although it is named as U_{21}^X mode due to its spatial variation, this acoustic mode is also highly hybrid and propagate as a surface wave with a frequency of 94.8 kHz at the stated propagation constant. The displacement vector profiles of the components U_X, U_Y and U_Z of this acoustic mode are shown in Figs. 3.10, 3.11 and 3.12, respectively.
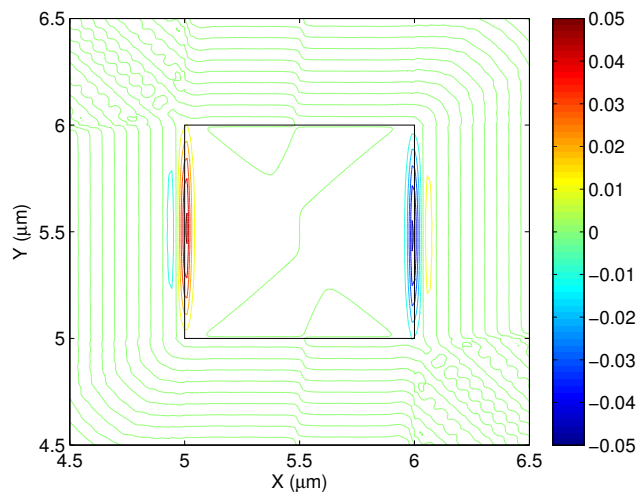
Fig. 3.10 Displacement vector profile of the U_X component of U_{21}^x acoustic mode at $k = 200 \ m^{-1}$.
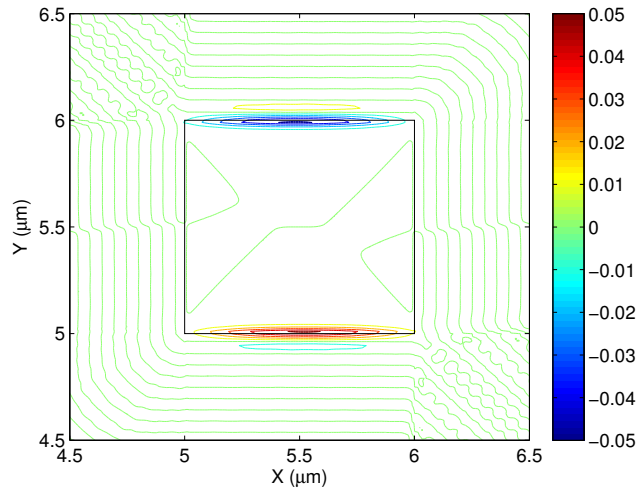
Fig. 3.11 Displacement vector profile of the U_Y component of U_{21}^x acoustic mode at $k = 200$ m^{-1}.
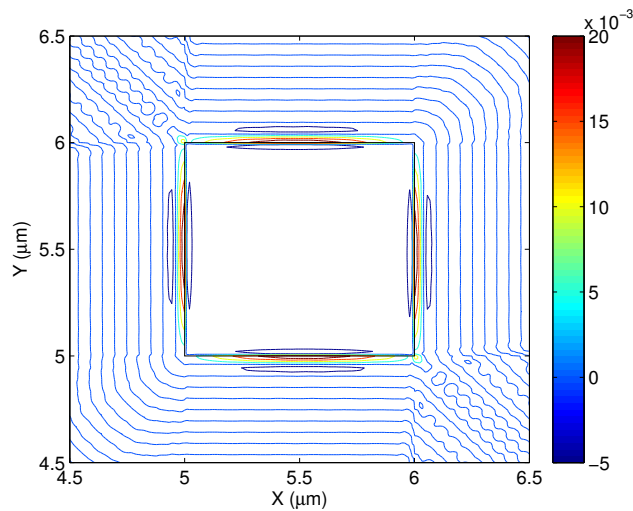
Fig. 3.12 Displacement vector profile of the U_Z component of U_{21}^x acoustic mode at $k = 200$ m^{-1}.

The displacement vectors of the resultant transverse U_T mode for this surface acoustic mode is presented in Fig. 3.13. It is clear that this surface acoustic mode appeared to compress the waveguide at the propagation constant $k = 200\ m^{-1}$.
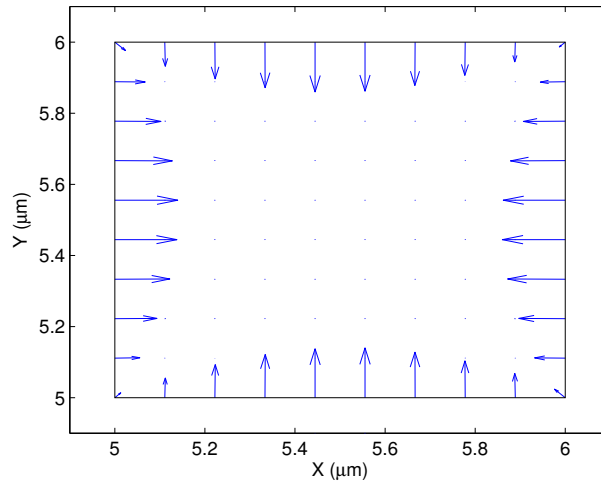
Fig. 3.13 Displacement vectors of U_T mode at $k = 200\ m^{-1}$ of the surface acoustic mode U_{21}^X.

3.8   Summary

The theoretical formulation of two dimensional optical waveguide with FEM has been presented in this chapter. Where the concerned problem is converted to a two dimensional problem and domain discretisazion is performed only upon the cross-section of the waveguide by meshing with triangular finite elements. After testing method validation for convergence using Aitken's extrapolation, the end results for a simple case of $1cm^2$ cross-section steel rod exposed in air are compared with available literature to demonstrate the model accuracy. At the end displacement vector profiles of two highly hybrid acoustic modes that may exist in the steel waveguide were presented.

Chapter 4

Low Index Contrast Silica Planar Waveguide

4.1   Introduction

Silica optical fibers are the most extensively used optical waveguides because of their wide availability and extremely low optical loss, but their planar versions are also widely used for the fabrication of various planar photonic integrated circuits (PICs).

In this chapter weakly guided acoustic waves in a low index contrast silica planar waveguide have been studied by using a full-vectorial FEM based numerical method. To keep the index contrast low a lightly doped silica rectangular core is used being embedded in un-doped silica cladding. The shear and longitudinal acoustic waves in this waveguide are obtained, firstly by ensuring any one type of acoustic waves, either shear or longitudinal, exists and then considering their co-existence. The effect of dopant concentration on such waves are also observed and presented.

4.2   Structure, materials and their acoustic properties

Silica fibers are the most commonly used optical waveguides due to their property of having the lowest loss so far shown by any optical waveguide and millions of kilometers have been laid down for long-distance communication networks. However, when various photonic components are considered for modern communication systems, often planar forms are used as functionality of a PIC can be increased for a compact, reliable and yet low-cost systems. Although, in the fabrication of PICs, semiconductor materials like InP or GaAs have the advantages of allowing the incorporation of active components such as semiconductor lasers

or alternatively electro-optic dielectric materials such as lithium niobate for high-speed modulators, however, for many passive devices such as power splitters and AWG filters, often planar silica guides are used as they have lower loss and cost less and also they provides lower coupling loss to a silica fibre.

Planar silica waveguide can be fabricated by using flame hydrolysis deposition (FHD) technique [Marques, 2002] or by using plasma enhanced chemical vapour deposition (PECVD) [Bellman, 2004]. Silica can be doped by Ge to increase the refractive index to form a waveguide core, and this process also increases equivalent acoustic index of the doped region compared to un-doped silica cladding and as a result, this optical waveguide will also supports acoustic waves. The longitudinal and shear acoustic wave velocities of the un-doped silica cladding are taken as, V_{LC} = 5933 m/s and V_{SC} = 3764 m/s, respectively. Similarly, the longitudinal and shear wave velocities in for 3% Ge-doped core are taken as V_{LG} = 5806 m/s and V_{SG} = 3677 m/s, respectively [Jen, 1986]. Although the material density of 3% Ge-doped silica is 2244 kg/m^3, here, for simplicity, the densities of the both doped and un-doped silica are taken as 2202 kg/m^3. These values along with the elastic coefficients are listed in Table 4.1 in Section 4.4. This waveguide will support both the longitudinal modes and shear modes. The acoustic waveguide is illustrated in Fig. 4.1, and its height and width are shown as H and W. For this chapter the height is considered as $1\mu m$ and width as $2\mu m$. It can be observed here that this waveguide has a two-fold symmetry and this symmetry can be exploited, as is discussed later in Section 4.3.
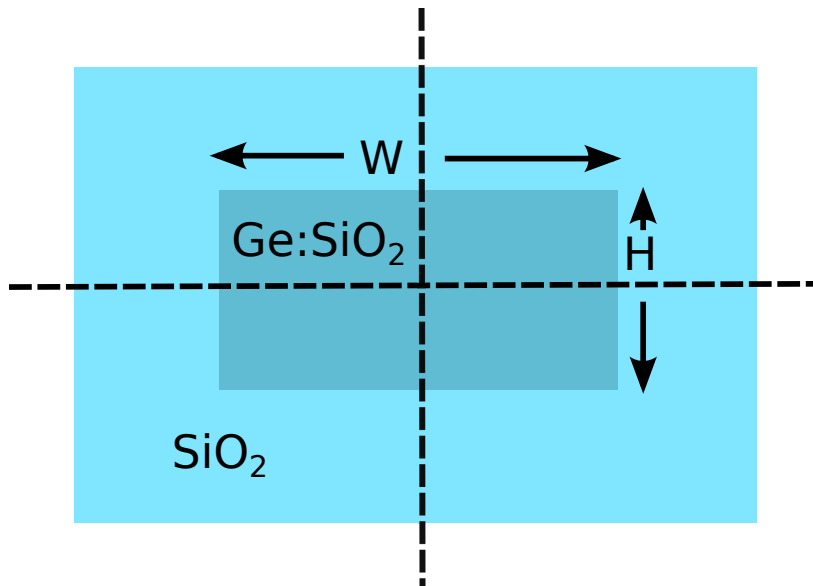
Fig. 4.1 Ge-doped planar silica waveguide.

4.3   Symmetry boundary conditions

Symmetry conditions of optical waveguides have been extensively exploited [Rahman, Book, 2013], whenever they exist, for the modal solutions of optical waveguides. This not only can avoid mode degeneration by separating two interacting modes, but also allow much improved solutions, with a given computer resource. Since this structure has a two-fold symmetry, only one-quarter of the waveguide needs to be considered, which will allow a much finer mesh division to be used. The combinations of $\mathbf{n} \times \mathbf{U}$ and $\mathbf{n}.\mathbf{U}$ at the vertical and horizontal symmetry lines can be used, and there are 4 combinations, which will give all the shear acoustic U_{mn}^{X} and U_{mn}^{Y} modes, and longitudinal acoustic U_{mn}^{Z} modes with various combinations of m and n values, being them even or odd, illustrated in Appendix B. The possible symmetry boundary conditions are shown in Fig. 4.2.
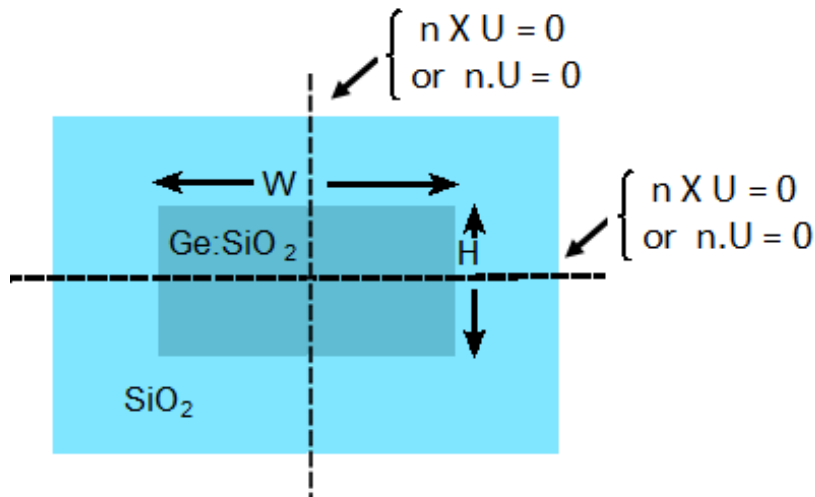
Fig. 4.2 Symmetry boundary conditions for planar silica waveguide.

4.4   Characterizing acoustic waves in silica planar waveguide

Initially, for this weakly guided Ge-doped silica planar waveguide, the analyses are performed assuming (Option I) the longitudinal acoustic velocities of Ge-doped silica core and un-doped silica cladding are equal, i.e., $V_{LG} = V_{LC}$, and then considering (Option II) the shear acoustic velocities of both the core and cladding are equal, i.e., $V_{SG} = V_{SC}$. The first option will ensure only shear acoustic waves exists in the guide, thus it will be decoupled from the longitudinal

acoustic modes, and the second option will ensure the longitudinal modes remain decoupled. At the end, a more realistic approach (Option III) is also considered, where all longitudinal and shear velocities are taken as unequal. All the longitudinal and shear velocities, densities and elastic coefficients for core and cladding materials are listed in the Table 4.1.

Table 4.1 Procedural options and acoustic properties of materials for the Ge-doped planar silica waveguide

Options		Velocity (m/s)		Density (kg/m^3)	Elastic Coefficient (GPa)		
		V_L	V_S	ρ	C_{11}	C_{12}	C_{44}
Option I	**Core**	5933	3677	2202	77.5115	17.9680	29.7718
	Clad	5933	3764	2202	77.5115	15.1170	31.1972
Option II	**Core**	5806	3764	2202	74.2286	11.8341	31.1973
	Clad	5933	3764	2202	77.5115	15.1170	31.1972
Option III	**Core**	5806	3677	2202	74.2286	14.6851	29.7718
	Clad	5933	3764	2202	77.5115	15.1170	31.1972

4.4.1 Option I: Shear acoustic modes for 3% Ge-doped core

The core is doped with GeO_2, thus both the longitudinal and shear velocities of the doped core are less than those of silica cladding. As shown in Table 4.1, for Option I, both the longitudinal velocities in core and cladding are considered to be equal to have decoupled shear acoustic modes. For this case, $\frac{\triangle V_S}{V_S} = 0.0231$, the material contrast is small and therefore this waveguide will act as a weakly guiding for the shear modes.

This waveguide supports two near degenerate fundamental shear modes. In a way similar to that for optical modes, one of the modes has dominant U_X component and other has a dominant U_Y component and these will be identified as U_{mn}^X and U_{mn}^Y modes, respectively, where m and n will identify their spatial variations. However, these modes also have other two non-dominant components, such as the U_{mn}^X mode, which will also have U_Y and U_Z displacement vectors. This confirms that even for a shear mode, there will be a material displacement along the axial direction also. So, any scalar approach would be unsuitable to find acoustic modes in such a waveguide. The U_X, U_Y and U_Z displacement vector profiles of the fundamental U_{11}^X mode at $k = 17.0 \ \mu m^{-1}$ are shown in Fig.4.3 when the waveguide width, W = 2 μm and its height, H = 1 μm. The outline of the waveguide is shown by solid black lines in the figure.

It can be observed that the dominant U_X profile of this mode, shown in Fig. 4.3(a), is nearly Gaussian in shape with its peak value at the center of the waveguide. On the
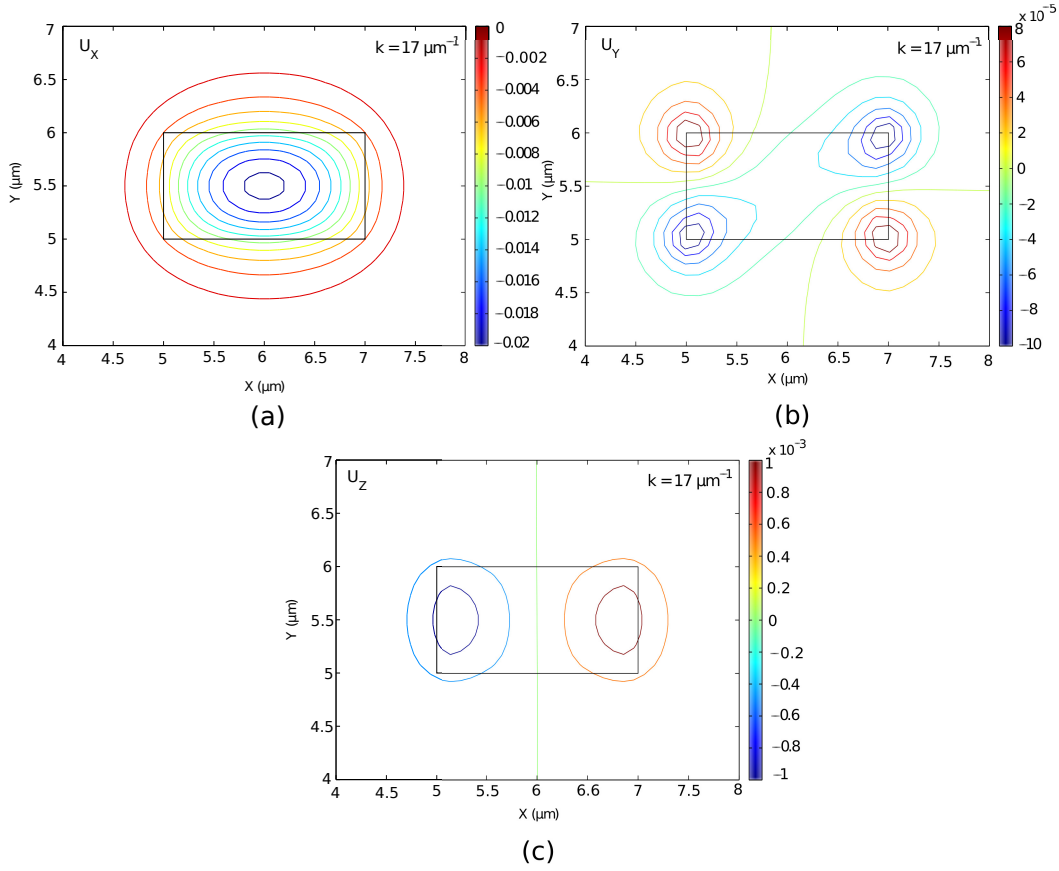
Fig. 4.3 U_X, U_Y and U_Z displacement vectors of the U_{11}^X mode.

other hand, the non-dominant U_Y vector as shown in Fig. 4.3(b), shows a higher order spatial variation with alternative positive and negative peaks at the adjacent corners of the waveguide where its peak value is about 2 orders of magnitude lower than that of the dominant displacement vector, U_X. The U_Z profile is shown in Fig. 4.3(c), which illustrates its positive and negative peaks along the two vertical side walls. Its maximum magnitude is about 5% of the fundamental displacement vector, U_X. In this case 200×200 mesh divisions were used for the full structure and the corresponding acoustic frequency was 10.0449 GHz.

It was observed that the Gaussian profile of the dominant U_X component of the fundamental U_{11}^X mode got more confine in the core with the increase in frequency, as well as their magnitude increases along with the reduction of full width half maxima (FWHM). Figure 4.4 depicts clearly its magnitude variation with the three steps of frequency changes as 4, 8 and 16 GHz. The FWHM of the displacement vectors has been calculated. The FWHM for the U_{11}^x mode in the x-direction was 2.9 μm at $f = 4$ GHz and this value reduces to 1.5 μm when the frequency increases to 16 GHz.
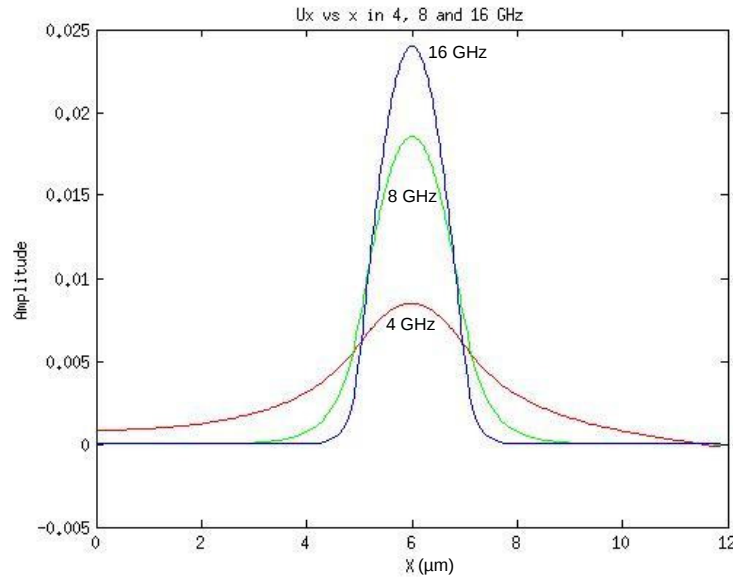
Fig. 4.4 The dominant U_X component of the U_{11}^X mode at 4, 8 and 16 GHz acoustic frequencies.

As this waveguide has a two-fold symmetry and this symmetry can be exploited by incorporating symmetry boundary conditions as discussed in Section 4.3. The displacement vector profiles of U_X, U_Y and U_Z components in U_{11}^X acoustic shear mode after applying for two-fold symmetry are shown in Fig. 4.5. By incorporating two-fold symmetry we can not only eliminate the modal degeneration but also can improve the accuracy of modal solution for a given computer resource. The core-clad interfaces are shown by the black lines in Fig. 4.5

However, for the fundamental U_{11}^Y mode, its acoustic frequency was 10.048 GHz for the same wavenumber, $k = 17 \ \mu m^{-1}$. As the waveguide width and height were not the same, eigenfrequencies of U_{11}^X and U_{11}^Y modes were not exactly the same but yet very close. For U_{11}^Y mode, the dominant U_Y displacement vector was Gaussian in shape with its spatial variation was similar to the dominant U_X of the U_{11}^X mode. For this U_{11}^Y mode, its non-dominant U_X displacement has four peaks at the four corners of the waveguide and U_Z shows its maximum values at the upper and lower horizontal interfaces. The displacement vector profiles of U_X, U_Y and U_Z components of the U_{11}^Y mode are shown in Fig. 4.6.

The displacement vectors of the resultant transverse U_T mode, found by vectorial addition of both the transverse components U_X and U_Y for U_{11}^X and U_{11}^Y modes separately are presented in Fig. 4.7 for propagation constant $k = 17 \ \mu m^{-1}$. For both the cases the material displacements are dominating by the dominant components of each fundamental

(a)   (b)

(c)
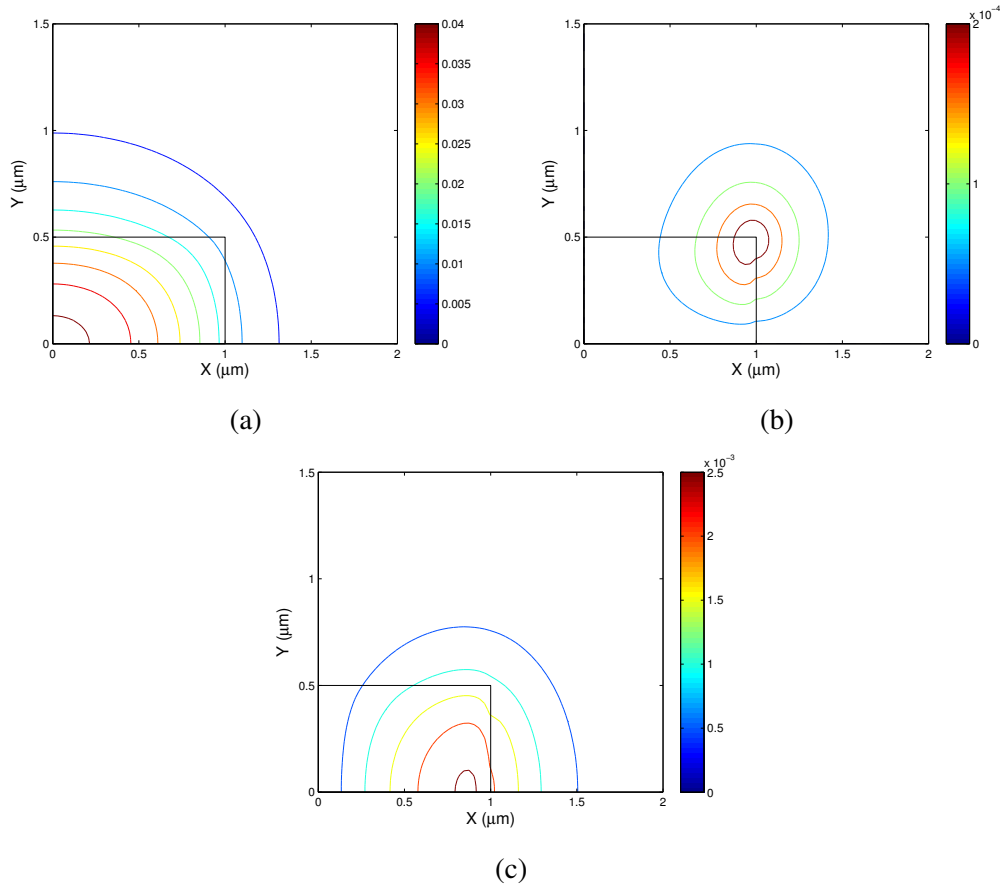
Fig. 4.5 U_X, U_Y and U_Z displacement vectors of the U_{11}^Z mode exploiting two-fold symmetry.

shear modes. Although their frequencies are much closer but not the same, total displacement in the transverse plane for these two modes are shown separately in Fig. 4.7.

The close proximity of two fundamental shear modes allows these modes to interact and eigenvectors become mixed - this cannot be avoided when the whole structures is simulated as both the eigenmodes appear in close proximity. If a finer mesh division can be used then this mode degeneration will reduce.

Dispersion curves of the fundamental shear acoustic U_{11}^X and U_{11}^Y modes are shown in Fig. 4.8. The variations of their phase velocities with the acoustic frequencies are shown here. For the fundamental U_{11}^X mode, as shown by a dashed blue line, it can be observed that when the frequency is reduced the phase velocity increases monotonically and reaches that of the cladding shear velocity, V_{CS}, as the mode approaches its effective cutoff near 3.59 *GHz*. It was shown earlier in Fig. 4.4, as the frequency is increased the mode becomes more confined within the core. It is to be noted that for whole range of acoustic frequencies the

(a)

(b)

(c)
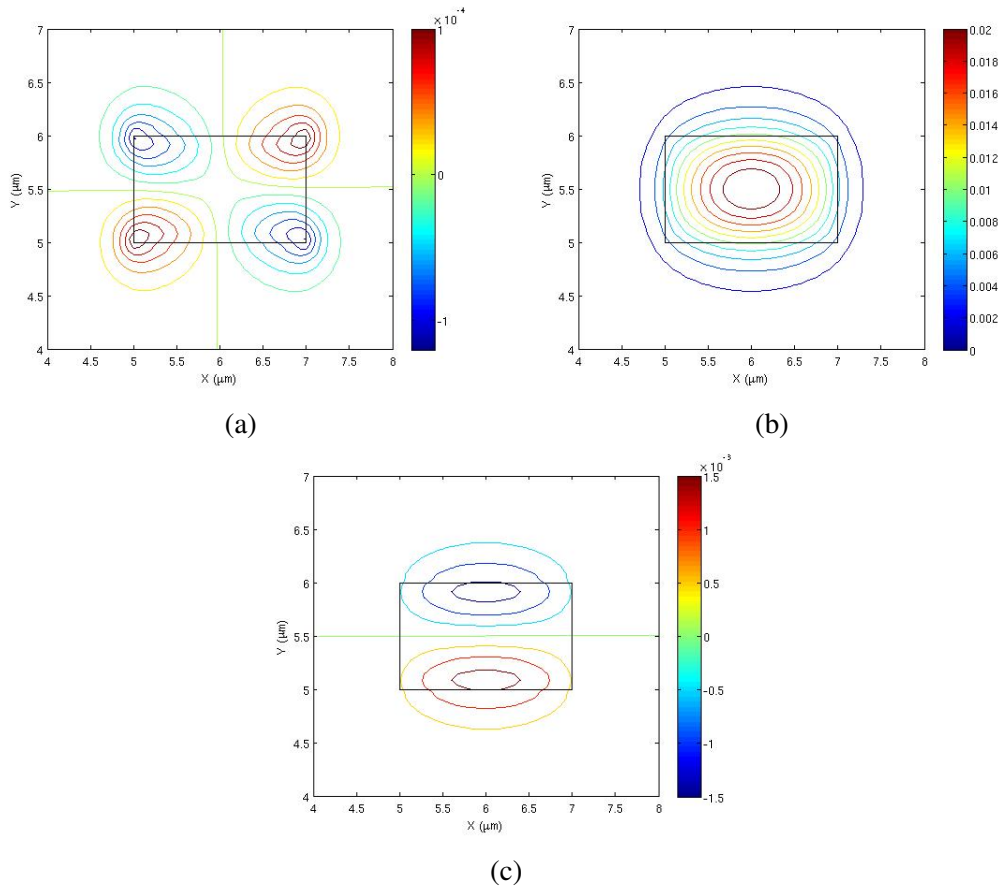
Fig. 4.6 U_X, U_Y and U_Z displacement vectors of the U_{11}^Y mode at $k = 17$ μm^{-1}.

(a)

(b)
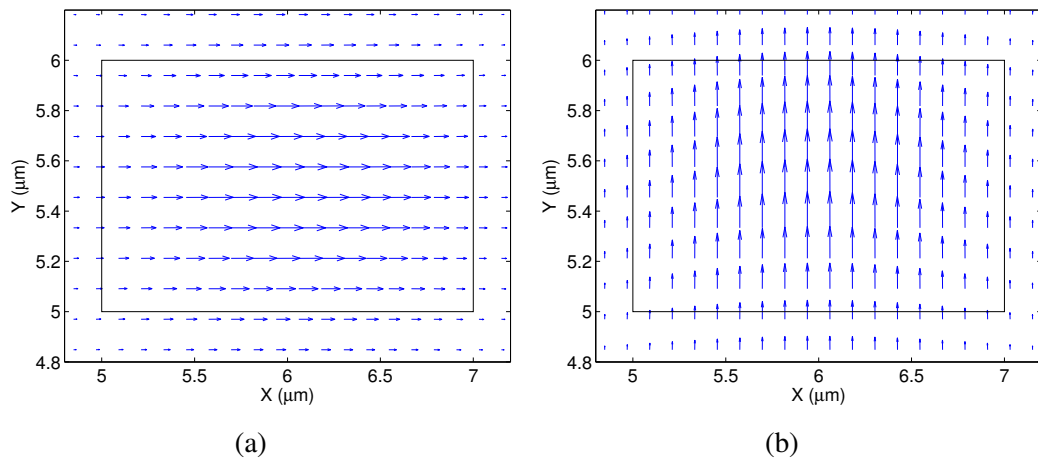
Fig. 4.7 Total displacement vectors, U_T, in the transverse plane at $k = 17$ μm^{-1} for (a) U_{11}^X and (b) U_{11}^Y modes.

phase velocity of the U_{11}^Y mode, represented by the solid red line, is higher than that of the U_{11}^X mode. The effective cutoff frequency of the U_{11}^Y mode was found near 3.593 *GHz*.
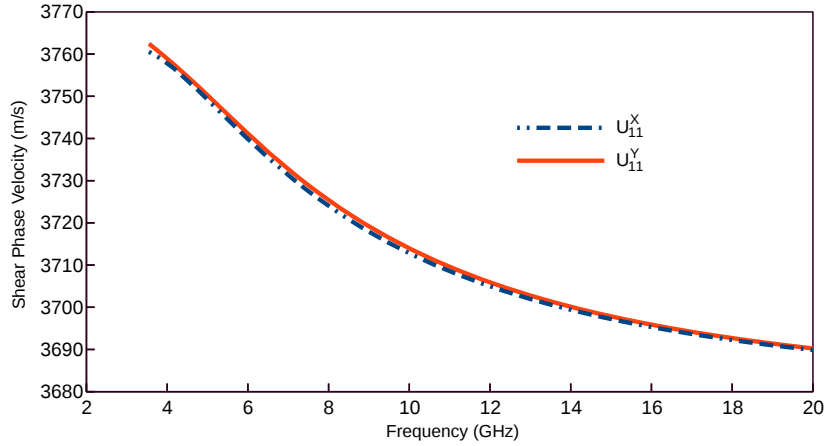
Fig. 4.8 Dispersion curves of acoustic shear U_{11}^X and U_{11}^Y modes.

Dispersion curves for several shear U_{mn}^X modes are calculated for a 2 $\mu m \times 1\ \mu m$ Ge-doped silica waveguide and shown in Fig. 4.9. It represents the variations of their phase velocities with the acoustic frequencies. Here the solid blue line represents the fundamental U_{11}^X mode. For this waveguide, the cutoff frequency of the second mode, U_{21}^X, shown by a red line is 7.19 *GHz*, so this waveguide will support only one shear mode (with the dominant U_X displacement) between 3.6-7.2 *GHz*. It should also be noted that the dispersion curves for the U_{12}^X and U_{21}^X are different as the height and width of the waveguide were not the same. Even when the height and width of a waveguide are equal (the waveguide has a 90° rotational symmetry), the U_{21}^X and U_{12}^X modes would be degenerated but by exploiting the symmetry conditions, as shown here, they can be isolated. It should be noted that similar dispersion curves for all the U_{mn}^Y modes can also be obtained. However, it should be noted that for identical height and width, U_{12}^X and U_{21}^Y will have the same eigenfrequency and as they also require the same symmetry conditions they cannot be isolated.

Dispersion curves of all the shear U_{mn}^Y modes are also calculated for this waveguide and shown in Fig. 4.10, which shows the variations of their phase velocities with the acoustic frequencies. The solid blue line represents the fundamental shear U_{11}^Y mode. It should be noted here also that the dispersion curves for the U_{12}^Y and U_{21}^Y are different as the height and width of the waveguide were different. The cutoff frequency of the second U_{21}^Y mode, shown by a red line was found as 7.191 *GHz*.

To get any point in the dispersion curve of any specific acoustic mode, such as in Fig. 4.9 in Chapter 4, for a given value of the acoustic propagation constant (k), the eigenvalue (ω^2) was determined by running the simulation code. Then the mode was checked, if it is spurious
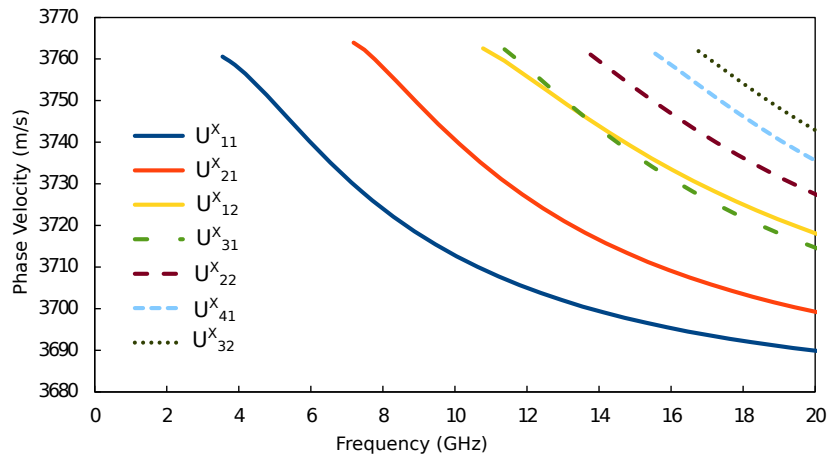
Fig. 4.9 Dispersion curves of acoustic shear U_{mn}^X modes.
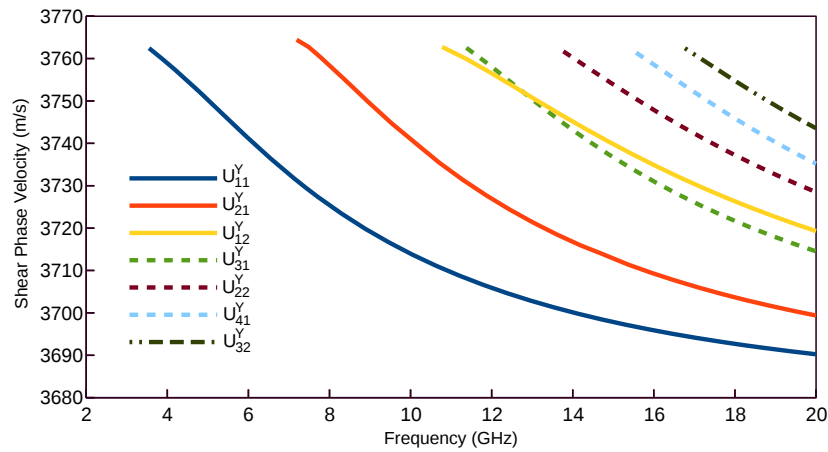
Fig. 4.10 Dispersion curves of acoustic shear U_{mn}^Y modes.

mode the code was again used to detect a proper acoustic mode. From the resulted eigenvalue, acoustic frequency (f) was calculated. Using Eq. (3.17) the value of the acoustic phase velocity was calculated and plotted. Whenever an acoustic mode at a particular frequency was to be viewed, its corresponding acoustic propagation constant, wherever presented, could have fractional values that can be seen in following chapters as well.

Although, the spatial variation of the dominant displacement vector can be easily identified or visualized, however these has not been much reported on the spatial variations of the other two non-dominant displacement vectors for the same mode. Rather, in many cases, a simpler scalar formulation has been used [Yoo, 2010] to find the modal solutions of the acoustic modes, where the non-dominant components are totally neglected, which is not the case here. By using full-vectorial FEM based numerical analysis it is possible to observe the non-dominant displacement components and their spatial variations.

At this point we will try to establish a relation between the spatial variations of the non-dominant displacement components with the dominant displacement component of the U_{mn}^X modes. If we observe the displacement vector profiles of the fundamental shear U_{11}^X acoustic mode, shown in Fig. 4.3, it would be clear that the dominant U_X component has half sine-wave spatial variation of ($m = 1$, $n = 1$). Here m and n represents the number of half sine-wave spatial variation in the x and y directions, respectively. But, its non-dominant U_Y components has spatial variations of (2, 2) that is shown in Fig. 4.3(b). Its non-dominant U_Z components, shown in Fig. 4.3(c) has spatial variations of (2, 1).

For a higher order U_{21}^X mode the spatial variations of the dominant component U_X and two non-dominant components, U_Y and U_Z are shown in Fig. 4.11. The U_X profile for this mode has two well defined half-wave variations ($m = 2$) along the x-direction and one half-wave variation ($n = 1$) along the y-direction. The U_Y profile for the same mode is shown in Fig. 4.11(b), which identifies 3 half-wave ($m + 1$) variations along the x-direction, and 2 half-wave ($n + 1$) variations along the y-direction. Similarly the U_Z profile for the U_{21}^X mode, shown in Fig. 4.11(c), shows 3 ($= m + 1$) and 1 ($= n$) half-wave variations along the x and y directions, respectively.

(a)

(b)

(c)
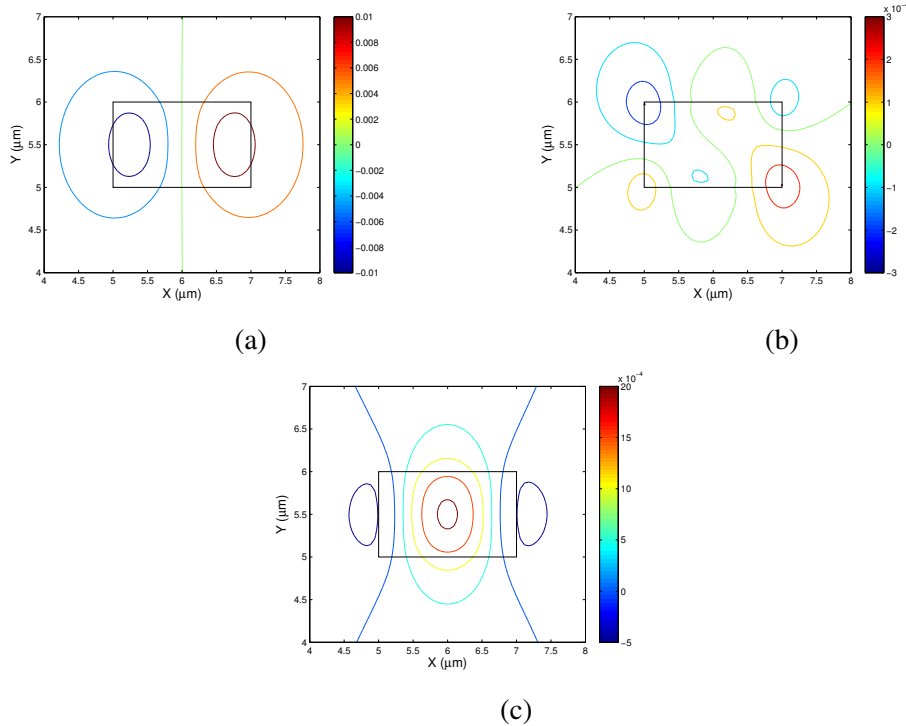
Fig. 4.11 U_X, U_Y and U_Z displacement vectors of the U_{21}^X mode.

Similarly, Fig. 4.12 shows all the displacement vector profiles of shear U_{12}^X mode. Here the dominant component U_X shows a spatial variation of ($m = 1$, $n = 2$), its non-dominant

U_Y components has a spatial variation of (2, 3), i.e. $(m + 1, n + 1)$, and its another non-dominant component U_Z has a spatial variation of (2, 2), i.e. $(m + 1, n)$. It is to be noted that although for modal degeneration it becomes difficult to identify the number of half sine-wave spatial variations in the non-dominating U_Y component shown in Fig. 4.12(b), but it is not impossible.

(a)

(b)

(c)
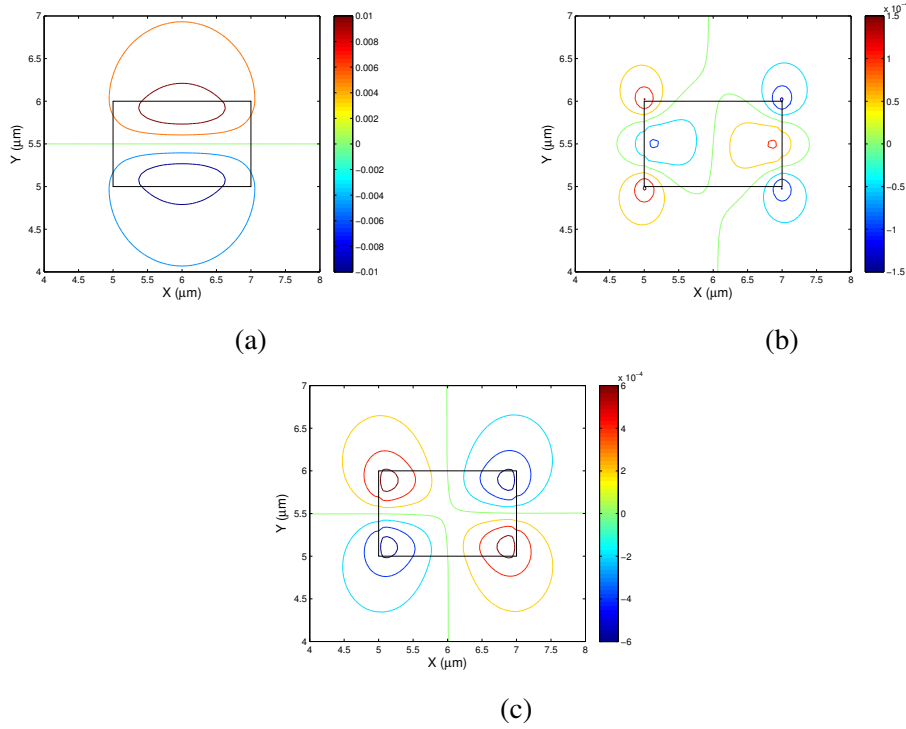
Fig. 4.12 U_X, U_Y and U_Z displacement vectors of the U_{12}^X mode.

This similarity in the pattern of spatial variation can be seen for all the dominant U_X components in higher order shear U_{mn}^X modes. It has also been verified that the relation for the spatial variation of the non-dominant shear U_Y component holds true for all the U_{mn}^X modes with $(m + 1)$ and $(n + 1)$ half-wave variations along the x and y-directions. For non-dominant U_Z component the spatial variation is $(m + 1)$ and (n) half-wave variations along the x and y-directions, and the same relations has been checked to be true for all U_{mn}^x modes. Just to support the concept we are presenting few other dominant U_X components along with non-dominant U_Z components for some higher order modes of this category at $k = 30 \, \mu m^{-1}$ in Fig. 4.13.

It can be concluded based on the observation that for any shear acoustic U_{mn}^X mode with a dominant U_X component, have half sine-wave spatial variation of (m, n), but its non-dominant U_Y and U_Z components have spatial variations of $(m + 1, n + 1)$ and $(m + 1, n)$, respectively.

(a)

(b)

(c)

(d)

(e)

(f)

(g)

(h)
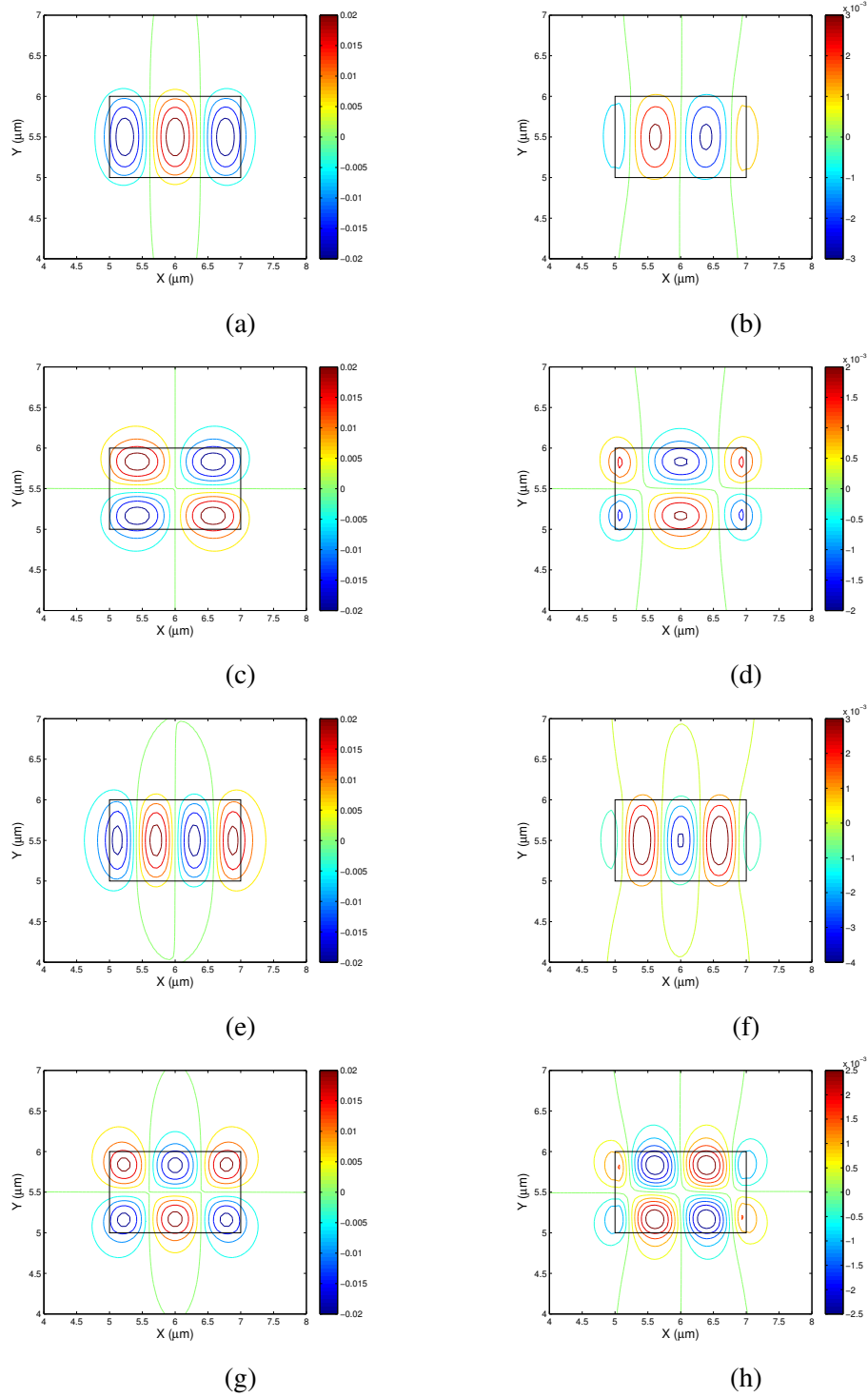
Fig. 4.13 U_X and U_Z displacement vectors of the U_{31}^X (a, b), U_{22}^X (c, d), U_{41}^X (e, f) and U_{32}^X (g, h) modes.

However, if we study the displacement vector profiles of the fundamental shear U_{11}^Y acoustic mode, as shown in Fig. 4.6, we can find that when the dominant U_Y component has half sine-wave spatial variation of ($m = 1$, $n = 1$), its non-dominant U_X mode has half sine-wave spatial variation of (2, 2), i.e. ($m + 1$, $n + 1$). But for this mode its non-dominant U_Z mode has half sine-wave spatial variation of (1, 2), i.e. (m, $n + 1$). It would be interesting to observe the spatial relation for the higher order shear modes with dominant U_Y component.

Figure 4.14 shows the dominant and non-dominant displacement vector profiles of the shear U_{21}^Y mode. For this set, when the dominant component U_Y exhibits a spatial variation of ($m = 2$, $n = 1$), its non-dominant U_X components shows a spatial variation of (3, 2), i.e. ($m + 1$, $n + 1$). But, its another non-dominant component U_Z has a spatial variation of (2, 2), i.e. (m, $n + 1$).

(a)   (b)

(c)
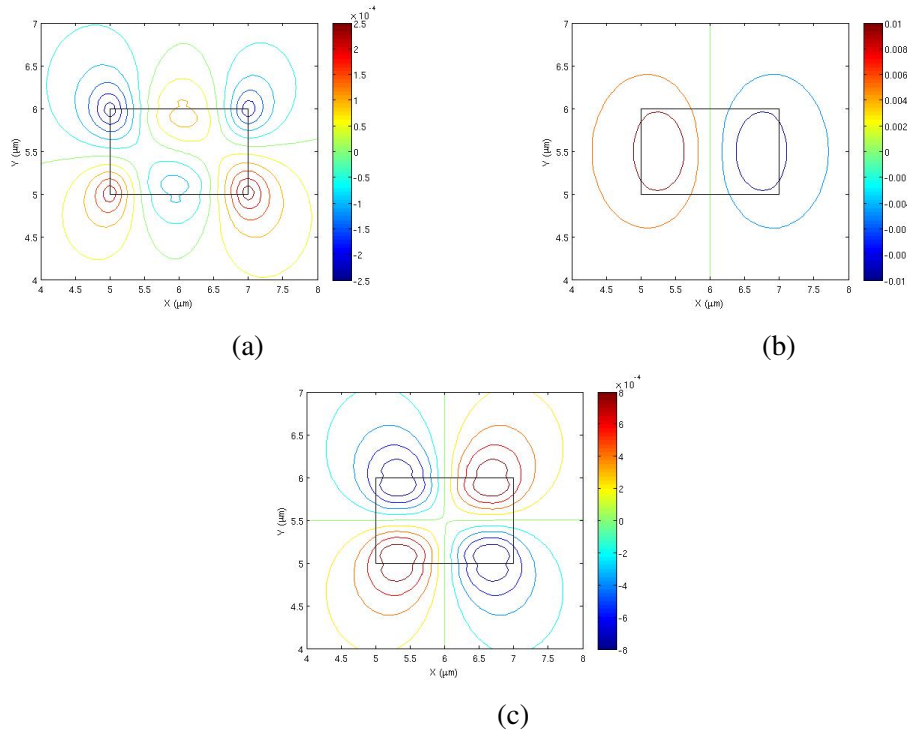
Fig. 4.14 U_X, U_Y and U_Z displacement vectors of the U_{21}^Y mode.

Similarly, in Fig. 4.15, all the displacement vector profiles of shear U_{12}^Y mode are shown. For this set of displacement profiles, the dominant component U_Y shows a spatial variation of ($m = 1$, $n = 2$), its non-dominant U_X components has a spatial variation of (2, 3), i.e. ($m + 1$, $n + 1$), and its another non-dominant component U_Z has a spatial variation of (1, 3), i.e. (m, $n + 1$).

In Fig. 4.16, all components of the displacement vector profiles of shear U_{31}^Y mode are shown. Here, the dominant component U_Y shows a spatial variation of ($m = 3$, $n = 1$), its

(a)

(b)

(c)
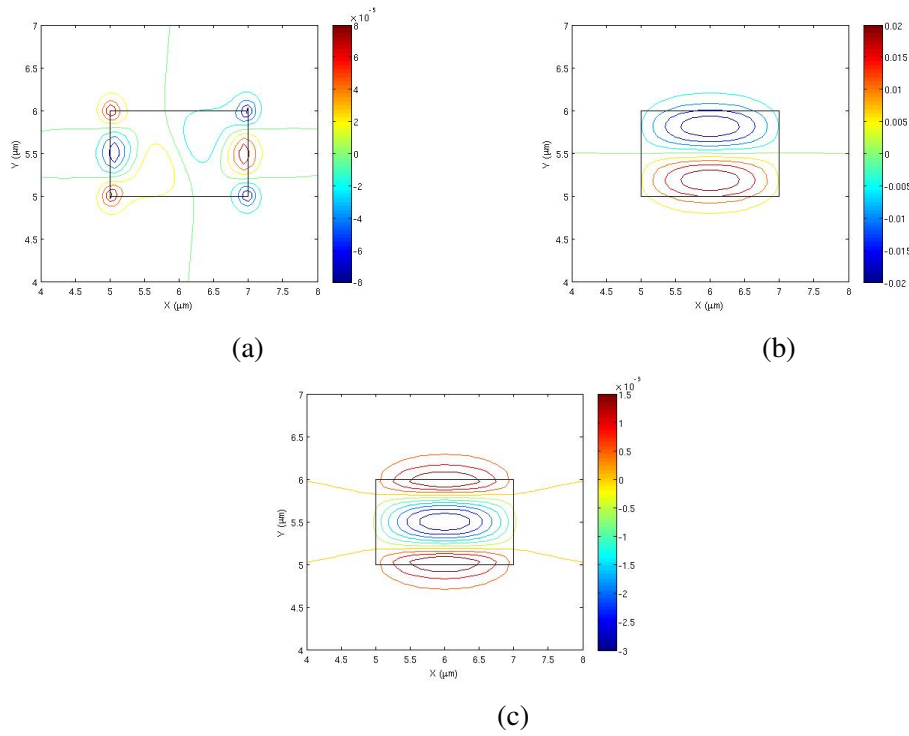
Fig. 4.15 U_X, U_Y and U_Z displacement vectors of the U_{12}^Y mode.

(a)

(b)

(c)
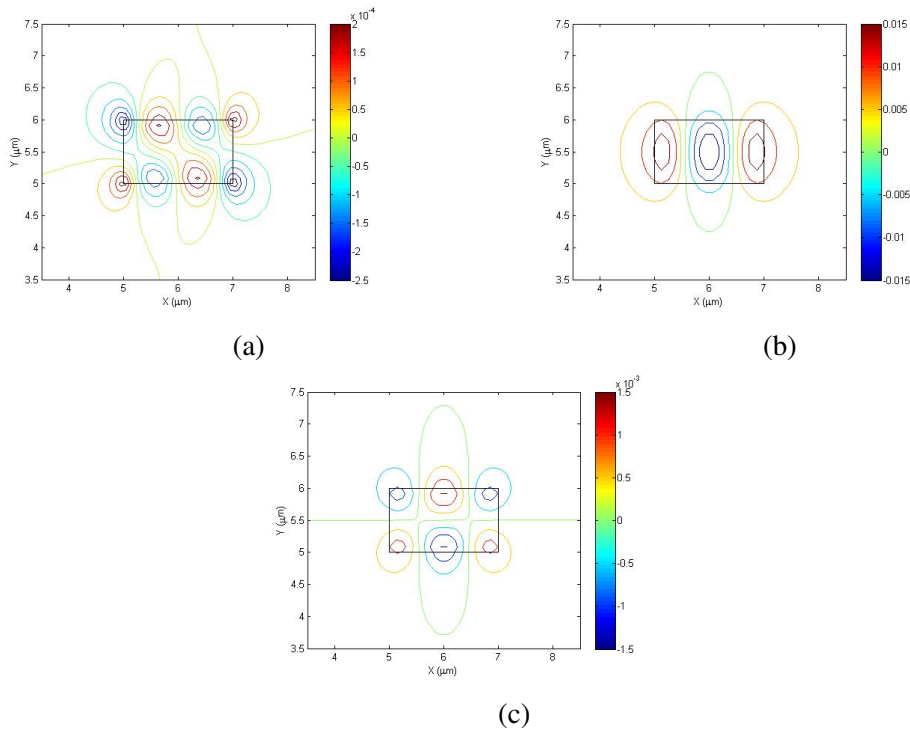
Fig. 4.16 U_X, U_Y and U_Z displacement vectors of the U_{31}^Y mode.

non-dominant U_X components has a spatial variation of (4, 2), i.e. ($m + 1$, $n + 1$), and its another non-dominant component U_Z has a spatial variation of (3, 2), i.e. (m, $n + 1$).

We have observed that these patterns of spatial variations are common for all the higher order shear modes with dominant U_Y components. Based on the observations it can be concluded that for any shear acoustic U^Y_{mn} mode with a dominant U_Y component that has half sine-wave spatial variation of (m, n), then its non-dominant U_X component has spatial variations of ($m + 1$, $n + 1$) and its another non-dominant U_Z component has (m, $n + 1$) half sine-wave spatial variation, which is different than that was identified for the shear modes with U_X dominant component.

Effects of mesh density, aspect ratio and frequency on mode degeneration

It is mentioned earlier that for modes with close proximity eigenvalues finer mesh division can play a role in reduction of mode degeneration. Which will be clear if we see the Fig. 4.17. In Fig. 4.3(b) indicates a trace of mode degeneration, where mesh division is taken as 200×200. The spatial variation of the U_Y vector for the same U^X_{11} mode, at $k = 17\ \mu m^{-1}$, but when mesh division is increased to 500×500 is shown in Fig. 4.17(a). This shows the degeneration has reduced, as four peaks at four corners of the waveguide are more clearly visible. It can also be observed that their peak magnitudes are nearly equal. Their exact values cannot be identified here, though, but from the numerical data obtained, they have been identified as $+1.2619 \times 10^{-4}$ and -1.2156×10^{-4}, respectively. However, when a lower mesh is used, the four peaks begin to mix and the positive and negative peaks become unequal and the U_Y profile transforms to show its peak at the center, as shown in Fig. 4.17(b), when the mesh division was reduced to 80×80.
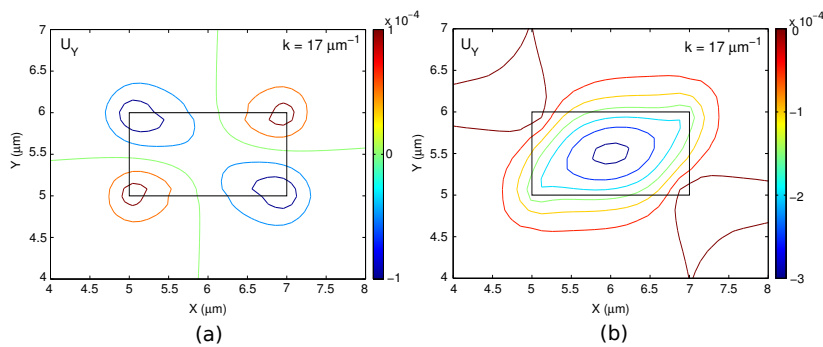
Fig. 4.17 U_Y displacement vectors of the U^X_{11} mode, when (a) 500×500 and (b) 80×80 mesh divisions.

To quantify this mode degeneration, next, the ratio of the minimum peaks with the maximum peaks is shown in Fig.18 with the mesh division used. It can be observed that

when a higher mesh division is used, in this case 500×500, the positive and negative peaks were almost equal in magnitude, and their ratio was 0.9633. On the other hand, when a smaller mesh is used, in this case 80×80, the larger peak becomes 8.47 times bigger than the smaller peak, and the profile shows a nearly Gaussian shape with its peak value now at the center of the waveguide as shown in Fig. 4.17(b). It can be stated that the U_{11}^x and U_{11}^y modes are mixing up at a progressive rate and non-dominant U_y vector of the U_{11}^x mode is being influenced by the dominant U_y vector of the U_{11}^y mode. However, this modal degeneration between two similar shear modes cannot be avoided, unless the symmetry of the structures is exploited, as discussed earlier in Section 4.3.
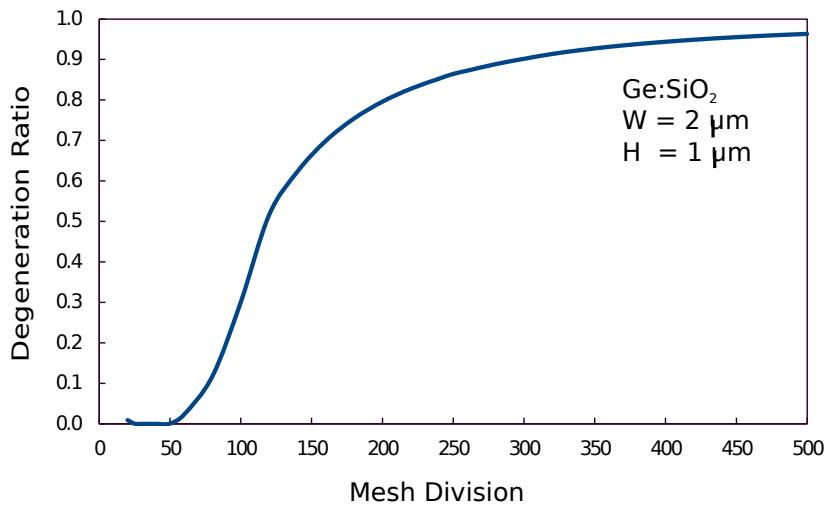
Fig. 4.18 Degeneration ratio against the mesh division for U_y displacement vectors of the U_{11}^x mode at $k = 17\ \mu m$.

Further analyses have been performed to quantify the mode degeneration with the aspect ratio of the guide at propagation constant, $k = 17\ \mu m^{-1}$, shown in Fig. 4.19. Here, the mesh division was kept same as 250×250 for a range of aspect ratio. To vary the aspect ratio the width of the guide was varied keeping the height constant at, $H = 1\ \mu m$. It can be noted that at lower aspect ratio, $W/H = 1.25$, i.e. with guide width as $W = 1.25\ \mu m$, the degeneration was worse and found to be 0.6031. It improved with the increase in guide width. At the beginning this change was rapid. At the guide with of $W = 2\ \mu m$ the degeneration improved further and the degeneration ratio was 0.8643. Afterwards, for further increase in aspect ratio the degeneration improved gradually, at guide width of $W = 4\ \mu m$ the ratio was calculated as 0.9458. When the aspect ratio of the waveguide is increased then this degeneration is reduced as the modal birefringence of the waveguide becomes higher and the non-dominant U_y vector of the U_{11}^x mode is being less influenced by the dominant U_y vector of the U_{11}^y mode.
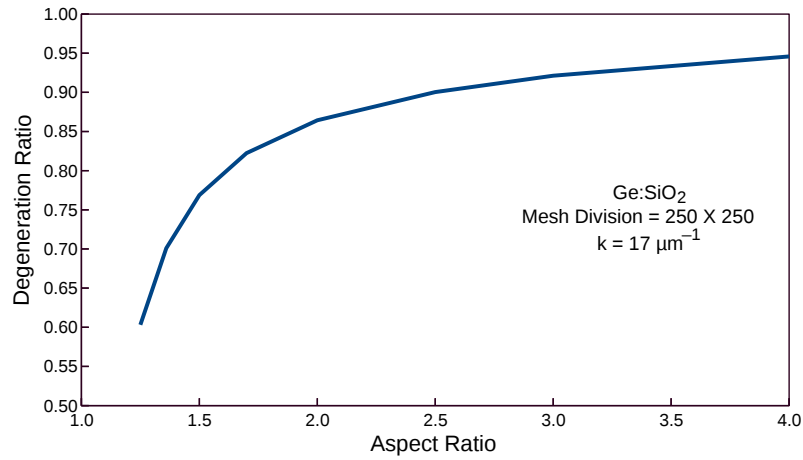
Fig. 4.19 Degeneration ratio against the aspect ratio of guide for U_y displacement vectors of the U_{11}^x mode.
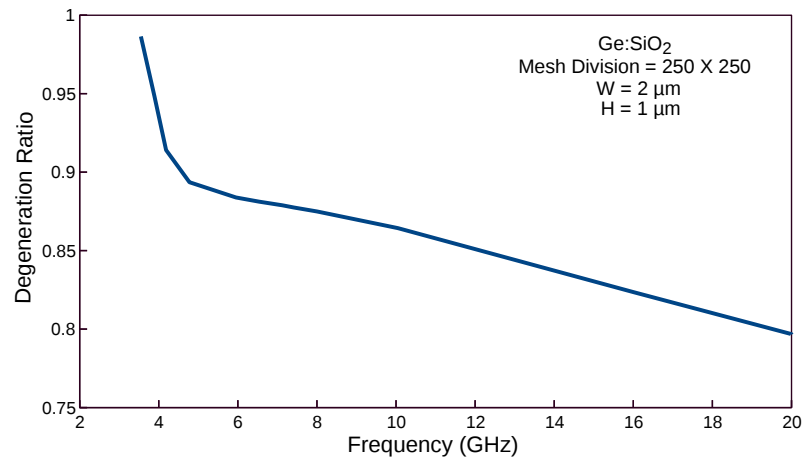
Fig. 4.20 Degeneration ratio against the acoustic frequency for U_y displacement vectors of the U_{11}^x mode.

At constant mesh density (250×250) with the guide width and height as $W = 2\ \mu m$ and $H = 1\ \mu m$, respectively, further analyses have been performed to observe the effect of acoustic frequency variation on the mode degeneration and shown in Fig. 4.20. It was noted that at $f = 20\ GHz$ the degeneration ratio was less and it was calculated as 0.7968. With the decrease in frequency this degeneration improves gradually and near $f = 6\ GHz$ the degeneration ratio was determined as 0.8838. After that the variation of the degeneration ratio with the reducing frequency was rapid. At near 3.55 GHz the degeneration ratio improved a lot and was calculated as 0.9864. It is to be noted that when the acoustic frequency is reduced, this degeneration is reduced, as the difference between the two similar eigenvalues

is increased and lower frequency range the difference between the eigenvalues being larger the reduction in degeneration was observed to be rapid.

Modal solution accuracy using Aitken's extrapolation

Besides the exploitation of the symmetry condition, if it exists, Aitken's extrapolation [Rahman, 1985] technique can also be used to improve the solution accuracy, as discussed in Section 3.7.1. To exploit this, the structure must be refined in a fixed geometric ratio. From three successive mesh refinements, final solutions can be extrapolated for a possible infinite mesh refinement as shown by Eq. (3.62). The geometric ratio does not have to be 1:2:4 but other ratio can also be used, but it should be noted that mesh divisions can only be of integer value and in all the regions the same mesh refinement ratio must be maintained.

Variations of the acoustic frequency of the fundamental U_{11}^x mode for $k = 17\ \mu m^{-1}$ with the mesh division for full structure, although were shown in Fig. 3.5 to test the convergence, here it is repeated with the quarter structure exploiting the two-fold symmetry in Fig. 4.21. Equal mesh divisions are used in both the transverse directions. When the number of the mesh division is increased, these solutions rapidly converge to their exact solutions. However, it can be easily observed that when 2-fold symmetry is used, as shown by a dotted green line, convergence is much faster than when the full structure is simulated as shown by a dashed blue line. The solution accuracy which can be obtained by a 50×50 mesh divisions for 2-fold symmetry will have the similar accuracy as that of using a 100×100 mesh for the full structure, but requiring a much higher computational resources.
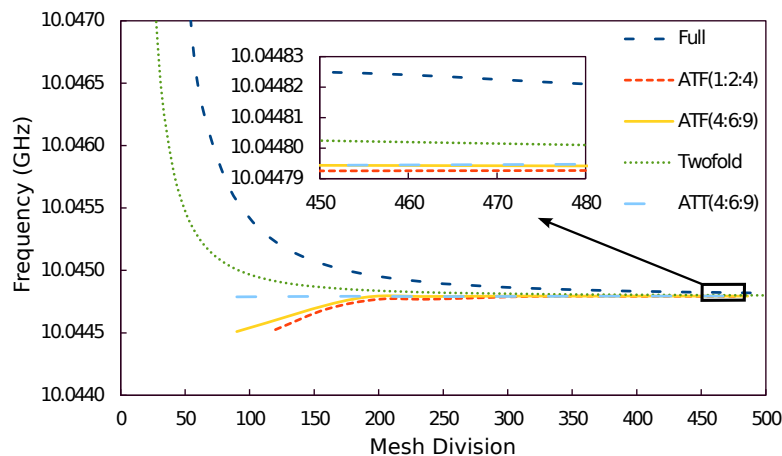
Fig. 4.21 Variation of eigen frequency with the mesh division for the U_{11}^x mode at $k = 17$ μm^{-1} for both full and quarter structures.

Besides that, when Aitken's extrapolation is used, the solution accuracy is much improved as shown by dashed red line. For the full structure, when the geometric ratio 1:2:4 and 1:1.5:2.25 (or 4:6:9) are used, as identified as ATF(1:2:4) and ATF(4:6:9), and shown by the red dashed and yellow solid lines, respectively, it can be observed that better solution accuracy can be obtained. However, it can be noted that 4:6:9 geometric ratio, shown by a yellow solid line, converges better than use of 1:2:4 (dashed red line). On the other hand, when the 4:6:9 geometric ratio for the quarter structure exploiting 2-fold symmetry, as shown by a dashed cyan line [ATT(4:6:9)], the best solution convergence can be obtained, for a given mesh division as here both symmetry and extrapolation have been used. To show this region more clearly, an expanded version of this region is shown as an inset.

Modal hybridness when $V_{LG} = V_{LC}$

It is shown here that the acoustic modes are fully vectorial in nature and for a shear mode, although its dominant displacement is along one of the transverse direction, however, other two non-dominant (another one transverse and one longitudinal) are also present. This makes the modes fully hybrid in nature. Similarly, modes in optical waveguides with 2-dimensional confinements are also fully hybrid in nature and this hybridness increases when the index contrast between core and cladding is increased. A study of modal hybridness is important for the calculation of polarization cross-talk [Somasiri, 2003] or in the design of polarization rotators [Rahman, 2001]. Hybridness can be defined as the ratio of the maximum value of the non-dominant component with the maximum value of the dominant components. As for each mode, there are two non-dominant components, so there will be two different hybridness values for each of the modes; however, the ratio between the longitudinal and transverse components is of greatest interest.

For the U_{11}^X and U_{11}^Y modes, the variations of the hybridness with the acoustic frequency are shown in Fig. 4.22. Here the hybridness for the shear modes has been defined as the ratio of the maximum U_Z vector to the maximum transverse displacement, which are U_X and U_Y for the U_{11}^X and U_{11}^Y modes, respectively. It can be observed that as the frequency is decreased modal hybridness increases and reaches its maximum value and then reduces as the modes approach their effective cutoff frequencies.

The modal hybridness of the U_{11}^X, U_{21}^X, and U_{31}^X modes are shown in Fig. 4.23. It can be observed that modal hybridness of the higher order modes are higher than that of the fundamental U_{11}^X mode, which is shown by the solid blue line. At acoustic frequency $f = 13$ GHz the hybridness of U_{11}^X mode was calculated as 0.053 and for higher order U_{21}^X, and U_{31}^X modes hybridness found to be 0.119 and 0.172, respectively. With the increase in frequency hybridness for all these modes decrease and at acoustic frequency $f = 20$ GHz the hybridness
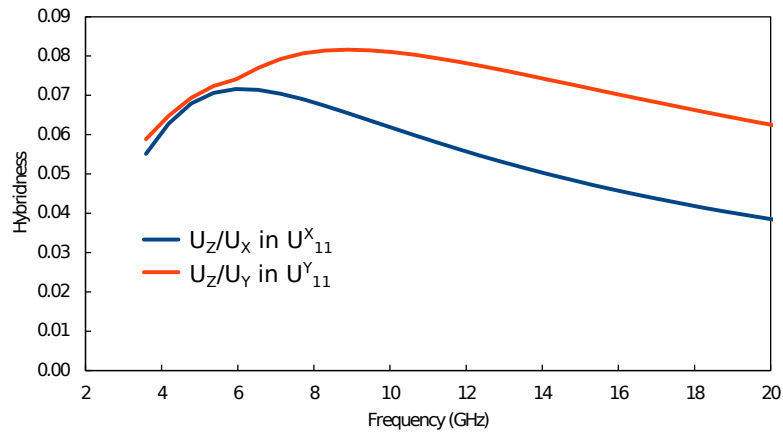
Fig. 4.22 Variation of modal hybridness of two fundamental shear modes with the frequency.

were found to be 0.0386, 0.0824 and 0.123 for U^X_{11}, U^X_{21}, and U^X_{31} modes, respectively. Based on these data it is clear that the rate of change of hybridness with frequency in less in the fundamental U^X_{11} mode and highest in the second order U^X_{21} mode.
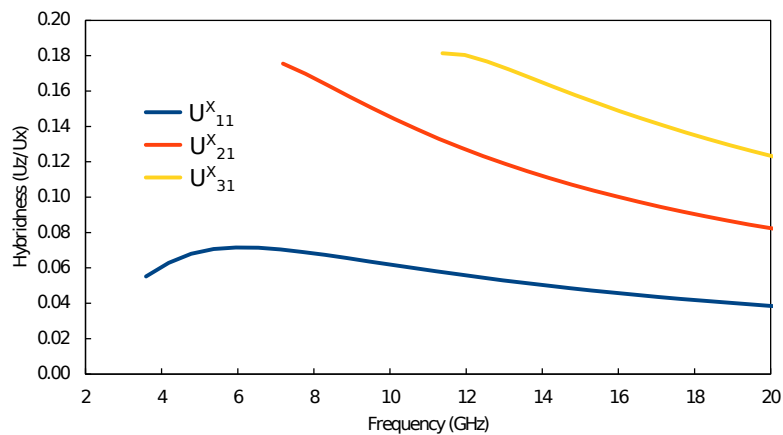
Fig. 4.23 Variation of the modal hybridness for the higher order modes with dominant U_X component.

The variation of the modal hybridness of the fundamental U^X_{11} mode with frequency for two different guide widths are shown in Fig. 4.24. The solid blue line represents the hybridness for a guide dimension of $2\ \mu m \times 1\ \mu m$ (W2H1) and the solid red line, that lies below, shows the variation in hybridness for a guide dimension of $4\ \mu m \times 1\ \mu m$ (W4H1). Because with the double width of the guide the dominant U_X component gets more space to spread in W4H1 dimension comparing the non-dominant U_Z component, where it localizes at the vertical left and right interfaces and there ratio is less than the hybridness in W2H1

dimension for a given higher frequency. For the W2H1 guide, at $f = 4\ GHz$ the hybridness was calculated as 0.628, it then increased with the frequency and attained its maximum value of 0.0716 near 6 GHz. After that it dropped down with the increased frequency and reached at a value of 0.0386 at 20 GHz. Where as the maximum hybridness for W4H1 guide was 0.0609 near 4 GHz that fell comparatively in a rapid way than that of W2H1 and reached a value of 0.0213 at 20 GHz.
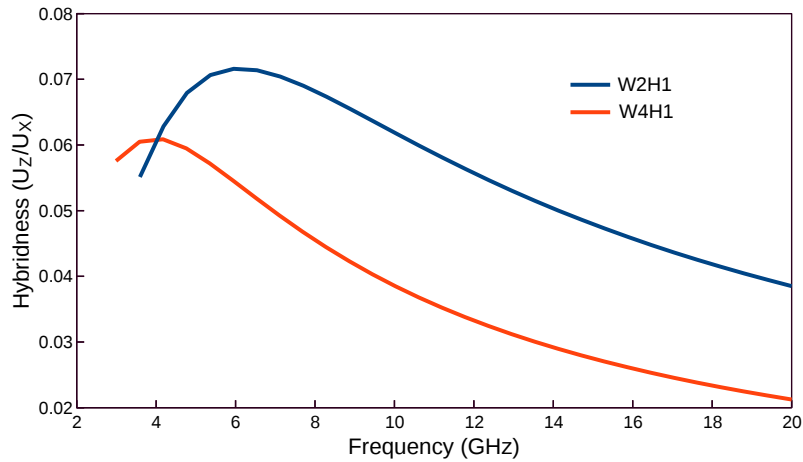
Fig. 4.24 Variation of the modal hybridness of U_{11}^X for different width.
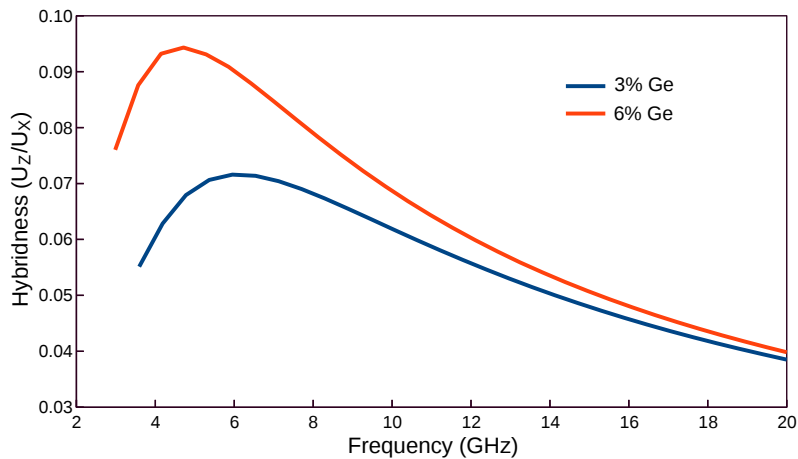
Fig. 4.25 Variation of the modal hybridness of U_{11}^X for different doping concentration.

The variation of the modal hybridness of the same U_{11}^X mode with frequency for two different doping concentration are shown in Fig. 4.25. Initially the hybridness for 6% doping concentration, shown by solid red line that lies above the hybridness for the 3% doping concentration, increased with the frequency and reached its maximum value of 0.0943 at

4.77 GHz and rapidly fell down with increasing frequency and at 20 GHz it was calculated as 0.0407.

Modal birefringence

As the waveguide under consideration, with W = 2 μm and H= 1 μm, does not have a 90° rotational symmetry so the propagation velocities of the fundamental U_{11}^X and U_{11}^Y modes were although close but not identical. For an optical waveguide the difference between the effective indices of the 2 polarized quasi-TE and quasi-TM modes is known as the modal birefringence. Similarly, here the phase velocities of the U_{11}^X and U_{11}^Y modes are slightly different. The variation of this modal birefringence (but defined in terms of their phase velocity difference) with the acoustic frequency is shown in Fig. 4.26 by a blue line for this waveguide. As the frequency is reduced, difference in their phase velocity increases, reaches a maxima, and then decreases. Subsequently another waveguide is studied where Ge-doping is increased to 6%, so that the difference between the shear velocities in the core and cladding, $\triangle V_S = V_{SG} - V_{SC}$, is now doubled. The variation of phase velocity difference for this guide is shown by a solid red line. In a way similar to that seen in optical waveguides, the modal birefringence is increased as the equivalent acoustic index contrast between core and cladding is increased. The peak birefringence appears at a lower frequency as with higher index contrast the modal cutoff point is also shifted to a lower frequency.
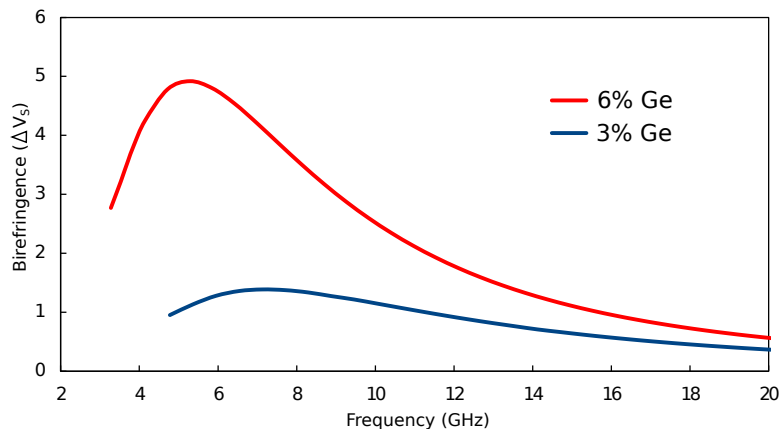
Fig. 4.26 Variation of modal birefringence with frequency for different Ge doped waveguides.

Phase velocity variation with frequency for increased doping and guide width

The variation of the phase velocity of the U_{11}^X mode with frequency for two different guide width are shown in Fig. 4.27. It is to be noted that the phase velocity variation for doubled

width guide that is denoted by the solid red line, lies below the solid blue line for all the range of frequencies. This is because with the increased guide width the acoustic mode gets more confined and the the phase velocity dropped down (equivalent effective acoustic index increases). At lower frequency this difference is much more than that at the higher frequency. Near 4 *GHz* frequency the phase velocities were found to be 3756.46 *m/s* and 3745.85 *m/s* for W2H1 and W4H1 guide dimensions, respectively. Where the difference is below 11 *m/s*. Near 20 *GHz* frequency the phase velocities were found to be 3689.91 *m/s* and 3687.65 *m/s* for W2H1 and W4H1 guide dimensions, respectively. Here the difference is more than 2 *m/s*.
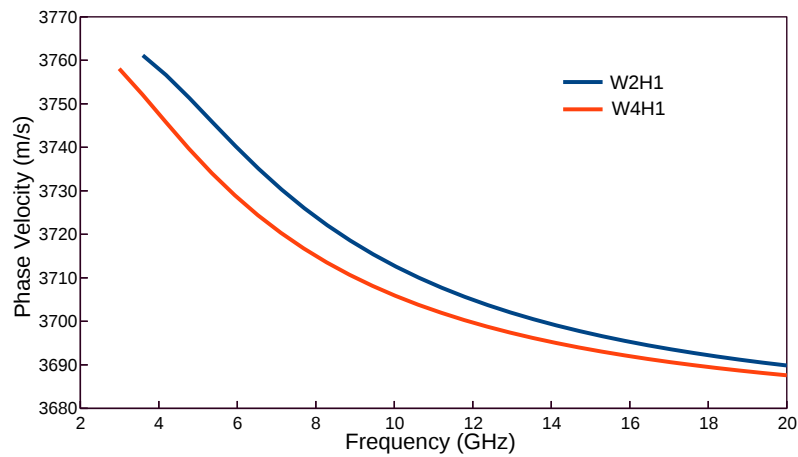
Fig. 4.27 Variation of the phase velocity of U_{11}^{X} mode for different width.
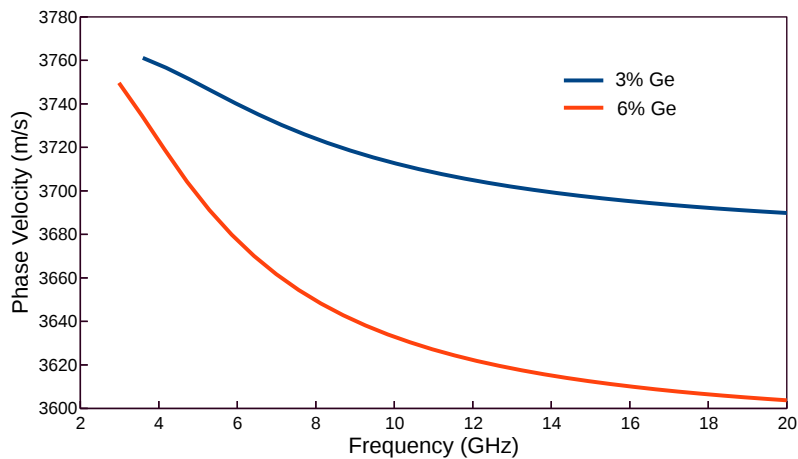
Fig. 4.28 Variation of the phase velocity of U_{11}^{X} mode for different doping concentration.

For any given acoustic frequency with the increased doping concentration the phase velocity of the U_{11}^{X} mode became much less. Figure 4.28 depicts the variation of phase

velocities for this mode at two different doping concentrations. At 20 GHz frequency the phase velocity for 6% Ge-doped silica waveguide was found as 3604.37 m/s and near 4 GHz frequency it was 3719.03 m/s. For higher doping concentration the acoustic mode gets more confined, so, phase velocity remains close to velocity of the core. Further, it is to be noted that the phase velocity changed more rapidly with frequency for higher doping concentration.

4.4.2   Option II: Longitudinal acoustic modes for 3% Ge-doped core

To obtain the longitudinal acoustic modes in their pure form without being influenced by the shear acoustic modes, the Option II in Table 4.1 is considered in this section. Here, both the shear velocities in core and cladding are considered to be equal and taken as 3764 m/s. For such case as $\frac{\triangle V_L}{V_L} = 0.0214$, i.e., the material contrast is being small, this waveguide will act as a weakly guiding for the longitudinal modes as well.

Like the shear modes this waveguide also supports longitudinal acoustic U_{mn}^Z modes. These longitudinal modes are also hybrid in nature. For these U_{mn}^Z modes the U_Z components are dominant modes. The other two non-dominant components are U_Y and U_X displacement vectors. The fundamental longitudinal U_{11}^Z mode is shown in Fig. 4.29. It can be observed that the dominant U_Z profile of this mode, exhibits nearly Gaussian in shape with its peak value at the center of the waveguide, which in shown in Fig. 4.29(c) . However, the non-dominant U_X vector as shown in Fig. 4.29(a), possesses a higher order spatial variation near the vertical left and right interfaces, where its peak value is about 2 orders of magnitude lower than that of the dominant displacement vector, U_Z. The U_Y profile is shown in Fig. 4.29(b), which illustrates its positive and negative peaks along the two horizontal side walls. Its maximum magnitude is about 7.5% of the fundamental displacement vector, U_Z. At propagation constant $k = 17$ μm^{-1}, the acoustic frequency was found to be 15.8517 GHz, phase velocity was about 5858.76 m/s.

The displacement vector of the resultant transverse U_T mode, found by vectorial addition of both the non-dominant components U_X and U_Y for U_{11}^Z mode is shown in Fig. 4.30 for propagation constant $k = 17$ μm^{-1}. It is to be noted that in the transverse plane the resultant displacement is formed can be classified as radial.

The dispersion curves of the longitudinal acoustic modes are shown in Fig. 4.31. When frequency is reduced the phase velocity of each mode increases nonlinearly. Although, U_{12}^Z (represented by a solid yellow line) and U_{21}^Z (represented by a solid red line) modes had near identical eigenvalues, however, it was possible to separate these modes as we have used the symmetrical boundary conditions, which were different for them. In this case the lower and

(a)

(b)

(c)
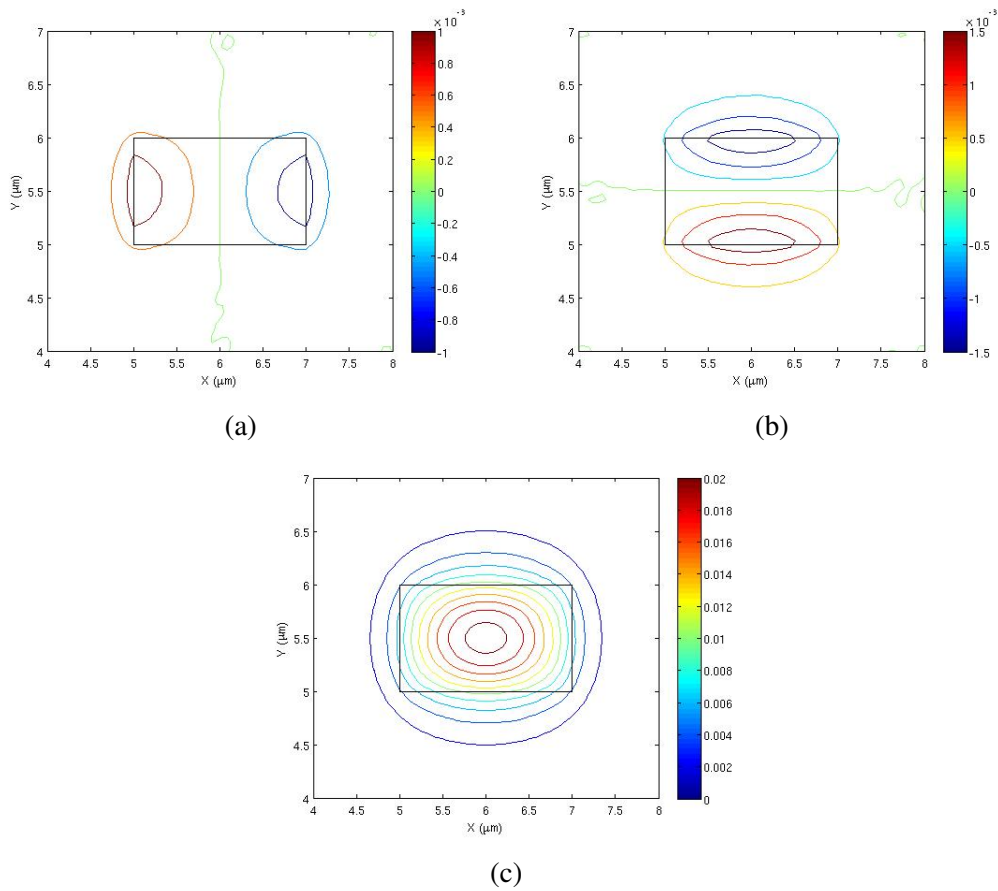
Fig. 4.29 U_X, U_Y and U_Z displacement vectors of the U_{11}^Z mode.
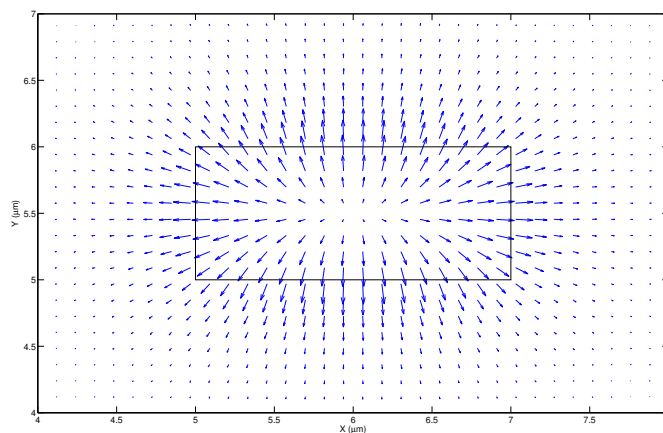
Fig. 4.30 Transverse plane displacement vector, U_T, at $k = 17$ μm^{-1} for U_{11}^Z mode.

upper velocity limits are the longitudinal acoustic wave velocities of the core and cladding, respectively.
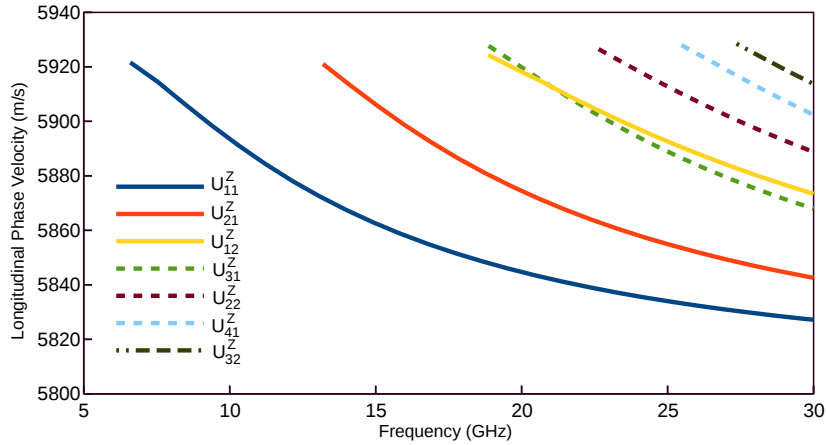
Fig. 4.31 Dispersion curves of acoustic longitudinal U_{mn}^Z modes.

(a)

(b)

(c)
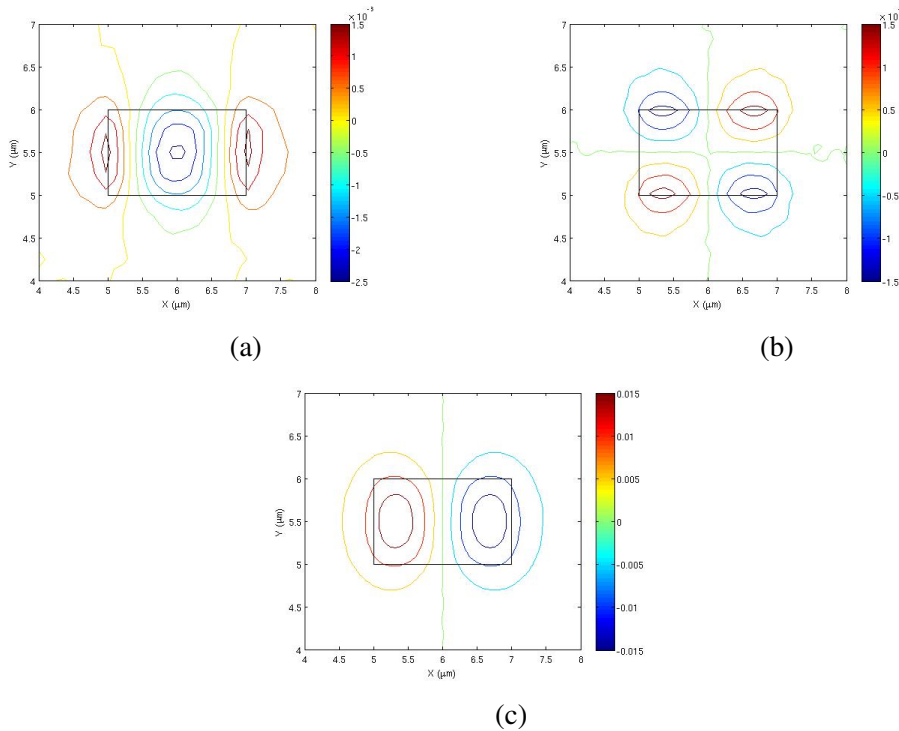
Fig. 4.32 U_X, U_Y and U_Z displacement vectors of the U_{21}^Z mode.

Now, let us establish the spatial variations pattern for the dominant and non-dominant displacement components of the U_{mn}^Z modes. The dominant U_Z component's displacement vector profile of the fundamental longitudinal U_{11}^Z acoustic mode, shown in Fig. 4.29(c), has a half sine-wave spatial variation of $m = 1$ and $n = 1$ in the x and y directions, respectively. However, its non-dominant U_X component, shown in Fig. 4.29(a), has spatial variations of (2, 1), i.e., $(m + 1) = 2$ and $n = 1$ in the x and y directions, respectively. Whereas, its

non-dominant U_Y component, shown in Fig. 4.29(b) has spatial variations of (1, 2), i.e., $m = 1$ and $(n + 1) = 2$ in the x and y directions, respectively.

Another higher order mode was also checked for this pattern conformity. For a higher order U_{21}^Z mode, shown in Fig. 4.32, the spatial variation of the dominant component U_Z profile for this mode has two well defined half-wave variations ($m = 2$) along the x-direction and one half-wave variation ($n = 1$) along the y-direction. The non-dominant U_X profile is shown in Fig. 4.32(a), which shows three half-wave ($m + 1$) variations along the x-direction, and one half-wave ($n = 1$) variations along the y-direction. Whereas, the U_Y profile for the U_{21}^Z mode, shown in Fig. 4.32(b), has 2 ($= m$) and 2 ($= n + 1$) half-wave variations along the x and y directions, respectively.

(a)

(b)

(c)
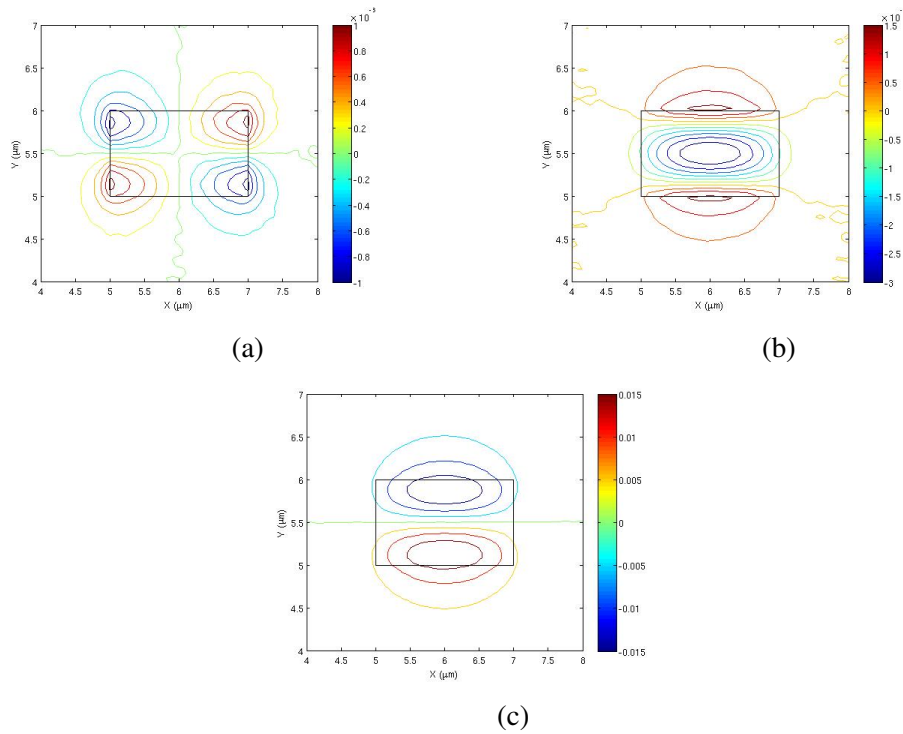
Fig. 4.33 U_X, U_Y and U_Z displacement vectors of the U_{12}^Z mode.

This similarity in spatial variation pattern can also be observed for longitudinal U_{12}^Z mode shown in Fig. 4.33. Where the dominant component U_Z shows a spatial variation of ($m = 1$, $n = 2$), its non-dominant U_X components has a spatial variation of (2, 2), i.e. ($m + 1, n$), and its another non-dominant component U_Y has a spatial variation of (1, 3), i.e. ($m, n + 1$).

We can come to a conclusion based on the observations that for any longitudinal acoustic U_{mn}^Z mode with a dominant U_Z component, which has half sine-wave spatial variations of (m, n), has two other non-dominant U_X and U_Y components having spatial variations of ($m + 1$, n) and ($m, n + 1$), respectively.

Modal hybridness for longitudinal modes

The variations of the hybridness with the acoustic frequency for the U_{11}^Z mode is shown in Fig. 4.34. As this fundamental longitudinal mode has two non-dominant components, hybridnessess for both are shown. Here the hybridness, Hb_X, for the longitudinal mode has been defined as the ratio of the maximum U_X vector to the maximum longitudinal displacement U_Z, shown by the solid blue line. The hybridness, Hb_Y, has been defined as the ratio of the maximum U_Y vector to the maximum longitudinal displacement U_Z, shown by the solid red line. It is to be noted that as the magnitude of the non-dominant U_Y component is higher than that of U_X component, the red line lies above the blue line for all the acoustic frequencies in consideration. It can be observed that as the frequency is decreased both the modal hybridness increase and reach their maximum values and then reduce as the modes approach there respected effective cutoff frequencies.
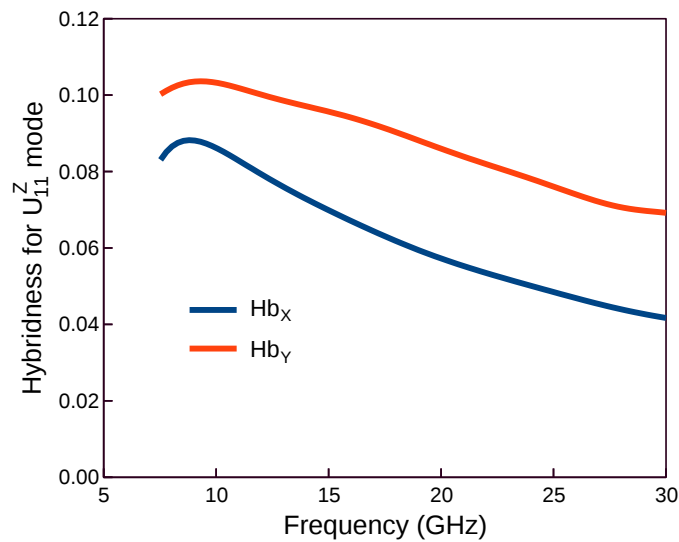
Fig. 4.34 Variation of modal hybridness of the fundamental longitudinal mode with the frequency.

The modal hybridness of the U_{11}^Z, U_{21}^Z, and U_{31}^Z modes are shown in Fig. 4.35. For the higher order modes the modal hybridness are higher than that of the fundamental U_{11}^Z mode that is shown by the solid blue line. Near the acoustic frequency of $f = 30\ GHz$ the hybridness of U_{11}^Z mode was calculated as 0.0414. For U_{21}^Z and U_{31}^Z higher order modes the hybridness were found to be 0.085 and 0.1269, respectively. With the decrease in acoustic frequency the hybridness for all these modes increased.

The variation of the modal hybridness of the fundamental U_{11}^Z mode with the acoustic frequency for two different guide widths are shown in Fig. 4.36. The solid blue line represents
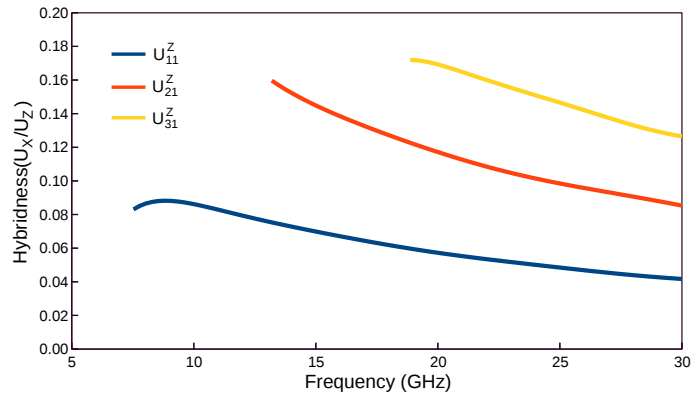
Fig. 4.35 Variation of the modal hybridness for the higher order modes with dominant U_Z component.

the hybridness for a guide dimension of $2~\mu m \times 1~\mu m$ (W2H1) and the solid red line, that lies below for all the range of acoustic frequencies, shows the variation in hybridness for a guide dimension of $4~\mu m \times 1~\mu m$ (W4H1). The maximum value of hybridness for W2H1 was recorded as 0.088, which occurs near 8.46 GHz and for W4H1 it was 0.0729 near 6.58 GHz. With the increase in frequency both of these hybridness start to decrease. Near 30 GHz the hybridness for W4H1 was calculated as 0.023. For the guide of dimension W4H1, with the double width the dominant U_Z component gets more space to spread, whereas the non-dominant U_X component localizes at the vertical left and right interfaces, so, there ratio becomes less than the hybridness in W2H1 dimension for a given frequency, this the reason the red line lies below the blue line.
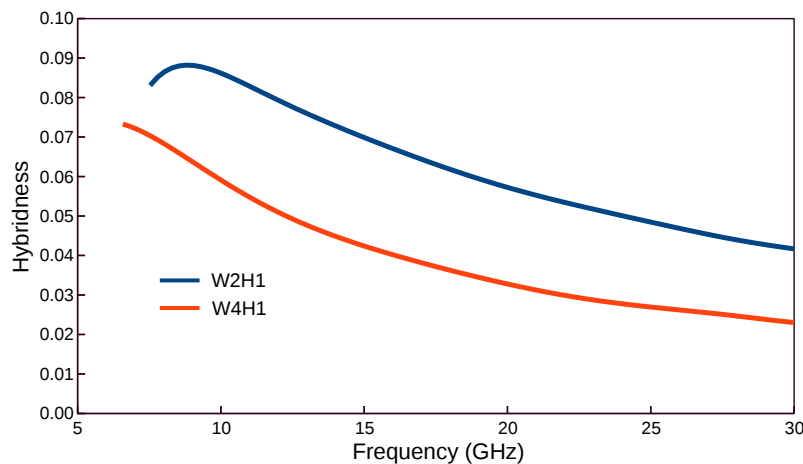
Fig. 4.36 Variation of the modal hybridness of U_{11}^{Z} for different width.

4.4.3   Option III: Quasi acoustic modes for 3% Ge-doped core

A different approach has been incorporated in analysing the acoustic modes for the Option III mentioned in Table 4.1. Instead of considering the provided longitudinal and shear velocities for the core and cladding, one set of analyses have been performed by allowing longitudinal velocities difference in Option I with a step of 10 m/s and another set of analyses have been evaluated by allowing shear velocities difference in Option II using same step size as before. In Option III the acoustic modes are formed not purely shear or longitudinal, rather they are known as quasi-shear or quasi-longitudinal acoustic modes. For a low index contrast waveguide like this, it is difficult to detect any distinguishable variation in the modes of this category comparing pure acoustic modes, those are analysed for Options I and II. Rather we have chosen a different approach to analyse the influence of pure longitudinal modes on quasi-shear acoustic modes and the influence of pure shear modes on quasi-longitudinal acoustic modes.

Quasi-shear acoustic modes

(a)

(b)

(c)
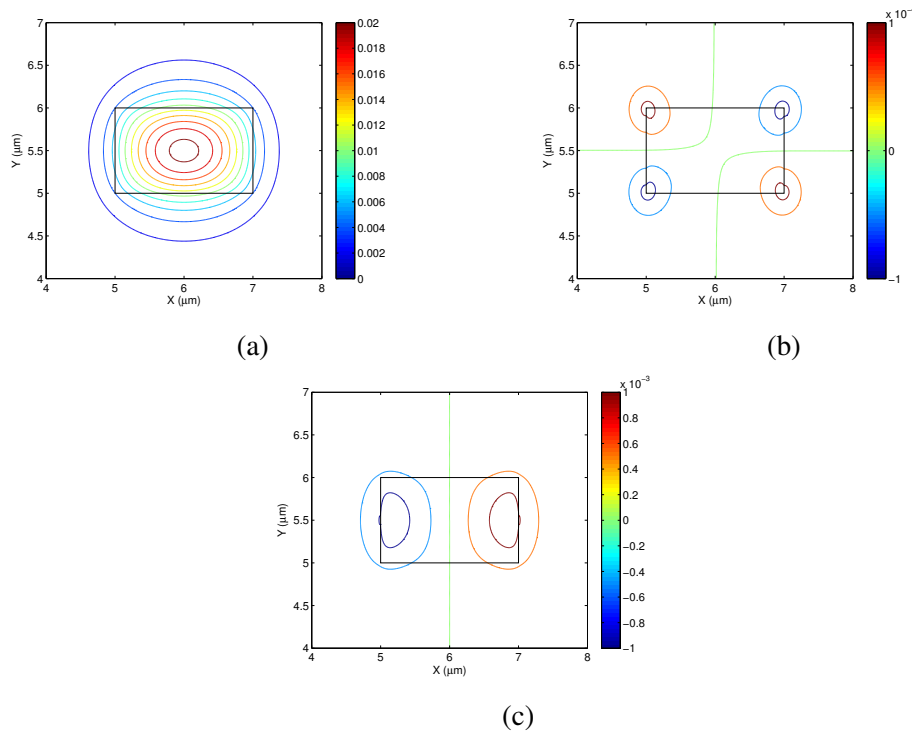
Fig. 4.37 U_X, U_Y and U_Z displacement vectors of the fundamental quasi-shear mode.

Considering the set of data given in the Option III of Table 4.1, as it is, U_X, U_Y and U_Z displacement components of fundamental quasi-shear mode at 16 GHz are shown in Fig.

4.37. It is clear that for this low index contrast waveguide the difference between the pure fundamental shear mode, shown in Fig. 4.3, and quasi-shear mode is very minor to be stated.
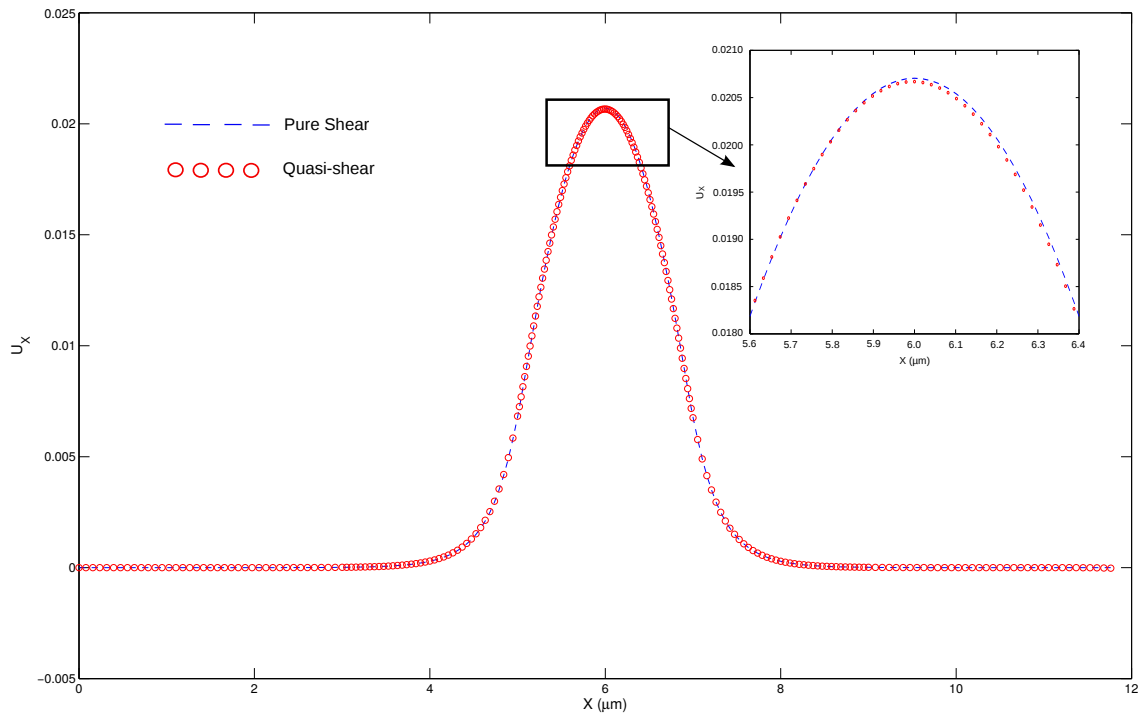
Fig. 4.38 The dominant U_X component of the fundamental quasi-shear mode along x-axis at 16 GHz.

To verify this the variation of the U_X components of both the pure shear and quasi-shear modes along x-axis at 16 GHz are shown in Fig. 4.38. As inset the tip of these profiles are given, where the red circles denotes the quasi-shear mode variation and the dashed blue line represent the variation of the pure shear mode. There is hardy distinguishable reduction in magnitude for the quasi-shear mode that can be noticed.

Let us now, consider a set of analyses by allowing longitudinal velocities difference in core and cladding with a step of 10 m/s in Option I of Table 4.1. The variations in the differences of phase shear velocities with the incorporated differences in cladding and core longitudinal velocities are shown in Fig. 4.39. It is to be noted that to be a weak guide for the acoustic mode the core longitudinal velocity needs to be smaller than the cladding longitudinal velocity. A gradual variation in the difference of the shear velocities are noticed, which is not linear.

The modal hybridness variation of the fundamental quasi-shear mode with the inserted difference in longitudinal velocities of core and caldding is presented in Fig. 40, where the hybridness is determined by the ratio of the maximum value of the U_X component to the
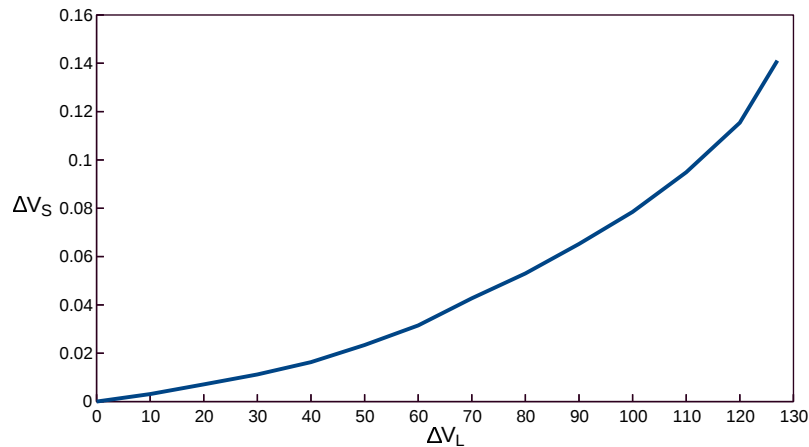
Fig. 4.39 Variation in the shear phase velocities difference with the incorporated difference in longitudinal velocities.

maximum value of the U_Z. It is to be noted that the hybridness is exponentially varied for this case and at $\triangle V_L = 127$, i.e. for the Option III in Table 4.1, the hybridness was measured as 0.0457.
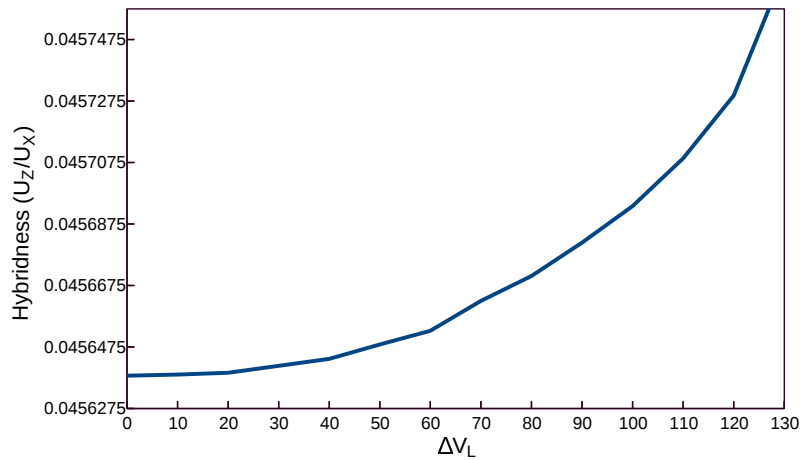
Fig. 4.40 Modal hybridness variation with the incorporated difference in longitudinal velocities.

Quasi-longitudinal acoustic modes

This set of analyses have been chosen by allowing shear velocities difference in core and cladding of Option II with a step of 10 m/s. The variations in the differences of phase longitudinal velocities with the incorporated differences in cladding and core shear velocities are shown in Fig. 4.41. A linear variation in the difference of the longitudinal velocities

are noticed for this case. But the change in longitudinal velocities was found more than the change in shear velocities was observed in Fig. 4.39.
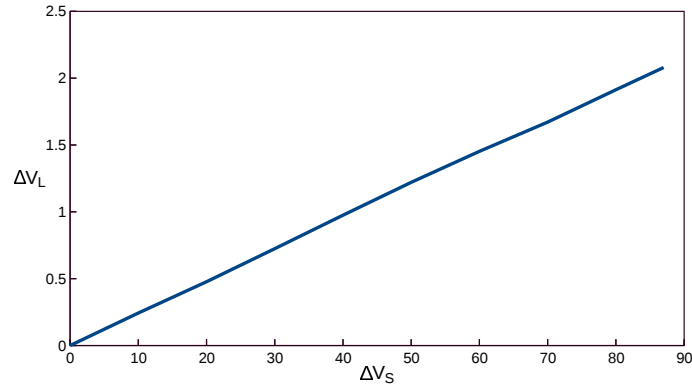
Fig. 4.41 Variation in the longitudinal phase velocities difference with the incorporated difference in shear velocities.

The modal hybridness variation of the fundamental quasi-longitudinal mode with the difference in shear velocities of core and cladding incorporated, is presented in Fig. 42, where the hybridness is determined by the ratio of the maximum value of the U_X component to the maximum value of the U_Z. It is to be noted that there is no significant variation in hybridness upto $\triangle V_S = 60$. After that the change is rapid but almost linear. At $\triangle V_S = 87$, i.e. for the Option III in Table 4.1, the hybridness for this case was calculated as 0.14658. All the measurements are made at $f = 16$ *GHz*. For this case the increase in hybridness is higher than that shown in Fig. 4.40.
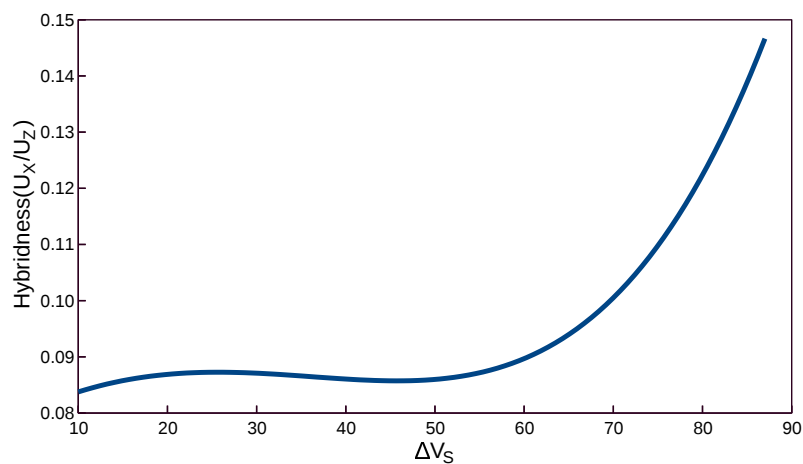
Fig. 4.42 Modal hybridness variation with the incorporated difference in shear velocities.

4.5   Summary

A rigorous analysis of acoustic modes is performed with the help of a full-vectorial acoustic mode solver by using computationally efficient finite element method. In this chapter, the advantages of using the symmetry conditions and the type of symmetry walls which can be used are discussed. It is also shown that by using Aitken's extrapolation the solution accuracy can also be improved with the use of finite computer resources. The spatial variations of the dominant and non-dominant displacement vectors of the longitudinal and shear acoustic modes are also shown here.

It is shown here that Ge:doped planar silica waveguide can support shear and longitudinal acoustic modes. Both the longitudinal and shear acoustic modes for a 3% Ge-doped silica waveguide with dimension 2 μm × 1 μm are regorously studied in this chapter. All these modes may have either dominant transverse or longitudinal component but also two other non-dominant components. The optical modes in a waveguide with two-dimensional confinement are also hybrid in nature, and the modal hybridness increases when index contrast is increased. To study the complex interaction between the fully hybrid acoustic modes and optical modes, a full vectorial approach needs to be used, as shown here. The numerical approach presented here can be used for a wide range of practical optical waveguides with either co- or anti-guiding acoustic modes to study their acousto-optical interactions.

Chapter 5

Light-sound Interaction in Ge-doped Planar Silica Waveguide of Moderate Contrast

5.1 Introduction

Light-sound interaction in Ge-doped silica fibres attracted interest for a very long time due to their extensive use as SMF [Nikles, 1997; Koyamada, 2004; McCurdy, 2005; Dragic, 2009 and Beugnot, 2012]. Beside the SMF, researcher also concentrated on acousto-optical interaction in the Ge-doped silica dispersion decreasing fibres (DDF) [Li, 2006], solid core and Micro-structured fibres [Dasgupta, 2011]. For most of literatures the main concentration was given in finding the Brillouin gain spectrum (BGS) of these fibres.

In [Koyamada, 2004], the authors use a parabolic profiled Ge-doped silica core of radius 1.2 μm, where the maximum dopant concentration was 22%. The silica cladding radius was 62.5 μm. The BGS measurements were carried out at wavelength, $\lambda_o = 1.55$ μm using a Brillouin optical time domain reflectometer (ANDO: AQ8603). The authors reported a BGS with three significant peaks at 9.72 GHz, 10.44 GHz and 11.17 GHz respectively when the total considered spectral range was from 9.2 to 11.6 GHz.

In [Dasgupta, 2011], a FEM based analysis technique was carried out through a commercial FEM solver (COMSOL, Multiphysics) to investigate the BGS in a step index Ge-doped silica fibre of radius 2 μm with 9% Ge-doping, to make it a optically single-moded fibre at wavelength, $\lambda_o = 1.55$ μm. The full width half maxima (FWHM) of the Lorntzian cures in BGS were arbitrarily considered as 50 MHz. The spectrum range was 9.4 to 11.6 GHz.

The BGS showed three significant peaks at 10 *GHz*, 10.5 *GHz* and 11.11 *GHz*, which were identified as spectrum due to acoustic longitudinal modes L_{01}, L_{02} and L_{03}, respectively.

It is amazingly noticeable that in the literature the contribution of shear acoustic waves in the Brillouin spectrum have not been mentioned or studied. According to [McCurdy, 2005], the radial material displacement plays a significant role in the SBS interaction in fibres with a complex radial index profile. Recently, it has been reported [Fernandes, 2015] to exhibit optical signal switching by the use of flexural acoustic mode generated by the use of two stacked piezoelectric transducers (PZTs) with orthogonal vibration directions, which can generate and adjust the spatial orientation of the acoustic flexural mode in a in-line wavelength selective core switch for multicore fibre. In this case, the transverse plane material displacements contributed by the flexural acoustic mode was used to achieve the switching goal. So, it is worthy to investigate the contributions of shear acoustic modes in Brillouin spectrum. Here, in this chapter, light-sound interactions in a 10% Ge-doped silica optical waveguide with a dimension of 6 μm × 3 μm embedded in a silica cladding have been evaluated. The BGS is also determined considering contributions of both shear and longitudinal acoustic modes.

5.2   Acoustic properties of the core and cladding

The Ge-doping reduces the light velocity in the silica core and increases the refractive index, as well as, it also reduces the acoustic velocity [Koyamada, 2004]. In a silica planar waveguide the core is doped with 10% Ge to increase the refractive index. This also increases the acoustic index of the core when compared to the undoped silica cladding [Li, 2007], thus this optical waveguide also confines both longitudinal and shear acoustic waves. The acoustic longitudinal and shear wave velocities and density of the 10% Ge-doped core are taken as V_{LG} = 5509.67 m/s, V_{SG} = 3474 m/s and ρ_G = 2342 kg/m^3, respectively [Jen, 1986 and Dragic, 2010]. By contrast, for the un-doped pure silica cladding, these are considered to be V_{LC} = 5933 m/s, V_{SC} = 3764 m/s and ρ_C = 2202 kg/m^3, respectively [Jen, 1986]. As the velocity of the longitudinal and shear acoustic modes are different, the materials are effectively 'anisotropic' and the resultant acoustic index contrast between core and cladding are also different. In this case if the cladding acoustic index is taken as 1.0, then the core acoustic index would be 1.071 and 1.077 for longitudinal and shear modes, respectively. The height (H) and width (W) of the core are taken as H = 3 μm and W = 6 μm, respectively, to ensure that optical mode is guided in this waveguide at the operating wavelength (λ_o) of 1550 nm. For this waveguide a two-fold symmetry is available and this has been exploited here to obtain better accuracy in their modal solutions for a give computer resource.

As considered in Chapter 4, here, for this strongly guided Ge-doped silica planar waveguide, the analyses are performed assuming (Option I) the longitudinal acoustic velocities of Ge-doped silica core and un-doped silica cladding are equal, i.e., $V_{LG} = V_{LC}$, and then considering (Option II) the shear acoustic velocities of both the core and cladding are equal, i.e., $V_{SG} = V_{SC}$. The first option will ensure only shear acoustic waves exists in the guide, thus it will be decoupled from the longitudinal acoustic modes, and the second option will ensure the longitudinal modes remain decoupled, i.e. will remain un-influenced by the shear modes. Based on the investigation presented in the Section 4.4.3, in Chapter 4, Option III is not considered for this waveguide. All the longitudinal and shear velocities, densities and elastic coefficients for core and cladding materials are listed in the Table 5.1.

Table 5.1 Procedural options and acoustic properties of materials for the 10% Ge-doped planar silica waveguide

Options		Velocity (m/s)		Density (kg/m^3)	Elastic Coefficient (GPa)		
		V_L	V_S	ρ	C_{11}	C_{12}	C_{44}
Option I	**Core**	5933	3474	2342	82.4395	25.9099	28.2648
	Clad	5933	3764	2202	77.5115	15.1170	31.1972
Option II	**Core**	5509.67	3764	2342	71.0948	4.7333	33.1807
	Clad	5933	3764	2202	77.5115	15.1170	31.1972

5.3   Option I: Shear acoustic modes for 10% Ge-doped core

As shown in Table 5.1, for Option I, here both the longitudinal velocities in core and cladding are considered to be equal to have decoupled shear acoustic modes. For this case, $\frac{\triangle V_S}{V_S} = 0.0770$, the material contrast is larger than 3% Ge-doped core. Therefore this waveguide will act as a better guide for the shear modes.

The displacement vector profiles of the fundamental shear U_{11}^X acoustic mode, for 10% Ge-doped core, are shown in Fig. 5.1. Here, the U_X component, dominant displacement vector profile in Fig. 5.1(a) has a Gaussian like shape with maximum material displacement at the core centre. But, the U_Y component in Fig. 5.1(b), non-dominant displacement vector profile, has four peaks near four corners of the cross-section of the waveguide. For the U_Z component in Fig. 5.1(c), another non-dominant displacement vector profile, opposite peaks are formed near the left and right vertical interfaces with a peak height of 2.77% of the dominating field profile.

As it is discussed in Section 4.4.1, here also, it can be observed that for any shear acoustic U_{mn}^X mode with a dominant U_X component, have half sine-wave spatial variation of (m, n), but its non-dominant U_Y and U_Z components have spatial variations of $(m+1, n+1)$ and $(m+1, n)$, respectively.
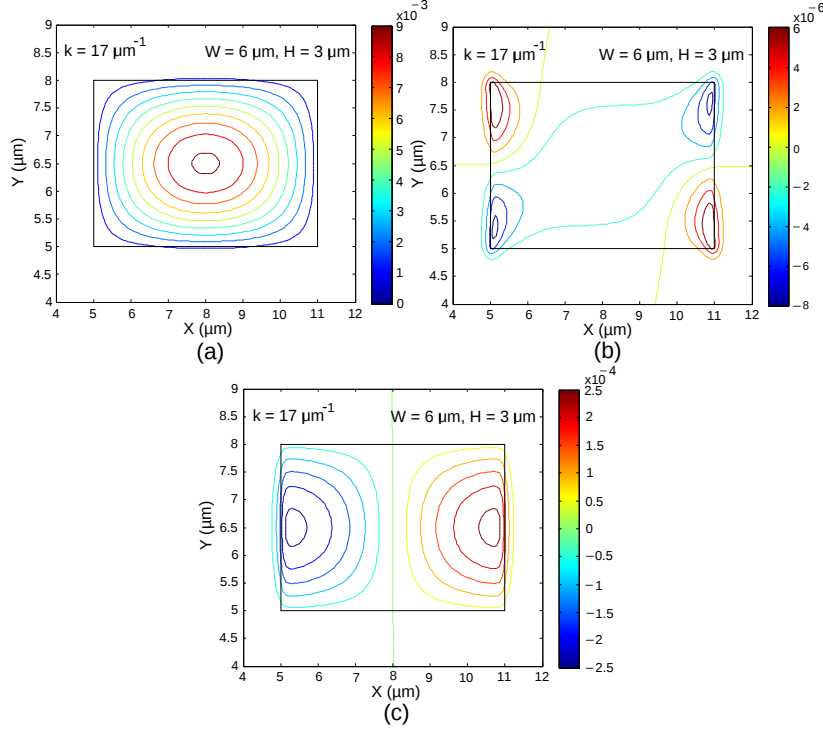
Fig. 5.1 Displacement vector profiles (a) U_X, (b) U_Y and (c) U_Z of the fundamental shear U_{11}^X acoustic mode.

As it is mentioned earlier, Ge-doping concentration can reduce the acoustic velocity of the core, which can be verified by observing the Fig. 5.2, where the variation of shear phase velocity with acoustic frequency for fundamental shear mode U_{11}^X for both 3% and 10% doping concentrations are shown. Here the solid blue line represents the phase velocity variation for U_{11}^X mode in 3% Ge-doped 2 $\mu m \times 1$ μm dimension core. The solid red line represents the phase velocity variation for U_{11}^X mode in 10% Ge-doped 6 $\mu m \times 3$ μm dimension core. It can be noted that the phase velocity variation in 10% Ge-doping is more monotonous at higher frequency range comparing that of the 3% Ge-doped core.

Due to higher doping concentration (10% in this case) of Ge, the acoustic index of the core is increased sufficiently and thus this waveguide supports higher order longitudinal and shear acoustic modes. Variations of the phase velocities with the acoustic frequency for several shear modes are shown in Fig. 5.3. When the frequency is reduced, the phase velocities of the different shear modes gradually increased. However, at a lower frequency
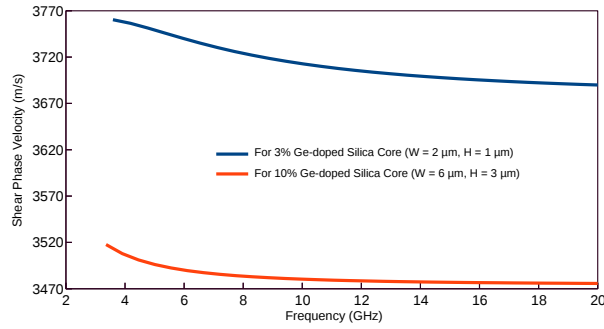
Fig. 5.2 Variations of the phase velocities with the acoustic frequencies for different doping concentration of shear mode U_{11}^X.

this change is rapid as the modes reach their cut-off conditions and their phase velocities approach those of the cladding velocities, V_{SC}, and beyond that no acoustic mode is guided. It can be noted that the effective cut-off frequency of a higher order mode appears at a higher frequency. The variation of the phase velocity of the fundamental shear mode, U_{11}^X, is shown by a blue line. The higher order longitudinal modes U_{21}^X and U_{12}^X are distinct and are depicted by red and yellow solid lines, respectively. They were different as the height (H) and width (W) of the guide were not equal. In case of H = W, they would have the same modal solution and it would be impossible to isolate these degenerate modes. This guide also supports two near degenerate fundamental shear modes U_{11}^X and U_{11}^Y, but however, as the symmetry conditions were exploited, these two modes were isolated (as they require different combinations of the symmetry walls).
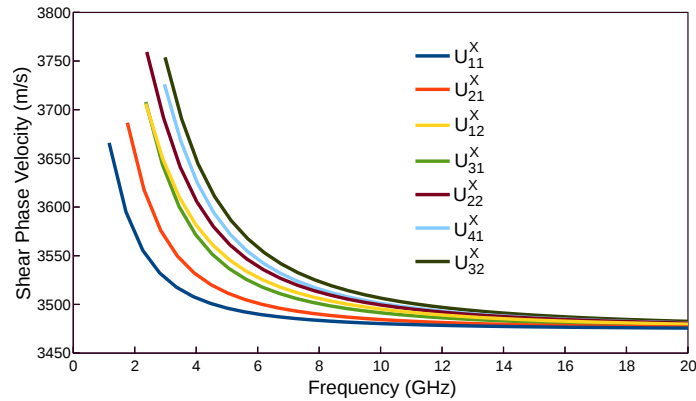
Fig. 5.3 Variations of the phase velocities with the acoustic frequencies for the shear modes.

Dispersion curves of the fundamental shear acoustic U_{11}^X and U_{11}^Y modes are shown in Fig. 5.4. Here, the variations of their phase velocities with the acoustic frequencies are shown. The solid blue line represents the fundamental U_{11}^X mode. It can be observed that

when the frequency is reduced the phase velocity increases monotonically and reaches that of the cladding shear velocity, V_{CS}, as the mode approaches its effective cutoff near 1.167 GHz. It is to be noted that for whole range of acoustic frequencies the phase velocity of the U_{11}^Y mode, represented by the solid red line, is slightly higher than that of the U_{11}^X mode. The effective cutoff frequency of the U_{11}^Y mode was found near 1.71 GHz. As the shear modes with U_Y dominant components were discussed in details in Chapter 4 for 3% Ge doped core, to avoid redundancy, these are not discussed for 10% Ge-doped core.
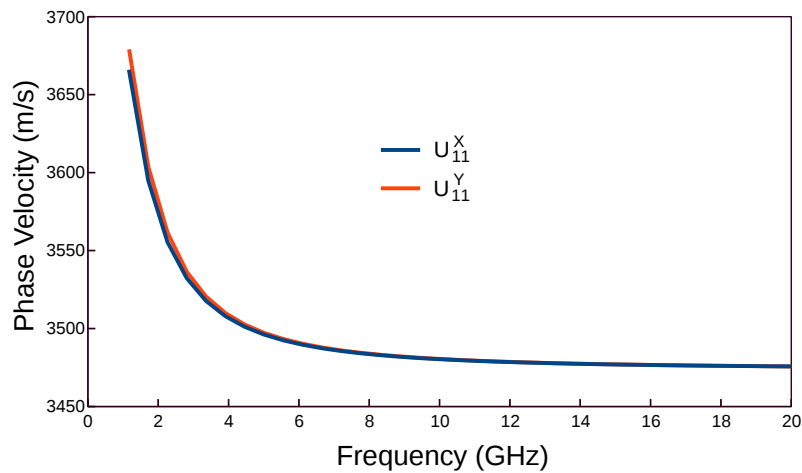
Fig. 5.4 Dispersion curves of acoustic shear U_{11}^X and U_{11}^Y modes in 10% Ge-doped core.

The variations of phase velocities of U_{11}^X and U_{11}^Y modes with the changing guide width are shown in Fig. 5.5. As the guide width increases for both modes the phase velocities decreases, but at the lower range of guide width the change in phase velocities are more rapid for the change in width. It can be noted that as the guide width increases the difference between the phase velocities of the two shear modes increases. Here, this difference is termed as birefringence. Since the importance was given to determine light-sound interactions, while finding out the acoustic modes for different guide widths the phase matched condition was ensured.

Figure 5.6 shows this birefringence against the guide width. It clearly shows that the birefringence increases with the width, but at higher width this birefringence reaches near its maximum value, it can be concluded that at guide with more than 10 μm, this change will become insignificant. In Fig. 5.6, the propagation constant for each guide width was chosen to maintain the phase match with the optical signal.
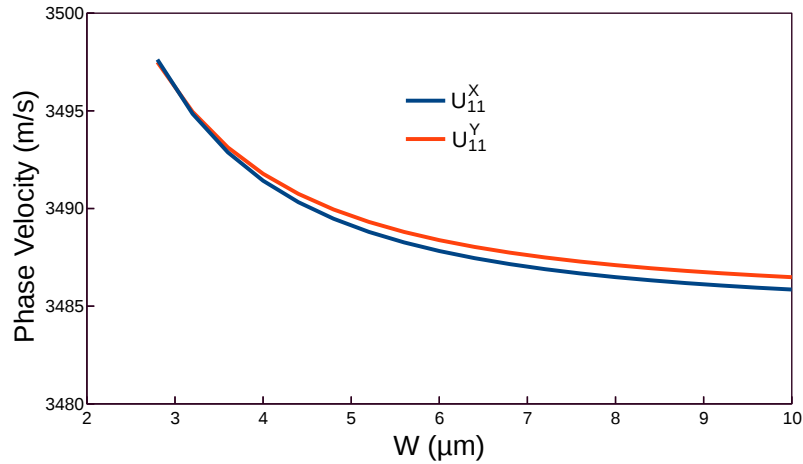
Fig. 5.5 Variation of phase velocity of U_{11}^X and U_{11}^Y modes with width.
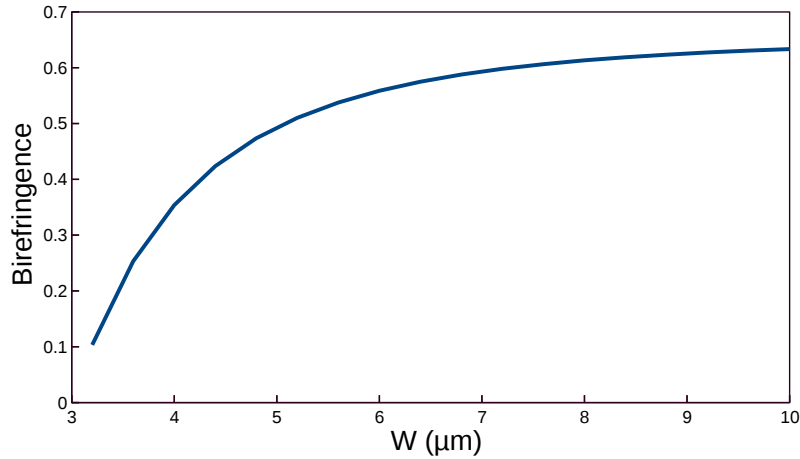
Fig. 5.6 Variation of birefringence with width.

5.3.1 Variation of the modal hybridness

The variations of the hybridness with the acoustic frequency for two non-dominant components U_Y and U_Z of fundamental shear U_{11}^X mode are shown in Fig. 5.7. Here the hybridness for the U_Z component has been defined as the ratio of the maximum U_Z vector to the maximum dominant transverse displacement U_X for the U_{11}^X mode, which is shown by the solid blue line. For the non-dominant U_Y component, the hybridness has been defined as the ratio of the maximum U_Y vector to the maximum dominant displacement U_X and shown by a solid red line. It can be observed that as the frequency is decreased modal hybridness increases for both the components, but the hybridness of the U_Z component is higher, as the U_Z component displacement occupied more space than that of the U_Y component, which were shown in the Figs. 5.1(b) and 5.1(c). Near $f = 20 \, GHz$ the hybridness of U_Z component was calculated as

0.0142 and for U_Y component it was 0.0003. The increase of hybridness for U_Y component after 4 GHz was more rapid and near 2 GHz it was 0.0085, whereas for U_Z component it was 0.0928.
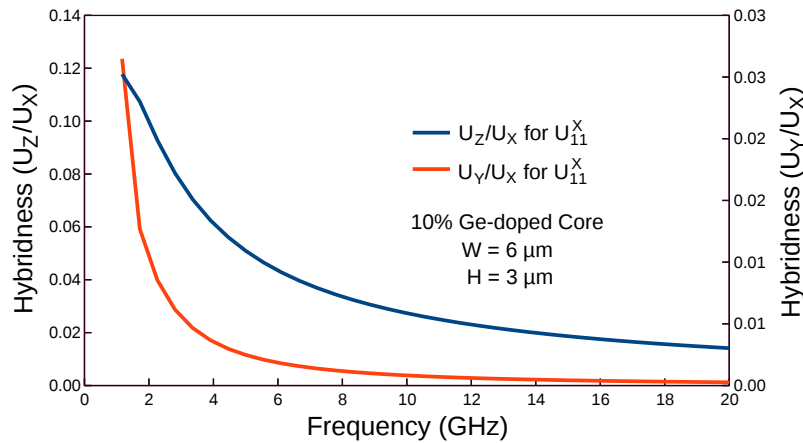
Fig. 5.7 Variations of hybridness with frequency for U_{11}^X mode in 10% Ge-doped core.

Figure 5.8 compares the variation of the hybridness with frequency for fundamental and higher order shear acoustic modes for 10% Ge-doped core. The solid red line represents the hybridness variations for U_{21}^X mode. Here both the cases the hybridness was measured by the ratio of the maximum value of U_Z component to the maximum value of U_X component. It was found that the hybridness for the higher order mode was higher for the tested range of frequencies. Near $f = 20$ GHz the hybridness for U_{21}^X mode was determined as 0.0286 and near 2 GHz it was 0.2244.
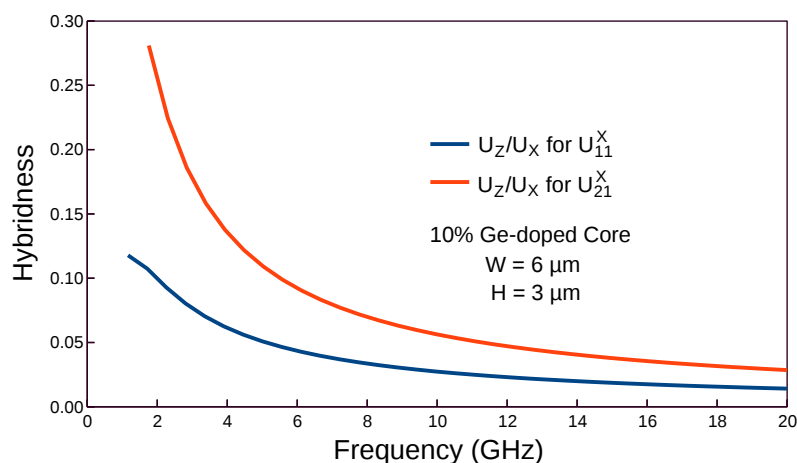
Fig. 5.8 Variations of hybridness with frequency for U_{11}^X and U_{21}^X modes in 10% Ge-doped core.

The variation of the hybridness in non-dominant components U_Y and U_Z of U_{21}^X mode shown in Fig. 5.9, which vary similar way, i.e. the hybridness of U_Z component is higher than that of the U_Y component, similar as that of the U_{11}^X mode shown in Fig. 5.7. Near $f = 20$ GHz the hybridness of U_Y component was calculated as 0.0227 and near $f = 2$ GHz it was 0.0005.
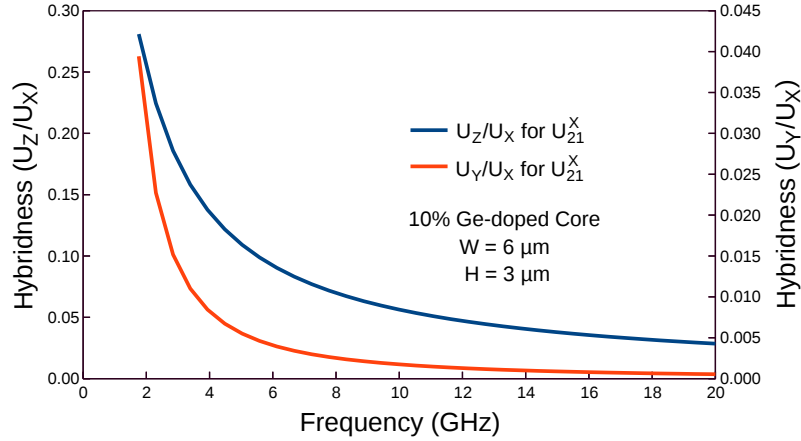
Fig. 5.9 Variations of hybridness with frequency for U_{21}^X mode in 10% Ge-doped core.

5.3.2 Spotsize Variation of shear mode

The U_X vector profile of the acoustic U_{11}^X mode varies with the waveguide width, it will be more clear by comparing the mode profiles for the core dimension of 2 $\mu m \times 1$ μm in Fig. 4.3 and that for 6 $\mu m \times 3$ μm core in Fig. 5.1, although the dopant concentrations and core hight were different. The variations of the spotsizes along the x and y directions with the width, W, for the U_X profile of U_{11}^X mode, when propagation constant $k = 12$ μm^{-1}, are shown in Fig. 5.10. Here, the acoustic spotsize is considered as the distance along the x and y-axes where the acoustic displacement profile is approximately equal to the $1/e$ times of the maximum value of a given acoustic mode. Here, the guide height is kept constant at H = 3 μm. The spotsize, σ_X, denoted by a blue line, decreases as the width is decreased but near the effective cut-off this value start increasing. Whereas, The spotsize, σ_Y, remains almost constant (as the height was kept constant) as guide width decreases but only near the cut-off, where the spotsize, σ_Y, increases.
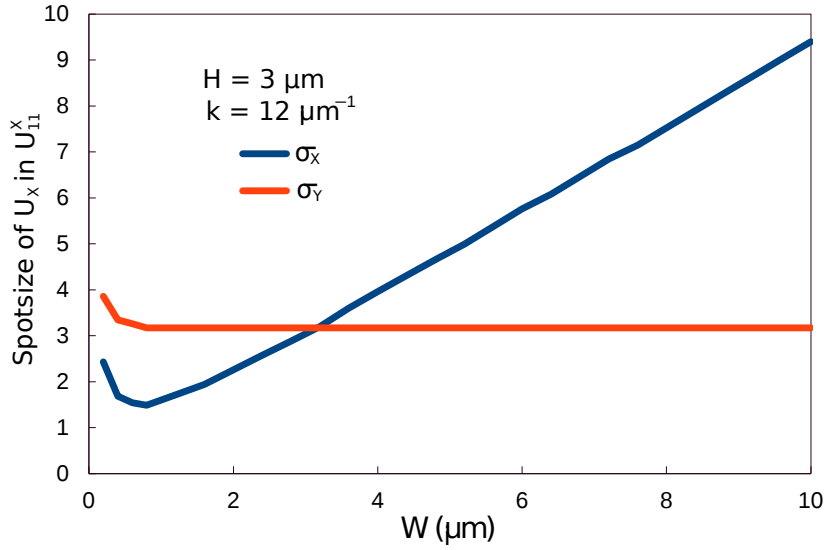
Fig. 5.10 Variations of spotsizes with width for U_{11}^{X} mode in 10% Ge-doped core.

5.4 Option II: Longitudinal acoustic modes for 10% Ge-doped core

In this section the Option II in Table 5.1 is considered to obtain the longitudinal acoustic modes in their pure form without being influenced by the shear acoustic modes. Here, both the shear velocities in core and cladding are considered to be equal and taken as 3764 m/s. For such case as $\frac{\triangle V_L}{V_L}$ = 0.0714, i.e., the material contrast is larger than that of the 3% Ge-doped core. It is expected that this waveguide will act as a stronger guide for the longitudinal modes as well.

This waveguide can guide longitudinal acoustic modes as the cladding longitudinal velocity is higher than that of the core. It was observed that the spatial variations of the displacement vector profiles of the longitudinal acoustic modes are different from those of the shear modes, as observed in Chapter 4. The dominant and non-dominant displacement vector profiles of the fundamental longitudinal, U_{11}^{Z} mode are shown in Fig. 5.11. It can be observed that its U_Z profile has one ($m = 1$) half-sine variation along the x and similarly one ($n = 1$) half-sine variation along the y-directions. On the other hand, the U_X profile of this U_{11}^{Z} mode has one additional spatial variation along the x-direction ($m = 2$) and its U_Y profile has one additional variation along the y-direction ($n = 2$). For a general U_{mn}^{Z} mode, its dominant component U_Z has (m, n) spatial variations; however its non-dominant U_X and U_Y components have (m+1, n) and (m, n+1) spatial variations, respectively.

The variations of the phase velocities of the fundamental and higher order longitudinal modes with the frequency are shown in Fig. 5.12. When frequency is decreased gradually,
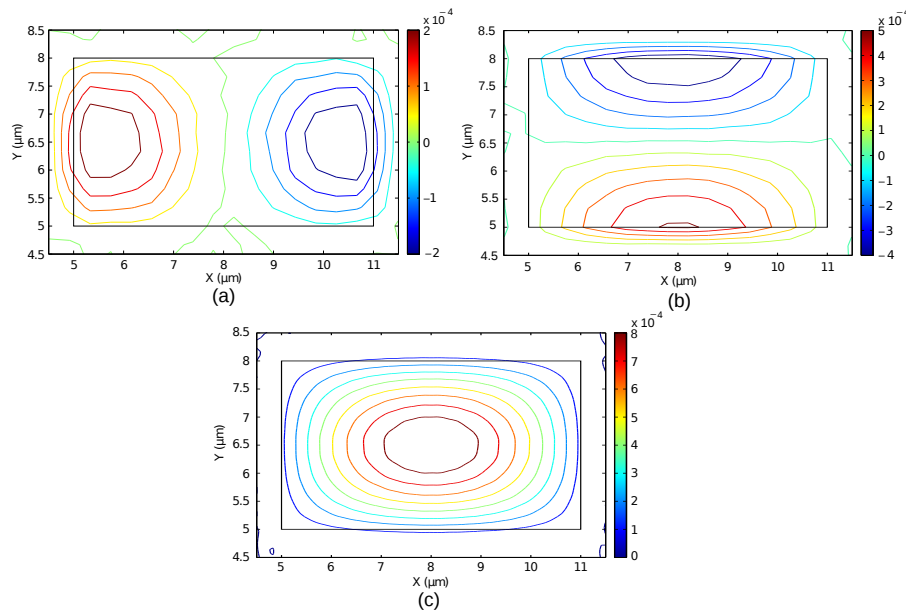
Fig. 5.11 Displacement vector profiles (a) U_X, (b) U_Y and (c) U_Z of the U_{11}^Z acoustic mode.

the velocities of the modes increase from near core velocity to cladding longitudinal wave velocity until they reaches to their cut-off when changes are rapid. The variations of the phase velocities of the U_{21}^Z and U_{12}^Z modes are shown by a red and a yellow lines, respectively and they are distinct. It can be observed that the red line lies below the yellow line for the whole range of the acoustic frequency considered here as the guide width was larger than the height. Here it can also be observed that a higher order mode reaches its cut-off at a higher frequency.
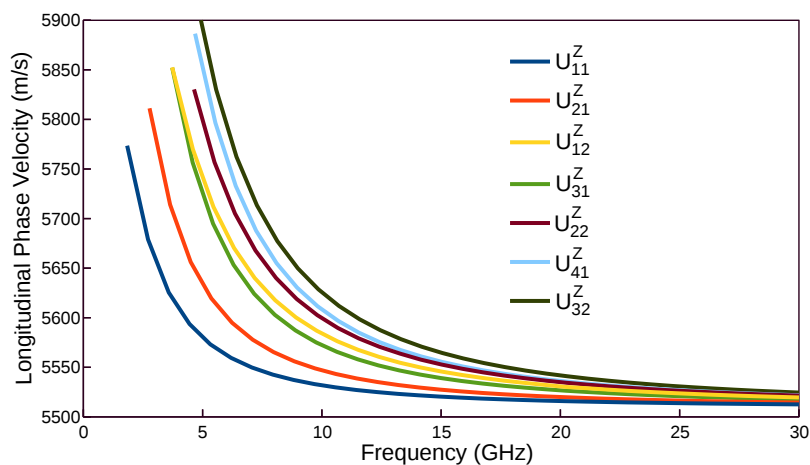
Fig. 5.12 Variations of the phase velocities with the acoustic frequencies for the longitudinal modes.

Figure 5.13 shows the variation of the phase velocity of the fundamental longitudinal mode U_{11}^Z mode with the change in guide width, at phase matched condition. As the guide width decreases the phase velocity of the U_{11}^Z mode gradually increases, at 10 μm guide width the velocity was calculated as 5527.62 m/s, whereas, at 4 μm it was 5535.67 m/s.
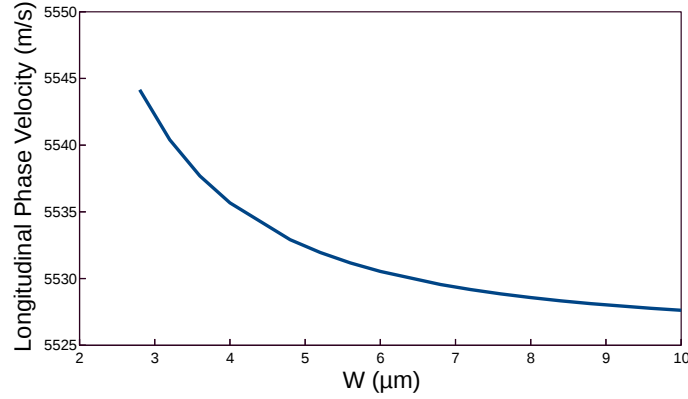
Fig. 5.13 Variation of phase velocity of U_{11}^Z mode with width.

5.4.1 Spotsize Variation of longitudinal mode

The acoustic U_Z vector profile of the fundamental acoustic longitudinal U_{11}^Z mode also varies with the waveguide width. To evaluate this, the propagation constant was not kept the same. The variations of the spotsizes along the x and y directions with the width, W, for the U_Z profile of U_{11}^Z mode are shown in Fig. 5.14. Here, the guide height is also kept constant at H = 3 μm. The spotsize, σ_X, denoted by a blue line, decreases as the width is decreased but the spotsize, σ_Y, remains almost constant as the guide height was constant. For Fig. 5.14, instead of considering fixed propagation constant, phase matched condition was ensured.
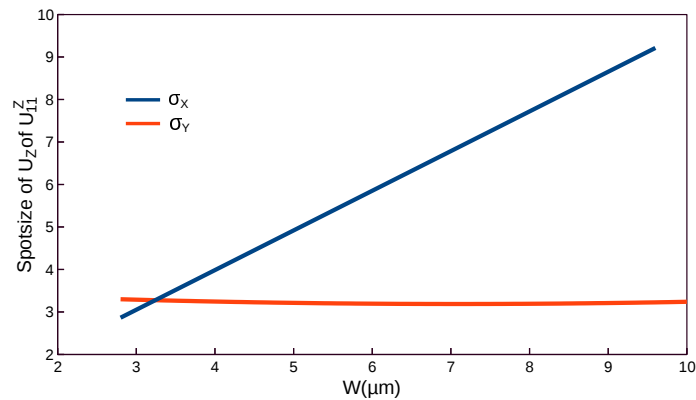
Fig. 5.14 Variations of spotsizes with width for U_{11}^Z mode in 10% Ge-doped core.

5.5   Optical modes in 10% Ge-doped core

Optical modes are categorised as quasi-TE (quasi transverse electric) or quasi-TM (quasi transverse magnetic) modes, because those have all the six components of the **H** and **E** fields.

A Ge-doped silica planar waveguide can also guide optical signals. A FEM approach based on the vector **H**-field formulation can be used for the analysis of the optical modes. This approach is one of the most numerically efficient and accurate approaches to obtain the modal field profiles and the propagation constants of the fundamental and higher order quasi-TE and quasi-TM modes.

Modal solutions of the optical waves in 10% Ge-doped silica planar waveguide, for a wavelength λ_o = 1550 nm, are obtained by using a full-vectorial **H**-field formulation [Rahman, 1984]. Here refractive indices of core and cladding are taken as 1.459 and 1.444, respectively. Both quasi-TE and quasi-TM modes can exist in this waveguide, but they have similar propagation constants and the profiles of their dominant **H**-fields are also similar. Although, in this section, some properties of the quasi-TM mode is briefly highlighted, in this thesis mainly the interaction of the shear and longitudinal acoustic modes with the fundamental quasi-TE, H_{11}^Y mode are studied.

All three components of the field profiles for the fundamental quasi-TE, H_{11}^Y, mode are shown in Fig. 5.15. The dominant magnetic H_Y field profile, shown in Fig. 5.15(b), exhibits a Gaussian like shape with maximum field strength at the centre of the core. Whereas, the non-dominant H_X field profile in Fig. 5.15(a) shows clearly four peaks near four corners of the transverse plane of the waveguide with the similar peaks (positive or negative) at the diagonal corner, with a peak height of 4×10^{-4}. Figure 5.15(c) shows another non-dominant field H_Z profile, where the opposite peaks are formed at the upper and lower horizontal interfaces with a peak value of 6% of the dominating H_Y field profile.

With the waveguide width the optical H_Y field vector profile of the quasi-TE H_{11}^Y mode varies. The variations of the spotsizes along the x and y directions with the width, W, are shown in Fig. 5.16. For the optical spotsize, the distance is considered along the x and y-axes where the optical field vector profile is approximately equal to or higher than the $1/e$ times of the maximum value of a given optical field. The spotsize, σ_{OX}, denoted by a blue line is found to decreases as the width is decreased but near the cut-off this value start increasing as the profile spreads out. Whereas, The spotsize, σ_{OY}, increase very slowly, but at lower guide width, this increment enhances a bit more, due to the spreads out of the profile near cutoff. Here also, the guide height is kept constant at H = 3 μm.

For optical modes the effective index, n_{eff}, is defined as,

(a)

(b)

(c)
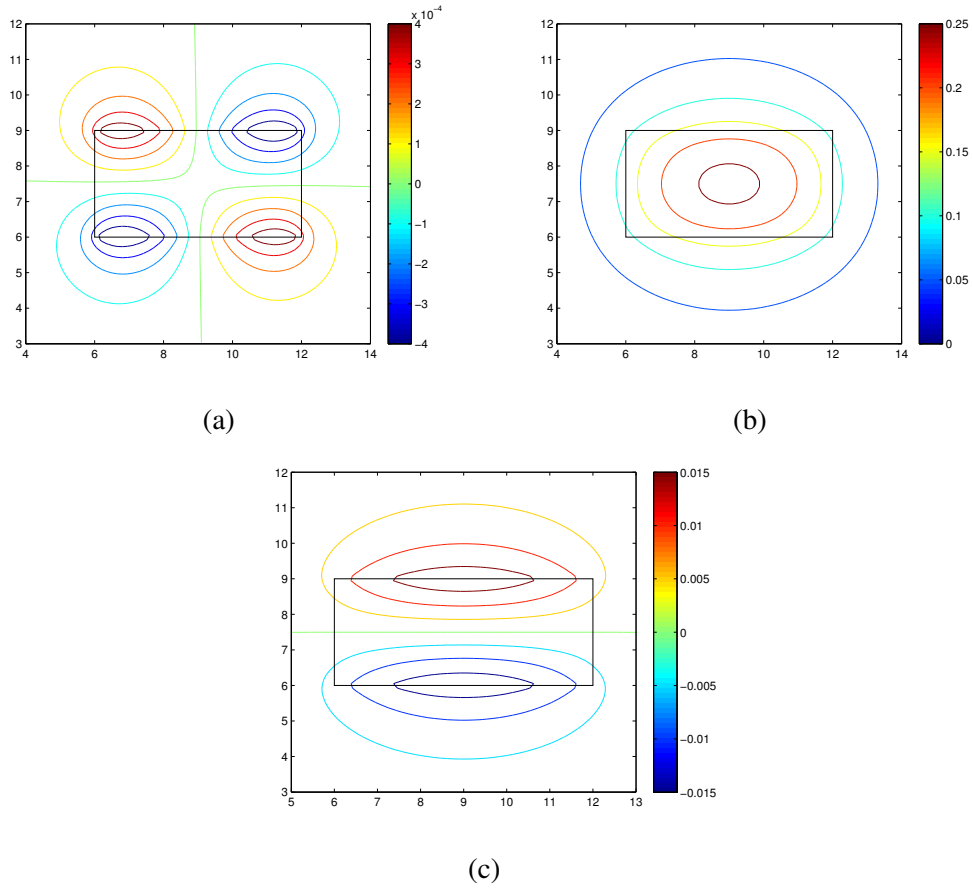
Fig. 5.15 H_X, H_Y and H_Z field profiles of the fundamental quasi-TE optical mode.
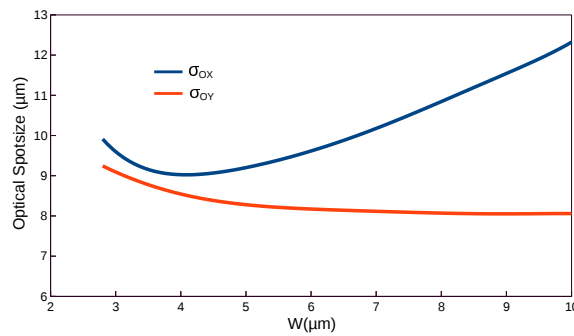
Fig. 5.16 Variations of spotsizes with width for H_{11}^Y mode in 10% Ge-doped core.

$$n_{eff} = \frac{\beta_o}{k_o} \qquad (5.1)$$

here β_o is the optical propagation constant, k_o is the optical wavenumber in free space.

The optical wavenumber in free space can be defined as,

$$k_o = \omega_o (\varepsilon_o \mu_o)^{\frac{1}{2}} \tag{5.2}$$

here ε_o is the permittivity in free space, μ_o is the permeability in free space and ω_o is the optical angular frequency.

Variations of effective index for both the quasi-TE and quasi-TM modes with guide width are shown in the Fig. 5.17. The dashed blue line represents the effective index (n_{eff}) for the quasi-TE H_{11}^Y mode and the solid red line represents the n_{eff} for the quasi-TM H_{11}^X mode. With the increase in guide width, both effective indices increases. It can be noted that the blue dashed line lies slightly above the red solid beyond guide width of 3 μm, as in this region the guide width is higher than the height of it.
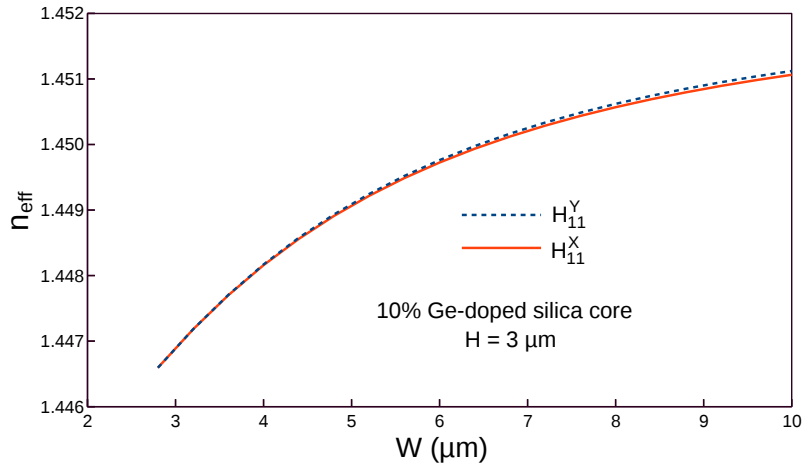
Fig. 5.17 Variations of n_{eff} with the guide width for the optical quasi-TE and quasi-TM modes.

The spotsize area variations for both the quasi-TM, H_{11}^X, and quasi-TE, H_{11}^Y, modes with guide width are shown in the Fig. 5.18. Here the spotsize area is defined as the accumulated areas of the elements for which the field values are equal or greater than $1/e$ times the maximum field value for that mode. It can be noted that for increasing guide width more after 3 μm, the soptsize area of the quasi-TM mode is higher, as the width of the guide is higher than the height, which is constant at $H = 3$ μm. The spotsize areas for both the modes increase with the increasing guide width. For both the modes the spotsize areas are minimum at $W = 3.2$ μm width and calculated as 22.132 μm^2 and 22.093 μm^2 for H_{11}^X and H_{11}^Y modes, respectively. Below 3 μm guide width the spotsize areas for both the modes tends to increase as the modes reach their respective cutoff frequencies and spread out.
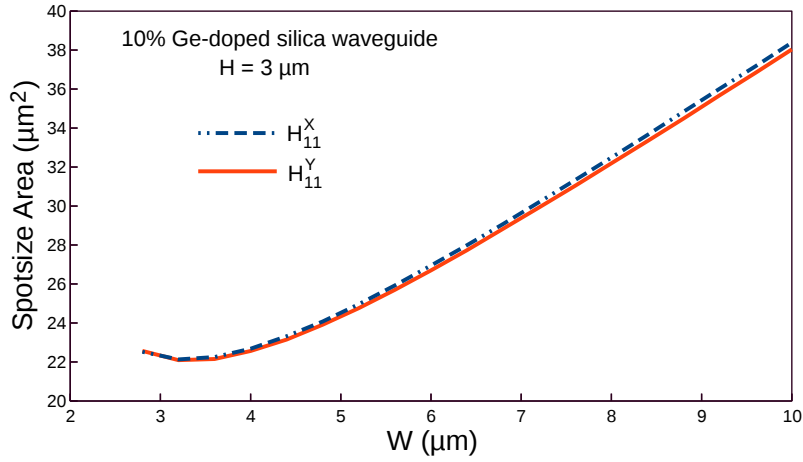
Fig. 5.18 Variations of the spotsize area of the H_{11}^Y and H_{11}^Y modes with the guide width, W.

The variations of the effective index (n_{eff}) and effective area (A_{eff}) of the H_{11}^Y mode with the guide width (W) are presented in Fig. 5.19 by a dashed blue and a red solid lines, respectively. The mode size area or the effective area (A_{eff}) can be given [Uthman, 2012] by,

$$A_{eff} = \frac{\left(\int\int_{\Omega_w} |E_t|^2 dxdy\right)^2}{\int\int_{\Omega_w} |E_t|^4 dxdy} \tag{5.3}$$

here E_t represents the transverse electric field vector and the surface integration is carried out over the whole cross section, Ω_w, of the waveguide.
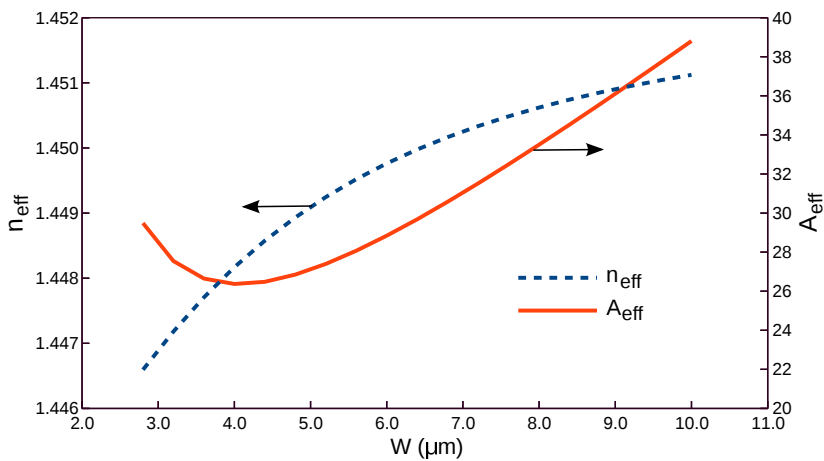
Fig. 5.19 Variations of the n_{eff} and A_{eff} of the H_{11}^Y mode with the guide width, W.

It can be observed that as the waveguide width, W, is reduced, initially the effective area, A_{eff}, reduces and reaches its minimum value of 26.37 μm^2 when W = 4 μm. However, if W is reduced further, its effective area increases rapidly as the optical mode approaches its effective cut-off condition. Moreover, when the guide width reduces, n_{eff} gradually falls from the effective index of a slab with height (H) 3 μm, to the cladding refractive index value. Below a width of 4 μm, the optical mode spreads out before reaching its cut-off. It should be noted that as modes spreads out more from the core into the cladding, the scattering loss at the core-cladding interface, leakage loss, and bending loss (if bent), increase rapidly and it cannot be used as an effective waveguide.

5.6 Light-sound interaction in 10% Ge-doped silica waveguide

In an optical waveguide, a guided optical signal can be scattered by the nonlinear interaction between the pump and Stokes fields and an acoustic wave through the SBS process. In such an event, since both the momentum and energy must be conserved, for a given propagation constant, β_o, of an existing optical mode, the propagation constant, k, of an acoustic mode can be found [Boyd, 2008] by using,

$$k = 2\beta_o \tag{5.4}$$

The SBS gain can be calculated from the overlap integral of the optical field with the displacement vector profile, $\mathbf{U}(x,y)$ [Rakich 2012 and Tartara, 2009], or with the density variation profile [Pant, 2011]. The density variation profile also holds strong correlation with the displacement vector profile and this normalized overlap [Rakich 2012 and Tartara, 2009] can be calculated as:

$$\Gamma_{ij} = \frac{\left(\int |H_{im}|^2 u_{jn} dx dy\right)^2}{\int |H_{im}|^4 dx dy \int |u_{jn}|^2 dx dy}; \quad m,n = x,y,z \tag{5.5}$$

here H_{im} is the mth component of the magnetic field profile (where m may be x, y or z) of the ith optical mode and u_{jn} is the nth component of the acoustic displacement profile (where n may be x, y or z) of the phase matched j^{th} acoustic mode. The SBS gain is directly related to this overlap integral through the elasto-optic coefficient, p_{12}.

The frequency and the intensity of the backward flow of the pump signal, termed the Stokes wave, depends essentially on the phase and momentum matching and the overlap between, respectively, the acoustic and optical waves. This phenomenon is further stimulated when interference occurs between the Stokes wave and the laser signal and this strengthens the acoustic wave through electrostriction. Since the scattered light undergoes a Doppler frequency shift, the SBS frequency, f_{SBS}, depends on the acoustic velocity and this can be calculated [Agrawal, Book, 2013 and Nikles, 1997] from,

$$f_{SBS} = \frac{2n_{eff}V}{\lambda_o} \tag{5.6}$$

here, V is the acoustic velocity, λ_o is optical wavelength and n_{eff} is the effective index of the optical mode.

The dominant H_Y field profile of the quasi-TE mode has similar profile to that of the dominant U_X, U_Y and U_Z vector fields of the fundamental U_{11}^X, U_{11}^Y and U_{11}^Z acoustic modes, respectively. The normalized amplitude variations of these profiles along x-axis for W = 6 μm, H = 3 μm, λ_o = 1.55 μm and k = 11.75 μm^{-1} are shown in Fig. 5.20. The k value selected here is the required propagation constant of the acoustic modes phase matched to quasi-TE optical mode at λ_o = 1.55 μm. The U_X, U_Y and U_Z displacement vector profiles are almost identical and they were difficult to identify individually. The H_Y profile of the quasi-TE mode at λ_o = 1550 nm is also shown by a solid black line in Fig. 5.20, which spreads more into the cladding region, compared to the acoustic mode profiles for this specific case.

Next, the overlap between the fundamental longitudinal, U_{11}^Z acoustic mode and the H_{11}^Y optical mode is calculated when varying the waveguide width and this is shown in Fig. 5.21 by the dashed blue line. When the guide width increases, the overlap increases more prominently at the beginning then reaches near to its maximum overlap value, after which it increases slowly. The overlap found at 10 μm width was 94%.

As expected, the overlap of U_Z displacement vector of the U_{21}^Z mode (with odd profile) with the H_Y field of H_{11}^Y mode (with even profile) was calculated to be zero. Following this, the overlaps of the dominant H_{11}^Y optical field with the higher order longitudinal U_{31}^Z acoustic mode but with symmetric (or even) displacement profiles is also determined and the overlap variation with the width is shown by a solid (red) line in Fig. 5.21. With the increase in the guide width, as the mode profile becomes more confined, the overlap decreases. It can be noted that, for this mode, the maximum overlap was found to be near 2.5%, at the lower guide width.
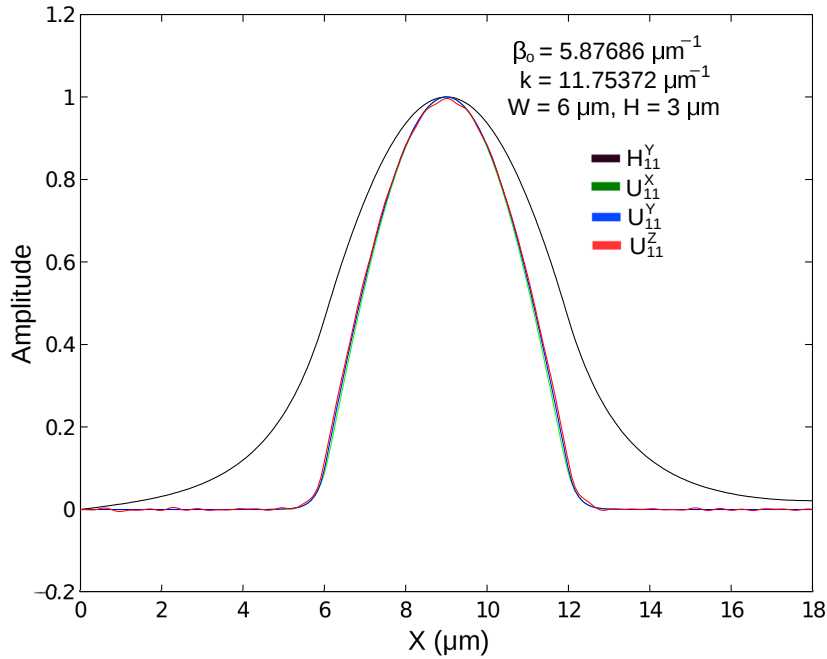
Fig. 5.20 Normalized field and displacement vector profiles along the *x*-axis.
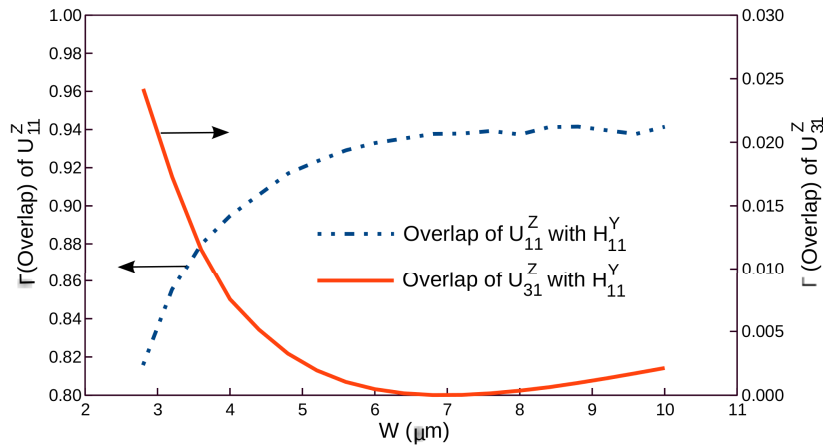
Fig. 5.21 Overlap of H_Y field of the H_{11}^Y mode with the U_Z displacement vector of the U_{11}^Z and U_{31}^Z modes with W.

After determining the propagation constant, β_o, of the interacting H_{11}^Y mode, the propagation constant of the acoustic mode can be found using Eq. (5.4). The corresponding phase velocity, *v*, of the acoustic mode can then be determined and thus Eq. (5.6) can yield the SBS frequency. In Fig. 5.22, the SBS frequency shifts with the guide width for the fundamental longitudinal acoustic mode, U_{11}^Z, and the third order longitudinal, U_{31}^Z mode are shown by a solid red and a dashed blue lines, respectively. Here the dashed blue line falls with the increasing guide width, whereas the solid red line reaches its minimum near the 4

μm width and rises again with the increase of width, although this variation is, very small, when compared to the variation for the higher order longitudinal U_{31}^Z mode.
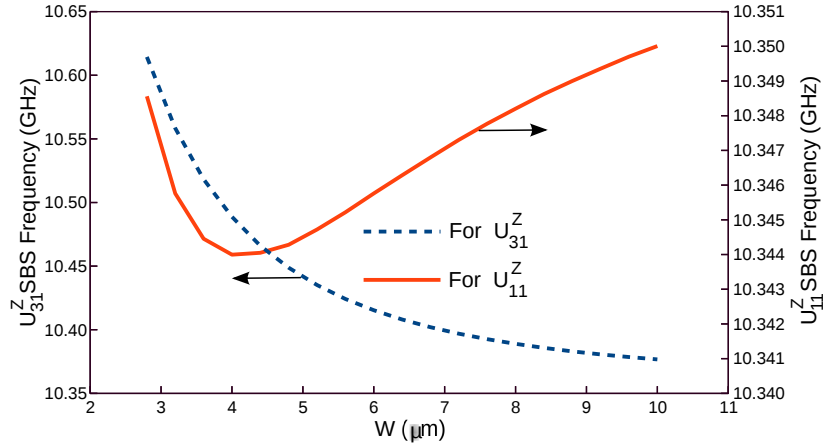
Fig. 5.22 SBS frequency shifts for the U_{11}^Z and U_{31}^Z modes with waveguide width.

The axial displacement of the material for the longitudinal mode causes a z-dependent density variation which produces an optical grating and influences the propagation of optical modes. Alternatively, if the transverse movement of materials is constant then it can cause bending of the guide. However, as the material displacement in the transverse plane is not constant, as shown in Fig. 5.1(a), this would also cause a density variation along the transverse plane. This would create a refractive index gradient with an axial periodicity related to its wavelength and this may also interact with the optical modes. As the field profiles of both the dominating fields of the acoustic shear modes are similar to the H_Y field profile of the H_{11}^Y mode, their overlap was found to be quite high. Such overlaps can be calculated by using the normalized form of Eq. (5.5) and shown in Fig. 5.23. It can be observed from this figure that the overlap of the U_X field profile of dominant fundamental acoustic shear mode U_{11}^X with the H_Y field profile of quasi-TE mode becomes higher when the guide width is wider. At a larger guide width, the U_X field profile of U_{11}^X becomes more elongated and this profile becomes closer in shape to the optical profile. Furthermore, it can be noted that the change of the overlap between the U_Y displacement profile of the U_{11}^Y mode and H_Y field profile with the guide width is slightly less than the overlap for the U_{11}^X mode as shown here and both of them are considerably lower than that of the U_{11}^Z mode, which was shown in Fig. 5.21.

Figure 5.24 shows the value of f_{SBS} for the both fundamental acoustic U_{11}^X and U_{11}^Y shear modes. The SBS frequency shift for the U_{11}^X mode shown by a dashed blue line in Fig. 5.24 is slightly lower than the SBS frequency shift denoted by red solid line for the U_{11}^Y mode. When the width increases from 2.8 μm to 10 μm, its optical effective index increases by 0.266%,
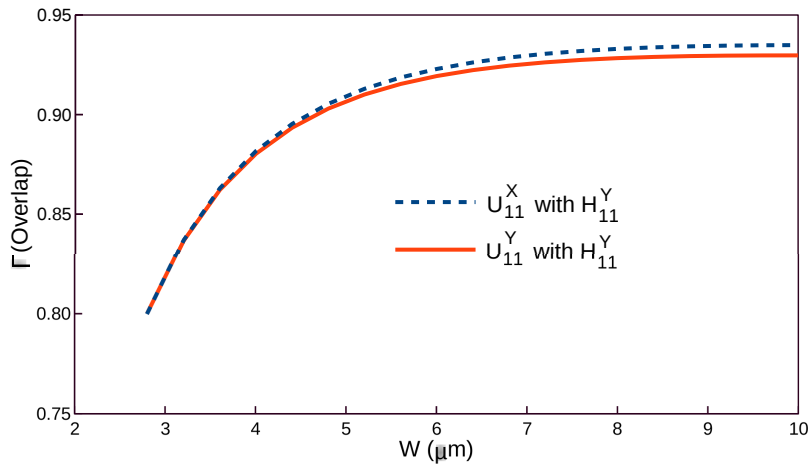
Fig. 5.23 Variations of the H_Y field overlap of the H_{11}^Y mode with the U_{11}^X and U_{11}^Y modes with the width.

while its phase matched acoustic velocity reduces by 0.337%. However, as the dispersion curves are not linear, this yield a minimum SBS frequency shift between 4-5 μm. In general, the total ranges of variation of the values of f_{SBS} for both the fundamental shear modes are quite small (as the numerical values of the changes are only seen in the third digit after the decimal point).
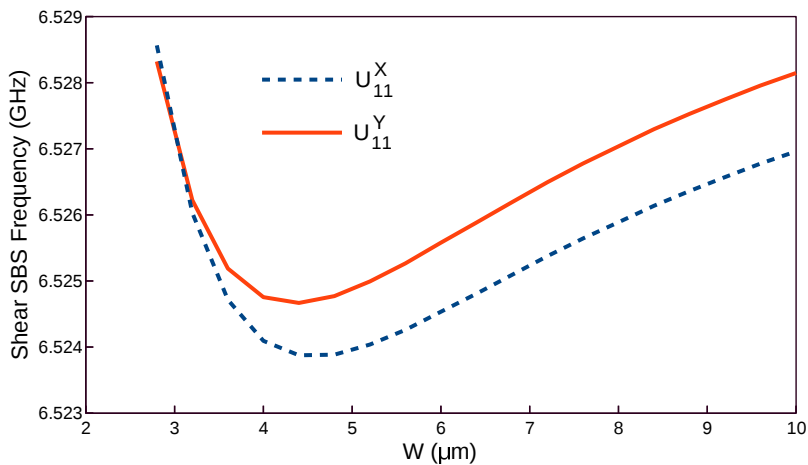
Fig. 5.24 Shear SBS Frequency shift with guide width.

For further investigation of the reason of curvature of the SBS frequency shift curve of both the shear acoustic modes three points on the SBS frequency shift curve of U_{11}^X at three different values of width were chosen and shown in Fig. 5.25. These three points are identified with small red circles and the corresponding acoustic propagation constants were determined as $k_1 = 11.7327$ μm^{-1}, $k_2 = 11.7441$ μm^{-1} and $k_3 = 11.764$ μm^{-1}, respectively.
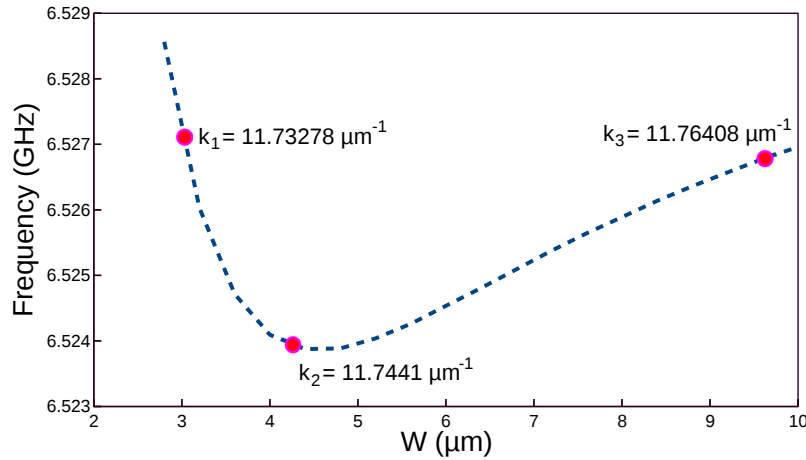
Fig. 5.25 Considered k at three places on SBS Frequency shift for U_{11}^X with guide width.

At these three propagation constants (k_1, k_2 and k_3), the variations of acoustic frequencies with guide width were determined for U_{11}^X mode and shown in Fig. 5.26. It can be noted that the solid blue line represents the frequency variation with the width for constant k_1 and it lies at bottom for the full range of the width, as it is less than both k_2 and k_3. Figure 5.26 indicates that for any constant k acoustic frequency decreases with increasing guide width.
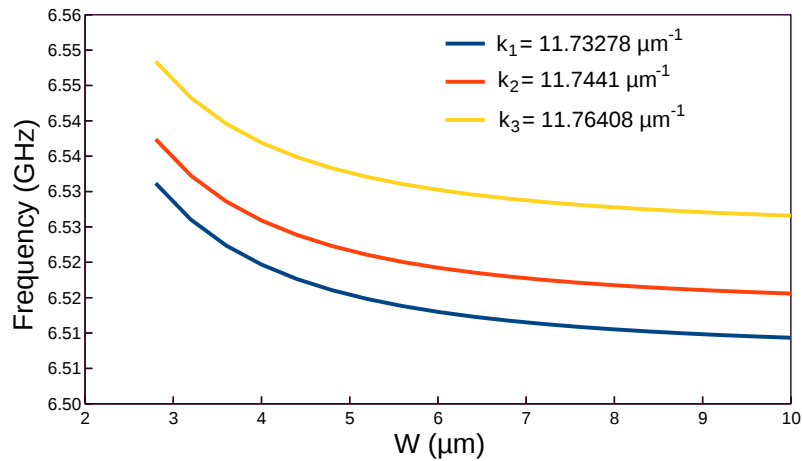
Fig. 5.26 Considered k at three places on SBS Frequency shift for U_{11}^X with guide width.

It can be noted that for any existing optical mode, when the guide width (W) increases the optical propagation constant (β_o) also increases, Fig. 5.17 would provide an idea about it following Eq. (5.1). As β_o increases, to maintain the phase matching, the acoustic propagation constant (k) also increases according to Eq. (5.4). Moreover, for any given waveguide the acoustic frequency increases with the increase of k. However, as the width also increases, due to these cumulative variations the result is the profile of the SBS frequency

with the width which was shown in Fig. 5.24. The SBS frequencies shown here are lower compared to those for the longitudinal modes, shown in Fig. 5.21, as the shear velocity of the doped SiO_2 was lower than that of the longitudinal velocity in the same material.

As the dominant H_Y field profile of the H_{11}^Y mode and the dominant displacement profiles of the fundamental acoustic modes are similar, their overlaps would be significant, as shown in Fig. 5.23. On the other hand, the overlap of this H_Y field profile of the quasi-TE mode with the non-dominant displacement vector profiles of the fundamental acoustic longitudinal and shear modes, which have odd symmetry, will cancel out and the resulting acousto-optical interactions would be negligible. However, it is expected that the maximum overlap of the H_Y field profile with the dominant U_X profile of the U_{31}^X mode will be small, and this was observed to be around 3.5%, shown in Fig. 5.27.
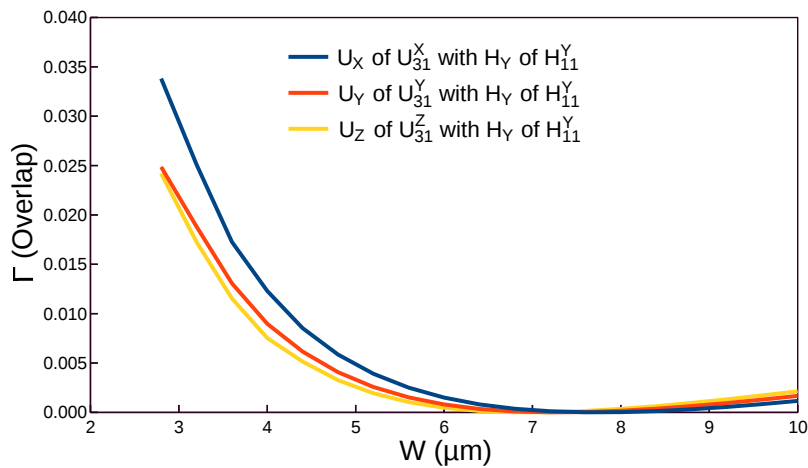
Fig. 5.27 Variations of overlaps of H_{11}^Y with the U_{31}^X, U_{31}^Y and U_{31}^Z modes with varying guide width.

SBS frequency shift for the shear and longitudinal third order U_{31}^X, U_{31}^Y and U_{31}^Z modes with varying guide width are shown in Fig. 5.28. Although the SBS frequency shift for the U_{31}^Z mode was shown in Fig. 5.22, it is again shown here for better comparison. It can be noted that the SBS frequencies for these third order modes gradually reduces with the increasing guide width and at $W = 6\ \mu m$ the SBS frequencies for U_{31}^X, U_{31}^Y modes were calculated as 6.5708 GHz and 6.5705 GHz, respectively.

However, it should be noted that although the overlap of U_X profile of the U_{21}^X mode with the optical field is zero as the former has odd symmetry, however the non-dominant U_Z profile of this mode may have a considerable overlap, as this displacement vector profile has an even symmetry. The variations of the overlap of U_Z field profile of U_{21}^X mode with the width is shown in Fig. 5.29 by a red solid line, where it increases along with the guide width. It is observed that the non-dominant U_Z field profile of U_{21}^X mode has a near 20% overlap
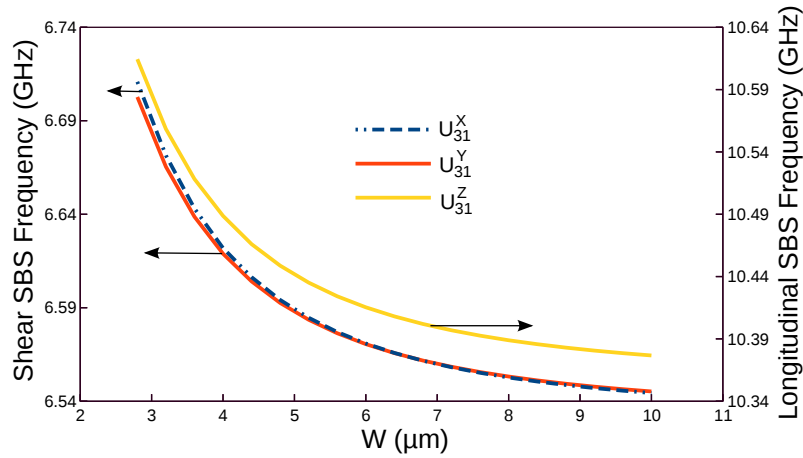
Fig. 5.28 SBS frequency shift for the U_{31}^X, U_{31}^Y and U_{31}^Z modes with varying guide width.

with the dominant profile of the quasi-TE mode and this is much higher than the overlap of the dominant displacement vector of the higher order mode. The SBS frequency shift for this shear mode is shown by the blue line, and this drops with the increasing width. Previously it was also observed, in Fig. 5.22, that for the U_{31}^Z longitudinal mode the value of f_{SBS} also reduces with the width, but had higher values as its longitudinal and shear velocities were higher.
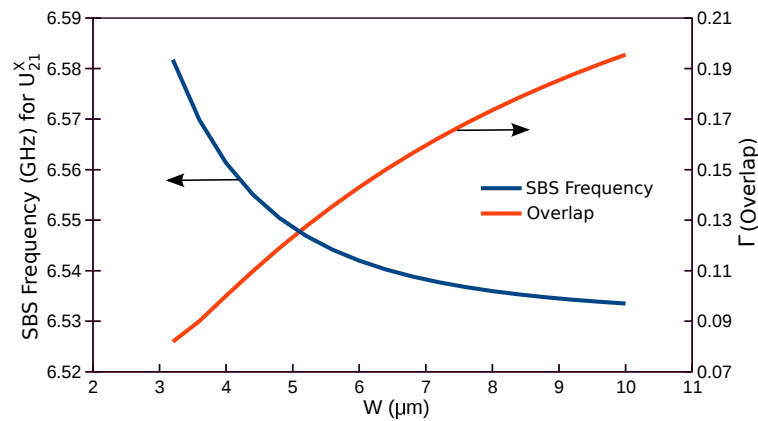
Fig. 5.29 SBS frequency and overlap for the U_Z component of the U_{21}^X mode with varying guide width.

Before calculation of the Brillouin gain coefficients, it is important to have the values of some parameters for 10% Ge-doped silica waveguide to be established. Among those, $\triangle v_B$, the Brillouin gain linewidth, which is related to the lifetime (T_B) of phonon, i.e. the quanta of acoustic vibration, in the material. It is the full-width at half-maximum (FWHM) of the

Lorentzian gain profile [Dasgupta, 2011]. This spectral width can be related to the damping time of acoustic wave by [Ogusu, 2004] $\triangle v_B = \frac{1}{\pi T_B}$. For 10% Ge-doped silica the acoustic wave damping time can be determined by [Koyamada, 2004],

$$T_B = \frac{10^{-6}}{2\pi \left(17.5 + 0.71 \times w\%\right)} \tag{5.7}$$

For $w = 10$, which is the doping concentration in percentage, the phonon decay time can be calculated as $T_B = 6.469~ns$ and that provides $\triangle v_B = 49.205~MHz$. For a given structure, it is a common practice to assume that $\triangle v_B$ to be equal for all acoustic modes and is often assumed to be around 30-50 MHz for all silica based fibers [Dasgupta, 2011]. The value 49.205 MHz is used as the Brillouin gain linewidth for all acoustic modes for this structure.

The another important parameter is p_{12}, the elasto-optic coefficient. Its value for 3.6% Ge-doped silica with refractive index, $n = 1.4492$, was considered to be 0.27 [Beugnot, 2012] for optical wavelength $\lambda_o = 1550~nm$. For silica, the value of $p_{12} = 0.286$ [Eggleton, 2013]. It is well known that for binary SiO_2 - GeO_2 glass the refractive index has a nearly linear relationship with its molar composition. It was also reported [Dragic, 2013] that for aluminosilicate optical fiber p_{12} shows a linear relation with the concentration of alumina in silica, which is shown in Fig. 5.30.
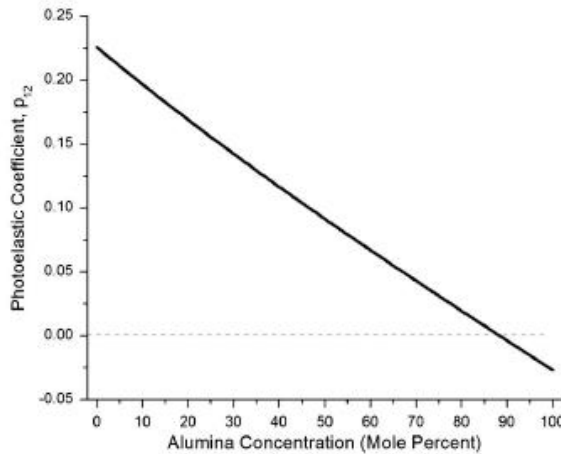
Fig. 5.30 Photoelastic constant, p_{12}, as a function of alumina concentration in silica [Dragic, 2013].

Considering these, the value of elasto-optic coefficient for 10% Ge-doped silica can be calculated. From the un-doped and 3.6% Ge-doped silica with the p_{12} values of 0.286 and 0.27, respectively, the value of photoelastic coefficient, p_{12}, for 10% Ge-doped silica can be extrapolated as 0.2416, which is shown in Fig. 5.31.
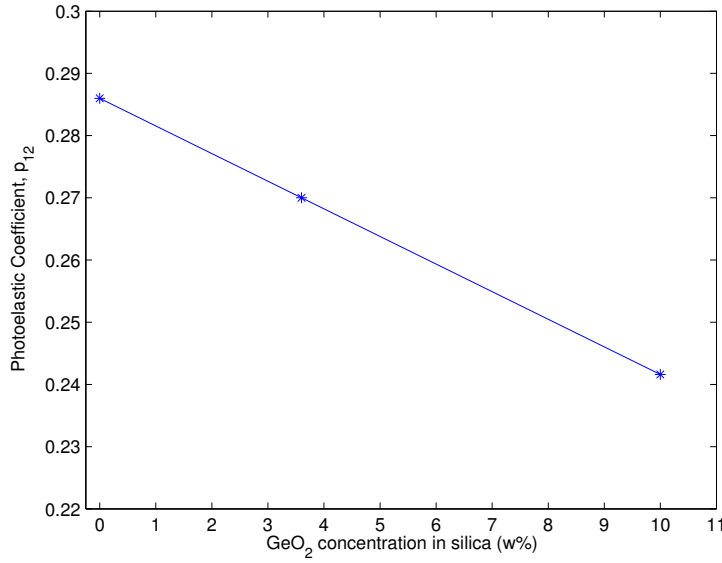
Fig. 5.31 Photoelastic constant, p_{12}, as a function of GeO_2 concentration in silica.

The peak Brillouin gain, g_B, can be calculated according to [Eggleton, 2013]:

$$g_B = \Gamma \frac{4\pi n^8 p_{12}^2}{\lambda_o^3 c\rho f_{SBS} \triangle v_B} \tag{5.8}$$

here, Γ is acousto-optical overlap, n is refractive index of the core, p_{12} is elasto-optic coefficient, λ_o is wavelength of the pump, ρ is density of silica, f_{SBS} is Brillouin frequency shift, c is speed of light at free space and $\triangle v_B$ is Brillouin gain linewidth.

At the phase matched condition Γ and f_{SBS} can be calculated from Eqs. (5.5) and (5.6), respectively as shown earlier. Subsequently using Eq. (5.8), the Brillouin gain coefficient for the 10% Ge-doped silica waveguide can also be calculated for fundamental and higher order acoustic waves. Among the fundamental and higher order acoustic shear and longitudinal modes, which have considerable contributions in Brillouin gain spectrum are only considered here. Other acoustic modes for being odd symmetric will either cancel out or may have negligible gain.

At the phase matched condition the value of the acoustic propagation constant can be calculated as $k = 11.7537\ \mu m^{-1}$ using Eg. (5.4). The overlap of U_Z component of the acoustic longitudinal U_{11}^Z mode with the H_Y field vector of quasi-TE, H_{11}^Y, mode was determined using Eq. (5.5) as 0.9329. It was the highest overlap calculated among all the overlaps with all other modes at this phase matched condition. The corresponding SBS frequency and

longitudinal phase velocity were calculated as $f_{SBS} = 10.3457\ GHz$ and $V = 5530.53\ m/s$, respectively. Using Eq. (5.8) the Brillouin gain peak for U_{11}^{Z} mode was found as $1.0554 \times 10^{-11}\ m/W$.

At phase matched condition the SBS frequency and shear phase velocity for the U_{11}^{X} mode were found as $f_{SBS} = 6.5245\ GHz$ and $V = 3487.81\ m/s$, respectively. The overlap between the dominating U_X component of the acoustic U_{11}^{X} mode with the H_Y field vector of quasi-TE, H_{11}^{Y}, mode was found as 0.9228 and the contributed Brillouin gain was calculated as $1.6554 \times 10^{-11}\ m/W$, which is higher than that of the U_{11}^{Z} mode, as the acoustic frequency of U_{11}^{Z} being higher resulted in lower Brillouin gain peak, following the Eq. (5.8).

The overlap of U_Y component of the acoustic U_{11}^{Y} mode with the H_Y field vector of quasi-TE, H_{11}^{Y}, mode was found as 0.9193 at $f_{SBS} = 6.5255\ GHz$ with a shear phase velocity of $V = 3488.37\ m/s$. The Brillouin gain peak contributed by this component was calculated as $1.6487 \times 10^{-11}\ m/W$.

Table 5.2 provides the overlaps, Brillouin gain coefficients, SBS frequencies and corresponding acoustic velocities of the shear and longitudinal acoustic modes at $k = 11.7537$ μm^{-1}.

Table 5.2 Overlaps and Brillouin gain coefficients for shear and longitudinal fundamental and higher order acoustic modes.

Mode	Component	f_{SBS} (GHz)	V (m/s)	Overlap (Γ)	g_B (m/W)
U_{11}^{X}	U^X	6.5245	3487.8198	0.9228	1.6554×10^{-11}
U_{11}^{Y}	U^Y	6.5255	3488.3785	0.9193	1.6487×10^{-11}
U_{11}^{Z}	U^Z	10.3457	5530.5325	0.9329	1.0554×10^{-11}
U_{21}^{X}	U^Z	6.5419	3497.1469	0.143	2.5591×10^{-12}
U_{21}^{Z}	U^X	10.3719	5544.5186	0.1459	1.6463×10^{-12}
U_{31}^{X}	U^X	6.5708	3512.5854	0.0014	2.6690×10^{-14}
U_{31}^{Y}	U^Y	6.5705	3512.3999	0.0008	1.4065×10^{-14}
U_{31}^{Z}	U^Z	10.4153	5567.7168	0.0004	5.3017×10^{-15}

The Brillouin gain spectrum (BGS) for 10% Ge-dopoed silica will now be determined considering the gain spectra due to various acoustic modes are statistically independent [Dasgupta, 2011]. The frequency dependent Brillouin gain, $g_B(f)$, has a Lorentzian spectral profile and can be given as [Nikles, 1997]:

$$g_B(f) = g_B \frac{(\triangle v_B/2)^2}{(f - f_{SBS})^2 + (\triangle v_B/2)^2} \tag{5.9}$$

where, g_B is the Brillouin gain peak, f_{SBS} is Brillouin frequency shift, and $\triangle v_B$ is Brillouin gain linewidth.

The BGS for the 10% Ge-doped silica waveguide in between 6 to 10.5 GHz is shown in Fig. 5.32. There are two significant peaks observed, the first peak is due to the contribution of U_{11}^X, U_{11}^Y modes, and the second peak caused by U_{11}^Z and U_{21}^Z modes. Due to comparatively larger value of linewidth the peaks of two shear fundamental components are not distinguishable.
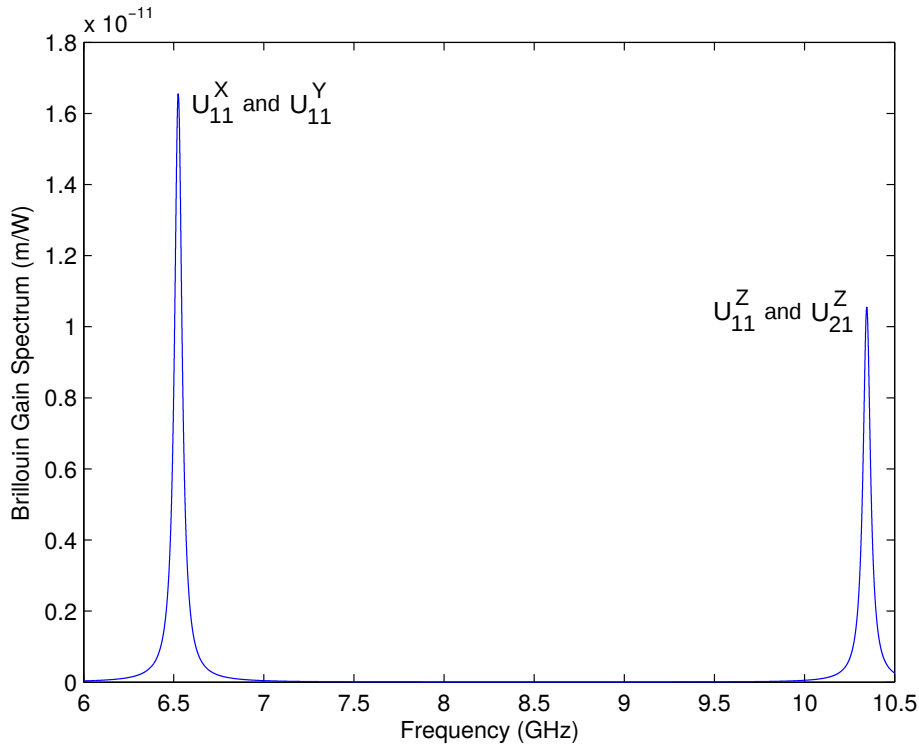
Fig. 5.32 Brillouin gain spectrum of 10% Ge-doped silica waveguide between 6 *GHz* to 10.5 *GHz*.

5.7   Summary

Modal solutions of the fundamental and higher order longitudinal and shear acoustic modes of a 10% Ge-doped planar silica waveguide are presented in this chapter. These are obtained by

using a full-vectorial finite element method. The dominant and non-dominant displacement vector profiles of both the shear and longitudinal acoustic modes are presented. Here existing symmetries of the waveguide have been exploited, not only to improve the solution accuracy but also to avoid degeneration of some of these modes. An **H**-field based full-vectorial program has also been used to find the optical modes of this waveguide.

Subsequently, as the same finite element mesh topology is used for both the acoustic and optical modal solutions, the overlap between the acoustic and optical modes were obtained accurately and more efficiently. Variations of the f_{SBS} and overlaps are shown for the fundamental and higher order longitudinal and shear acoustic modes with the fundamental quasi-TE optical mode.

It was observed that all the acoustic modes are hybrid in nature with all the three components of the displacement vectors being present. It was also shown that the non-dominant displacement vectors have smaller magnitudes but also have higher order spatial variations. Further, it was observed that for the fundamental acoustic modes (for both longitudinal and shear modes) the overlap of the non-dominant displacement vectors (being anti-symmetric) with the dominant H_Y profile (of the fundamental quasi-TE mode) is zero.

It was also shown that the non-dominant displacement vector of higher order acoustic modes can have a symmetric profile and also a considerably higher overlap with the optical mode. Although the overlap of the dominant displacement vector of a mode with odd spatial variations was zero with the fundamental quasi-TE mode, but the overlap of its non-dominant displacement vector was significantly high and cannot be ignored. Shown here that the overlap of U_Z component for the U_{21}^X is higher than the overlap of U_Z component for the U_{31}^X.

Also Brillouin gain coefficients of shear U_{11}^X, U_{11}^Y, U_{21}^X, U_{31}^X, U_{31}^Y modes and longitudinal U_{11}^Z, U_{21}^Z, U_{31}^Z modes were calculated and presented. Along with these the Brillouin gain spectrum from 6 *GHz* to 10.5 *GHz* is provided, which shows significant two peaks around 6.5245 *GHz* and 10.3457 *GHz*.

A rigorous study of light-sound interactions in optical waveguide can be useful in the development of novel SBS sensors or in the design of optical waveguide to deliver high power. Thus the results presented have shown that to study light-sound interaction in an effective way, the use of full-vectorial acoustic and optical modal approaches are necessary.

Chapter 6

High Index Contrast Air-clad Silica Waveguide

6.1 Introduction

Light-sound interactions in small optical waveguides are considerably complex. The fascinating dynamics of these interactions were realizable in some key areas of modern physics [Maldovan, 2013], which attracted interests of many researchers recently. Micro and nano-structured photonic crystal fibres (PCF) could be presented as examples, where tight confinement of both light and sound in subwavelength-scale lolid silica glass core provided new characteristics for Brillouin scattering, these are basically different from those of the standard optical fibres, which include generation of strongly localized multiple high-frequency hybrid acoustic shear and longitudinal modes with in the tiny core and five-fold increase in threshold power [Dainese, 2006]. Another example would be the concept of cavity or surface optomechanics [Matsko, 2009], which came in highlight after finding the strong light-sound coupling in optical micro-cavities and these could find applications in many temperature sensors.

Silica based subwavelength-diameter optical fibres are yet under utilized. Such hair-like slivers of silica glass can be fabricated by tapering optical fibres. Where the non-linear effects are enhanced and can find the implications in some areas of sensing where bulky optical fibres are not that much suitable [Beugnot, 2014, Oct.]. Brillouin scattering in such small optical waveguides were remain unexplored until recently [Beugnot, 2014, Oct.]. In that work, the authors presented numerical results incorporating elastodynamics based on electrostrictive stress on Brillouin scattering in photonic silica microwires (diameter varies from 1 μm to 1.35 μm), which showed well conformity with the experimental results as well.

Moreover they claimed first to report the surface acoustic wave Brillouin scattering (SAWBS) in the backward direction, where the pump wavelength was $\lambda_o = 1550$ *nm* and showed that silica photonic microwires reveals many widely spaced Brillouin frequencies (in the range of near 6 *GHz* to 10 *GHz*) which are from hybrid shear and longitudinal waves, as observed in small-core photonic crystal fibres (PCFs) [Dainese, 2006].

The same group earlier reported [Laude, 2013] elastic energy spectrum of the range 1 *GHz* to 45 *GHz* for both forward and backward Brillouin scattering in 1.5 $\mu m \times 1$ μm dimension of silica and silicon waveguides separately. Although they presented some selected acoustic mode profiles, but did not highlight Brillouin gain spectrum at all.

In this chapter, details mode evolution of highly hybrid surface acoustic wave, shear and longitudinal waves in a 1.5 $\mu m \times 1$ μm air cladded silica strip optical waveguide is presented. Along with this, the variation of Brillouin gain coefficient with guide width for each of these waves and Brillouin gain spectrum from 5 *GHz* to 10 *GHz* for this optical waveguide is presented.

6.2 Waveguide and acoustic properties

A silica strip waveguide having rectangular cross-section with width 1.5 μm and height 1 μm was chosen to ensure the guidance of single optical mode at a wavelength of 1.55 μm. Figure 6.1 shows the optical waveguide.
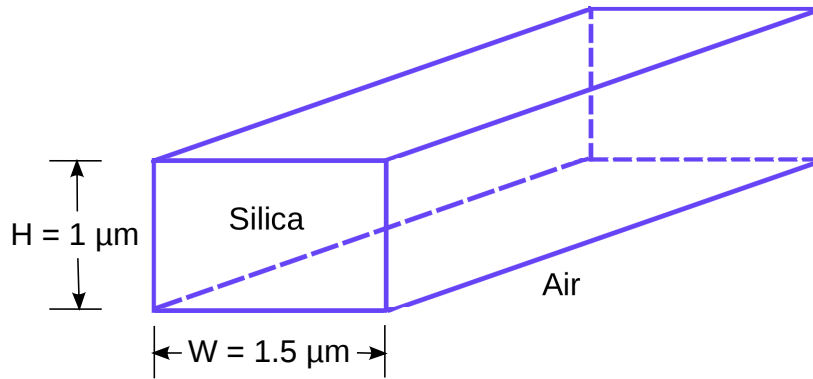
Fig. 6.1 An air cladded silica optical waveguide.

This strip waveguide surrounded by air also confines acoustic waves. In this chapter, acoustic longitudinal and shear wave velocities and density of core are taken as $V_{LG} = 5970$ m/s, $V_{SG} = 3760$ m/s and $\rho_G = 2201$ kg/m^3, respectively [Littler, 2006]. Since air does not support any shear wave, for the air cladding, its longitudinal velocity and density are considered to be $V_{LC} = 340$ m/s and $\rho_C = 1.29$ kg/m^3, respectively [Jiang, 2011]. For this

waveguide a two-fold symmetry is available, which has been exploited here to obtain better accuracy for their modal solutions for a given computer resource.

Table 6.1 presents the list of these acoustic properties used along with the calculated elastic coefficients for silica and air.

Table 6.1 Material properties of the air cladded silica waveguide

Material	Velocity (m/s)		Density (kg/m^3)	Elastic Coefficient (GPa)		
	V_L	V_S	ρ	C_{11}	C_{12}	C_{44}
Silica	5970	3760	2201	78.4456	16.2119	31.1169
Air	340	0.0	1.29	149.124×10^{-6}	149.124×10^{-6}	0.0

6.3 H_{11}^Y: Fundamental quasi-TE optical mode

Modal solutions of the optical waves in this air-clad strip silica waveguide, at a wavelength $\lambda_o = 1550$ nm, are obtained by using a full-vectorial **H**-field formulation [Rahman, 1985]. Here refractive indices of core and cladding are taken as 1.444 and 1.0, respectively, which represent a high index contrast optical waveguide. Both quasi-TE and quasi-TM modes can exist in this waveguide, but they have similar propagation constants and the profiles of their dominant **H**-fields are also similar. In this chapter the interaction of the shear and highly hybrid acoustic modes with the fundamental quasi-TE, H_{11}^Y mode are studied. The H_X, H_Y and H_Z vector field profiles of the quasi-TE optical mode, after exploiting two-fold symmetry of this waveguide, are presented in Fig. 6.2. The black lines indicates the interfaces between the air and silica. The non-dominant H_X vector quarter field profile is shown in Fig. 6.2(a). It clearly shows that H_X field is near the corner with a peak height of 0.12. This suggests there will be four peak in the full waveguide. Another non-dominant vector H_Z quarter field profile is shown in Fig. 6.2(c), where half of the upper horizontal interface profile with a peak value of 0.7 is shown. The dominant magnetic H_Y quarter field vector profile, which originally exhibits a Gaussian shape with maximum field strength at the centre of the core, is shown in Fig. 6.2(b). Its peak magnitude was calculated as close to 2.

The variations of the effective index (n_{eff}) and effective area (A_{eff}) of the fundamental H_{11}^Y mode with the guide width (W) are presented in Fig. 6.3 by a solid blue and a dashed red lines, respectively.

As the waveguide width (W) reduces, keeping the height constant ($H = 1 \ \mu m$), initially, the effective area A_{eff} reduces and reaches its minimum value of 1.025 μm^2 at $W = 0.9$

(a)

(b)

(c)
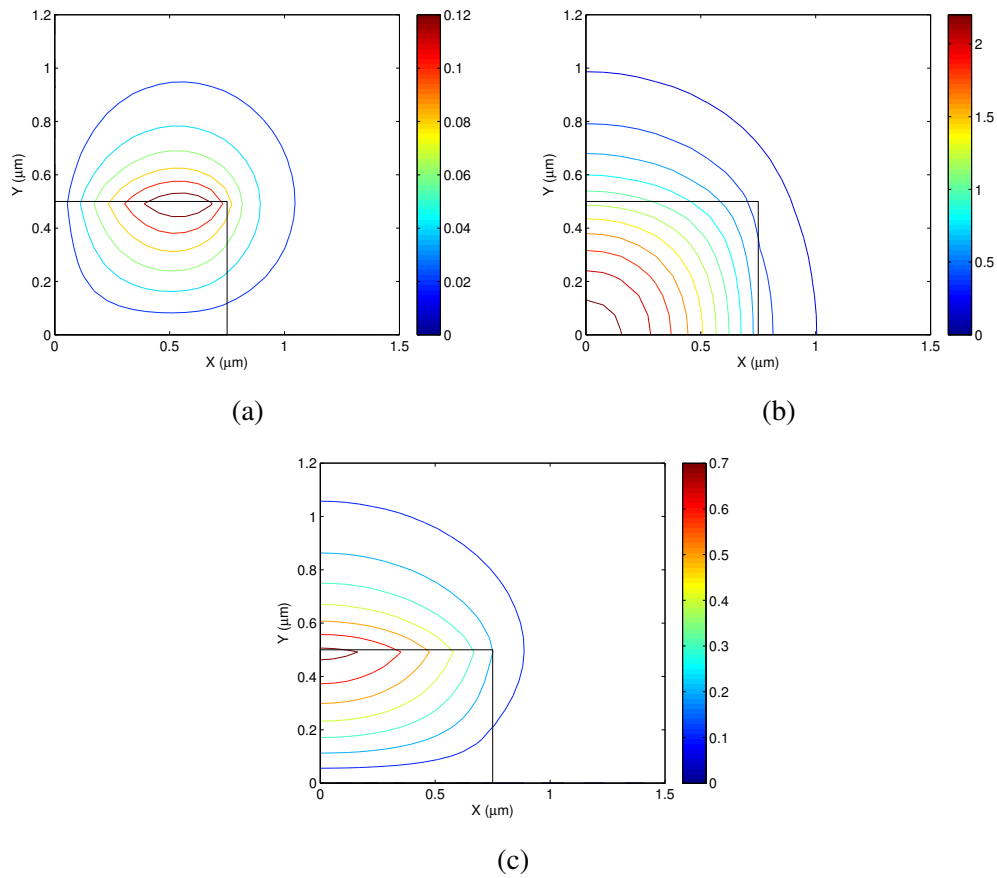
Fig. 6.2 H_X, H_Y and H_Z field profiles of the fundamental quasi-TE optical mode (only the quarter of the waveguide is shown).
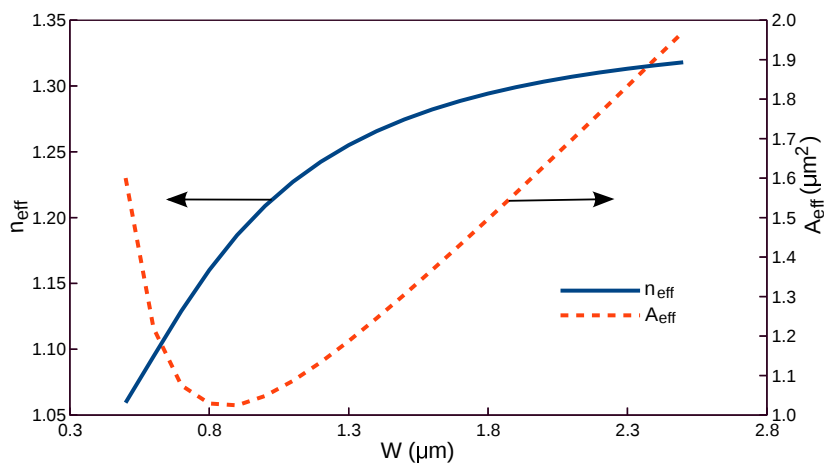
Fig. 6.3 Variation of effective index and effective area of the H_Y field profile of quasi-TE optical mode with width, W.

μm. When W is further reduced, its effective area increases rapidly as the optical mode approaches its effective cut-off condition. On the other hand, when the guide width reduces, n_{eff} gradually falls from the refractive index of the core, to the cladding refractive index value. Below a width of 0.9 μm, the optical mode spreads out before reaching its effective cut-off.

After observing the variation of effective area with width in Fig. 6.3, it is obvious that with the waveguide width the optical H_Y field vector profile of the quasi-TE H_{11}^Y mode varies. With the width, W, the variations of the spotsizes along the x and y directions are shown in Fig. 6.4, where the guide height is kept constant at H = 1 μm. Along the x and y-axes where the optical field vector profile is approximately equal to or higher than the $1/e$ times of the maximum value of a given optical field, that distance is considered as a measurement of the spotsize. The spotsize, σ_{OX}, denoted by a dot-dash blue line in Fig. 6.4. It is found to decrease as the width is decreased but near the cut-off this value start increasing as the mode profile spreads out. The minimum spotsize value for it was measured as 1.5 μm at the guide width of 0.9 μm. Whereas, along the y-axis, the spotsize σ_{OY}, remains almost constant with the decreasing guide width at a magnitude of 1.7714 μm. Below the guide width of 1.1 μm it starts to increase very slowly. This is due to the spreads out of the profile near cutoff.
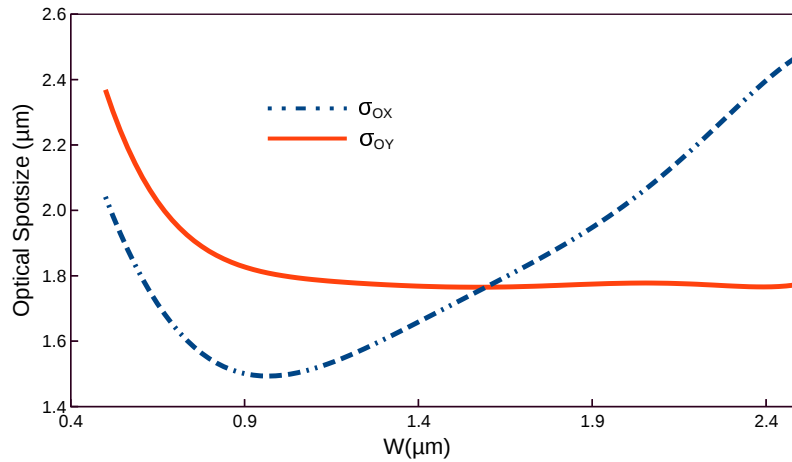
Fig. 6.4 Variations of spotsizes with width for H_{11}^Y mode in air caldded silica strip waveguide.

6.4 Highly hybrid acoustic modes and their evolutions

As stated earlier, acoustic modes in waveguide with two-dimensional confinement are hybrid in nature. However, the modal hybridness of the acoustic modes found in the high-index contrast air-clad silica strip waveguide is much higher than that of the acoustic modes in

embedded Ge-doped silica waveguide, discussed earlier in Chapter 5. The acoustic modes of this guide are difficult to categorize as pure shear or longitudinal modes. The quasi-shear and quasi-longitudinal modes may have dominant transverse or longitudinal displacements but also have displacements in other directions. This is because the air cladding acoustic velocity is much less than the corresponding core velocities.

6.4.1   Quasi-shear acoustic U_{mn}^X and U_{mn}^Y modes

The dispersion curves of acoustic U_{mn}^X modes are shown in Fig. 6.5, they mainly have U_X dominant components. On wards these modes are termed as quasi-shear acoustic modes. For such quasi-shear acoustic modes the variations of the phase velocities with the acoustic frequency are shown in Fig. 6.5. The phase velocities of the different quasi-shear modes gradually increase when the frequency is reduced. However, this change becomes rapid at a lower frequency, as the modes reach their cut-off conditions and their phase velocities approach the acoustic longitudinal velocity of the silica. It can be clearly observed that the cut-off frequency of a higher order mode appears at a higher frequency. The blue solid line in Fig. 6.5 represents the variation of the phase velocity of the fundamental shear U_{11}^X mode. The higher order shear modes U_{12}^X and U_{21}^X are distinct and are depicted by red and green solid lines, respectively. As the height (H) and width (W) of the guide were not equal, these modes were different. In case of $H = W$, it would be impossible to isolate these degenerate modes, as they would have the same modal solution, unless we exploit structural symmetry boundary conditions.
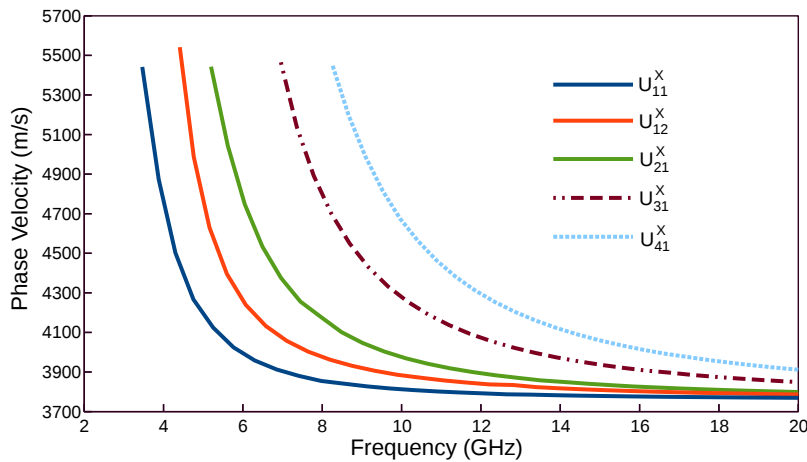
Fig. 6.5 Variation of the phase velocities with the acoustic frequencies for the fundamental and higher order acoustic quasi-shear modes.

The acoustic mode profile in a high index contrast silica waveguide is complex and this also transforms with the frequency. The displacement vector profiles of the fundamental acoustic quasi-shear mode, U_{11}^X, has quite different displacement distribution and their spatial variations along the x or y-directions inside the core. To illustrate it clearly, both the contour and coloured vector displacement profiles of U_X component of the fundamental quasi-shear U_{11}^X acoustic mode at 21 GHz are shown in Fig. 6.6.

(a)   (b)
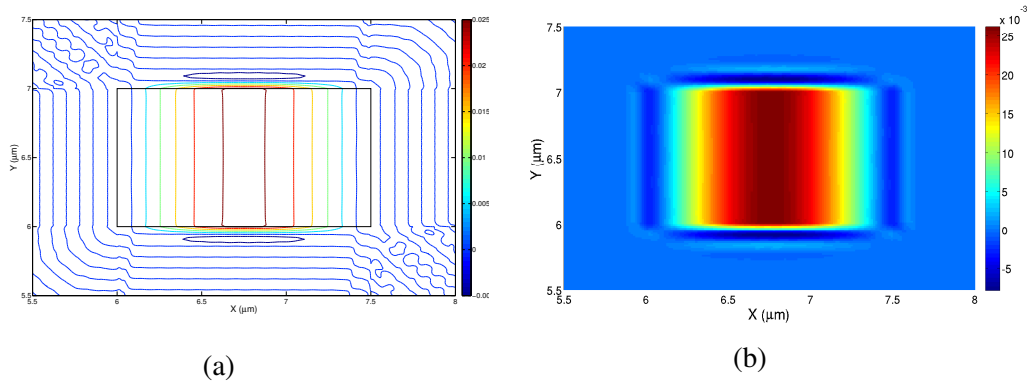
Fig. 6.6 (a) Contour and (b) coloured, vector displacement profiles of U_X component of the fundamental quasi-shear U_{11}^X acoustic mode at 21 GHz.

Its dominant component, U_X, has nearly Gaussian distribution along the x-axis, but with damped oscillations at the core-cladding interfaces. To illustrate this clearly, its variation along the x-direction is shown in Fig. 6.7(a). The damped oscillation, shown here, starts with a slightly deep displacement with sign opposite of the Gaussian peak. Along y-axis this displacement is nearly constant inside the core, reduced sharply at the upper and lower interfaces and similar damped oscillations at the interfaces were observed, which is shown in Fig. 6.7(b).

(a)   (b)
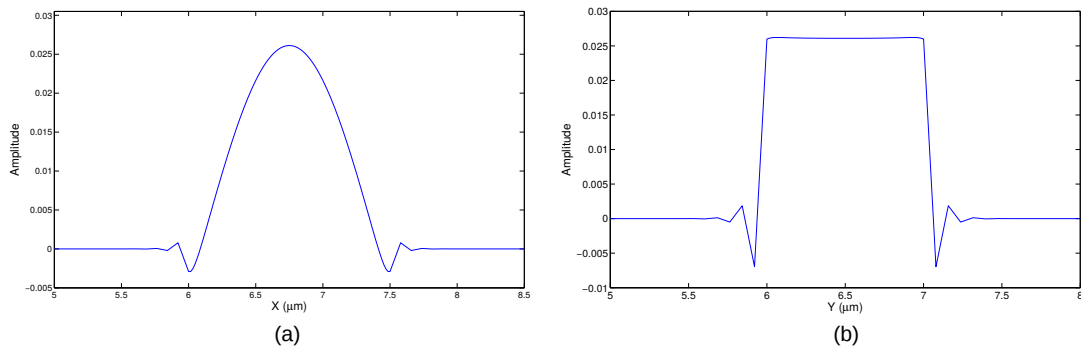
Fig. 6.7 Variations of the of U_X component of the fundamental quasi-shear acoustic U_{11}^X mode along (a) the x-axis and (b) the y-axis at 21 GHz.

At higher frequencies, this displacement at the interfaces are much more spreaded along the vertical boundaries. But, when the frequency starts to decrease, the magnitude of the damped oscillatory peaks start increasing and also start localizing near the left and right vertical interfaces inside the core, as shown in Fig. 6.8(a). Near 8 GHz frequency the positive and negative amplitudes of displacements along x-axis become almost equal and it is shown in Fig. 6.8(b).

(a)   (b)
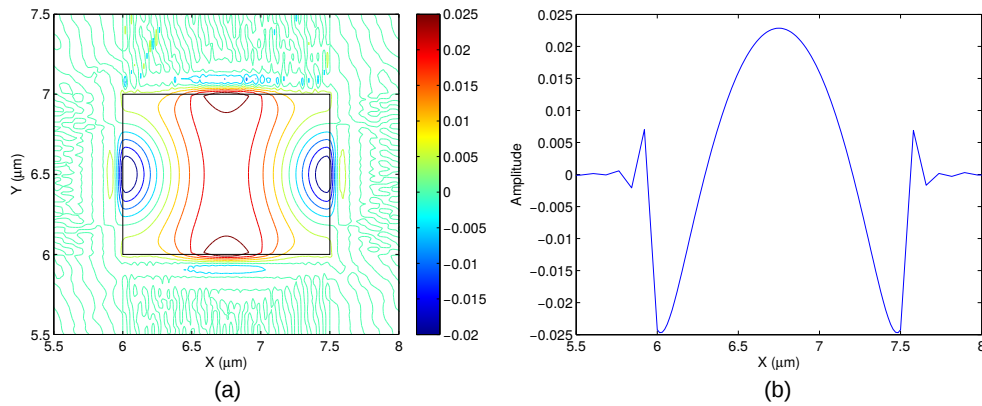
Fig. 6.8 (a) Vector displacement profile and (b) variations of amplitude along x-axis of U_X component of the fundamental quasi-shear acoustic mode U_{11}^X at 8 GHz.

Whereas, along y-axis, magnitude of the negative displacement reaches one-third of the positive peak and the earlier near flat peak, shown in Fig. 6.7(b), ends up with a sag of 12.5% of the peak amplitude at the center, as shown in Fig. 6.9.
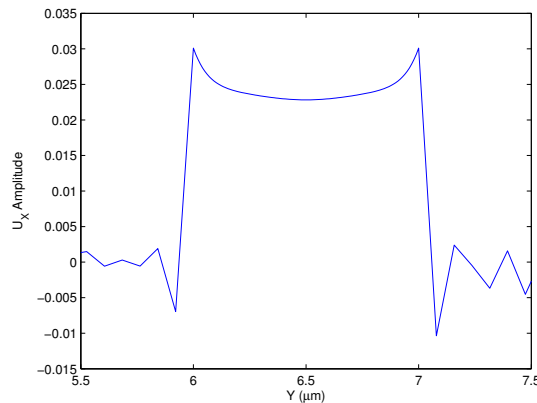
Fig. 6.9 Variations of amplitude along y-axis of U_X component of the fundamental quasi-shear acoustic mode U_{11}^X at 8 GHz.

The evolution of the fundamental acoustic quasi-shear mode, U_{11}^X, continues further down the frequency until it reaches its effective cutoff. Figure 6.10(a) shows the displacement

vector profile of the U_X component of the U_{11}^X mode near 4 GHz frequency. It can be observed that the displacement depth at the vertical interfaces decreased, spreaded again and localized at the corner of the interfaces, while it losses its sharpness, but still it maintains its Gaussian like peak, which is shown in Fig. 6.10(b). Along the y-axis, the sag at the center of the peak reduces further by 2% of the peak amplitude and forms a wavy shape, as shown in Fig. 6.10(c). It was observed that at the higher mesh density, in few cases, some noise was generated and speckle of noise patterns were present outside the core with the acoustics mode profiles, as can be seen in Figs. 6.8(a) and 6.10(a), respectively. In these cases, while plotting magnitude variation along y-direction, the natural damped oscillation of the acoustic vibration those were present beyond the core-cladding interfaces were overshadowed with these noise speckles and resulted in unequal damping patterns in right and left side of the displacement magnitude variation plots shown in Fig. 6.9 and Fig. 6.10(c).

(a)

(b)

(c)
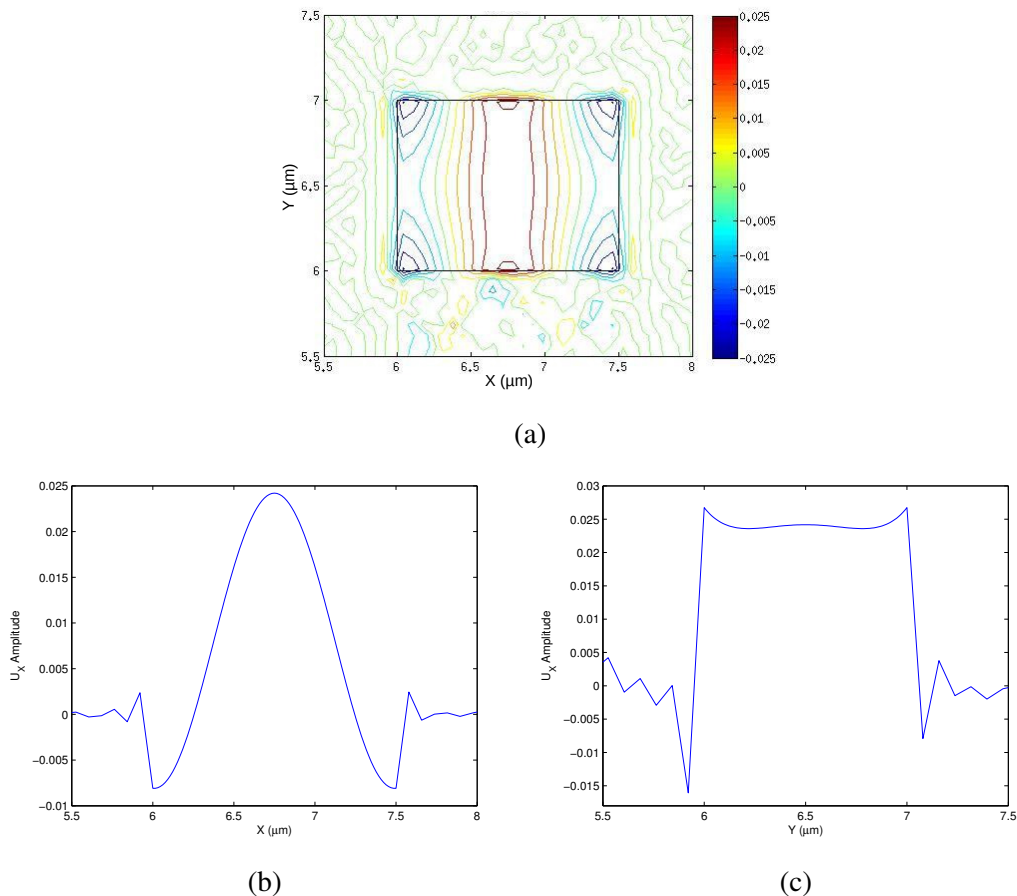
Fig. 6.10 (a) Vector displacement profile, variations of amplitude (b) along x-axis and (c) along y-axis of U_X component of the fundamental quasi-shear acoustic mode U_{11}^X at 4 GHz.

On the other hand, displacement profile of non-dominant U_Y component of the fundamental quasi-shear acoustic U_{11}^X mode shows multiple peaks at the upper and lower interfaces unlike that of the distribution profile observed in low index contrast Ge-doped silica waveguide, discussed Chapter 4. The displacement vector profile of U_Y component of the U_{11}^X mode at 21 GHz is shown in Fig. 6.11. Where eight peaks of half-sine spatial variations with consecutive maxima and minima are formed both in the upper and lower horizontal interfaces.
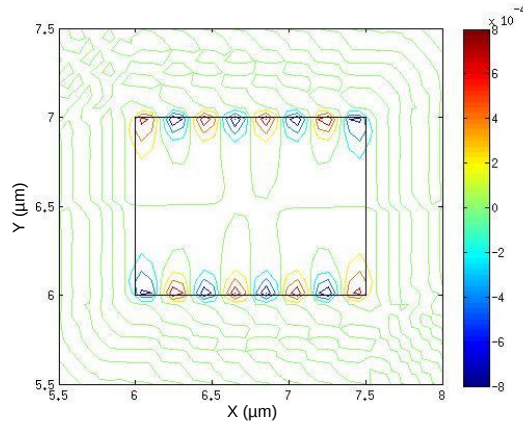
Fig. 6.11 Vector displacement profile of U_Y component of the fundamental quasi-shear acoustic mode U_{11}^X at 21 GHz.

The variations of amplitude of this U_Y component of the fundamental quasi-shear acoustic mode U_{11}^X along x-axis and y-axis are shown in Figs. 6.12(a) and 6.12(b), respectively. The positions of the lines were selected in the middle along x-axis and through the peaks along y-axis. Where the Fig. 6.12(a) reveals that there are significant amount of displacement present at the left and right vertical interfaces as well and at the core centre the displacement is near zero.

Figures 6.13(a) and 6.13(b) show the U_Y component vector displacement profiles of the U_{11}^X mode at 20 GHz and 10 GHz, respectively. The hybridness of the U_Y component with respect to the dominant U_X component was observed to be 0.032 at near 20 GHz, which increases with the decreasing frequency. It can be observed that at 20 GHz, the number of half-sine spatial variations at the upper and lower interfaces was 8 as shown in Fig. 6.13(a), but slightly increased in width comparing those shown in Fig. 6.11. When the frequency decreases this number reduces to 4 at 10 GHz, shown in Fig. 6.13(b), where the width of the half-sine peaks spreads more. These can be seen clearly in Fig. 6.14, where the variations of amplitude along y-axis of U_Y component of the U_{11}^X mode are shown at 20 GHz, in Fig. 6.14(a) and at 10 GHz, in Fig. 6.14(b).
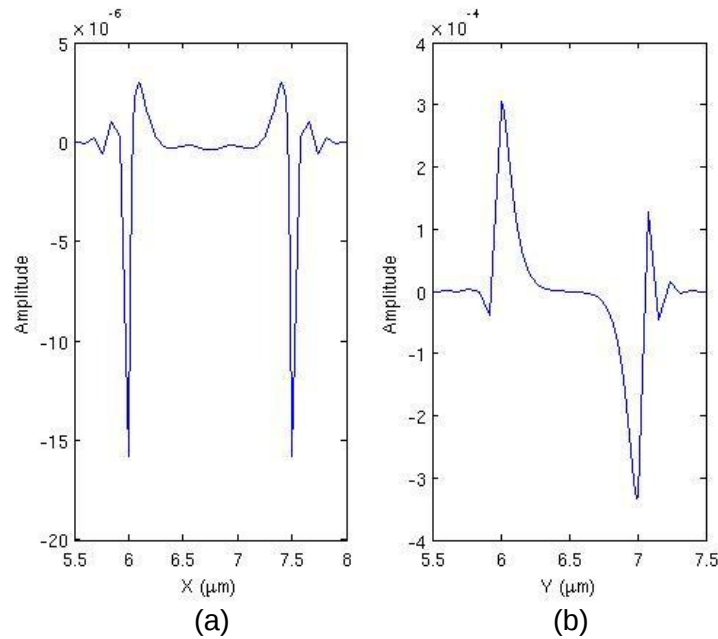
Fig. 6.12 Variations of amplitude (a) along *x*-axis and (b) along *y*-axis of U_Y component of the fundamental quasi-shear acoustic mode U_{11}^X at 21 *GHz*.
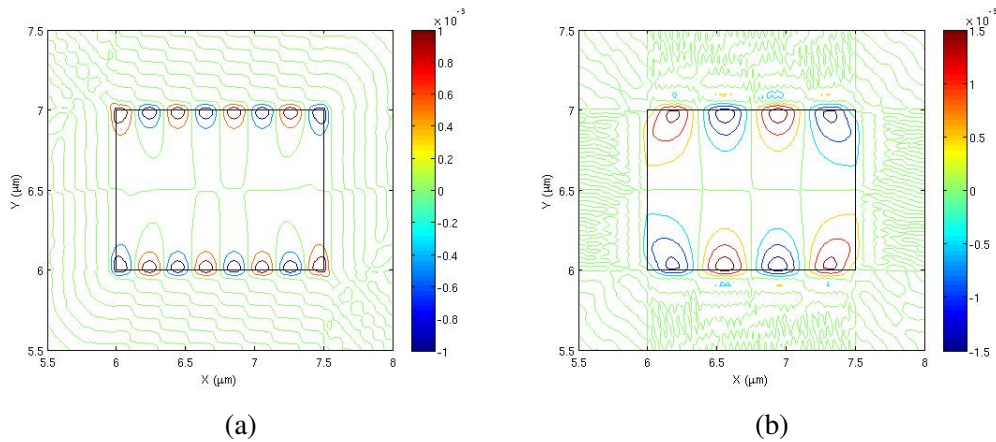
Fig. 6.13 Non-dominant U_Y displacement profiles of the fundamental quasi-shear U_{11}^X acoustic mode (a) at 20 *GHz* and (b) 10 *GHz*.

If the frequency is reduced further, the half-sine peaks at center stretched out and push the peaks at the interface corner, making them smaller, that is starts visible at 8 *GHz* [as shown in Fig. 6.15(a)], where the hybridness increases to 0.11. Central four-peaks are pushed further down to the corner of the interface with further decrease of frequency, which is quite visible near 4 *GHz* [as shown in Fig. 6.15(b)], while their half-sine width spread further more and near cutoff there remains only four half-sine variations in the core. Near 4 *GHz* the
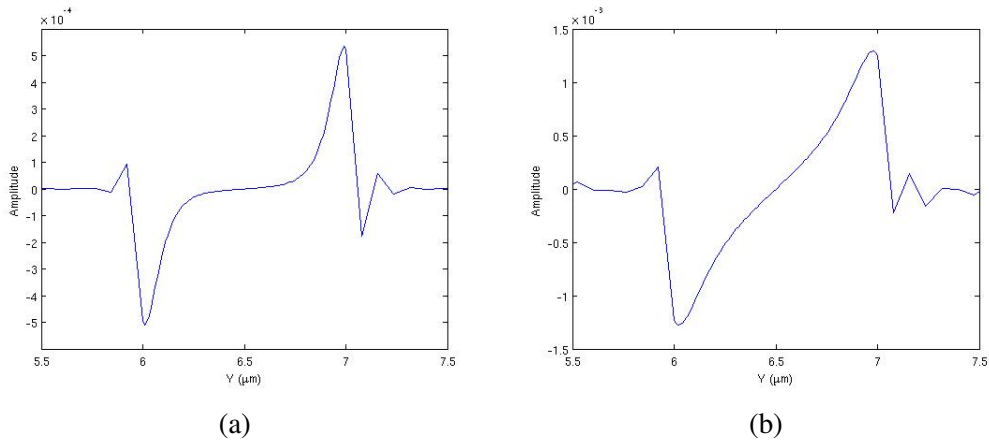
Fig. 6.14 Variations of amplitude along *y*-axis of U_Y component of the fundamental quasi-shear acoustic mode U_{11}^X at (a) 20 *GHz* and (b) 10 *GHz*.

hybridness was found to be 0.14. Only at lower frequencies, it may have only 4 peaks at four corners similar to that shown earlier, in Chapter 4, for a small-index contrast Ge-doped silica guide. However, as discussed here, the evolution of displacement profile with frequency is more complex for a high-index contrast acoustic waveguide.
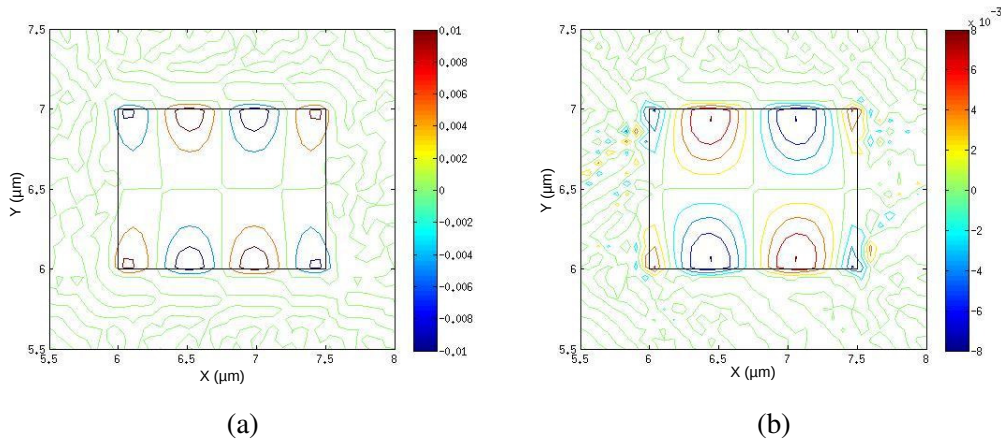
Fig. 6.15 Vector displacement profiles of U_Y component of the fundamental quasi-shear U_{11}^X acoustic mode (a) at 8 *GHz* and (b) 4 *GHz*.

Unlike the U_Y component, the displacement profile of the other non-dominant U_Z component of the fundamental quasi-shear acoustic mode, U_{11}^X, partially resembles the displacement profile of the dominant component, except that the number of spatial variation is two. Here, also, the damped oscillation is present at the core-cladding interfaces. The depth of displacements at the interfaces are small and much more spreaded along the interfaces at the higher

frequency (at 21 GHz), as shown in Figs. 6.16(a) and 6.16(b). Figure 6.16(c) shows the amplitude variation of the U_Z component of the U_{11}^X mode along the x-axis at 21 GHz.
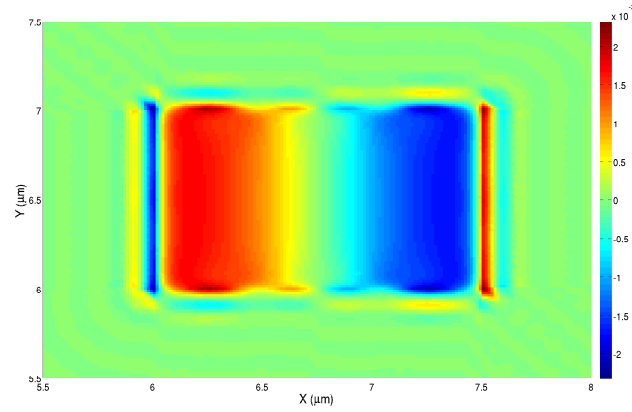
(a)
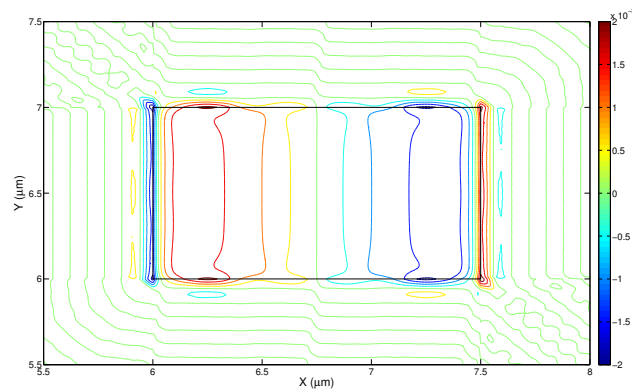
(b)
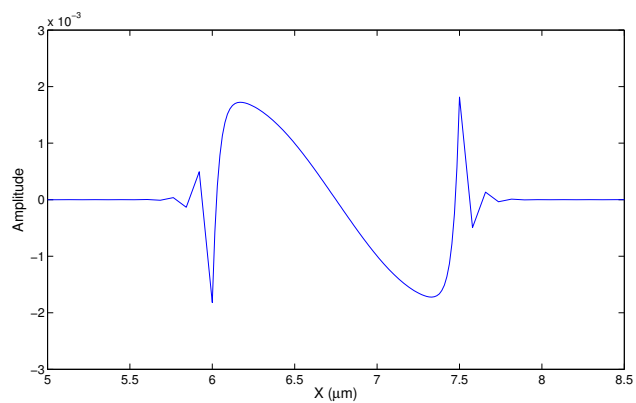
(c)

Fig. 6.16 (a) Coloured, (b) contour of the vector displacement profile and (c) variations of amplitude along x-axis of U_Z component of the U_{11}^X mode at 21 GHz.

Figure 6.17(a) shows the coloured displacement profile of the U_Z component of the fundamental quasi-shear mode, U_{11}^X, at a lower frequency, 10 GHz. When the frequency decreases further, with the increase in depth of the first peaks of oscillations at the interfaces, as observed in the dominant component, these are also start to become localized near the centres of vertical interfaces as shown in Fig. 6.17(b), which is at 8 GHz. However, two peaks of spatial variation at centre of the core reduce further and become less than the spiky peaks at vertical interfaces with the further more decrease in frequency. In addition, sharp displacements at the four corners of the guide become more noticeable around 4 GHz. Both the displacement vector profile of the of the U_Z component of the U_{11}^X mode and its variation along x-axis at 4 GHz frequency are shown in Fig. 6.18.
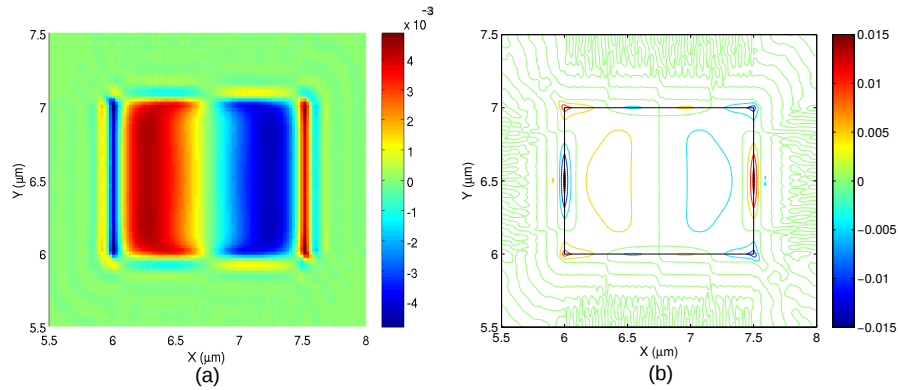
Fig. 6.17 Vector displacement profiles of U_Z component of the fundamental quasi-shear U_{11}^X acoustic mode (a) at 10 GHz and (b) at 8 GHz.
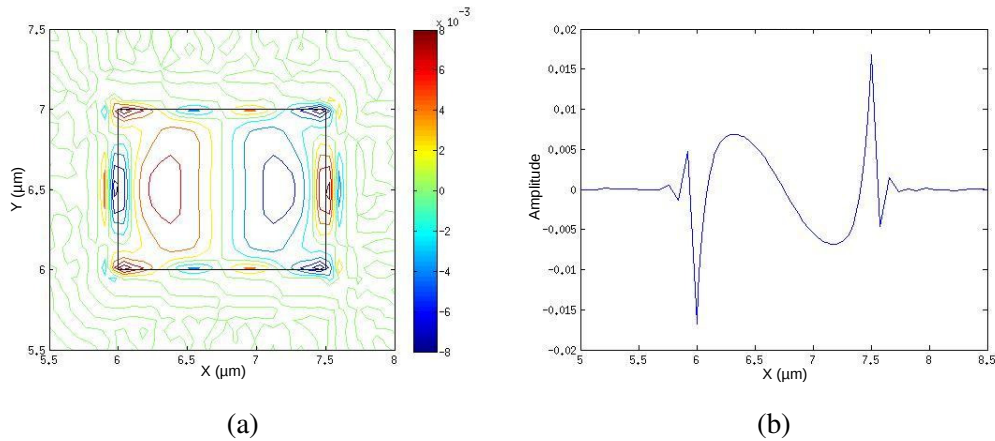
Fig. 6.18 (a) Vector displacement profile and (b) variations of amplitude along x-axis of U_Z component of the U_{11}^X mode at 4 GHz.

Vector displacement profiles of the U_X, U_Y and U_Z components of the higher order acoustic U_{21}^X mode at 21.137 GHz for propagation constant $k = 35$ μm^{-1} are shown in

Fig. 6.19. The dominant U_X component of this hybrid mode has 2 consecutive maxima and minima along the x-axis, each spreads vertically with almost constant amplitude of $\pm$ 0.025, as shown in Fig. 19(a), but has significant displacements along the left and right vertical interfaces, as seen earlier in Fig. 6.7(b) for the fundamental U_{11}^X mode. Whereas, the non-dominant U_Y component, as shown in Fig. 6.19(b), has 9 consecutive maxima and minima peaks along both upper and lower horizontal interfaces, this number was 8 at higher frequency for the U_Y component of the fundamental quasi-shear mode as shown in Fig. 6.13(a). The another non-dominant U_Z component in Fig. 6.19(c) has 3 spatial variation along the x-axis with peak height of 20% of that of the dominant displacement field and also has significant displacements along the left and right vertical interfaces .

(a)　　　　　　　　　　　　　　　　　　　(b)

(c)
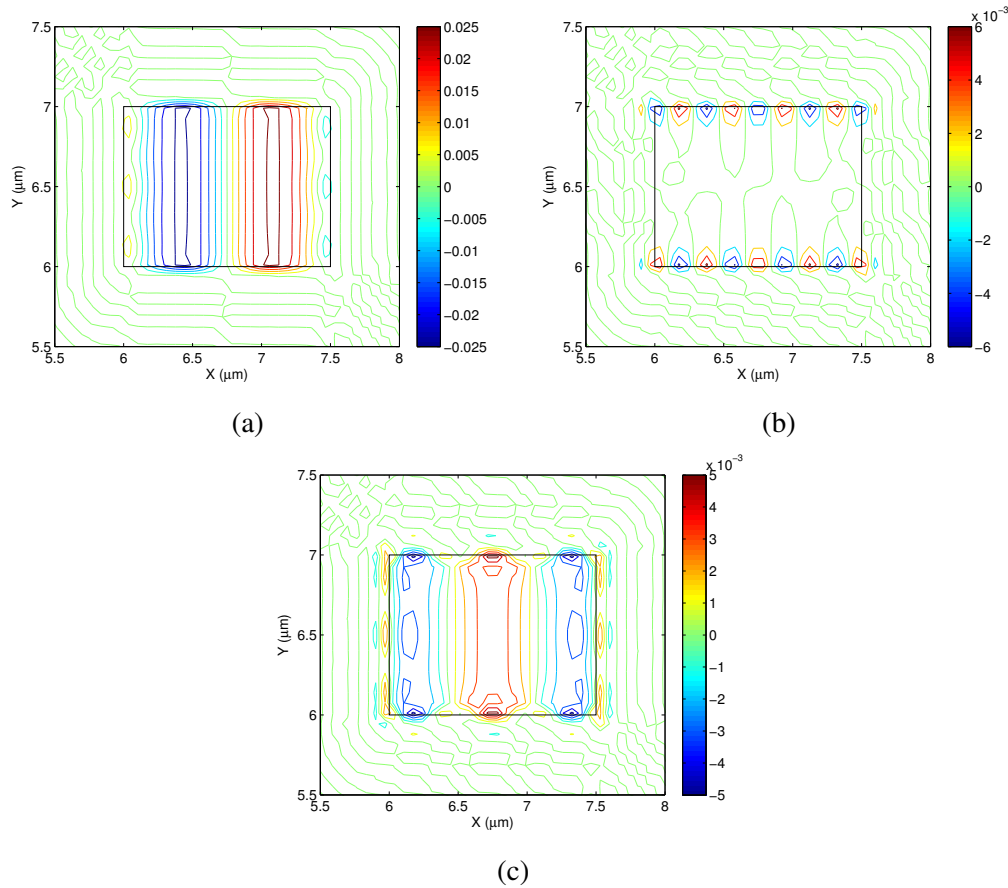
Fig. 6.19 Vector displacement profiles of (a) U_X, (b) U_Y and (c) U_Z components of the U_{21}^X mode at 21.137 *GHz.*

This pattern of the spatial variations in the components of the higher order acoustic modes were found similar for those modes having higher variations along the x-axis in their fundamental components. This can be verified observing the Fig. 6.20, which shows all three displacement components of the U_{31}^X mode at 21.37 *GHz* frequency and at propagation

constant of $k = 35 \ \mu m^{-1}$. It can noticed that for this mode, the dominant U_X component, shown in Fig. 6.20(a), has 3 consecutive minima and maxima, where as the non-dominant U_Z component, shown in Fig. 6.20(c), has 4 consecutive minima and maxima. The another non-dominant U_Y component, as shown in Fig. 6.20(b), has 10 consecutive maxima and minima peaks along both upper and lower horizontal interfaces.

(a)   (b)

(c)
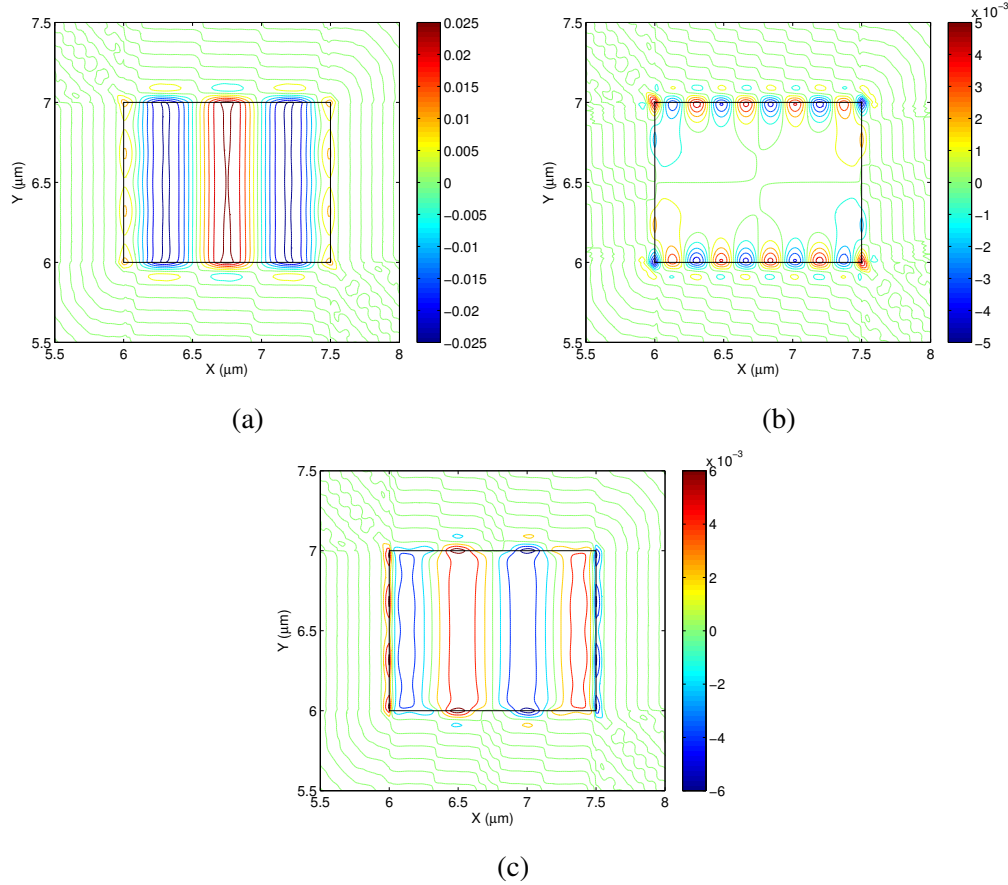
Fig. 6.20 Vector displacement profiles of (a) U_X, (b) U_Y and (c) U_Z components of the U_{31}^X mode at 21.37 GHz.

Figure 6.21 shows the dominant U_X and non-dominant U_Z components of the acoustic U_{41}^X mode at 21.69 GHz, here also the propagation constant was $k = 35 \ \mu m^{-1}$. Here also the similarity in the spatial variation patterns can be noticeable.

But, for the higher order quasi-shear modes, those have larger spatial variation along the y-axis instead of the the x-axis in their dominant components, show a little different variations in mode spreading pattern. Here, the maximum or minimum peak has tendency to localize at the centre instead of spreading with constant amplitude horizontally. It would be more clear by observing Fig. 6.22(a) that shows the dominant U_X component of the acoustic U_{12}^X mode at propagation constant $k = 35 \ \mu m^{-1}$. The non-dominant U_Y component, as shown
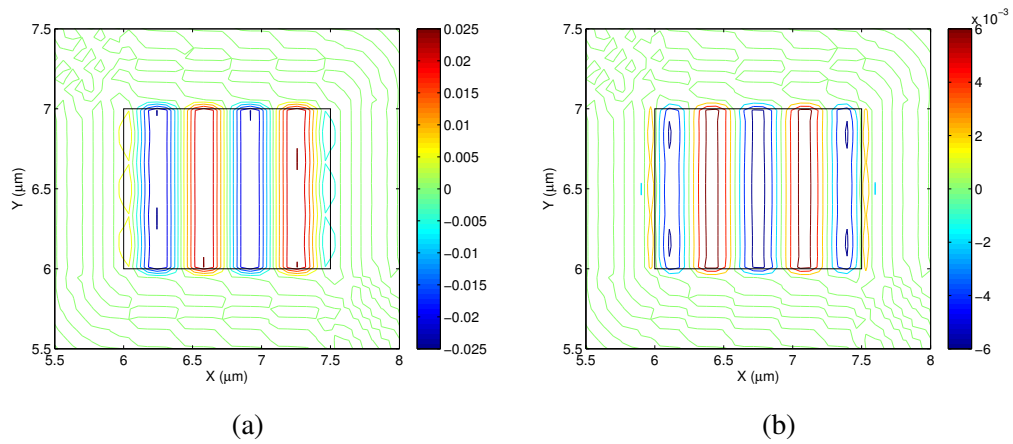
Fig. 6.21 Vector displacement profiles of (a) U_X and (b) U_Z components of the U_{41}^X mode at 21.69 GHz.
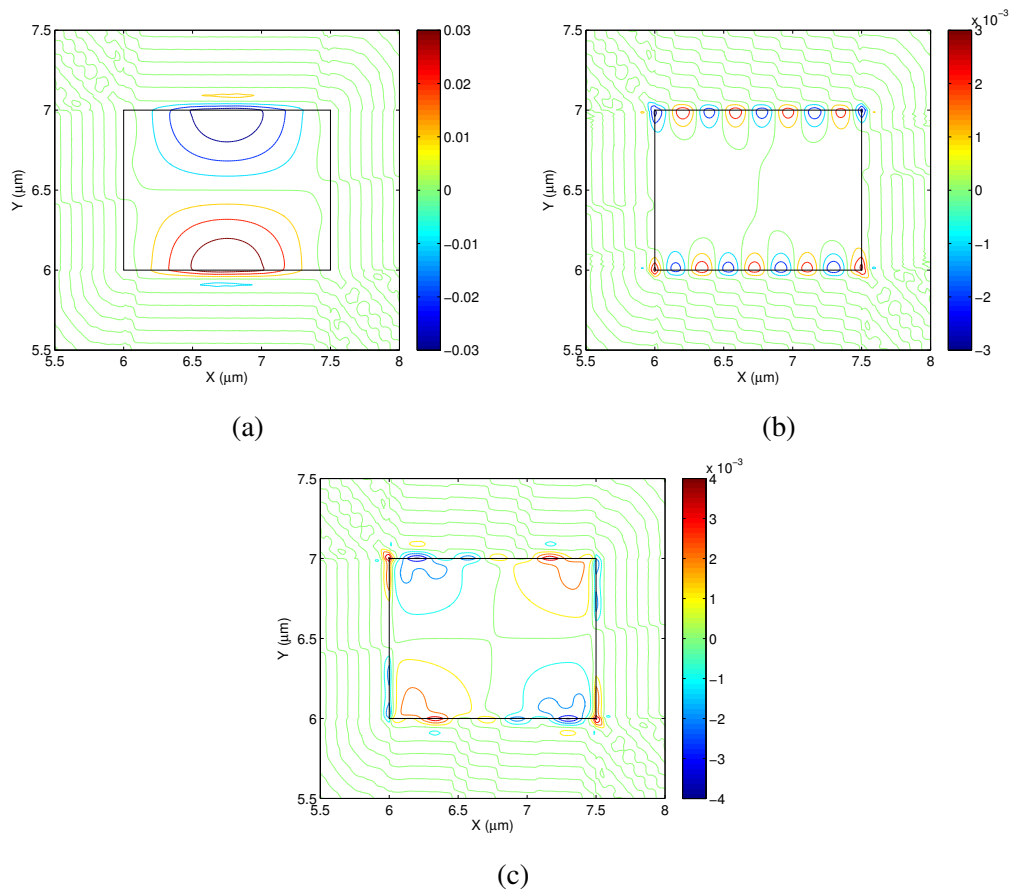
Fig. 6.22 Vector displacement profiles of (a) U_X, (b) U_Y and (c) U_Z components of the U_{12}^X mode at 21.0766 GHz.

in Fig. 6.22(b), has 9 consecutive maxima and minima peaks along both upper and lower horizontal interfaces, as it is seen in the U_Y component of the acoustic U_{21}^X mode in Fig. 6.19(b). Whereas, the U_Z component has four peaks at the four corners of the interfaces.

Figure 6.23, shows the displacement vector profiles for the U_X, U_Y and U_Z components of the higher order acoustic U_{13}^X mode at 21.3266 GHz for propagation constant $k = 35\ \mu m^{-1}$. The U_X component in Fig. 6.23(a) shows one half sine wave variation along x-direction and along y-direction the variation is three. The non-dominant U_Y component, as shown in Fig. 6.23(b), has 10 consecutive maxima and minima peaks along both upper and lower horizontal interfaces. Whereas, the non-dominant U_Z component has three consecutive minima and maxima along y-direction and two along x-direction with significant displacements at the left and right interface boundaries, as shown in Fig. 6.23(c).

(a)

(b)

(c)
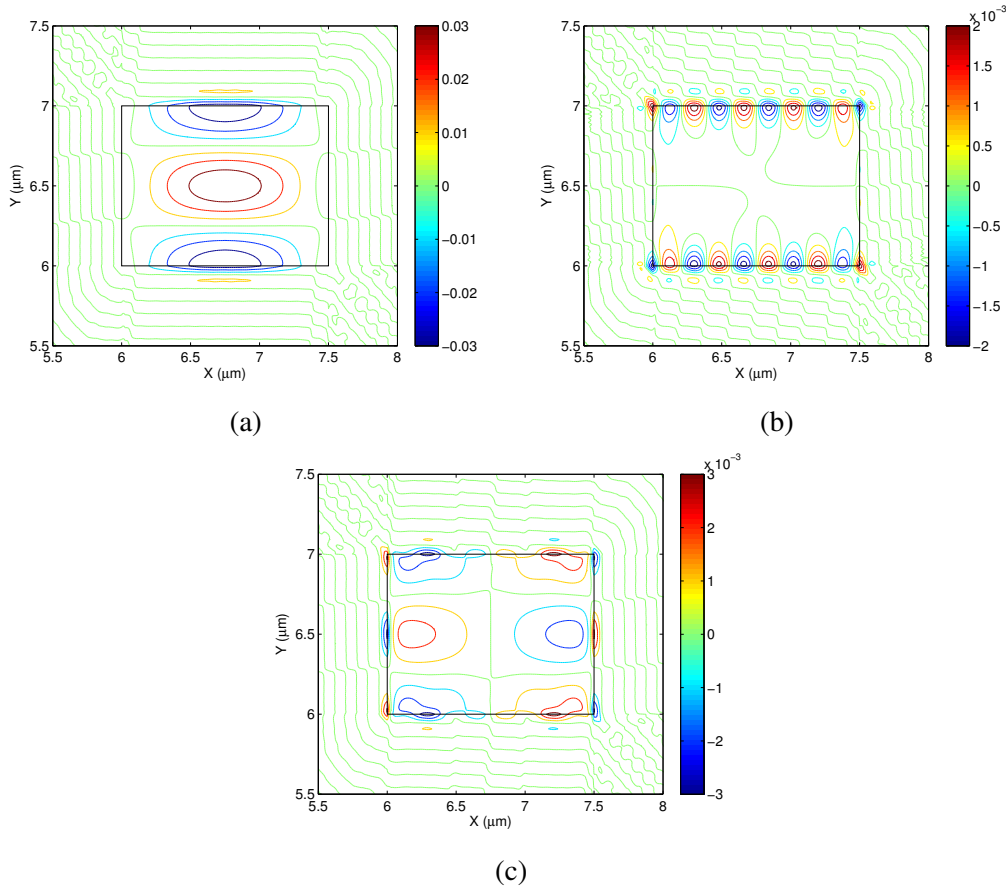
Fig. 6.23 Vector displacement profiles of (a) U_X, (b) U_Y and (c) U_Z components of the U_{13}^X mode at 21.3266 GHz.

This guide also supports two near degenerate fundamental shear modes, U_{11}^X and U_{11}^Y. By using the symmetry conditions these two modes were isolated as they require different boundary combinations at the symmetry walls. The variation of the phase velocities with

acoustic frequency for the two fundamental acoustic shear modes, U_{11}^X and U_{11}^Y, are shown together in Fig. 6.24. Phase velocity of any U_{mn}^X mode is different than that of the U_{mn}^Y mode as for this guide $W \neq H$. This introduces modal birefringence, here they can be denoted by the difference between their phase velocities. It was observed that the modal birefringence increases with the reduction of frequency.
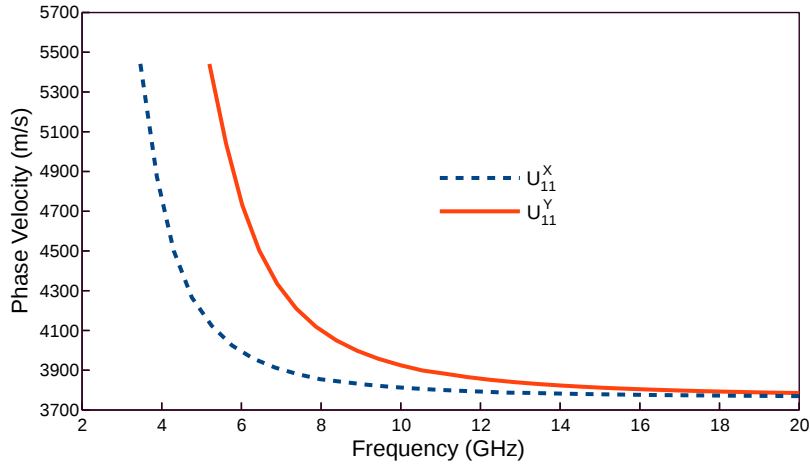
Fig. 6.24 Variations of the velocities with the acoustic frequencies for the two near degenerate fundamental acoustic quasi-shear U_{11}^X and U_{11}^Y modes.

The vector displacement profiles of U_{11}^Y mode are similar to that of U_{11}^X modes, except, the directions are reversed. The displacement profile of dominant U_Y component of the U_{11}^Y mode is constant along the x-axis and near Gaussian along the y-axis. These are shown in Fig. 6.25.

As the frequency starts to decrease, the constant horizontally distribution of displacement of the U_Y component of the U_{11}^Y mode along the x-axis takes wavy shape at lower frequencies. It can be noticeable in Fig. 6.26(a) at propagation constant $k = 13 \ \mu m^{-1}$ and $f = 8.38$ GHz. Whereas, along the y-axis the displacement along the upper and lower interfaces increases significantly, almost more than double, and at the core centre the peak magnitude remain same as it maintains its Gaussian like shape, but with damped oscillation beyond the interfaces, as shown in Fig. 6.26(b).

For the non-dominant U_X component the spatial variations appeared along the vertical side walls. Since, for the core, H is less than W, the number of half-sine spatial variations at both vertical interfaces, for U_X component, was found to be 6 at higher frequency and shown in Fig. 6.27.

This number of half-sine spatial variations at both vertical interfaces, for U_X component reduces to 4 as mode approaches towards its cutoff frequency. Figure 6.28 shows the
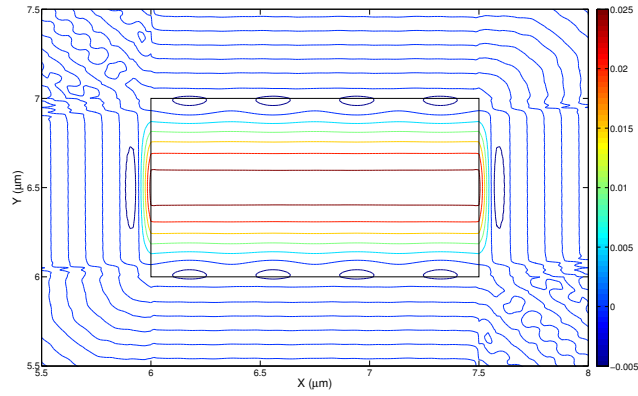
(a)
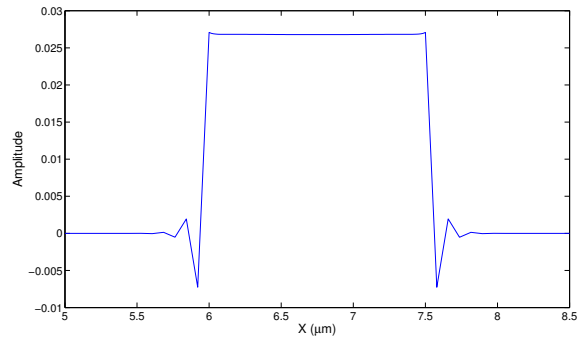
(b)
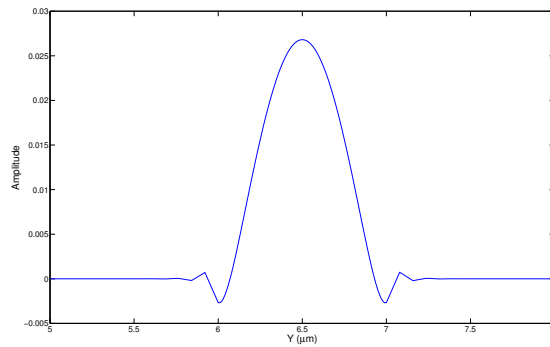
(c)

Fig. 6.25 (a) Vector displacement profile and variations of amplitude along (b) *x*-axis and (c) *y*-axis of U_Y component of the U_{11}^Y mode at 21.0686 *GHz*.

displacement vector profile of the U_X component of the U_{11}^Y mode at 8.38 *GHz* when the propagation constant was calculated as $k = 13 \ \mu m^{-1}$.

(a)   (b)
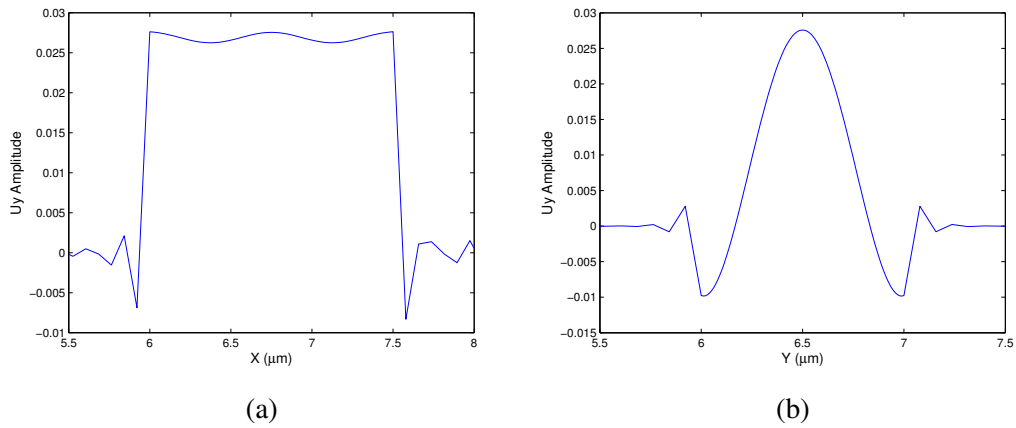
Fig. 6.26 (a) Vector displacement profile and variations of amplitude along (b) x-axis and (c) y-axis of U_Y component of the U_{11}^Y mode at 8.38 GHz.
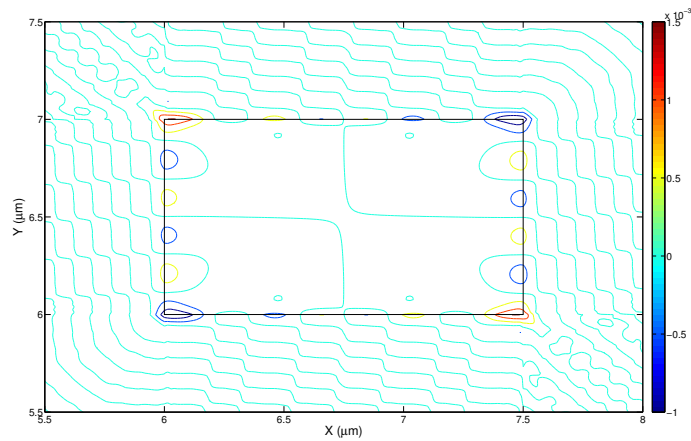
Fig. 6.27 Vector displacement profile of U_X component of the U_{11}^Y mode at 21.0686 GHz.
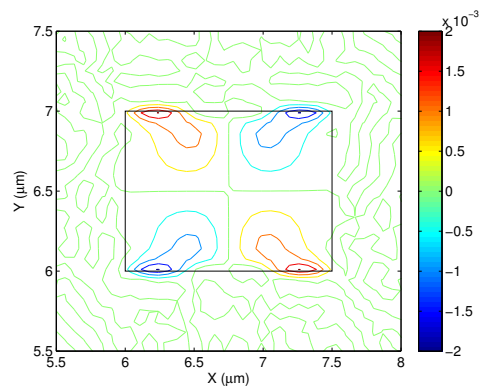
Fig. 6.28 Vector displacement profile of U_X component of the U_{11}^Y mode at 8.38 GHz.

Whereas for the non-dominant U_Z component the spatial variations appeared along the horizontal side walls, shown in Fig. 6.29(a), with significant displacements spread along the upper and lower horizontal interfaces, as shown in Fig. 6.29(b), at the higher frequency.
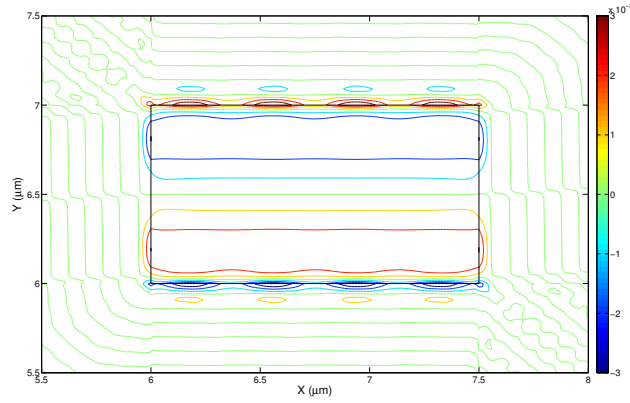
(a)
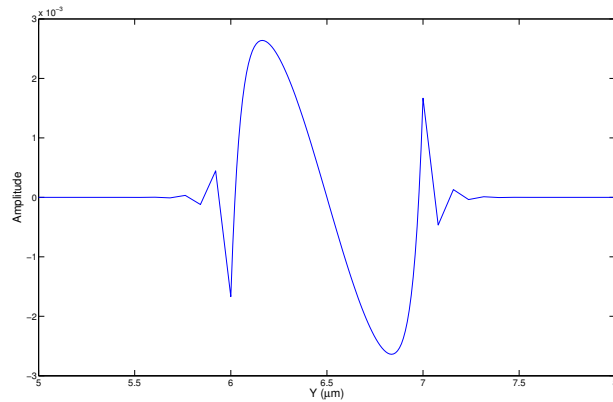
(b)

Fig. 6.29 (a) Vector displacement profile and (b) variations of amplitude along *y*-axis of U_Z component of the U_{11}^Y mode at 21.0686 *GHz*.

When the frequency starts to reduced, both the interfaces displacements along with the positive and negative peaks along the horizontal side walls start to increase in magnitude. As shown in Fig. 6.30(a), at 8.38 *GHz* frequency the magnitudes of the interface displacements were found to be more than three times as seen in Fig. 6.29(b) and the magnitudes of the positive and negative peaks along the horizontal side walls increased by 2.7 times comparing those at higher frequency 21.0686 *GHz*. As the frequency starts to decrease further, the interfaces displacements start to decrease but the magnitudes of the positive and negative peaks along the horizontal side walls keep increasing and near cutoff frequency around 5.1957 *GHz*, the interfaces displacements disappear, whereas the positive and negative peaks reaches
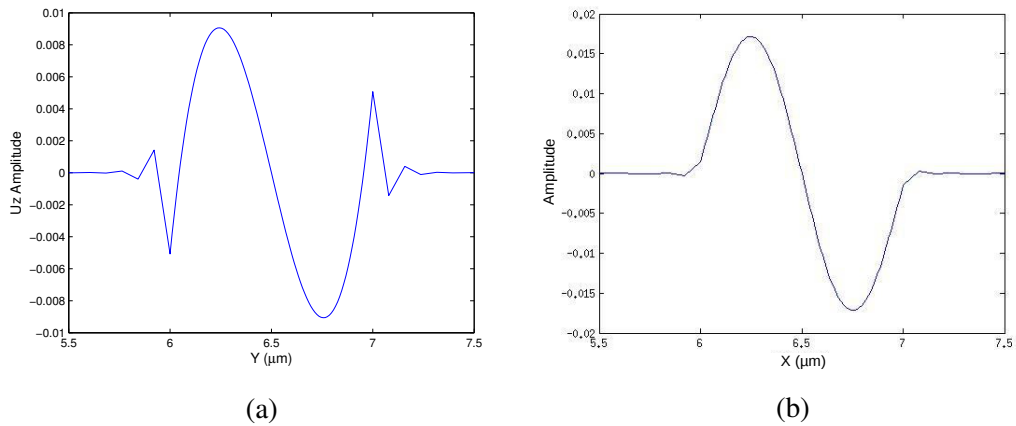
Fig. 6.30 Vector displacement profile of U_Z component of the U_{11}^Y mode at (a) 8.38 GHz and (b) 5.1957 GHz.
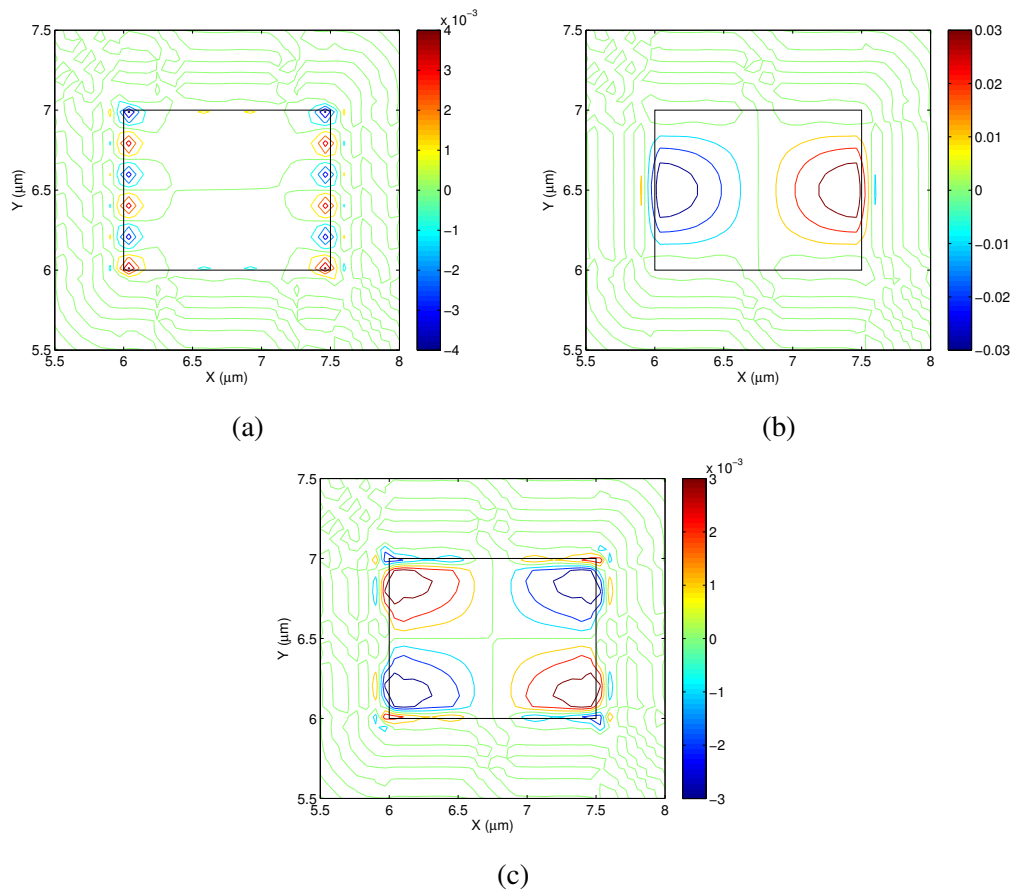
Fig. 6.31 Vector displacement profiles of (a) U_X, (b) U_Y and (c) U_Z components of the U_{21}^Y mode at 21.4262 GHz.

a magnitude of ten times higher as seen in higher frequency. The variation of displacement along the y-axis of the U_Z component at 5.1957 GHz shown in Fig. 6.30(b).

For the higher order U_{mn}^Y modes with dominant U_Y components the displacement profiles are different when $m < n$ then those where $n < m$, unlike those were seen in case of U_{mn}^X modes, as the displacement profiles in Figs. 6.19, 6.20 and 6.21 are different than in Figs. 6.22 and 6.23, where it varies in opposite manner. For any U_{mn}^Y mode with $n < m$, the displacement profiles of the dominant U_Y field and non-dominant U_Z field will vary as seen earlier in dominant U_X and non-dominant U_Z fields in Figs. 6.22 and 6.23, except, the directions are reversed. Similarly, in Fig. 6.31(b), which shows the displacement profile U_Y of the U_{21}^Y mode at 21.4262 GHz and $k = 35$ μm^{-1}, are differently distributed. Here, the dominant displacement field has a tendency to localize at centre, instead distributing vertically with constant magnitude. For the U_Z displacement vector field profile the positive and negative peaks formed at the corner of interfaces, which is shown in Fig. 6.31(c).

Hybridness of the fundamental quasi-shear modes

As stated earlier, the hybridness for the component along the direction of propagation of any mode is considered to be important. The hybridness of the both fundamental quasi-shear acoustic U_{11}^X and U_{11}^Y are shown in Fig. 6.32, where the hybridness are calculated from the ratio of non-dominant U_Z field's maximum displacement value to the values of corresponding dominants fields maximum displacements. It can be noticed that the hybridness for the U_{11}^Y mode, which is represented by the dashed red line, is higher than that of the U_{11}^X mode, shown by the solid blue line, for any given acoustic frequency between 20 GHz to cutoff.
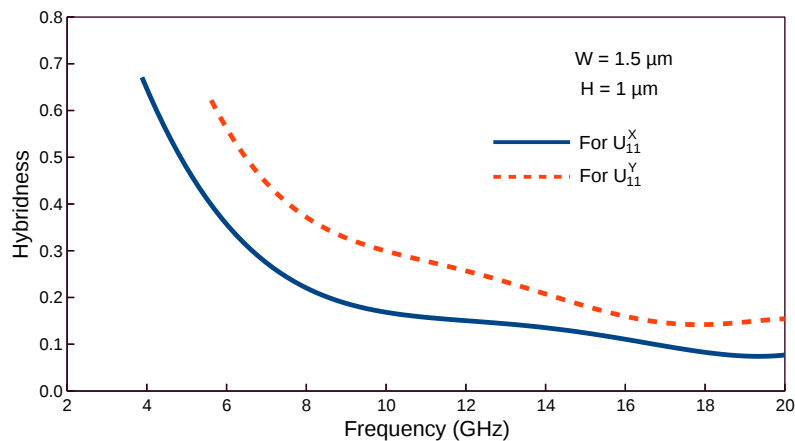
Fig. 6.32 Variation of the hybridness with frequency for the U_{11}^X and U_{11}^Y modes.

Figure 6.33 shows the variation of the modal hybridness of the U_Z component of the acoustic U_{11}^X mode with respect to its dominant field profile with the varying silica guide width. Although in Fig. 6.32 the hybridness for both the transverse components were shown, but it was at a fixed guide width, whereas at a fixed propagation constant, $k = 10 \ \mu m^{-1}$, the hybridness of the U_Z component of the acoustic U_{11}^X mode is shown in Fig. 6.33. At $2.5 \mu m$ width, the hybridness was near 0.19, which increases with the reduction in guide width and at $1.5 \mu m$ the hybridness is 0.32. It rises further with the reduction of the width of the guide and at $0.7 \mu m$ the hybridness is 0.81.
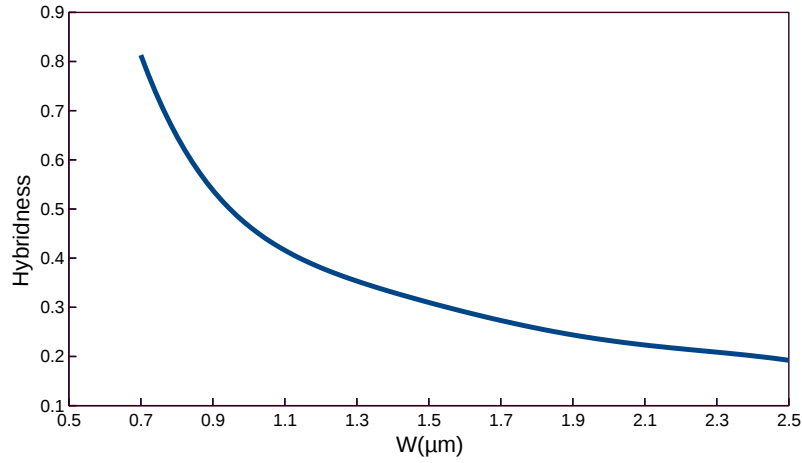
Fig. 6.33 Variation of hybridness of the U_{11}^X acoustic mode with W at $k = 10 \ \mu m^{-1}$.

6.4.2   Surface acoustic mode U_{11}^{HZ}

In this chapter, the emphasis are given to analyses of those acoustic modes, which may have significant contribution towards Brillouin gain spectrum in air-clad strip silica waveguide. In addition to the quasi-shear modes, this air-clad silica strip waveguide also supports another set of hybrid modes, having comparative larger hybridness with different spatial distribution and evolution pattern. Among which, at lower frequency range, one mode was particularly observed to have spatial variations similar to that of the U_{11}^Z mode discussed in Ge-doped silica waveguide in Chapters 4 and 5, except that, rather its U_Y component was found dominant. Subsequently, this highly hybrid mode is identified here as the U_{11}^{HZ} mode, which appeared as surface acoustic wave at higher acoustic frequency.

In general, in the standard optical fibres light is sensitive solely to longitudinal and shear bulk acoustic waves, which leads to well-known common non-linear effects like stimulated Brillouin scattering (SBS) and guided acoustic wave Brillouin scattering (GAWBS). Whereas, in sub-wavelength optical waveguides the situation changes dramatically [Beugnot, 2014,

Oct.]. Because the guided light and the evanescent field see the outer surface, thus the guided light can shake the waveguide by the process of electrostriction that generates the surface acoustic waves (SAW). Thus the associated propagating surface ripples will then lead to small periodic changes of the effective refractive index along the optical waveguide. Then guided light undergoes Bragg scattering according to the phase matching condition in the backward direction when passing through the moving refractive index surface grating, as link the SBS in optical fibres due to the longitudinal acoustic waves. This backscattered light also experience a small shift in its frequency due to Doppler effect according to the light-sound energy conservation. The velocity of the surface acoustic waves significantly differs from those of the shear and longitudinal acoustic modes. Surface acoustic wave travels between 0.87 and 0.95 times the velocity of a shear acoustic wave [Beugnot, 2014, Oct.]. It is to be noted that for this waveguide the shear acoustic velocity was considered as 3760 m/s for silica.

The dispersion curve of the highly hybrid acoustic U_{11}^{HZ} mode is shown in Fig. 6.34. It can be observed that the phase velocity of this mode around 20 GHz frequency was found near 3419 m/s, whereas the shear acoustic velocity of silica is 3760 m/s. So, its velocity was found between the values, as stated earlier. In an optical microwire of 1 μm dia, this valocity was reported [Beugnot, 2014, Oct.] as 3400 m/s. In the air-clad strip waveguide, with the decrease in frequency the change in phase velocity of this mode was found insignificant, whereas after 6 GHz acoustic frequency the phase velocity started to change gradually and the change become notably rapid after 4 GHz of acoustic frequency. This rapid change in velocity enhances the evolution of the modal displacement profiles. In the lower range of acoustic frequencies this wave was found to be as bulk wave rather than surface acoustic wave.

The spatial profile of the vector U_Y displacement of U_{11}^{HZ} mode at 3.24 GHz is shown in Fig. 6.35(a). It can be observed that this component possesses damped oscillations starting from the upper and lower horizontal interfaces. Its spatial variation in the core along the y-direction was observed to have an odd-symmetry with zero displacement at the center and maximum, with a magnitude about 0.02, at the horizontal interfaces. As if, both peaks are clipped from the maximum points, as shown in Fig. 6.35(b). The ratio of the first peak of the damped oscillation to the main peak (peak ratio) was calculated to be 0.5 at frequency 3.24 GHz, which reduces as the frequency increases.

Similarly, the U_X component of this highly hybrid mode have a similar pattern as U_Y component, but with an odd symmetry along the x-direction. The spatial profile of the vector U_X displacement of U_{11}^{HZ} mode at 5.71 GHz is shown in Fig. 6.36(a). This component also possesses damped oscillations at the left and right vertical air-silica interfaces. Figure 6.36(b)
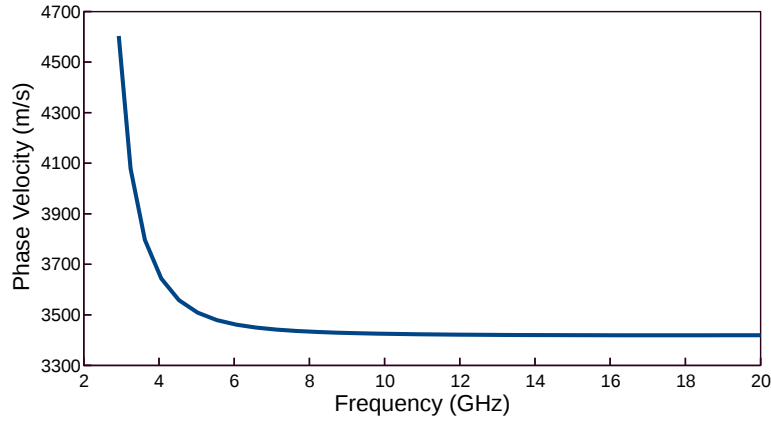
Fig. 6.34 Variations of phase velocity with acoustic frequencies for the highly hybrid acoustic mode U_{11}^{HZ}.

(a)   (b)
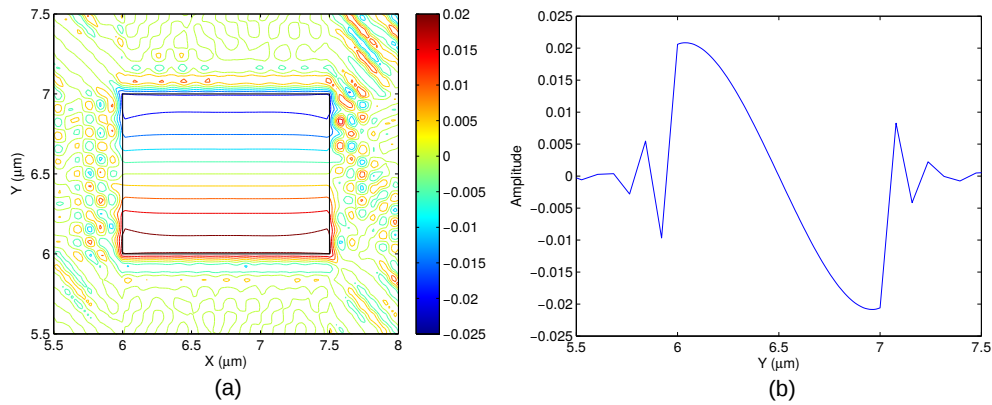
Fig. 6.35 (a) Vector displacement profile and (b) amplitude variations along the *y*-axis of U_Y component of the highly hybrid acoustic mode U_{11}^{HZ} at 3.24 *GHz*.

shows the variation of the displacement of this component along *x*-direction, where the ratio of the first peak of the damped oscillation to the main peak (peak ratio) was calculated to be 0.3429. Whereas, at 3.24 *GHz* frequency the peak ratio was observed to be 0.46 with main peak amplitude of 0.005.

The spatial variation of U_Y component of U_{11}^{HZ} mode starts to localize at the centre of upper and lower horizontal interfaces when frequency increases. At *f* = 5.71 *GHz* the vector displacement profile of U_Y component is shown in Fig. 6.37(a), where it has peak amplitude of 0.025 with the peak ratio of 0.3125. The resultant vector displacement profile at transverse plane, U_T, of this mode at 5.71 *GHz* frequency is shown in Fig. 6.37(b), which matches exactly with the transverse displacement profile in an air-clad silica strip waveguide of the same dimension at the same frequency reported in [Laude, 2013] that is shown in Fig. 6.38.
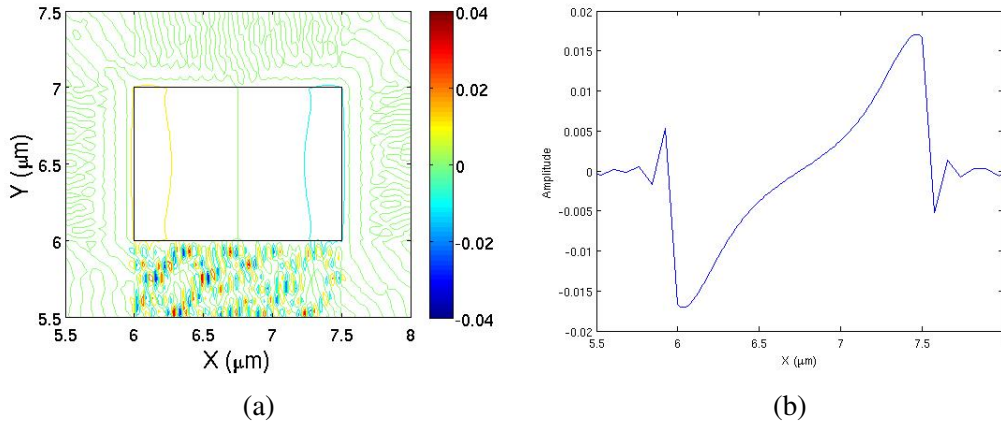
Fig. 6.36 (a) Vector displacement profile and (b) amplitude variations along the x-axis of U_X component of the highly hybrid acoustic mode U_{11}^{HZ} at 5.71 GHz.

Here U_T is the resultant transverse vector was found by vectorically adding U_X and U_Y displacement profiles.
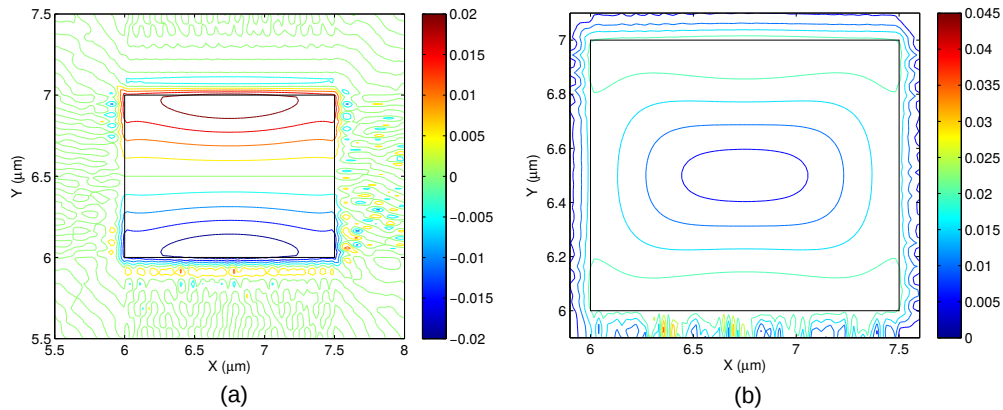
Fig. 6.37 Vector displacement profiles of (a) U_Y component and (b) transverse plane component U_T of the highly hybrid acoustic mode U_{11}^{HZ} at 5.71 GHz.

As frequency increases further, at 20.13 GHz the peaks of U_Y, with amplitude 0.6, become more localized at the centers of upper and lower horizontal interfaces, as shown in Fig. 6.39(a), and get narrower with a near zero displacement value at the center, as can be seen in Fig. 6.39(b). Where, the peak ratio reached a value of 0.3.

But for the U_X of the U_{11}^{HZ} mode with the increase of frequency, the tendency of its displacement profiles were found to be concentrated along the both left and right vertical interfaces instead localizing at the centre that was observed for the U_Y component. Near $f =$ 10.355 GHz, the displacement profile of the U_X component is shown in Fig. 6.40(a) and its variation along the x-direction is shown in Fig. 6.40(b).
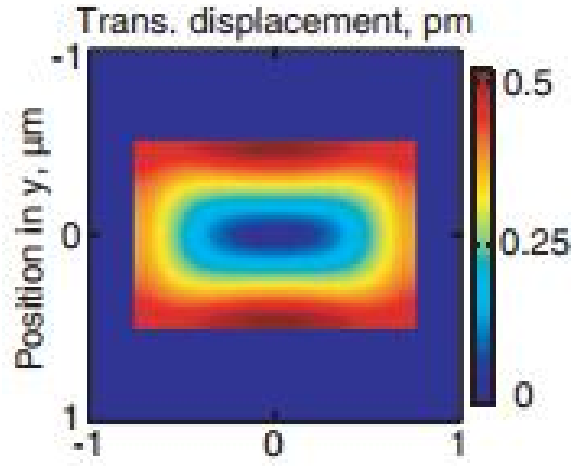
Fig. 6.38 Transverse plane displacement component of the highly hybrid acoustic mode at 5.71 *GHz* [Laude, 2013].
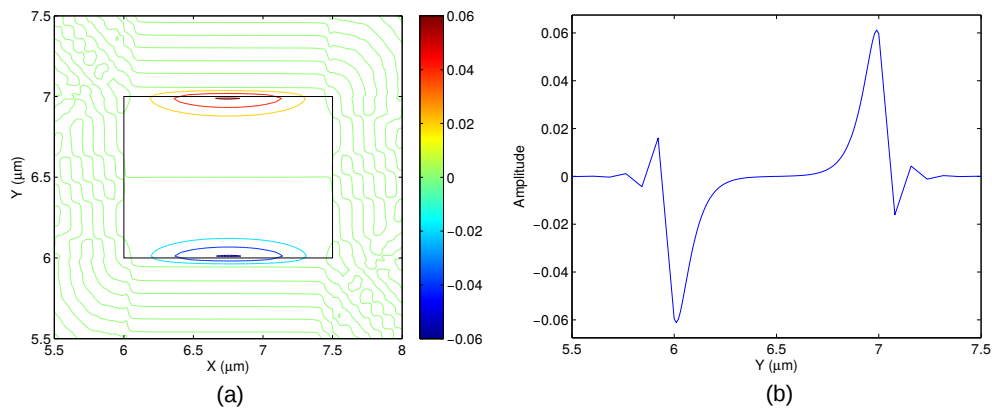
Fig. 6.39 (a) Vector displacement profile and (b) amplitude variations along the *y*-axis of U_Y component of the highly hybrid acoustic mode, U_{11}^{HZ} at 20.13 *GHz*.

With the further increase of frequency the displacement profiles of the U_X component get more compact along the left and right vertical interfaces and the peak ratio started to drop but the peak amplitude increases. At 20.13 *GHz*, when the main peak amplitude was 0.018, the peak ratio was found 0.28. Near $f = 20.13$ *GHz*, with propagation constant $k = 37$ μm^{-1}, the displacement profile of the U_X component is shown in Fig. 6.41(a) and its variation along the *x*-direction is shown in Fig. 6.41(b).

The coloured vector displacement profile of U_Z component of U_{11}^{HZ} mode at frequency 3.24 *GHz* is shown in Fig. 6.42(a). It has the most interesting evolution pattern among all the components of the U_{11}^{HZ} acoustic mode. At 3.24 *GHz* frequency, its amplitude variation along the *x*-direction through the center of the waveguide, shown in Fig. 6.42(b), has a 'U' shaped
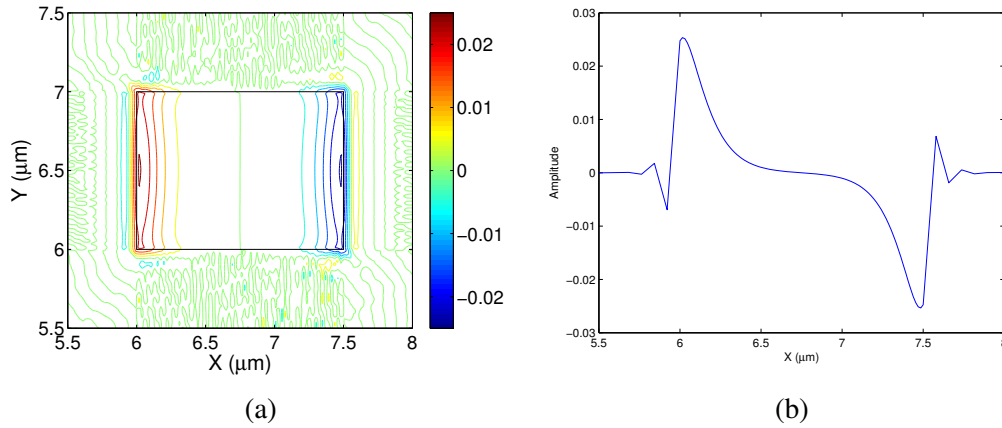
Fig. 6.40 (a) Vector displacement profile and (b) amplitude variations along the *x*-axis of U_X component of the highly hybrid acoustic mode U_{11}^{HZ} at 10.355 *GHz*.
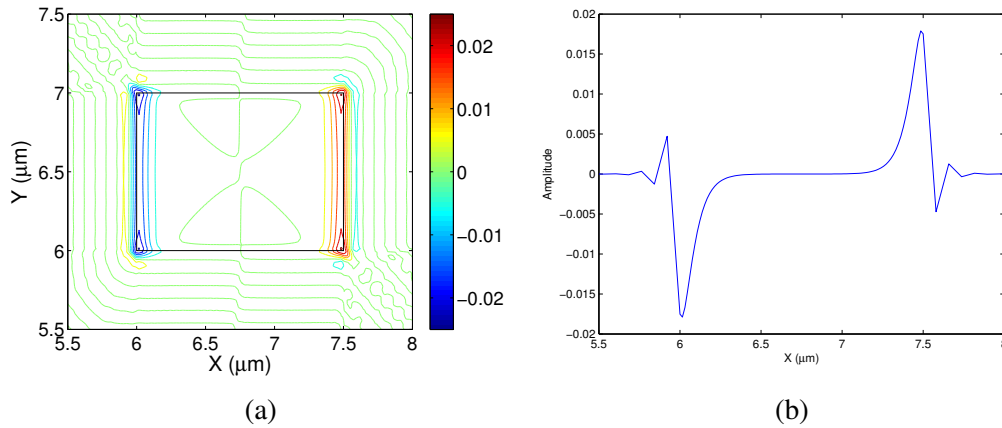
Fig. 6.41 (a) Vector displacement profile and (b) amplitude variations along the *x*-axis of U_X component of the highly hybrid acoustic mode U_{11}^{HZ} at 20.13 *GHz*.

peak of amplitude 0.0125 with damped oscillations at the left and right interfaces, having peak ratio of 0.12. Whereas the amplitude variation along *y*-direction showed a similar damped oscillation but with a very high peak ratio of 0.8.

At a higher frequency, 4.53 *GHz*, the peak starts to become flat along the *x*-direction but with a reduced amplitude of 0.0082 and a higher damped oscillation peak, where the peak ratio was found as 0.244. The variation of amplitude of the U_Z component along the *x*-direction is shown in Fig. 6.43(a). Along *y*-direction, shown in Fig. 6.43(b), the shape of the peak remain similar but the height of the damped oscillation increased significantly with a peak ratio of 1.585.

Af *f* = 5.71 *GHz*, the peak of the amplitude variation of U_Z component along *y*-direction started to flatten, whereas along *x*-direction it had a sag of 6.4% of the peak amplitude, as
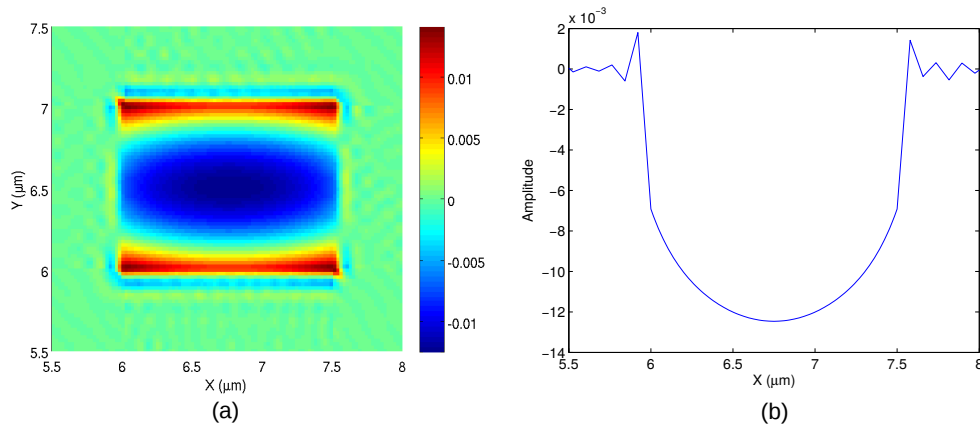
Fig. 6.42 (a) Vector displacement coloured profile and (b) variations of amplitude along x-axis of U_Z component of the highly hybrid acoustic mode U_{11}^{HZ} at 3.24 GHz.
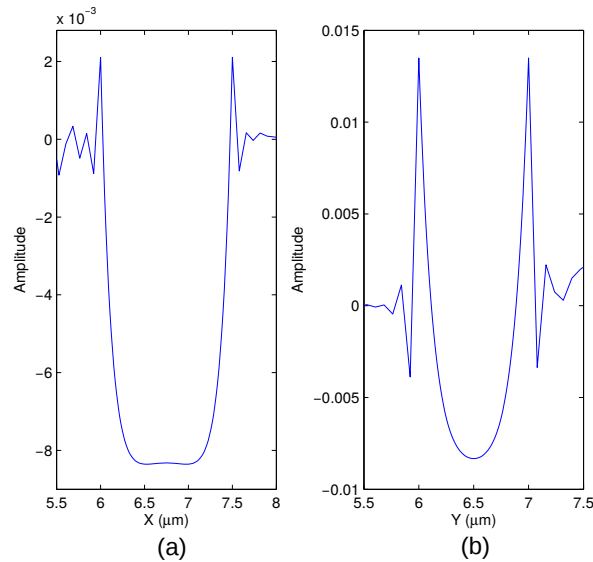
Fig. 6.43 Variations of amplitude along (a) x-axis (b) y-axis of U_Z component of the highly hybrid acoustic mode U_{11}^{HZ} at 4.53 GHz.

shown in the Fig. 6.44(b). The peak ratio was found to be 1.29 and 2.42 along horizontal and vertical interfaces, respectively. Figure 6.44(a) represents the colour displacement vector profile of this U_Z component, which matches very well with the axial displacement profile of the mode reported in [Laude, 2013] at the same frequency, which is shown in Fig. 6.45.

For further increase in frequency, the peak of U_Z component starts to decrease, whereas the first peak of the damped oscillation increases in magnitude significantly. The peak along y-direction started to have sag around 7.12 GHz. Figure 6.46 shows the variation of amplitude
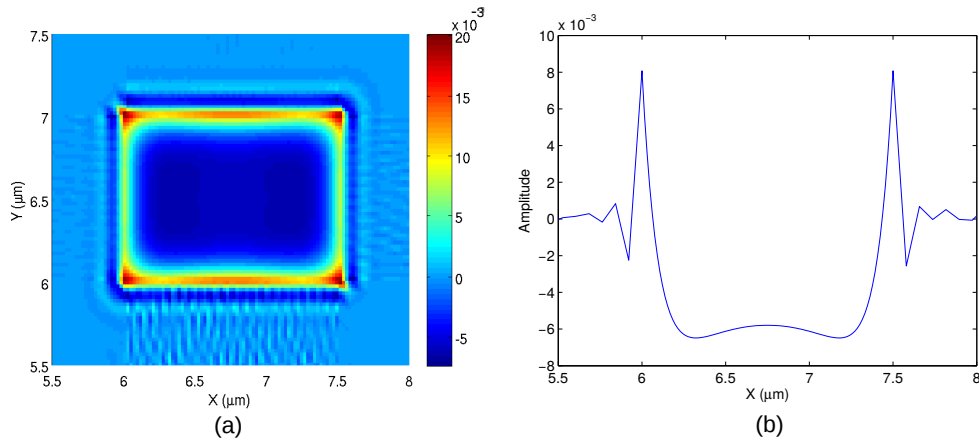
Fig. 6.44 (a) Vector displacement coloured profile and (b) variations of amplitude along x-axis of U_Z component of the highly hybrid acoustic mode U_{11}^{HZ} at 5.71 *GHz*.
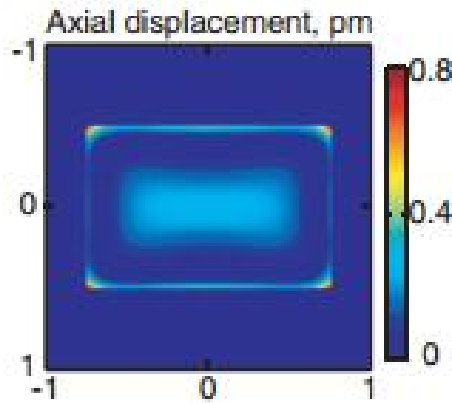
Fig. 6.45 Axial displacement component of the highly hybrid acoustic mode at 5.71 *GHz* [Laude, 2013].

of the U_Z component along the x and y-directions at 7.12 *GHz* frequency. These changes continue further when frequency is increased.

At 20.13 *GHz*, the earlier peak of U_Z component become almost zero inside the core, whereas the first peak of the damped oscillation attained a magnitude of 0.0122 and 0.045 along horizontal and vertical interfaces, respectively. It become evident that at the higher frequency, shown in Fig. 6.47(b), the molecular displacement contributed by U_Z component of U_{11}^{HZ} mode localized at the boundary of the core rather than at the centre. Figure 6.47(a) shows the magnitude of the spatial variation of this U_Z component along the x-direction.
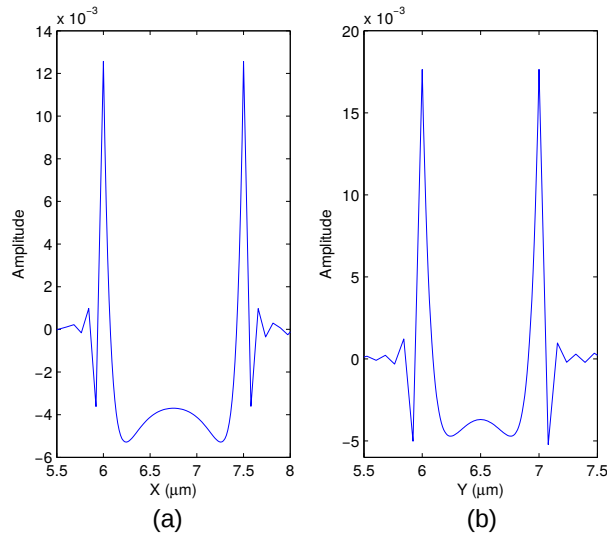
Fig. 6.46 Variations of amplitude along (a) x-axis (b) y-axis of U_Z component of the highly hybrid acoustic mode U_{11}^{HZ} at 7.12 GHz.
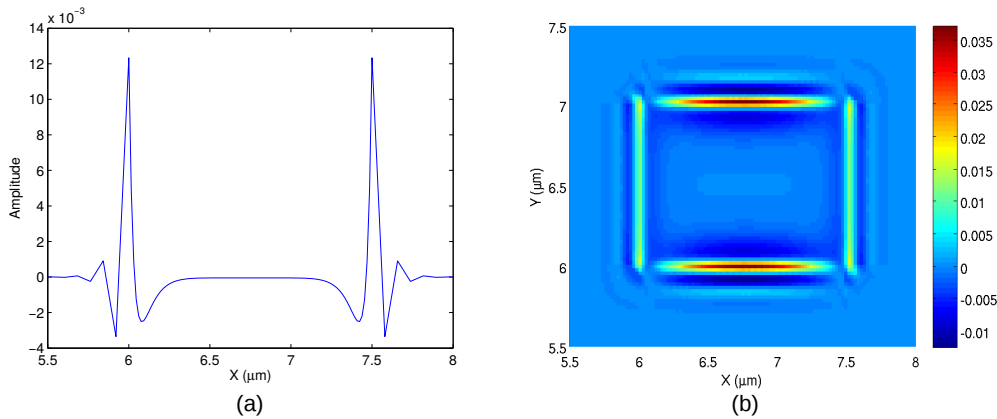
Fig. 6.47 (a) Variations of amplitude along x-axis and (b) vector displacement coloured profile of U_Z component of the highly hybrid acoustic mode U_{11}^{HZ} at 20.13 GHz.

6.4.3   Complex highly hybrid acoustic mode (CHHM)

At $f = 9.81$ GHz, another highly hybrid acoustic mode was observed with comparatively large dominant U_Z component, having almost 8.3 times larger peak amplitude than that of those in other non-dominant displacement components U_X and U_Y. The non-dominant U_X component of this highly hybrid mode has 6 consecutive maxima and minima, as shown in Fig. 6.48(a), like a sixth lateral (along x) order mode. It is almost constant along the y-direction inside the core with damped oscillations at the boundary edges of both vertical interfaces. The peak ratio for this component was measured 0.143. Whereas, another non-dominant component U_Y, had 4 consecutive maxima and minima like a forth order vertical mode, as shown in Fig.

6.48(b), with horizontal flat profile inside the core. It has similar damped oscillations, with peak ratio of 0.086, at the both horizontal boundary edges.

(a)   (b)
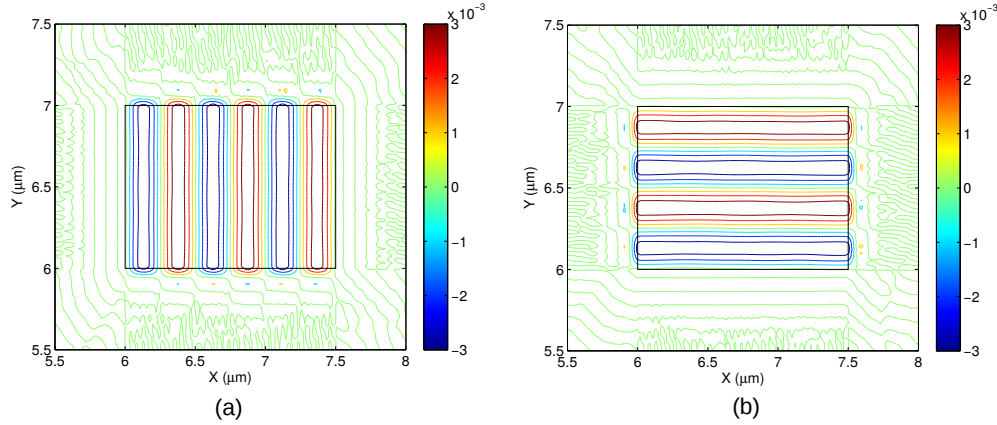
Fig. 6.48 Vector displacement profiles (a) of U_X component and (b) of U_Y component of the complex highly hybrid acoustic mode (CHHM) at 9.81 GHz.

Figure 6.49(a) shows the amplitude variation along the x-direction of the non-dominant U_X component and the amplitude variation along the y-direction of the non-dominant U_Y component of this CHHM mode is shown in Fig. 6.49(b), both obtained at 9.81 GHz frequency at the phase matched condition where propagation constant was $k = 10.33346$ μm^{-1}.

(a)   (b)
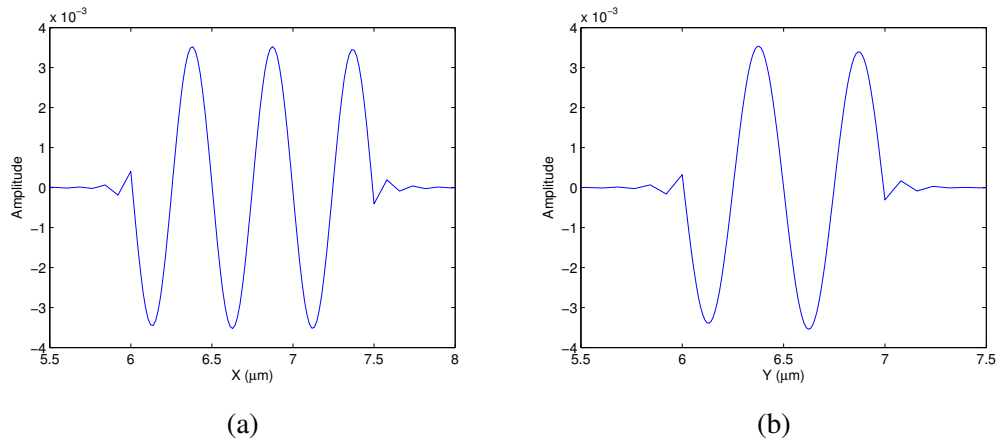
Fig. 6.49 Amplitude variations along the (a) x-axis of U_X component and (b) y-axis of U_Y component of the CHHM mode at 9.81 GHz.

The resultant vector displacement profile at transverse plane, U_T, vectorically calculated from these non-dominant components of this complex highly hybrid acoustic mode (CHHM) and shown in Fig. 6.50, matches very well with the transverse displacement profile of a mode reported in [Laude, 2013] at 9.81 GHz, which is shown in Fig. 6.51.
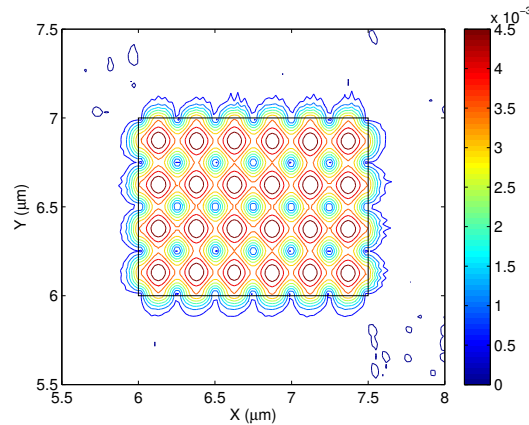
Fig. 6.50 Transverse plane component U_T of the complex highly hybrid acoustic mode (CHHM) at 9.81 *GHz*.
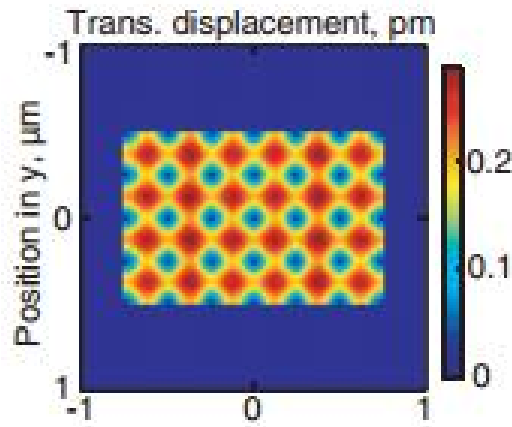
Fig. 6.51 Transverse plane displacement component of the highly hybrid acoustic mode at 9.81 *GHz* [Laude, 2013].

The dominant U_Z displacement vector profile of this CHHM mode is also shown in Fig. 6.52(a), which matches again with the axial displacement profile reported in [Laude, 2013] and shown in Fig. 6.53. However, from the contour profile it is difficult to visualize its transverse variations. For this reason its variation along the *x*-direction (through the center of the core) is shown in Fig. 52(b).

The phase velocity of this complex highly hybrid mode was calculated 5965.38 m/s. It was observed that this U_Z component had a wavy peak, shown in Fig. 6.52(b), with depth of oscillation at peak around 0.08 and damped oscillations at boundary edges with magnitude of peak ratio as 0.28 and 0.265 along *x* and *y*-directions, respectively. Which indicates, the first peak of the damped oscillation in the vertical left and right interfaces were slightly higher to
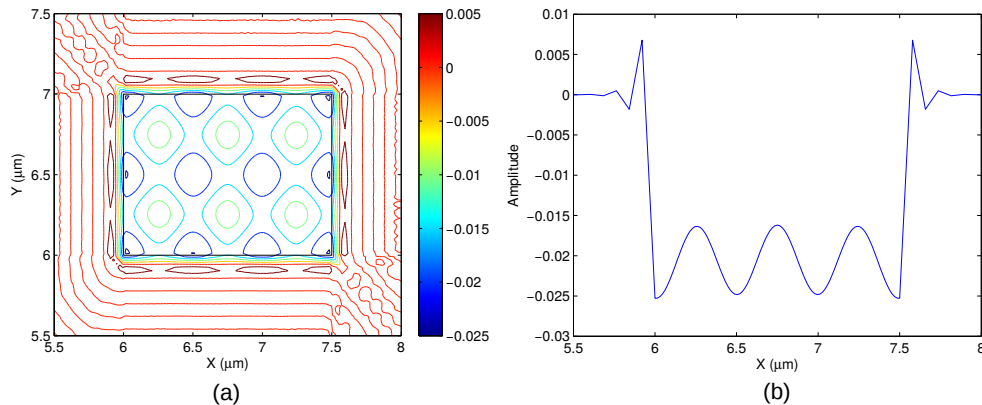
Fig. 6.52 (a) Vector displacement profile and (b) variations of amplitude along x-axis of the U_Z component of the CHHM mode at 9.81 GHz.

those of in the horizontal upper and lower interfaces. So, overall the U_Z component of the complex highly hybrid mode has a nearly flat profile along both the x and y directions, but with ripples, as shown in Fig. 6.52(a).
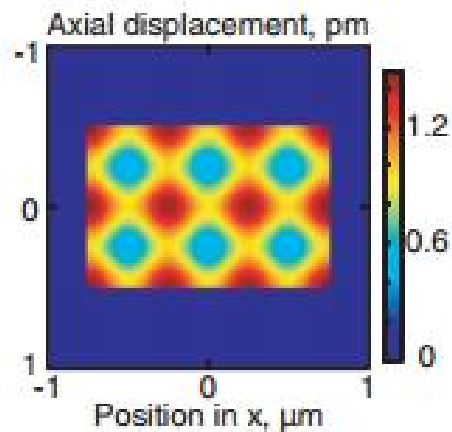
Fig. 6.53 Axial displacement component of the highly hybrid acoustic mode at 9.81 GHz [Laude, 2013].

6.5 Light-sound interaction in air cladded silica waveguide

When phase and momentum of acoustic and optical waves match, the grating induced by the acoustic wave reflects back the optical signal as Stokes wave, while its frequency is being down shifted. Since the scattered light undergoes a Doppler frequency shift, as it is reflected back from the acoustic wave induced moving grating, the SBS frequency, f_{SBS}, depends on

the acoustic velocity and this can be calculated using Eq. (5.6), discussed in Chapter 5. To understand the light-sound interaction in a air-clad strip silica waveguide properly, in this section, overlaps of the most of the acoustic modes discussed so far with the H_Y dominant field component of optical quasi-TE mode, their corresponding Brillouin gain coefficients, other few parameters are calculated.

It has been shown earlier that the acoustic U_X vector profile of the acoustic U_{11}^X mode varies with the waveguide width. The variation of the U_X component spotsize area with the width, W, for the U_{11}^X mode, when propagation constant $k = 10 \mu m^{-1}$, is shown in Fig. 6.54 by a dashed blue line. Here, the acoustic spotsize area is considered as the summation of elements area for which the acoustic displacement profile is equal or more than $1/e$ times of the maximum value of a given acoustic mode. Here, the guide height is kept constant at $H = 1 \mu m$. It can be observed here that the spotsize area increases as the width is increased.

It has been shown earlier in Fig. 6.3 that effective area of the optical field profile increases with the increases of guide width. As the acoustic spotsize area also increases with width, the value of overlap between these two modes also increases. The overlap between these two phase-matched optical and acoustic modes, is also calculated by using Eq. (5.5) while varying the waveguide width and is shown in Fig. 6.54 by a solid red line. As the guide width increases, the overlap, at the beginning, increases more rapidly after which it increases slowly. The overlap found at W = 2.5 μm was more than 84%.
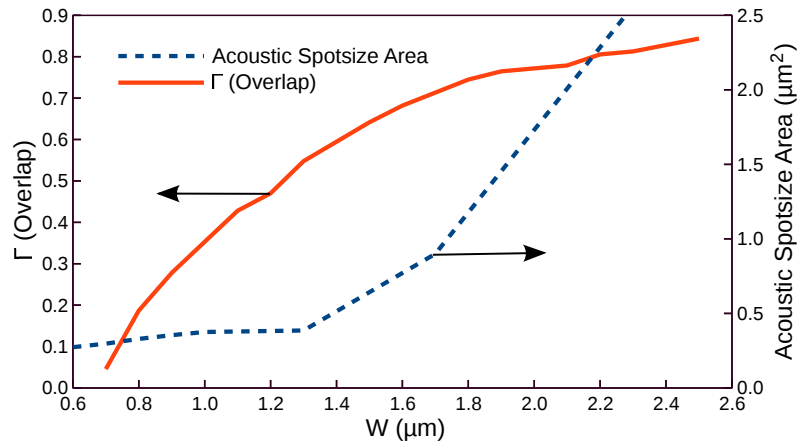
Fig. 6.54 Acoustic spotsize area (at k = 10 μm^{-1}) and Overlap between U_X component of U_{11}^X acoustic mode and H_Y field of quasi-TE optical mode with W.

Next, after determining the optical propagation constant, β_o, of the interacting H_{11}^Y mode, the propagation constant of the interacting acoustic modes were found using Eq. (5.4). The corresponding phase velocity, v, of the acoustic mode can then be determined and thus Eq. (5.6) can yield the resulting SBS frequency. The dashed red line in Fig. 6.55 shows the SBS

frequency shifts with the guide width for the fundamental shear acoustic mode, U_{11}^X. Here the SBS frequency falls with the increasing guide width and reaches its minimum 6.456 GHz near the 1.9 μm width and rises only slightly with the further increase of width.
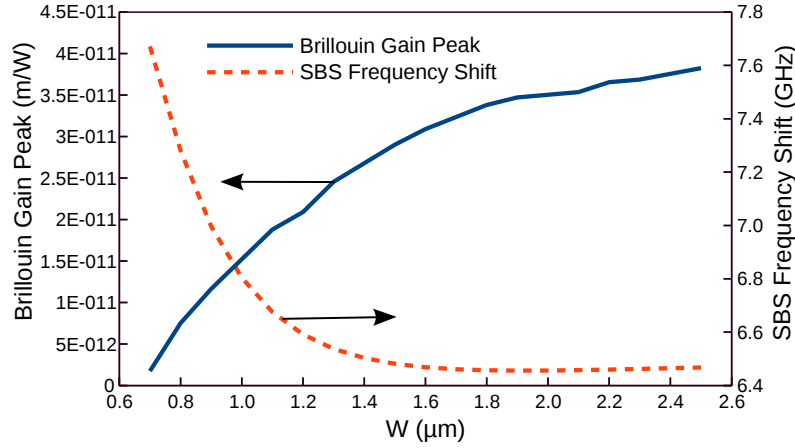
Fig. 6.55 SBS frequency shift and variations of Brillouin gain peak (g_B) of U_X displacement vector of the U_{11}^X mode with W.

For silica, the value of the opto-elastic coefficient can be considered as $p_{12} = 0.286$ [Eggleton, 2013] and the linewidth is considered as $\triangle v_B = 26.97$ MHz [Eggleton, 2013]. At the phase matched condition Γ and f_{SBS} can also be calculated from Eqs. (5.5) and (5.6), respectively as shown earlier in Chapter 5. Subsequently using Eq. (5.8), the Brillouin gain coefficient for strip silica waveguide can also be calculated. The solid blue line in Fig. 6.55, represents the g_B with varying width, W. As overlap of U_X component of U_{11}^X with H_Y field profile of quasi-TE mode increases with width, as seen in Fig. 6.54, the peak Brillouin gain also increases with the width. It attains a value of $2.9 \times 10^{-11} m/W$ at the guide width of 1.5 μm, which agrees with the peak Brillouing gain reported for silica in [Faris, 1993] at 532 nm optical wavelength, and increases to $3.82 \times 10^{-11} m/W$ at the guide width of 2.5 μm. As the Brillouin gain coefficient at 2.5 μm width reaches near saturation, for further increase in width its value can attain $4.52 \times 10^{-11} m/W$, which is Brillouin gain peak for silica reported in [Eggleton, 2013].

It was mentioned that modes in the high index contrast acoustic guide are hybrid in nature. The parameter hybridness is defined as the ratio of the maximum non-dominant displacement with the maximum dominant displacement. Earlier, evolution of the displacement profiles for the quasi-shear U_{11}^X and highly hybrid U_{11}^{HZ} and CHHM modes were shown. Their relative magnitudes were also mentioned.

As the fundamental acoustic shear mode displacement profile spreads in all over the core, its overlap with the dominant H_Y field profile of the H_{11}^Y mode is significant. On the

other hand, the overlap of this H_Y field profile of the quasi-TE mode with the non-dominant displacement vector profiles of the fundamental acoustic shear modes, which have odd symmetry, will cancel out and the resulting acousto-optical interactions would be negligible. It is expected, the overlap of the H_Y field profile with the dominant U_X profile of the U_{31}^X mode will be small, and this was calculated to be around 0.28%. Further, it should be noted that although the overlap of U_X profile of the U_{21}^X mode with the optical field is zero as the former has odd symmetry, however the non-dominant U_Z profile of this mode may have a considerable overlap, as this displacement vector profile has an even symmetry. It is calculated that the non-dominant U_Z field profile of U_{21}^X mode has a nearly 3.9% overlap with the dominant profile of the quasi-TE mode at guide width of $1.5 \mu m$. The variations of the overlap of U_Z field profile of U_{21}^X mode with the width is shown in Fig. 6.56 by a blue solid line, which increases with the guide width. Beside this, the contribution of this displacement profile in Brillouin gain peak with varying width is shown by a dashed red line in Fig. 6.56.
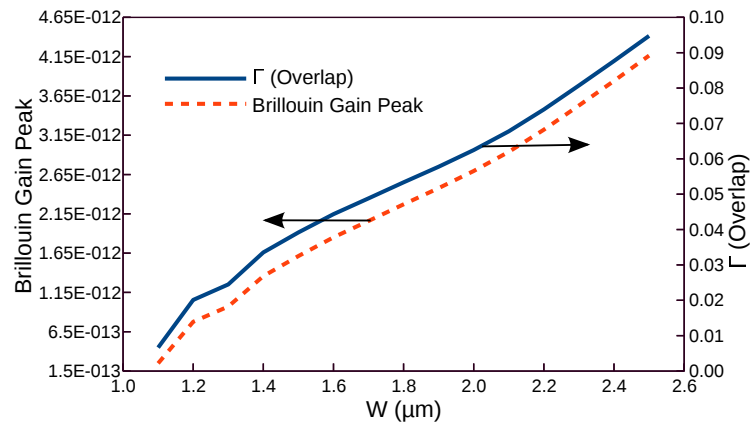
Fig. 6.56 Variations of Brillouin gain peak (g_B) of U_{21}^X acoustic mode and variations of overlap between its U_Z component and H_Y field of quasi-TE optical mode with the guide width.

Unlike the Brillouin gain peak variation of U_Z component of acoustic U_{21}^X mode with width, as shown in Fig. 6.56, the Brillouin gain peak variation of U_Z component of the highly hybrid acoustic U_{11}^{HZ} mode drops with the increase in width, as shown by the red solid line in Fig. 6.57. It is due the nature of overlap variation with width between U_Z component of U_{11}^{HZ} and H_Y component of fundamental quasi-TE mode, H_{11}^Y, shown by the dashed blue line. It can be easily understood with displacement profile evolution of U_Z component of U_{11}^{HZ}, which was discussed earlier. At phase matched condition and at 5.71 GHz the overlap of U_Z component of U_{11}^{HZ} was found 0.2947 and the Brillouin gain peak at 1.5 μm core width was

$1.51 \times 10^{-11} m/W$. For odd symmetry, the overlaps of the U_X and U_Y components of U_{11}^{HZ} were zero.
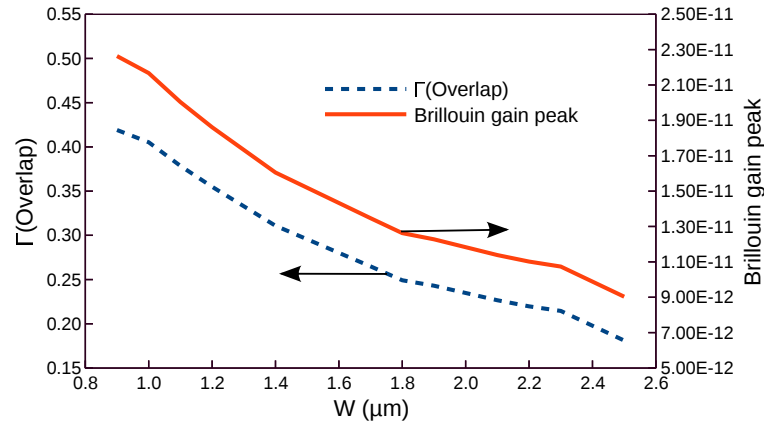
Fig. 6.57 Variations of Brillouin gain peak (g_B) of highly hybrid acoustic mode U_{11}^{HZ} and variations of overlap between its U_Z component and H_Y field of quasi-TE optical mode with the guide width.

Whereas, for phase matched condition at 9.81 GHz the overlap of the U_Z component of the CHHM mode was found 0.6029 and its contribution towards the Brillouin gain peak at 1.5 μm core width for this component was $1.8 \times 10^{-11} m/W$. However, because of odd symmetry overlaps of the U_X and U_Y components of the CHHM mode, respectively, were also zero, as expected.

The Brillouin gain spectrum (BGS) for silica is determined by the strong attenuation of sound wave in it. Due to the exponential decay of acoustic waves, the frequency dependent Brillouin gain, $g_B(f)$, has a Lorentzian spectral profile and can be calculated using Eq. (5.9), as discussed in Chapter 5.

Figure 6.58 shows the Brillouin gain spectrum (BGS) for air-clad strip silica waveguide in between 5 to 10 GHz. There are three significant peaks observed, the fist peak is the contribution of U_{11}^{HZ} mode, the second peak caused by U_{11}^{X} mode and the last one contributed by the complex highly hybrid mode (CHHM).

Since the Brillouin gain peak contributed by U_{11}^{X} and CHHM modes are found most significant, onward, in evaluating all parameters values quasi-shear U_{11}^{X} mode along with the CHHM mode will be considered.

The figure of merit can be used to determine the diffraction efficiency of acousto-optical devices, but few of them are independent of device configuration. In this regard, the most
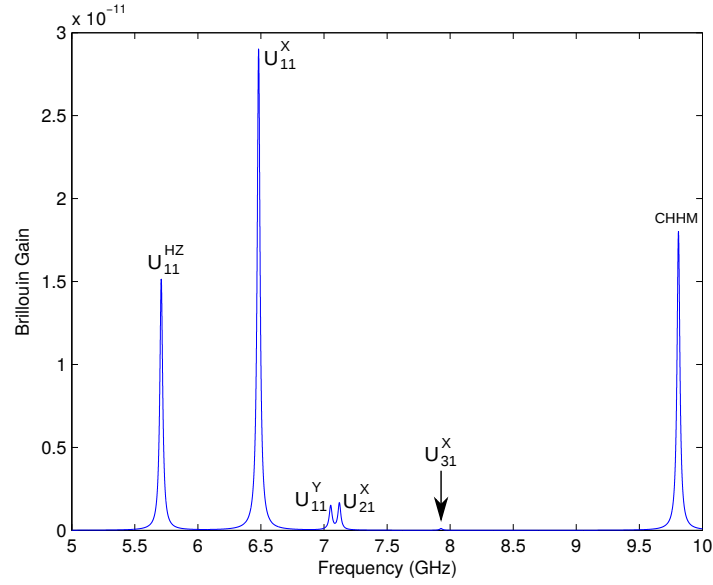
Fig. 6.58 Brillouin gain spectrum of strip silica waveguide surrounded by air between 5 GHz to 10 GHz.

suitable figure of merit is given [Ogusu, 2004] by:

$$M = \frac{n^7 p_{12}^2}{\rho v} \tag{6.1}$$

here, n is refractive index of the core, p_{12} is elasto-optic coefficient, ρ is density of silica and v is phase velocity of the phase matched acoustic mode. For silica it was calculated as 1.2344×10^{-7} sm^2/kg considering phase velocity of quasi-shear U_{11}^X mode and 8.156×10^{-8} sm^2/kg for the CHHM mode.

Now, phonon is termed as a quanta of the material vibration caused by acoustic wave in optical waveguides. The phonon life time for silica can be found [Ogusu, 2004] by:

$$T_B = \frac{1}{\alpha_A v} \tag{6.2}$$

here, α_A is the acoustic attenuation coefficient and v phase velocity of acoustic mode. For silica $T_B = 4.57$ ns [Ogusu, 2004].

If we consider the phase velocity of quasi-shear U_{11}^X mode in phase matched condition at 6.48 GHz, which was 3941.05 m/s, α_A was calculated as 555.23 cm^{-1}, where as for CHHM mode, it was, 366.84 cm^{-1}. These are equal to loss value of 24.114 dB/cm and 15.932 dB/cm, respectively.

The strength of acoustic wave induced index grating can be calculated [Eggleton, 2013] from:

$$G = g_B \frac{P_{th}L}{A_{eff}} \tag{6.3}$$

where, A_{eff} is optical mode effective area at phase matched condition, g_B is the Brillouin gain peak, L is the length of the waveguide and P_{th} is the threshold power for stimulated Brillouin scattering.

Finally, we calculate the threshold power for stimulated Brillouin scattering in an one centimetre long air-clad strip silica optical waveguide, by using the formula [Pant, 2011]:

$$P_{th} = 21 \frac{A_{eff}}{K g_B L_{eff}} \tag{6.4}$$

where, A_{eff} is optical mode effective area at phase matched condition, K is used to consider the polarization variation, g_B is the Brillouin gain peak and L_{eff} is the effective length of the waveguide. For small length $L \cong L_{eff}$.

If we consider $A_{eff} = 1.3050326 \, \mu m^2$, $K = 1$, $L = 1$ cm and $g_B = 2.908 \times 10^{-11} \, m/W$ for quasi-shear U_{11}^X mode, the threshold power for stimulated Brillouin scattering is 94.24 W. For $g_B = 1.8008 \times 10^{-11} \, m/W$ for CHHM mode, the threshold power for stimulated Brillouin scattering is 152.1862 W, which are quite high, but rapidly decreases with the increase of wageguide length. For both the modes the strength of acoustic wave induced index grating is 21. All the values calculated so far for the modes U_{11}^X and CHHM are listed in Table 6.2 for better referencing.

Table 6.2 Calculated parameter values for 1 *cm* long air-clad strip silica waveguide.

Parameters	For U_{11}^X mode	For CHHM mode
Z (Acoustic impedance)	$8.674 \times 10^6 \, kg/(m^2s)$	$1.313 \times 10^7 \, kg/(m^2s)$
v (Phase velocity)	$3941.05 \, m/s$	$5964.95 \, m/s$
g_B (Brillouin gain peak)	$2.908 \times 10^{-11} \, m/W$	$1.8008 \times 10^{-11} \, m/W$
P_{th} (SBS threshold power)	$94.24 \, W$	$152.1862 \, W$
α_A (Acoustic attenuation coefficient)	$24.114 \, dB/cm$	$15.932 \, dB/cm$
M (Figure of merit)	$1.2344 \times 10^{-7} \, sm^2/kg$	$8.156 \times 10^{-8} \, sm^2/kg$
G (strength of grating)	21	21

All the parameters values presented in Table 6.2 for U_{11}^X and CHHM modes are also calculated for the high hybrid surface acoustic mode U_{11}^{HZ} and listed in Table 6.3.

Table 6.3 Calculated parameter values for U_{11}^{HZ} mode in 1 *cm* long air-clad strip silica waveguide.

Parameters	For U_{11}^{HZ} mode
Z (Acoustic impedance)	8.1309×10^6 $kg/(m^2 s)$
v (Phase velocity)	3471.75 m/s
g_B (Brillouin gain peak)	6.0383×10^{-12} m/W
P_{th} (SBS threshold power)	453.86 W
α_A (Acoustic attenuation coefficient)	27.354 dB/cm
M (Figure of merit)	1.0103×10^{-7} sm^2/kg
G (strength of grating)	21

Beside these the SBS frequency, phase velocity and overlap for some of the modes in this waveguide are also listed below in Table 6.4.

Table 6.4 SBS frequency, phase velocity and overlaps for shear and highly hybrid acoustic modes in 1 *cm* long air-clad strip silica waveguide.

Mode	Component	f_{SBS} (*GHz*)	V (*m/s*)	Overlap (Γ)
U_{11}^{HZ}	U^Z	5.71	3471.75	0.2947
U_{11}^{X}	U^X	6.4815	3941.05	0.6416
U_{11}^{Y}	U^Y	7.053	4288.52	0.0346
U_{21}^{X}	U^Z	7.122	4330.5	0.0391
U_{31}^{X}	U^X	7.9284	4820.84	0.0028
U_{41}^{X}	U^Z	8.8056	5354.21	0.00001
CHHM	U^Z	9.81	5964.95	0.6029

6.6   Summary

Modal solutions of the fundamental and higher order acoustic shear modes of a strip silica waveguide exposed to air are presented, obtained by using a full-vectorial finite element method. For the first time, the evolution of fundamental dominant and non-dominant displacement vector profiles of acoustic shear mode are presented here. Existing symmetries of the waveguide have been exploited, which aided in not only to improve the solution accuracy but also to avoid degeneration of some of these modes. An **H**-field based full-vectorial program has also been used to find the optical modes of this waveguide.

Subsequently, as the same finite element mesh topology is used for both the acoustic and optical modal solutions, the overlap between the acoustic and optical modes were obtained accurately and more efficiently. Variations of the overlaps are shown for the fundamental and higher order acoustic modes with the fundamental quasi-TE optical mode.

It was observed for the air-clad strip silica waveguide that all the acoustic modes are highly hybrid in nature with all the three components of the displacement vectors. It was also shown that the non-dominant displacement vectors have smaller magnitudes but also have higher order spatial variations. Further, it was observed that for the fundamental acoustic modes the overlap of the non-dominant displacement vectors (being anti-symmetric) with the dominant H_Y profile (of the fundamental quasi-TE mode) is zero.

It was also shown here that the non-dominant displacement vector of higher order acoustic modes can have a symmetric profile, which can yield a considerable overlap with the optical mode. It has also been shown the Brillouin gain peak with varying width for the fundamental and higher order hybrid acoustic modes.

For nano-structured waveguides to incorporate the enhancement of the SBS process due to forces exerted by the radiation pressure of the guided optical wave and the waveguide boundary vibration may need to be considered. The value of the force, which in this chapter considered as zero, in the right hand side of Eq. (3.58), can be formulated from the spatial derivatives of Poynting vectors resulting from **H**-field, and also, the force due to the boundary element displacement can also be included in the program if necessary. Their incorporation will make the program a strong tool for analysing light-sound interaction in on-chip nano-structured waveguides.

Chapter 7

Conclusion and Future Aspects

7.1   Conclusion

As a conclusive chapter, the strength of this newly developed full-vectorial finite element based computer simulation code in determining and analysing acoustic wave propagation in optical waveguide and also evaluating interactions with the phase matched optical wave in optical waveguide of micro-meter dimension have been demonstrated here. Further, it will present the weakness of this code in determining acousto-optical interactions in nano-scale on-chip integrated optics, as it does not considered optical radiation pressure and motion of boundaries in formulation. Based on the recently published literature nearly 10% of the acousto-optical interactions value in nano-scale photonic devices could be due to radiation pressure and motion of boundaries. This chapter will conclude providing hints, how to incorporate these two important force parameters in the existing program to make it a strong simulation tool for on-chip nano-scale photonic devices as future expansion of this research work.

The main objective of this research was to develop further a full-vectorial FEM based computer simulation code to perform rigorous characterization of acoustic waves in low and hight index contrast optical waveguides and simultaneously study the interaction between optical and acoustic waves, specially due to SBS process. The achievements are stepwise illustrated below.

- A full-vectorial FEM based computer simulation code has been developed that can use real eigenvalue solver to get the modal solutions and perform rigorous characterization and study the evolution of fundamental and higher-order acoustic modes profiles that may exists in low and high contrast silica optical waveguides, especially giving preferences to the shear and longitudinal acoustics waves. The use of real eigenvalue solver

opened the possibility of increasing the mesh density in simulation that previously was limited to 100×100, when complex eigenvalue solver was used.

- The program is further developed to exploit symmetry boundary conditions that can be applicable at the symmetry axes of the generated modes to enhance strongly the modal solution accuracy and thus to eliminate modal degenerations, which were not possible at all before.

- Incorporate denser mash topology in the developed computer simulation code to bring further accuracy in the modal solutions that may be applicable for low and high index contrast silica waveguides. Now it is possible to use mesh density upto 1000×1000, which can be helpful in simulating efficiently the complex structures of different microfibres and photonic crystal fibres, which enables to detect minute variation in acoustic mode profile at the interfaces.

- Air has been incorporated as one of the guide medium in the simulation code for the acoustic wave, which made it possible to study on the evolution of the displacement vector profiles of the longitudinal and shear fundamental and higher-order acoustics modes with frequency in high index contrast silica waveguide with air cladding. Further, it aided to investigate the light-sound interactions in an air-clad silica waveguide to study the effect of SBS and associated frequency shift. The overlap between the highly hybrid acoustic modes and fundamental H_{11}^Y optical mode, thus to determine the Brillouin gain spectrum for a given bandwidth.

The structure of this thesis is organized in such a way to cover the development of the model for the molecular displacements to depict the propagation of the acoustic waves, generation of a full-vectorial finite element method based computer code to simulate this model and implications of this simulation code to characterize acoustic waves, rigorously, in low, moderate and high index contrast silica waveguides. Further to evaluate interactions of light and sound in these optical waveguides, specially the stimulated Brillouin scattering, in terms of overlap between the fundamental and higher order shear and longitudinal acoustics modes and fundamental quasi-TE, H_{11}^Y, optical mode, SBS frequency shift and Brilloin gain spectrum.

A categorical literature review has been presented in Chapter 1, which discussed the basic introduction to the research field of light-sound interactions in low and hight index contrast silica planar waveguide, particularly highlighting the detrimental effect of non-linear SBS process in high power delivery. It covered briefly, other optical non-linearities and existing numerical methods to study their effects. A short illustration was given regarding the aims

and objectives of this research. At the end the structure of the thesis also presented outlining the content of each chapter. Further it highlighted the aim and objectives.

The Chapter 2 began with the introduction to the basic concepts of acoustic waves in isometric medium, showing that the acoustic wave propagates through a optical guide by displacement of particles, where the guide material density and elasticity has major roles to play, thus modulates the optical refractive index through variation of material density along transverse plane and longitudinal direction, respectively. It also discussed in greater details the physical quantities, those are related to the acoustic wave propagation and may arise the possibility of maximum interactions with optical waves in planar silica optical waveguides. Also it will aid to categorize acoustic modes depending on the placements of dominating acoustic displacement components related to the direction of propagation. Moreover, reduced form of stress and strain notations were introduced to generate the systems of governing equations of the acoustic wave propagation with help of strain field related to the acoustically vibrating body, equation of motion and Hooke's law. These were used to find the governing wave equation considering the particle displacements in the two dimensional guide, considered to be small. Also, for an isotropic solid, longitudinal and shear wave velocities relation with the various elastic constants and material density were provided. At the end, families of acoustic wave propagation modes, for instance, longitudinal, shear, surface and plate wave also were introduced.

The Variational approach based finite element method were provided in Chapter 3. Moreover, it presented the path way to incorporate FEM formulation using real eigenvalue solver in acoustic wave propagation, and thus generation of 2D molecular displacement profiles of acoustic modes as end results. Here domain discretisazion was performed only upon the cross-section of the waveguide by meshing with triangular finite elements. It introduced symmetry boundary conditions, used for the first time in acoustic mode profile generation, to increase modal solution accuracy and eliminate modal degeneration. Furthermore, it demonstrated the strength of this simulation code proving its solution convergence with the help of Aitken's formula, also provided some comparison with the previous work done in complex domain and with the published results for a 1 cm^2 steel waveguide in vacuum. At the end displacement vector profiles of two highly hybrid acoustic modes that may exist in the steel waveguide were presented.

A rigorous analysis of acoustic modes in the low index contrast silica planar waveguide consisting of a 3% Ge-doped core and pure silica as cladding was performed with the help of the developed full-vectorial acoustic mode solver by using computationally efficient finite element method in Chapter 4, also the advantages of using the symmetry conditions and the type of symmetry walls which can be used were discussed. In this chapter, the general

concept of mode pattern recognition was introduced for a low index contrast silica planar waveguide, based on the pattern of spatial variations of displacement vector profiles of the fundamental and higher order shear and longitudinal acoustic modes. The spatial variations of the dominant and non-dominant displacement vectors of the longitudinal and shear acoustic modes were also shown. It was shown that by using Aitken's extrapolation the solution accuracy can also be improved with the use of finite computer resources. Furthermore, it provided the detail study of the variations of dispersion, birefringence and hybridness with acoustic frequency for these acoustic modes, first considering decoupled modes, then considering co-existing shear and longitudinal modes. Also, the the influence of increasing doping concentration in the core was presented here. Thus, this chapter mainly concentrated on characterization of both the longitudinal and shear acoustic modes for a 3% Ge-doped silica planar waveguide with dimension 2 $\mu m \times 1$ μm and were regorously studied in this chapter. All these modes may have either dominant transverse or longitudinal component but also two other non-dominant components. As 3% Ge:doped planar silica waveguide can support shear and longitudinal acoustic modes, this can also support optical wave but at a shorter visible wavelength. However, for a silica waveguide operating at 1550 nm wavelength, waveguide dimension or Ge doping needs to be increased. In such cases the co-guidance of the acoustic and optical mode will give rise to SBS above a certain threshold power.

The Chapter 5 mainly focused on the interactions between the fundamental and higher order shear and longitudinal acoustic modes and fundamental quasi-TE optical H_{11}^Y mode in terms of their coupling in phased matched condition through determining overlap between their mode profiles by considering displacement vector for acoustic wave and full-vectorial **H**-field for optical wave. This study was performed in a moderately higher index contrast silica planar waveguide with a 10% Ge-doped core with a dimension of 6 $\mu m \times 3$ μm, embedded in a pure silica cladding. It discussed also the displacement vector profiles, variation of modal dispersions, hybridness and birefringence with acoustic frequency and SBS frequency shift with the guide width variation. Modal solutions of the fundamental and higher order longitudinal and shear acoustic modes including the dominant and non-dominant displacement vector profiles of the both acoustic modes were presented in details. The existing symmetries of the waveguide were being exploited for not only to improve the solution accuracy but also to avoid degeneration in some of these modes. Further, an **H**-field based full-vectorial program was used to find the optical modes of this waveguide. Since the same finite element mesh topology were used for both the acoustic and optical modal solutions, the overlap between the acoustic and optical modes were obtained accurately and more efficiently. Variations of the f_{SBS} and overlaps were shown for the fundamental and higher order longitudinal and shear acoustic modes with the fundamental quasi-TE optical

mode. It was observed that all the acoustic modes are hybrid in nature with all the three components of the displacement vectors and the non-dominant displacement vectors have smaller magnitudes but with higher order spatial variations. Moreover, it was shown that for the fundamental longitudinal and shear acoustic modes the overlap of the non-dominant displacement vectors, being anti-symmetric, with the dominant H_Y profile of the fundamental quasi-TE mode was zero. It was also shown that the non-dominant displacement vector of higher order acoustic modes can have a symmetric profile and also a considerably higher overlap with the optical mode. Although the overlap of the dominant displacement vector of a mode with odd spatial variations was zero with the fundamental quasi-TE mode, but the overlap of its non-dominant displacement vector was shown significantly high, which cannot be ignored. In this chapter, also Brillouin gain coefficients of some shear and longitudinal modes were calculated and presented. Along with these the Brillouin gain spectrum from 6 *GHz* to 10.5 *GHz* was provided, which showed significant two peaks around 6.5245 *GHz* and 10.3457 *GHz*.

The study of the unique features of the mode evolution in a high index contrast optical waveguide formed by an air-clad strip silica core of dimension 1.5 *μm* × 1 *μm* were demonstrated in Chapter 6. For the first time it showed in details that the evolution of the highly hybrid acoustic modes in silica planar waveguide with frequency for this index combinations with relatively higher contrast. The displacement vector profiles were compared with the published results. Moreover, this chapter also provided the analysis of variations of the modal dispersions, hybridness and birefringence with acoustic frequency for these highly hybrid acoustic modes and showed the interactions with quasi-TE optical mode through overlap and SBS frequency shift and thus delivered the Brilloin gain spectrum from 5.5 *GHz* to 10 *GHz* for this optical waveguide. The modal solutions of the fundamental and higher order acoustic shear modes and highly hybrid modes were obtained by using a full-vectorial finite element method. Existing symmetries of the waveguide were also exploited and an **H**-field based full-vectorial program was used to find the optical modes. To improve efficiency and accuracy in finding the overlap between the acoustic and optical modes, same finite element mesh topology were used for both the acoustic and optical modal solutions. Variations of the overlaps for the fundamental and higher order acoustic modes with the fundamental quasi-TE optical mode were shown. The Brillouin gain peak with varying width for the fundamental and higher order hybrid acoustic modes were also shown. The strength of Bragg gratings, threshold SBS power for this air-clad silica guide were also evaluated and further comments were added on figure of merit (FOM) and acoustic attenuation coefficient.

For nano-structured waveguides to incorporate the enhancement of the SBS process due to forces exerted by the radiation pressure of the guided optical wave and the waveguide

boundary vibration may need to be considered. The value of the force, which in this thesis considered as zero, in the right hand side of Eq. (3.58), can be formulated from the spatial derivatives of Poynting vectors resulting from **H**-field, and also, the force due to the boundary element displacement can also be included in the program if necessary. Their incorporation will make the program a strong tool for analysing light-sound interaction in on-chip nano-structured waveguides.

A rigorous study of light-sound interactions in optical waveguide can be useful in the development of novel SBS sensors or in the design of optical waveguide to deliver high power. Thus the results presented in this thesis shown that to study light-sound interaction in an effective way, the use of full-vectorial acoustic and optical modal approaches are very much necessary.

7.2   Future works

It is hard to explore and investigate all arena of SBS in such a short period of time. The potential the developed program has, can be considered only paved the path for future, which opened a door for researcher to explore for higher Brillouin gain in different combinations of materials, incorporating different complex structures and so on. Few are illustrated below, those were in mind, to be completed in future.

To attain large Brillouin gain in a very short distance of centimetre scale with moderate pump power of 100 mW, faces challenges that can be overcome in two ways. Either, to construct devices by using materials with high refractive index and elasto-optic coefficient to highly confine optical and acoustic modes, or, by using multiple pass structure. Soft glasses like chalcogenide have large elasto-optic coefficient and refractive index, which based on Eq. (5.8) may suggest that the devices constructed with such glasses, arsenic selenide (As_2Se_3) and arsenic sulphide (As_2S_3), may exhibits large Brillouin gain that are commonly used in nonlinear optics. The large refractive index and elasto-optic coefficient of these materials will also provide nonlinear index of refraction (n_2), resulting in a large Kerr effect. Although, in chatcogenide fibres to excite SBS by using moderate level of optical power of tens of milliwatts requires large length of several meters due to its large mode area. If, by keeping the average pump power at milliwatt level, pump is pulsed to attain a peak power of several watts, SBS can be induced even for a length of tens of centimeters. A SBS ring laser was recently reported that used a continuous wave pump power of 37 mW in a 3 m long suspended core. In As_2Se_3 fibre slow- and fast-light have been demonstrated recently using average pump power (tens of milliwatts) in with much shorter length than silica. Hence, chalcogenide

glasses are highly efficient for exiting SBS and other nonlinear effects in shorter lengths. Chalcogenide based on Tellurium (Te) can be investigated to harness higher SBS gain.

Surface plasmon polaritons are electromagnetic waves of infrated or visible frequency that travel along a metal-air or metal-dielectric interfaces, which involves with charge motion in the metal and electromagnetic waves in the dielectric or air. These are categorize as a type of surface wave and the guidance along the interfaces is much similar in the way the light can be guided in optical fibre. If a silicon microwire is considered with thin layer of gold on it, which can be potential guide structure to exploit the interaction of guided surface acoustic wave with surface plasmon polaritons. This can be a strong candidate in SBS harnessing, which is not yet reported in literature.

Appendix A

Stress, Strain and Reduction of Notations

Stress and strain vectors

The stress and strain tensors were briefly covered in Sections 2.2 and 2.3 of the thesis. These are derived in three dimensional forms and given in more details in this section. The common forms of the notations after reduction are used based on the symmetry of stress and strain tensors.

Strain tensor

Due to the applying stress, consider, a point R in the material is displaced to point R'. The distances of these points from the reference point O, as shown in Fig. A1, are r and r + u, respectively. Here, u is the displacement vector. Considering the material distance between points R and W is ℓ. The distance of point W from reference is r + δr. Due to displacement after applying stress the material distance changed to ℓ'. Now it can be shown that,

$$\ell^2 = (\delta r)^2 = (\delta x_1)^2 + (\delta x_2)^2 + (\delta x_3)^2 \tag{A.1}$$

and

$$\ell'^2 = (\delta r + \delta u)^2 = \ell^2 + 2\delta r \delta u + (\delta u)^2 \tag{A.2}$$

The displacement component along the x-direction, δu_x can be expressed as,
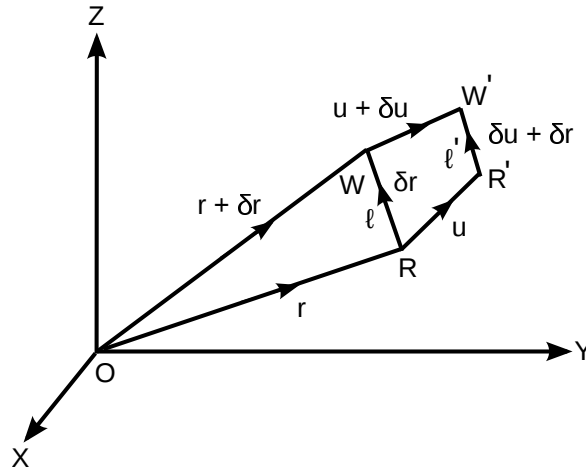
Fig. A.1 Material displacement due to stress [Sriratanavaree, Thesis, 2014].

$$\delta u_x = \frac{\partial u_x}{\partial x}\delta x + \frac{\partial u_x}{\partial y}\delta y + \frac{\partial u_x}{\partial z}\delta z \qquad (A.3)$$

Similar notations can be used for δu_y and δu_z, the displacement components along y and z-directions, respectively. For convenient summarization of these relations by tensor notations, we can write,

$$\delta u_i = \sum_j \frac{\partial u_i}{\partial x_j}\delta x_j \qquad (A.4)$$

where i can be x, y, z and the summation over j is easily understood for a given i.

Using this concept and applying Taylor expansion for Eq. (A.2), allowing upto second order term of δx_i, we have,

$$\ell'^2 = \ell^2 + 2\frac{\partial u_i}{\partial x_j}\delta x_i \delta x_j + \frac{\partial u_i}{\partial x_i}\frac{\partial u_i}{\partial x_k}\delta x_i \delta x_k \qquad (A.5)$$

here, as discussed in Section 2.3, the notation implies the double summations over the three independent suffixes i, j and k on the right hand side of Eq. (A.5). It can be noted that vector δr is replaced by δx_i and the scalar product $I.J$ is shown by $I_i J_j$.

The true measure of the material deformation is the change occurred in ℓ^2. In case the change in δr were used instead, the change would end up in rotation rather than the change in length ℓ, that is why δr is not used as a measure of deformation.

Now, the second term in Eq. (A.5) can be written as,

$$\frac{\partial u_i}{\partial x_j}\delta x_i \delta x_j = \frac{1}{2}\left(\frac{\partial u_i}{\partial x_j} + \frac{\partial u_j}{\partial x_i}\right)\delta x_i \delta x_j \tag{A.6}$$

Also changing the suffix k in the third term of Eq. (A.5) with suffix j and rewriting the Eq. (A.5), we have,

$$\ell'^2 = \ell^2 + 2S_{ij}\delta x_i \delta x_j \tag{A.7}$$

here the strain tensor S_{ij} can be expressed as,

$$S_{ij} = \frac{1}{2}\left(\frac{\partial u_i}{\partial x_j} + \frac{\partial u_j}{\partial x_i} + \frac{\partial u_i}{\partial x_i}\frac{\partial u_i}{\partial x_j}\right) \tag{A.8}$$

Since S_{ij} is symmetric, which can be implied from its definition, for small deformation, being of second order neglecting the last term of Eq. (A.8), we have,

$$S_{ij} = \frac{1}{2}\left(\frac{\partial u_i}{\partial x_j} + \frac{\partial u_j}{\partial x_i}\right) \tag{A.9}$$

henceforth this term will be used.

Now, alternatively, we can use a vector symbol **S** and define the strain S_{ij} as,

$$\mathbf{S} = \begin{bmatrix} S_{11} & S_{12} & S_{13} \\ S_{21} & S_{22} & S_{23} \\ S_{31} & S_{32} & S_{33} \end{bmatrix} = \begin{bmatrix} S_{xx} & S_{xy} & S_{xz} \\ S_{yx} & S_{yy} & S_{yz} \\ S_{zx} & S_{zy} & S_{zz} \end{bmatrix} \tag{A.10}$$

here the subscripts 1, 2 and 3 are equivalent to x, y and z, respectively, which are common in literature.

Again, differentiating Eq. (A.9) with respect to time, t, we have,

$$\frac{\partial S_{ij}}{\partial t} = \frac{1}{2}\left(\frac{\partial v_i}{\partial x_j} + \frac{\partial v_j}{\partial x_i}\right) \tag{A.11}$$

here $v = \frac{\partial u}{\partial t}$ is the particle velocity in the material, which is equivalent to the one-dimensional equation of mass conservation that can be given as, $\frac{\partial}{\partial z}\rho_m v + \frac{\partial}{\partial t}\rho_m = 0$, but provides more information. If only the diagonal terms are taken, it can be seen that $\nabla.v = \frac{\partial v_i}{\partial x_i}$ and the mass conservation equation can be written as,

$$\rho_{m0}\nabla.v + \frac{\partial \rho_{ml}}{\partial t} = 0 \tag{A.12}$$

Considering non-zero ρ_{m0} and we can use the following relation from Eq. (A.11),

$$\nabla.v = \frac{\partial}{\partial t}(S_{11} + S_{22} + S_{33}) \tag{A.13}$$

Which is equivalent to $\frac{\partial}{\partial z}\rho_m v + \frac{\partial}{\partial t}\rho_m = 0$ and will be verified in different way. The diagonal terms are associated with the longitudinal strain and the off-diagonal terms are associated with the shear strain.

It can be noted that the volume of a small portion $\delta \bigvee$ of the material is $\delta x_1 \delta x_2 \delta x_3$ and after deformation it becomes $\delta \bigvee'$, where,

$$
\begin{aligned}
\delta \bigvee' &= (\delta x_1 + \delta u_1)(\delta x_2 + \delta u_2)(\delta x_3 + \delta u_3) \\
&= \delta \bigvee \left(1 + \frac{\partial u_1}{\partial x_1}\right)\left(1 + \frac{\partial u_2}{\partial x_2}\right)\left(1 + \frac{\partial u_3}{\partial x_3}\right) \\
&\approx \left(1 + \frac{\partial u_1}{\partial x_1} + \frac{\partial u_2}{\partial x_2} + \frac{\partial u_3}{\partial x_3}\right)
\end{aligned}
\tag{A.14}
$$

The change in volume,

$$\delta \bigvee' - \delta \bigvee = \delta \bigvee (S_{11} + S_{22} + S_{33}) \tag{A.15}$$

It can be notice from Eq. (A.15), that the sum of the diagonal components of the strain tensor is the relative change in volume, $\frac{\delta \bigvee' - \delta \bigvee}{\delta \bigvee}$. The shear term do not contribute to a change in volume, which can be realize by placing Eq. (A.13) in Eq. (A.12). From this the following results can be found,

$$\rho_{ml} = -\rho_{m0}(S_{11} + S_{22} + S_{33}) \tag{A.16}$$

which is similar to Eq. (A.13) when,

$$\frac{\rho_{ml}}{\rho_{m0}} = -\frac{(\delta\mathbb{V}' - \delta\mathbb{V})}{\delta\mathbb{V}} \tag{A.17}$$

Stress tensor

If $\mathbb{V}$ is the volume of a body, the force in x-direction on the body can be given as, $\int F_x d\mathbb{V}$, here F_x is a scalar quantity. A scalar quantity can be expressed as the divergence of a vector. Thus it can be written,

$$
\begin{aligned}
F_x &= \nabla.A \\
F_y &= \nabla.B \\
F_z &= \nabla.C
\end{aligned} \tag{A.18}
$$

From the Gauss's theorem, it can be written as,

$$\int_{\mathbb{V}} F_x d\mathbb{V} = \int_{\mathbb{V}} \nabla.A d\mathbb{V} = \int_S A dS \tag{A.19}$$

here the surface integral is taken around the enclosing volume $\mathbb{V}$.

To express volume integration of each force component, three components are needed, so, it will total nine components, A_x, A_y, A_z, B_x, B_y, B_z, C_x, C_y and C_z to represent $\int F_x d\mathbb{V}$, $\int F_y d\mathbb{V}$ and $\int F_z d\mathbb{V}$. In tensor notation, $F_i = \frac{\partial T_{ij}}{\partial x_j}$, which is the brief form of,

$$
\begin{aligned}
F_i &= \sum_j \frac{\partial T_{ij}}{\partial x_j} \\
\therefore F_x &= \frac{\partial T_{xx}}{\partial x} + \frac{\partial T_{xy}}{\partial y} + \frac{\partial T_{xz}}{\partial z}
\end{aligned} \tag{A.20}
$$

this is similar for other components as well. Here T_{ij} is the stress tensor, its relation to the previously mentioned notations are, $A_x = T_{xx} = T_{11}$, $A_y = T_{xy} = T_{12}$, $A_z = T_{xz} = T_{13}$, so and so forth.

Now, the average force on an element of volume $d\mathbb{V}$ can be given as,

$$\frac{1}{d\bigvee} \int \nabla.\mathbf{T}d\bigvee$$

$$\Rightarrow \frac{1}{d\bigvee} \int \frac{\partial T_{ij}}{\partial x_j}d\bigvee$$

$$\Rightarrow \frac{1}{d\bigvee} \int T_{ij}dS_j \qquad\qquad (A.21)$$

$$\Rightarrow \frac{1}{d\bigvee} \oint \mathbf{T}.\mathbf{n}\, dS$$

where $\nabla.T$ is defined as $\frac{\partial T_{ij}}{\partial x_j}$ and dS_j is the surface element vector directed along the outward normal.

Considering the force on the surface is in the z-direction, which has, therefore, three normal components in its surface that may compromise the vector C in Eq. (A.18) and these are T_{xz}, T_{yz} and T_{zz}. As shown in Fig. A.2(b), the first two terms are shear stress and tend to distort the surface of an isotropic material. The last term is the longitudinal stress, as shown in Fig. A.2(a). As illustrated in Fig. 2.3, all stress component are applied to a cube. Again, as $\int T_{ij}dS_j = \int T_{ji}dS_i$, it can be shown that $T_{ij} = T_{ji}$, which implies $\mathbf{T}$ is a symmetric tensor.
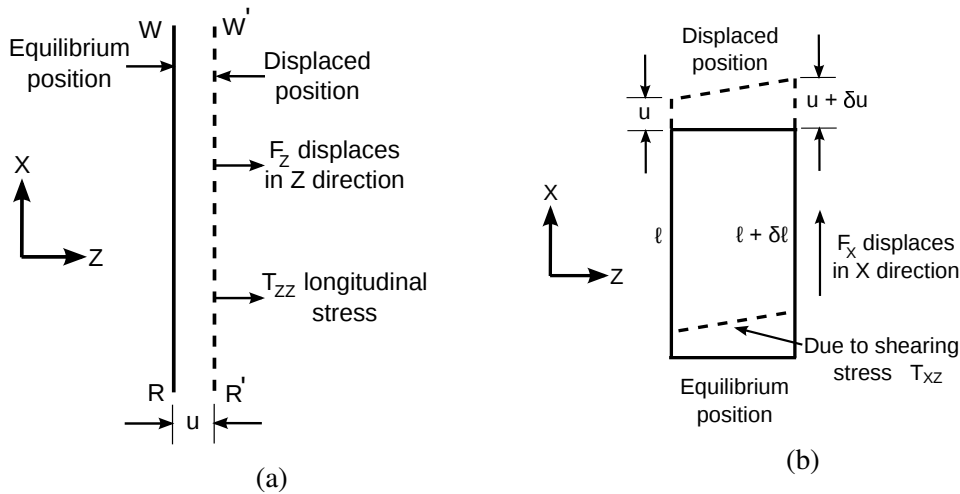
Fig. A.2 Effects of (a) longitudinal and (b) shear stresses normal to the surface [Sriratanavaree, Thesis, 2014].

Equation of motion

Due to internal stresses, the force on an element of volume $d\bigvee$ is $\int T.n\,dS$. Hence, if only the internal stresses are applied, the equation of motion for the first-order displacement can be written as,

$$\rho_{m0}\frac{\partial^2 u^e}{\partial t^2} = lim_{d\bigvee \to 0}\left(\frac{\int \mathbf{T}.\mathbf{n}\,dS}{d\bigvee}\right) \tag{A.22}$$

Hence,

$$\rho_{m0}\frac{\partial^2 u^e}{\partial t^2} = \nabla.\mathbf{T}$$
$$\Rightarrow \rho_{m0}\frac{\partial^2 u^e}{\partial t^2} = \frac{\partial T_{ij}}{\partial x_j} \tag{A.23}$$

where ρ_{m0} is the density of material.

Abbreviated subscripts and symbolic notation

In order to minimise the complexity of the strain and stress tensors, it is worthy to apply symmetry and as well to use abbreviated subscripts. Here, in this section, abbreviated subscript notations are illustrated and there uses are highlighted.

For strain tensor

It has been mentioned earlier that the strain tensor can be defined as,

$$S_{ij} = \frac{1}{2}\left(\frac{\partial u_i^e}{\partial x_j} + \frac{\partial u_j^e}{\partial x_i}\right) \tag{A.24}$$

Since, the strain is a symmetric tensor, it can be shown that $S_{xy} = S_{yx}$, so and so forth. Thus, it is possible to use reduced notation with showing lesser subscripts. In Eq. (A.24), superscript 'e' is used to indicate in element. The standard reduce notation of the strain can be expressed in matrix form as,

$$\mathbf{S} = \begin{bmatrix} S_{11} & S_{12} & S_{13} \\ S_{21} & S_{22} & S_{23} \\ S_{31} & S_{32} & S_{33} \end{bmatrix} = \begin{bmatrix} S_1 & \frac{S_6}{2} & \frac{S_5}{2} \\ \frac{S_6}{2} & S_2 & \frac{S_4}{2} \\ \frac{S_5}{2} & \frac{S_4}{2} & S_3 \end{bmatrix} \tag{A.25}$$

It can be noted that the notations follows a cyclic order, where, the longitudinal strains corresponding to subscripts 1, 2 and 3, respectively, and the shear strains corresponding to the subscripts 4, 5 and 6, respectively. Which is summarized in Table A.1, below.

Table A.1 Reduced tensor notation.

Tensor notation	Reduced notation	Corresponding Strain
xx	1	Longitudinal in the x-direction
yy	2	Longitudinal in the y-direction
zz	3	Longitudinal in the z-direction
$yz = zy$	4	Shear y - z
$zx = xz$	5	Shear z - x
$xy = yx$	6	Shear x - y

The strain tensor can be expressed in the form of column matrix as shown below,

$$\begin{bmatrix} S_1 \\ S_2 \\ S_3 \\ S_4 \\ S_5 \\ S_6 \end{bmatrix} = \begin{bmatrix} \frac{\partial}{\partial x} & 0 & 0 \\ 0 & \frac{\partial}{\partial y} & 0 \\ 0 & 0 & \frac{\partial}{\partial z} \\ 0 & \frac{\partial}{\partial z} & \frac{\partial}{\partial y} \\ \frac{\partial}{\partial z} & 0 & \frac{\partial}{\partial x} \\ \frac{\partial}{\partial y} & \frac{\partial U_y}{\partial x} & 0 \end{bmatrix} \begin{bmatrix} u_x^e \\ u_y^e \\ u_z^e \end{bmatrix} \tag{A.26}$$

This was only possible due to the terms $\frac{1}{2}$ used in Eq. (A.25), it is suitable to define the matrix in Eq. (A.26) with symbolic notation as below [Auld, 1973],

$$\mathbf{S} = \nabla_S u^e \tag{A.27}$$

here $\nabla_S u^e$ is defined as the symmetric part of ∇u^e for an element. $\nabla_S u^e$ is actually the first matrix of the right hand side of Eq. (A.26). While unreduced, the symmetric ∇_S is apparent because of Eq. (A.24).

From Eq. (A.26) it is obvious that for longitudinal motion and propagation both in the x-direction can be expressed by the relation $S_1 = \frac{\partial u_x^e}{\partial x}$, which depicts a longitudinal wave passing through a flat plate. Whereas, for a plane shear wave that has propagation in the z-direction but the particle displacement occurs in the y-direction, can be defined by the relation $u_x^e = u_z^e = 0$ and $S_4 = \frac{\partial u_y^e}{\partial z}$. For this case, all other strain components are zero. This corresponds to the flexural motion of a thin strip.

For stress tensor

Reduced notation can also be used for stress tensor. It can be written as,

$$
\mathbf{T} = \begin{bmatrix} T_{xx} & T_{xy} & T_{xz} \\ T_{yx} & T_{yy} & T_{yz} \\ T_{zx} & T_{zy} & T_{zz} \end{bmatrix} = \begin{bmatrix} T_1 & T_6 & T_5 \\ T_6 & T_2 & T_4 \\ T_5 & T_4 & T_3 \end{bmatrix} = \begin{bmatrix} T_1 \\ T_2 \\ T_3 \\ T_4 \\ T_5 \\ T_6 \end{bmatrix} \tag{A.28}
$$

here the convention is to omit the $\left(\frac{1}{2}\right)$ terms [Auld, 1973].

Now the equation of motion relating the stress terms is,

$$
\nabla.\mathbf{T} = \rho_{m0} \frac{\partial v}{\partial t} \tag{A.29}
$$

This can be related to the reduced notation as,

$$
\rho_{m0} \frac{\partial}{\partial t} \begin{bmatrix} v_x \\ v_y \\ v_z \end{bmatrix} = \nabla.\mathbf{T} = \begin{bmatrix} \frac{\partial}{\partial x} & 0 & 0 & 0 & \frac{\partial}{\partial z} & \frac{\partial}{\partial y} \\ 0 & \frac{\partial}{\partial y} & 0 & \frac{\partial}{\partial z} & 0 & \frac{\partial}{\partial x} \\ 0 & 0 & \frac{\partial}{\partial z} & \frac{\partial}{\partial y} & \frac{\partial}{\partial x} & 0 \end{bmatrix} \begin{bmatrix} T_1 \\ T_2 \\ T_3 \\ T_4 \\ T_5 \\ T_6 \end{bmatrix} \tag{A.30}
$$

For instance, if the stress field has only one component, a shear stress $T_5 = T_{xz}$ propagating in z-direction, then $\nabla.\mathbf{T}$ becomes $\frac{\partial T_5}{\partial z}$ and it corresponds to an acceleration in the x-direction.

For elasticity

The elasticity tensor C_{ijkl} can also be represented using reduced notation. Since, $S_{ij} = S_{ji}$ and $T_{ij} = T_{ji}$, it follows that $C_{ijkl} = C_{jikl} = C_{ijlk} = C_{jilk}$. As discussed earlier in Section 2.3.4, this reduced the total number of independent elements in elasticity matrix from 81 to 36. Thus it can be written as,

$$
\begin{bmatrix} T_1 \\ T_2 \\ T_3 \\ T_4 \\ T_5 \\ T_6 \end{bmatrix} = \begin{bmatrix} C_{11} & C_{12} & C_{13} & C_{14} & C_{15} & C_{16} \\ C_{21} & C_{22} & C_{23} & C_{24} & C_{25} & C_{26} \\ C_{31} & C_{32} & C_{33} & C_{34} & C_{35} & C_{36} \\ C_{41} & C_{42} & C_{43} & C_{44} & C_{45} & C_{46} \\ C_{51} & C_{52} & C_{53} & C_{54} & C_{55} & C_{56} \\ C_{61} & C_{62} & C_{63} & C_{64} & C_{65} & C_{66} \end{bmatrix} \begin{bmatrix} S_1 \\ S_2 \\ S_3 \\ S_4 \\ S_5 \\ S_6 \end{bmatrix}
\tag{A.31}
$$

$$
\mathbf{T} = C.\mathbf{S}
\tag{A.32}
$$

where the general terms is C_{IJ}, capital subscripts are used to denote the reduced notation and considering $C_{IJ} = C_{JI}$, thus, further due to symmetry, the total number of independent elements in elasticity matrix reduces to 21.

For instance: Cubic crystal

Certain symmetric conditions possessed by most of the crystals can reduce the required number of elements in elastic coefficient matrix. For example, material having cubic crystal lattice, seems similar in $\pm x$, $\pm y$ and $\pm z$ directions. Which implies, among the elements of the elastic matrix, $C_{11} = C_{22} = C_{33}$, $C_{44} = C_{55} = C_{66}$ and $C_{12} = C_{13} = C_{23}$. All other diagonal terms are zero due to the mirror symmetry. Hence for a cubic crystal, the elastic coefficient matrix can be like,

$$
C = \begin{bmatrix} C_{11} & C_{12} & C_{13} & 0 & 0 & 0 \\ C_{21} & C_{22} & C_{23} & 0 & 0 & 0 \\ C_{31} & C_{32} & C_{33} & 0 & 0 & 0 \\ 0 & 0 & 0 & C_{44} & 0 & 0 \\ 0 & 0 & 0 & 0 & C_{55} & 0 \\ 0 & 0 & 0 & 0 & 0 & C_{66} \end{bmatrix}
\tag{A.33}
$$

When, a shear wave is propagating along the z-axis having motion in the x-direction, it can be written based on the Eq. (A.26),

$$S_5 = \frac{\partial u_x^e}{\partial z} \tag{A.34}$$

Again, using Eqs. (A.31) and (A.33), it can be shown,

$$T_5 = C_{44}S_5 \tag{A.35}$$

Further, assuming that the RF components vary as $e^{j\omega t}$, then it can be written, $v_x = j\omega u_x^e$, based on Eqs. (A.29) and (A.30), we have,

$$\frac{\partial T_5}{\partial z} = j\omega \rho_{m0} v_x \tag{A.36}$$

However, from Eqs. (A.34) and (A.35), we have,

$$C_{44}\frac{\partial v_x}{\partial z} = j\omega T_5 \tag{A.37}$$

For the shear wave propagation, Eqs. (A.36) and (A.37) are the transmission-line equations. Further assuming that wave propagates as $e^{\pm jk_S z}$, it can be noticed that for shear wave in cubic crystal, we have,

$$k_S^2 = \omega^2 \left(\frac{\rho_{m0}}{C_{44}} \right) \tag{A.38}$$

On the other hand, if we consider longitudinal wave in the z-direction having only u_x^e or v_x finite, the longitudinal propagation constant, k_L, can be given as,

$$k_L^2 = \omega^2 \left(\frac{\rho_{m0}}{C_{11}} \right) \tag{A.39}$$

For instance: isotropic material

For isotropic material the elastic coefficient matrix form is the same as given in Eq. (A.33) for cubic crystal. The additional applied condition for the isotropic symmetry is $C_{11} - C_{12} = 2C_{44}$. It can be noted that the term C_{12} corresponds to the ratio longitudinal stress and longitudinal strain in the x and y-directions, respectively. such terms occur, when the material is compressed in one direction, in perpendicular direction it tends to expand. The relation given came form the requirement that the tensor C keeps the same from. However, the axes are rotated from their original position. It follow that for isotropic material, there are only two independent elastic constants. These are the Lame constants and can be defined as,

$$\lambda = C_{12}$$
$$\mu = C_{44} \tag{A.40}$$

Which provides,

$$C_{11} = C_{12} + 2C_{44} = \lambda + 2\mu \tag{A.41}$$

Appendix B

Boundary Conditions in Symmetry Axes

Categorising symmetry axes boundary conditions

If the structure of the waveguide exhibits a two-fold symmetry, only considering one-quarter of the waveguide will allow a much finer mesh division to be used. This not only can avoid mode degeneration by separating two interacting modes, but also allow much improved solutions for a given computer resource. The combinations of $\mathbf{n} \times \mathbf{U}$ and $\mathbf{n}.\mathbf{U}$ at the vertical and horizontal symmetry lines can be used, and these will provide 4 combinations, thus all the shear acoustic U_{mn}^X and U_{mn}^Y modes, and longitudinal acoustic U_{mn}^Z modes with various combinations of m and n values, being them even or odd, can be extracted. The possible symmetry boundary conditions were shown in Fig. 4.2.

In the Table B.1, all of these 4 combinations based on the presence of the displacement profile on the symmetric vertical and horizontal axes are listed. If displacement profiles exists, '$\checkmark$' is provided, other wise 'X' is given.

Table B.1 Detecting presence of displacement fields at the symmetry boundary walls

Categories	Horizontal Symmetry Wall			Vertical Symmetry Wall		
	U_X	U_Y	U_Z	U_X	U_Y	U_Z
1	$\checkmark$	X	$\checkmark$	$\checkmark$	X	X
2	X	$\checkmark$	X	X	$\checkmark$	$\checkmark$
3	$\checkmark$	X	$\checkmark$	X	$\checkmark$	$\checkmark$
4	X	$\checkmark$	X	$\checkmark$	X	X

Figs. B.1, B.2, B.3 and B.4 further illustrate the physical meaning of the existence of the displacement profiles in the horizontal and vertical symmetry walls.
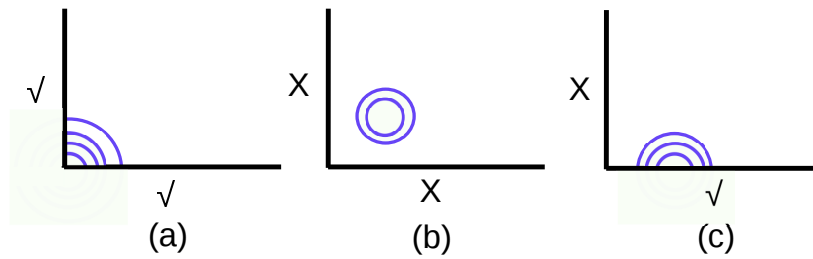
Fig. B.1 Drawn two-fold symmetric displacement profile of (a) U_X, (b) U_Y and (c) U_Z components of U_{11}^X mode fall in category 1.
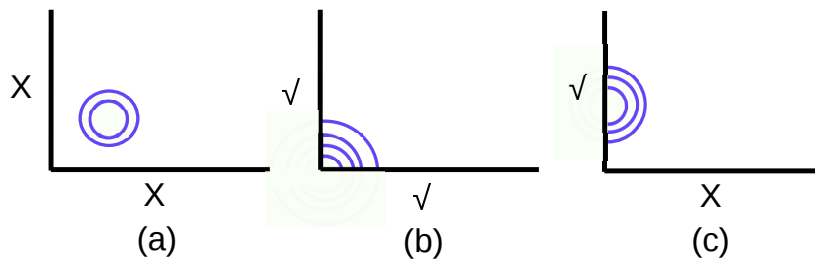
Fig. B.2 Drawn two-fold symmetric displacement profile of (a) U_X, (b) U_Y and (c) U_Z components of U_{11}^Y mode fall in category 2.
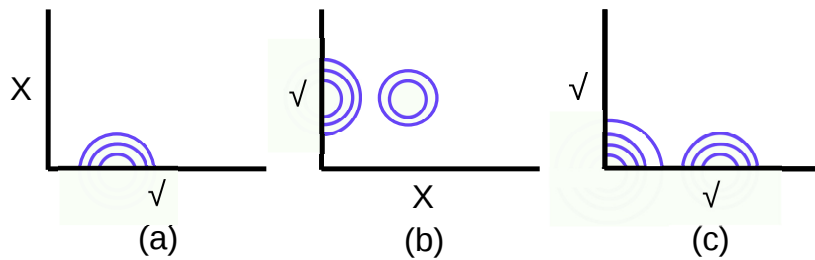
Fig. B.3 Drawn two-fold symmetric displacement profile of (a) U_X, (b) U_Y and (c) U_Z components of U_{21}^X mode fall in category 3.
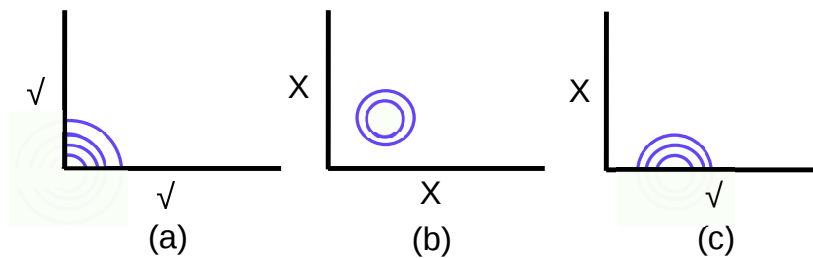
Fig. B.4 Drawn two-fold symmetric displacement profile of (a) U_X, (b) U_Y and (c) U_Z components of U_{12}^X mode fall in category 4.

In general, the category 1 includes all shear acoustic U_{mn}^X modes with m and n both odd, all shear acoustic U_{mn}^Y modes with m and n both even and all longitudinal acoustic U_{mn}^Z modes

with m being even and n being odd. Whereas, the category 2 consists of all shear acoustic U_{mn}^{X} modes with m and n both even, all shear acoustic U_{mn}^{Y} modes with m being even and n being odd and all longitudinal acoustic U_{mn}^{Z} modes with m being odd and n being even. But, the category 3 can be used for all shear acoustic U_{mn}^{X} modes with m being even and n being odd, all shear acoustic U_{mn}^{Y} modes with m being odd and n being even and all longitudinal acoustic U_{mn}^{Z} modes with m and n both odd. Finally, the category 4 covers all shear acoustic U_{mn}^{X} modes with m being odd and n being even, all shear acoustic U_{mn}^{Y} modes with m being even and n being odd and all longitudinal acoustic U_{mn}^{Z} modes with m and n both even.

The possible selection of categories for the most of the acoustic mode profiles which are discussed in the text of this thesis, are listed in the Table B.2 below. To extract two-fold symmetry profile of the listed modes, the choice of category in the left column will be applicable.

Table B.2 Four categories applicable to symmetry boundary walls

Categories	Acoustic Modes
1	$U_{21}^{Z}, U_{41}^{Z}, U_{11}^{X}, U_{31}^{X}, U_{22}^{Y}$ etc.
2	$U_{32}^{Z}, U_{41}^{Y}, U_{22}^{X}, U_{31}^{Y}$ etc.
3	$U_{11}^{Z}, U_{31}^{Z}, U_{12}^{Y}, U_{21}^{X}, U_{41}^{X}$ etc.
4	$U_{22}^{Z}, U_{12}^{X}, U_{21}^{Y}, U_{41}^{Y}$ etc.

List of Publications

Journal Papers

[1] B. M. A. Rahman, M. M. Rahman, S. Sriratanavaree, N. Kejalakshmy, and K. T. V. Grattan, "Rigorous analysis of the transverse acoustic modes in optical waveguide by exploiting their structural symmetry", *App. Opt.*, vol. 53, no. 29, pp. 6797–6803, Oct. 2014.

[2] B. M. A. Rahman and M. M. Rahman, "Characterization of sound-light interaction in a silica planar optical waveguide by finite element method", *J. Opt. Soc. Am. B*, vol. 33, no. 5, pp. 810–818, Apr. 2016.

[3] M. M. Rahman and B. M. A. Rahman, "Evolution of acoustic modes and acousto-optical interaction in an air-clad silica strip waveguide", submitted to *J. Lightwave Technol.*

Book Chapter

[1] B. M. A. Rahman, M. M. Rahman, S. Sriratanavaree, N. Kejalakshmy, and K. T. V. Grattan, "Rigorous analysis of acousto-optic interactions in optical waveguides", expected to publish in *Springer Book: Recent trends in computational photonics.*

Conference Papers

[1] B. M. A. Rahman and M. M. Rahman, "Characterization of Light-sound Interaction in Optical Waveguides", Invited paper, *2nd International conference on opto-electronics and applied optics 2015 (IEEE OPTRONIX-2015)*, University of British Columbia, AMS conferences, UBC campus, Vancouver, Canada, 16th -17th Oct., 2015.

[2] M. M. Rahman and B. M. A. Rahman, "Interactions of Acoustic and Optical Waves in Ge-doped Silica Planar Optical Waveguide", *Advanced Photonics Congress*, Boston, USA, 27 Jun. - 01 Jul., 2015

Conference Poster

[1] M. M. Rahman and B. M. A. Rahman, "Acousto-optical interaction in Ge-doped silica planar optical waveguide", *Optical wave and waveguide theory and numerical modelling workshop (OWTNM 2015)*, City University London, UK, 17-18 Apr. 2015.

References

A

◇ K. S. Abedin, "Observation of strong stimulated Brillouin scattering in single-mode As_2Se_3 chalcogenide fiber", *Opt. Exp.*, vol. 13, no. 25, pp. 10266–10271, Dec. 2005.

◇ G. P. Agrawal, *Nonlinear Fiber Optics*, 5th ed. Waltham, MA, USA: Academic Press, 2013.

◇ S. Ahmed, "Finite-element method for waveguide problems," *Electronics Lett.*, vol. 18, no. 4, pp. 387-389, 1968.

◇ M. N. Alahbabi, Y. T. Cho and T. P. Newson, "Simultaneous temperature and strain measurement with combined spontaneous Raman and Brillouin scattering", *Opt. Lett.*, vol. 30, issue. 11, pp. 1276–1278, Jun. 2005.

◇ M. N. Al-Ahbabi,"Distributed optical fibre sensors based on the coherent detection of spontaneous Brillouing scattering", *Ph. D. Thesis*, ORC, University of Southampton, p. 14, Jun. 2005.

◇ M. H. Al-Mansoori and M. A. Mahdi, "Multiwavelength L-band Brillouin-erbium comb fiber laser utilizing nonlinear amplifying loop mirror," *J. Lightwave Technol.*, vol. 27, no. 22, pp. 5038–5044, Nov. 2009.

◇ I. Aryanfar, C. Wolff, M. J. Steel, B. J. Eggleton and C. G. Poulton, "Mode conversion using stimulated Brillouin scattering in nanophotonic silicon waveguide," *Opt. Exp.*, vol. 22, no. 23, pp. 29270–29282, Nov. 2014.

◇ O. Aso, M. Tadakuma and S. Namiki, "Four-wave Mixing in optical fibers and its application", *Furukawa Review*, no. 19, pp. 63–68, Apr. 2000.

◇ B. A. Auld and G. S. Kino, "Normal mode theory for acoustic waves and its application to the interdigital transducer," *IEEE Trans. Electron Devices*, vol. 18, no. 10, pp. 898-908, Oct. 1971.

◇ B. A. Auld, *Acoustic Fields and Waves in Solids*, John Wiley & Sons, 1973.

B

◇ G. Bahl, M. Tomes, F. Marquardt and T. Carmon, "Observation of spontaneous

Brillouin cooling," *Nat. Phys.*, vol. 8, pp. 203–207, 2012.

◇ G. Bahl, K. H. Kim, W. Lee, J. Liu, X. Fan and T. Carmon, "Brillouin cavity optomechanics with microfluidic devices," *Nat. Commun.*, vol. 4, no. 1944, Feb. 2013.

◇ R. A. Bellman, G. Bourdon, G. Alibert, A. Beguin, E. Guist, L. B. Simpson, P. Lehuede, L. Guiziou, and E. LeGuen, "Ultralow loss high delta silica Germania planar waveguide," *J. Electrochemical Soc.*, vol. 151, no. 8, pp. G541-G547, 2004.

J. -C. Beugnot, T. Sylvestre, H. Maillotte, G. Melin and V. Laude, "Guided acoustic wave Brillouin scattering in photonic crystal fibers," *Opt. Lett.*, vol. 32, no. 1, pp. 17–19, Jan. 2007.

◇ J. -C. Beugnot, T. Sylvestre, D. Alasia, H. Maillotte, V. Laude, A. Monteville, L. Provino, N. Traynor, S. F. Mafang and L. Thevenaz, "Complete experimental characterization of stimulated Brillouin scattering in photonic crystal fiber," *Opt. Exp.*, vol. 15, no. 23, pp. 15517–15522, Nov. 2007.

◇ J. -C. Beugnot and V. Laude, "Electrostriction and guidance of acoustic phonons in optical fibers," *Phys. Rev. B*, vol. 86, no. 22, 224304, Dec. 2012.

◇ J. -C. Beugnot, R. Ahmad, M. Rochette, V. Laude, H. Maillotte and T. Sylvestre, "Reduction and control of stimulated Brilloin scattering in polymer-coated chalcogenide optical microwires," *Opt. Lett.*, vol. 39, no. 3, pp. 482–485, Feb. 2014.

◇ J. -C. Beugnot, S. Lebrun, G. Pauliat, H. Maillotte, V. Laude and T. Sylvestre, "Brillouin light scattering from surface acoustic waves in a subwavelength-diameter optical fibre," *Nature Communications*, vol. 5, article no. 5242, pp. 1-6, Oct. 2014.

◇ J. M. C. Boggio, J. D. Marconi and H. L. Fragnito, "Experimental and numerical investigation of the SBS-threshold increase in an optical fiber by applying strain distributions," *J. Lightwave Technol.*, vol. 23, no. 11, pp. 3808–3814, Nov. 2005.

◇ R. W. Boyd, *Nonlinear Optics*, 3rd ed. New York, USA: Academic Press, 2008.

◇ L. Brillouin, "Diffusion de la lumière et des rayons X par un corps transparent homogène: Influence de l'agitation thermique." *Ann. Phys.(Paris)*, vol. 17, no. 88-122, p. 21, 1922.

◇ T. F. S. Buttner, I. V. Kabakova, D. D. Hudson, R. Pant, E. Li, and B. J. Eggleton, "Multi-wavelength gratings formed via cascaded stimulated Brillouin scattering," *Opt. Exp.*, vol. 20, no. 24, Nov. 2012.

◇ T. F. S. Buttner, I. V. Kabakova, D. D. Hudson, R. Pant, C. G. Poulton, A. C. Judge and B. J. Eggleton, "Phase-locking and pulse generation in multi-frequency Brillouin oscillator via four wave mixing," *Scientific Reports*, vol. 4, no. 5032, May 2014.

C

⋄ G. Canat, A. Durecu, G. Lesueur, L. Lombard, P. Bourdon, V. Jolivet and Y. Jaouen, "Characteristics of the Brillouin spectra in Erbium-Ytterbium fibers", *Opt. Exp.*, vol. 16, no. 5, pp. 3212–3222, Mar. 2008.

⋄ R. Y. Chiao, C. H. Townes and B. P. Stoicheff, "Stimulated Brillouin scattering and coherent generation of intense hypersonic waves", *Phy. Rev. Lett.*, vol. 12, no. 21, pp. 592–595, May 1964.

⋄ S. Chin, L, Thevenaz, J. Sancho, S. Sales, J. Capmany, P. Berger, J. Bourderionnet and D. Dolfi, "Broadband true time delay for microwave signal processing, using slow light based on stimulated Brillouin scattering in optical fibers," *Opt. Exp.*, vol. 18, no. 21, pp. 22599–22613, Oct. 2010.

⋄ Y. T. Cho and T. P. Newson, "Brillouin-based distributed fibre temperature sensors at 1.53 μm using Raman amplification", 15th *International conference on optical fiber sensors technical digest (OFS)*, pp. 305–309, May 2002.

⋄ R. W. Clough, "The finite element method in plane stress analysis," *Proceedings of 2nd ASCE Conference on Electronic Computation*, Pittsburgh, Pa., Sep. 1960.

⋄ R. Courant, "Variational methods for the solution of problems of equilibrium and vibrations," *Bull. Amer. Math. Soc.*, vol. 49, no. 1, pp. 1-23, 1943.

D

⋄ P. Dainese, P. St. J. Russell, N. Joly, J. C. Knight, G. S. Wiederhecker, H. L. Fragnito, V. Laude and A. Khelif, "Stimulated Brillouin scattering from multi-GHz-guided acoustic phonons in nanostructured photonic crystal fibres," *Nature Phys.*, vol. 2, pp. 388-392, Jun. 2006.

⋄ M. J. Damzen, V. I. Vlad, V. Babin and A. Mocofanescu, *Stimulated Brillouin Scattering: Fundamentals and Applications*, Temple Back, Bristol, UK: Institute of Physics, 2003.

⋄ S. Dasgupta, F. Poletti, S. Liu, P. Petropoulos, D. J. Richardson, L. Grüner-Nielsen and S. Herstrom, "Modelling Brillouin gain spectrum of solid and microstructured optical fibers using a finite element method," *J. Lightwave Technol.*, vol. 29, no. 1, pp. 22–30, Jan. 2011.

⋄ J. B. Davies, Chapter:2, *The finite element method*, in *Numerical Technique for Microwave and Milimeter-wave Passive Structure*, Edited by: T. Itoh, John Wiley & Sons, 1989.

⋄ P. D. Dragic, "Simplified model for effect of Ge doping on silica fibre acoustic properties," *Electronics Lett.*, vol. 45, no. 5, pp. 256-257, Feb. 2009.

⋄ P. D. Dragic, "The acoustic velocity of Ge-doped silica fibers: A comparison of two models," *Int. J. App. Glass Sci.*, vol. 1, no. 3, pp. 330-337, Aug. 2010.

⋄ P. Dragic, J. Ballato, A. Ballato, S. Morris, T. Hawkins, P. -C. Law, S. Ghosh and M. C. Paul, "Mass density and the Brillouin spectroscopy of aluminosilicate optical fibers," *Opt. Mat. Exp.*, vol. 2, no. 11, pp. 1641–1654, Nov. 2012.

⋄ P. D. Dragic, J. Ballato, S. Morris and T. Hawkins, "Pockel's coefficient of alumina in aluminosilicate optical fiber," *J. Opt. Soc. Am. B*, vol. 30, no. 2, pp. 244-250, Feb. 2013.

E

⋄ B. J. Eggleton, C. G. Poulton and R. Pant, "Inducing and harnessing stimulated Brillouin scattering in photonic integrated circuits," *Adv. Opt. Phot.*, vol. 5, pp. 536–587, Dec. 2013.

F

⋄ G. W. Faris, L. E. Jusinski and A. P. Hickman, "High-resolution stimulated Brillouin gain spectroscopy in glasses and crystals," *J. Opt. Soc. Am. B*, vol. 10, no. 4, pp. 587-599, Apr. 1993.

⋄ G. M. Fernandes, N. J. Muga, A. M. Rocha and A. N. Pinto, "Switching in multicore fibers using flexural acoustic waves," *Opt. Exp.*, vol. 23, no. 20, pp. 26313-26325, Oct. 2015.

⋄ C. Florea, M. Bashkansky, Z. Dutton, J. Sanghera, P. Pureza and I. Aggarwal, "Stimulated Brillouin scattering in single-mode As_2S_3 and As_2Se_3 chalcogenide fibers," *Opt. Exp.*, vol. 14, no. 25, pp. 12063–12070, Dec. 2006.

⋄ K. L. J. Fong, "A study of curvature effects on guided elastic waves," *Ph. D. Thesis*, Department of Mechanical Engineering, Imperial College London, Oct. 2005.

H

⋄ M. W. Haakestad and H. E. Engan, "Acoustic characterization of a birefringent two-mode photonic crystal fiber," *Opt. Exp.*, vol. 14, no. 16, pp. 7319–7328, Jun. 2006.

⋄ A. -C. Hladky-Hennion, "Finite element analysis of the propagation of acoustic waves in waveguides," *J. Sound Vib.*, vol. 194, no. 2, pp. 119-136, Jul. 1996.

⋄ A. H. Hartog, "A distributed temperature sensor based on liquid-core optical fibers", *J. Lightwave Technol.*, vol. LT-1, no. 3, pp. 498-509, Sep. 1983.

I

⋄ U. S. Inan and R. A. Marshall, *Numerical Electromagnetics: The FDTD Method*, NY,

USA: Cambridge University Press, 2011.

J

⋄ C. K. Jen, A. Saffaai-Jazi, and G. W. Farnell, "Leaky modes in weakly guiding fiber acoustic waveguides," *IEEE Tran. Ultrason. Ferroelectr. Freq. Control*, vol. UFFC-33, no. 6, pp. 619-627, Nov. 1986.

⋄ J. Jiang, K. Baik and T. G. Leighton, "Acoustic attenuation, phase and group velocities in liquid-filled pipes II: simulation for spallation neutron sources and planetary exploration," *J. Acoust. Soc. Am.*, vol. 130, no. 2, pp. 695-706, Aug. 2011.

K

⋄ A. Kobyakov, S. Kumar, D. Q. Chowdhury, A. B. Ruffin, M. Sauer, S. R. Bickham and R. Mishra, "Design concept for optical fibers with enhanced SBS threshold," *Opt. Exp.*, vol. 13, no. 14, pp. 5338–5346, Jul. 2005.

⋄ Y. Koyamada, S. Sato, S. Nakamura, H. Sotobayashi and W. Chujo, "Simulating and designing Brillouin gain spectrum in single-mode fibers," *J. Lightwave Technol.*, vol. 22, no. 2, pp. 631–639, Feb. 2004.

⋄ J. Kushibiki, H. Maehara and N. Chubachi, "Acoustic properties of evaporated chalcogenide glass films," *Elect. Lett.*, vol. 17, no. 9, pp. 322–323, Apr. 1981.

L

⋄ P. E. Lagasse, "Higher-order finite-element analysis of topographic guides supporting elastic surface waves," *J. Acoust. Soc. Am.*, vol. 53, no. 4, pp. 1116–1122, Jan. 1973.

⋄ V. Laude, A. Khelif, S. Benchabane, M. Wilm, T. Sylvestre, B. Kibler, A. Mussot, J. M. Dudley and H. Maillotte, "Phononic bandgap guidance of acoustic modes in photonic crystal fibers," *Phy. Rev. B*, vol. 71, no. 045107, Jan. 2005.

⋄ V. Laude and J. -C Beugnot, "Generation of phonons from electrostriction in small-core optical waveguides," *AIP Adv.*, vol. 3, no. 042109, Apr. 2013.

⋄ P. -C. Law, Y. -S. Liu, A. Croteau and P. D. Dragic, "Acoustic coefficients of P_2O_5-doped silica fiber: acoustic velocity, acoustic attenuation, and thermo-acoustic coefficient," *Opt. Mat. Exp.*, vol. 1, no. 4, pp. 686–699, Aug. 2011.

⋄ K. J. Lee, K. S. Hong, H. C. Park and B. Y. Kim, "Plarization coupling in a highly birefringent photonic crystal fiber by torsional acoustic wave," *Opt. Exp.*, vol. 16, no. 7, pp. 4631–4638, Mar. 2008.

⋄ D. M. H. Leung, "Characterization of silicon photonics devices," *Ph. D. Thesis*, School of Engineering and Mathematical Sciences, City University London, Jan. 2013.

◇ M. -J. Li, S. Li and D. A. Nolan, "Silica glass based nonlinear optical fibers," *IC020: Optical Comm.*, International society for optics and photonics, vol. 6025, 602503, pp. 1-9, 2006.

◇ M. -J. Li, X. Chen, J. Wang, S. Gray, A. Liu, J. A. Demeritt, A. B. Ruffin, A. M. Crowley, D. T. Walton, and L. A. Zenteno, "Al-Ge co-doped large mode area fiber with high SBS threshold," *Opt. Exp.*, vol. 15, no. 13, pp. 8290-8299, Jun. 2007.

◇ J. Li, H. Lee and K. J. Vahala, "Microwave synthesizer using an on-chip Brillouin oscillator," *Nat. Commun.*, vol. 4, no. 2097, Jun. 2013.

◇ S. D. Lim, H. C. Park, I. K. Hwang and B. Y. Kim, "Combined effects of optical and acoustic birefringence on acousto-optic mode coupling in photonic crystal fiber," *Opt. Exp.*, vol. 16, no. 9, pp. 6125–6133, Apr. 2008.

◇ I. C. M. Littler, L. B. Fu, E. C. Magi, D. Pudo and B. J. Eggleton, "Widely tunable, acousto-optic resonances in chalcogenide As_2Se_3 fiber," *Opt. Exp.*, vol. 14, no. 18, pp. 8088-8095, Sep. 2006.

M

◇ M. Maldovan, "Sound and heat revolutions in photonics," *Nature*, vol. 503, pp. 209-217, Nov. 2013.

◇ Y. S. Mambem, E. Burov, L. -A. de Montmorillon, Y. Jaouen, G. Moreau, R. Gabet and F. Taillade, "Importance of residual stresses in the Brillouin gain spectrum of single mode optical fibers," *Opt. Exp.*, vol. 20, no. 2, pp. 1790–1797, Jan. 2012.

◇ D. Marpaung, B. Morrison, M. Pagani, R. Pant, D. -Y. Choi, B. L. Davies, S. J. Madden and B. J. Eggleton, "Low-power, chip-based stimulated Brillouin scattering microwave photonic filter with ultrahigh selectivity," *Optica*, vol. 2, no. 2, pp. 76–83, Jan. 2015.

◇ P. V. S. Marques, J. R. Bonar, A. M. P. Leite, and J. S. Aitchison, "Simultaneous UV direct writing of channel waveguides and Bragg gratings in Germanium-doped planar silica," *IEEE J. Select.Topics Quantum. Elect.*, vol. 8, no. 6, pp. 1316-1322, 2002.

◇ A. B. Matsko, A. A. Savchenkov, V. S. Ilchenko, D. Seidel and L. Maleki, "Optomechanics with surface-acoustic-wave whispering-gallery modes," *Phys. Rev. Lett.*, vol. 103, 257403, pp. 1-4, Dec. 2009.

◇ A. H. McCurdy, "Modelling of stimulated Brillouin scattering in optical fibers with arbitrary radial index profile," *J. Lightwave Technol.*, vol. 23, no. 11, pp. 3509-3516, 2005.

◇ C. McIntosh, A. Yeniay, J. Toulouse and J. -M. P. Delavaux, "Stimulated Brillouin scattering in dispersion-compensating fibers," *Opt. Fiber Technol.*, vol. 3, no. OF970213,

pp. 173-176, 1997.

◇ M. D. Mermelstein, "SBS threshold measurements and acoustic beam propagation modeling in guiding and anti-guiding single mode optical fibers," *Opt. Exp.*, vol. 17, no. 18, pp. 16225–16237, Aug. 2009.

◇ MIT open course ware module-3 (Constitutive equations), available at: [*web.mit.edu*/16.20/*homepage*/3 *constitutive*/*constitutive files*/*module 3 no solutions.pdf*]

◇ F. Mouhat and F. -X. Coudert, "Necessary and sufficient elastic stability conditions in various crystal systems," *Phys. Rev. B*, vol. 90, no. 22, 224104, 2014.

◇ G. Mur, "Edge elements, their advantages and their disadvantages," *IEEE Tran. Magnetics*, vol. 30, no. 5, pp. 3552-3557, Sep. 1994.

N

◇ NDT course material (Ultrasound), available at: [*https* : //*www.nde − ed.org*/*EducationResources*/*CommunityCollege*/*Ultrasonics*/*Physics*/*modepropagation.htm*]

◇ M. Nikles, L. Thevenaz and P. A. Robert, "Brillouin gain spectrum characterization in single-mode optical fibers," *J. Lightwave Technol.*, vol. 15, no. 10, pp. 1842-1851, Oct. 1997.

O

◇ K. Ogusu and H. Li, "Brillouin-gain coefficient of chalcogenide glasses," *J. Opt. Soc. Am. B*, vol. 21, no. 7, pp. 1302-1304, Jul. 2004.

◇ M. M. Opalinska, J. R. Taylor and R. Kashyap, "Amplification of light pulses in the visible through stimulated Raman scattering," *Opt. Comm.*, vol. 100, no. 1-4, pp. 207-210, Jul. 1993.

P

◇ R. Pant, C. G. Poulton, D. -Y. Choi, H. McFarlane, S. Hile, E. Li, L. Thevenaz, B. L. -Davies, S. J. Madden and B. J. Eggleton,"On-chip stimulated Brillouin scattering," *Opt. Exp.*, vol. 19, no. 9, pp. 8285–8290, Apr. 2011.

◇ R. Pant, D. Marpaugn, I. V. Kabakova, B. Morrison, C. G. Poulton and B. J. Eggleton,"On-chip stimulated Brillouin scattering for microwave signal processing and generation," *Laser Phot. Rev.*, vol. 8, no. 5, pp. 653–666, 2014.

◇ K. Park and Y. Jeong, "A quasi-mode interpretation of acoustic radiation modes for analyzing Brillouin gain spectra of acoustically antiguiding optical fibers," *Opt. Exp.*, vol. 22, no. 7, pp. 7932–7946, Apr. 2014.

◇ C. G. Poulton, R. Pant, A. Byrnes, S. Fan, M. J. Steel, and B. J. Eggleton,"Design for

broadband on-chip isolator using stimulated Brillouin scattering in dispersion-engineered chalcogenide waveguides," *Opt. Exp.*, vol. 20, no. 19, pp. 21235–21246, Sep. 2012.

◇ Z. A. Pyatakova and G. V. Belokopytov, "Acoustic-optical interaction in photonic crystals: frequency dependence of Bragg angle," *Moscow Uni. Phy. Bulletin*, vol. 64, no. 3, pp. 282–286, 2009.

Q

◇ W. Qiu, P. T. Rakich, H. Shin, H. Dong, M. Soljacic and Z. Wang,"Stimulated Brillouin scattering in nonoscale silicon step-index waveguides: a general framework of selection rules and calculating SBS gain," *Opt. Exp.* vol. 21, no. 25, pp. 31402–31419, Dec. 2013.

R

◇ B. M. A. Rahman and J. B. Davies, "Finite element solution of integrated optical waveguides," *J. Lightwave Technol.*, vol. LT-2, no. 5, pp. 682-688, Oct. 1984.

◇ B. M. A. Rahman, and J. B. Davies, "Vector-H finite element solution of GaAs/GaAlAs rib waveguide," *IEE Proceedings Pt. J.*, vol. 132, pp. 349-353, 1985.

◇ B. M. A. Rahman, S. S. A. Obayya, N. Somasiri, M. Rajarajan, K. T. V. Grattan, and H. A. El-Mikathi, "Design and characterization of compact single-section passive polarization rotator," *J. Lightwave Technol.*, vol. 19, pp. 512-519, 2001.

◇ B. M. A. Rahman and A. Agrawal, *Finite Element Modelling Methods for Photonics*, Norwood, MA, USA: Artech House, 2013.

◇ B. M. A. Rahman, M. M. Rahman, S. Sriratanavaree, N. Kejalakshmy, and K. T. V. Grattan, "Rigorous analysis of the transverse acoustic modes in optical waveguide by exploiting their structural symmetry," *App. Opt.*, vol. 53, no. 29, pp. 6797–6803, Oct. 2014.

◇ P. T. Rakich, C. Reinke, R. Camacho, P. Davids, and Z. Wang,"Giant enhancement of stimulated Brillouin scattering in the subwavelength limit," *Phys. Rev. X*, vol. 2, pp. 011008(1–15), Jan. 2012.

◇ D. Royer and E. Dieulesaint, *Elastic Waves in Solids I: Free and Guided Propagation*, Springer-Verlag, Berlin Heidelberg, Germany, 2000.

◇ A. B. Ruffin, M. -J. Li, X. Chen, A. Kobyakov and F. Annunziata, "Brillouin gain analysis for fibers with different refractive indices," *Opt. Lett.*, vol. 30, no. 23, pp. 3123–3125, Dec. 2005.

◇ P. St. J. Russell, D. Culverhouse and F. Farahi, "Theory of forward stimulated Brillouin scattering in dual-mode single-core fibers," *IEEE J. Quan. Elect.*, vol. 27, no. 3, pp. 836–842, Mar. 1991.

S

◇ A. Saffaai-Jazi, "Acoustic modes in optical fiberlike waveguides," *IEEE Trans. Ultrason. Ferroelectr. Freq. Control*, vol. 35, no. 5, pp. 619-627, Sep. 1988.

◇ J. Sancho, N. Primerov, S. Chin, Y. Antman, A. Zadok, S. Sales and L. Thevenaz, "Tunable and reconfigurable multi-tap microwave photonic filter based on dynamic Brillouin gratings in fibers," *Opt. Exp.*, vol. 20, no. 6, pp. 6157–6162, Mar. 2012.

◇ H. S. Seo, K. Oh and U. C. Paek, "Gain optimization of Germanosilicate fiber Raman amplifier and its application in the compensation of Raman-induced crosstalk among wavelength division multiplexing channels", Invited paper, *IEEE J. Quant. Electron.*, vol. 37, no. 9, pp. 1110–1116, Sep. 2001.

◇ Y. -R. Shen, *Principles of nonlinear optics*, 1984.

◇ H. Shin, W. Qiu, R. Jarecki, J. A. Cox, R. H. Olsson, A. Starbuck, Z. Wang and P. T. Rakich, "Tailoring stimulated Brillouin scattering in nanoscale silicon waveguide," *Nat. Commun.*, vol. 4, no. 1944, pp. 1–10, Jun. 2013.

◇ K. Shiraki, M. Ohashi and M. Tateda, "Performance of strain-free stimulated Brillouin scattering suppression fiber," *J. Lightwave Technol.*, vol. 14, no. 4, pp. 549–554, Apr. 1996.

◇ N. Somasiri and B. M. A. Rahman, "Polarization crosstalk in high index contrast planar silica waveguides with slanted sidewalls," *J. Lightwave Technol.*, vol. 21, pp. 54-60, 2003.

◇ K. Y. Song, K. S. Abedin, K. Hotate, M. G. Herraez and L. Thevenaz, "Highly efficient Brillouin slow and fast light using As_2Se_3 chalcogenide fiber," *Opt. Exp.*, vol. 14, no. 13, pp. 5860–5865, Jun. 2006.

◇ S. Sriratanavaree, "Characterisation of acoustic waves in optical waveguide," *Ph. D. Thesis*, School of Engineering and Mathematical Science, City University London, Jan. 2014.

◇ B. Stiller, M. Delque, J. -C. Beugnot, M. W. Lee, G. Melin, H. Maillotte, V. Laude and T. Sylvestre, "Frequency-selective excitation of guided acoustic modes in a photonic crystal fiber," *Opt. Exp.*, vol. 19, no. 8, pp. 7689–7694, Apr. 2011.

◇ G. O. Stone, "High-order finite elements for inhomogeneous acoustic guiding structures," *IEEE Trans. Microw. Theory Tech.*, vol. MTT-21, no. 8, pp. 538–542, Aug. 1973.

◇ V. R. Subradeepa, "Stimulated Brillouin scattering thresholds in optical fibers for lasers linewidth broadened with noise", *Opt. Exp.*, vol. 21, no. 4, pp. 4677–4687, 2013.

T

◇ L. Tartara, C. Codemard, J. -N. Maran, R. Cherif and M. Zghal, "Full modal analysis of the Brillouin gain spectrum of an optical fiber," *Opt. Comm.*, vol. 282, no. 12, pp. 2431–2436, Jun. 2009.

◇ L. Thevenaz, M. Nikles, A. Fellay, M. Facchini and P. Robert, "Truly distributed strain and temperature sensing using embedded optical fibers," *Proc. SPIE*, vol. 3330, pp. 301–314, 1998.

◇ R. N. Thurston, "Elastic waves in rods and clad rods", *J. Acoust. Soc. Am.*, vol. 64, pp. 1–37, 1978.

◇ J. Toulouse, "Optical nonlinearities in fibers: review, recent examples, and systems applications", *J. Lightwave Tech.*, vol. 23, no. 11, pp. 3625–3641, Nov. 2005.

U

◇ M. Uthman, B. M. A. Rahman, N. Kejalakshmy, A. Agrawal, H. Abana, and K. T. V. Grattan, "Stabilized large mode area in tapered photonic crystal fiber for stable coupling," *IEEE Photon. J.*, vol. 4, no. 2, pp. 340–349, Apr. 2012.

V

◇ K. Vilhelmsson, "Simultaneous forward and backward Raman scattering in low-attenuation single-mode fiber", *J. Lightwave Technol.*, vol. LT-4, no. 4, pp. 400–404, Apr. 1986.

W

◇ B. Ward and J. Spring, "Finite element analysis of Brillouin gain in SBS-suppressing optical fibers with non-uniform acoustic velocity profiles", *Opt. Exp.*, vol. 17, no. 18, pp. 15685–15699, Aug. 2009.

Y

◇ A. Yeniay, J. -M. Delavaux and J. Toulouse, "Spontaneous and stimulated Brillouin scattering gain spectra in optical fibers", *J. Lightwave Technol.*, vol. 20, no. 8, pp. 1425–1432, Aug. 2002.

◇ S. Yoo, C. A. Codemard, Y. Jeong, J. K. Sahu, and J. Nilsson, "Analysis and optimization of acoustic speed profiles with large transverse variation for mitigation of stimulated Brillouin scattering in optical fibers," *Appl. Opt.*, vol. 49, pp. 1188-1199, 2010.

◇ L. Yuan, L. Yange, Z. Junfa, T. Boyin and Y. Aidong, "Investigation on Brillouin

scattering characteristics in photonic crystal fibers," *Front. Optoelectron. China*, vol. 3, no. 3, pp. 260–263, 2010.

Z

◇ O. C. Zienkiewicz and R. L. Taylor, *The Finite Element Method for Solid and Structural Mechanics*, 7th edi., Oxford, UK: Elsevier Butterworth-Heinemann, 2005.

◇ O. C. Zienkiewicz, R. L. Taylor, and J. Z. Zhu, *The Finite Element Method: Its Basis and Fundamentals*, 7th ed. Waltham, MA, USA: Butterworth-Heinemann, 2013.

◇ W. Zou, Z. He and K. Hotate, "Experimental study of Brillouin scattering in fluorine-doped single-mode optical fibers," *Opt. Exp.*, vol. 16, no. 23, pp. 18804–18812, Nov. 2008.

◇ W. Zou and J. Chen, "All-optical generation of Brillouin dynamic grating based on multiple acoustic modes in a single-mode dispersion-shifted fiber," *Opt. Exp.*, vol. 21, no. 22, pp. 14771-14779, Jun. 2013.